UNIVERSITY OF STRATHCLYDE
Department of Bioengineering

A distributed feedback organic semiconductor laser platform for assessing the risk of cardiovascular disease

by

Anne-Marie Haughey

A thesis presented in fulfilment of the
requirements for the degree of
Doctor of Engineering

December 2014

Declaration of Authorship

This thesis is the result of the author's original research. It has been composed by the author and has not been previously submitted for examination which has led to the award of a degree.

Signed: _____

Date: _____

Frontispiece

T3 DFB lasers within a 96 well microtiter plate, excited with UV radiation (left). DFB laser sensing principle - functionalisation of the T3 surface with single stranded oligos can be used to couple complementary oligos to the laser surface. Binding is detected via a shift in laser emission wavelength (below).

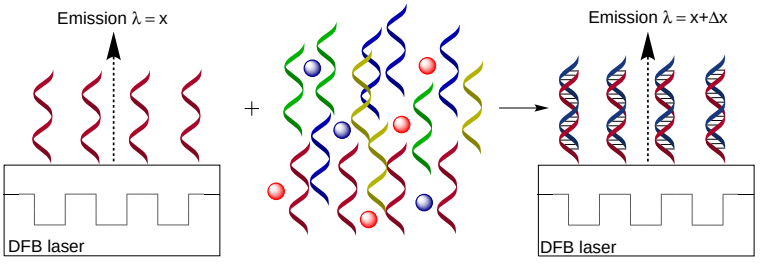

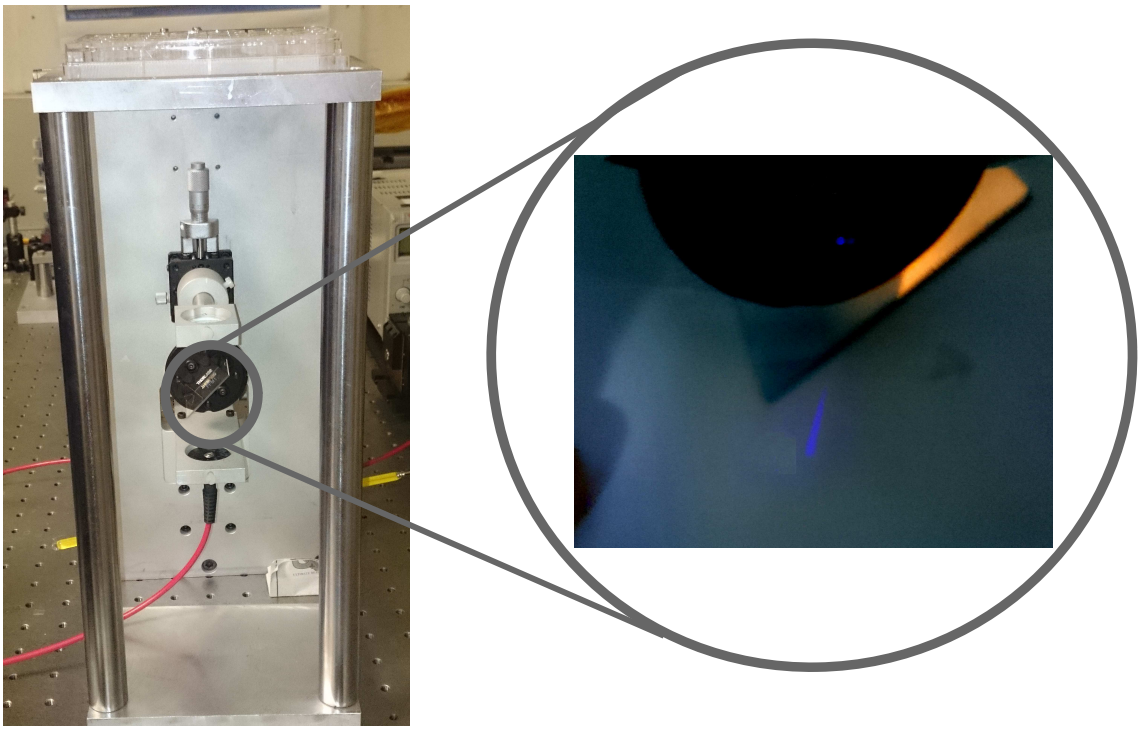

Set-up used for excitation of lasers within a microtiter plate. Laser emission is shown on a white card held over the optical fibre mount.

Abstract

Organic distributed feedback (DFB) lasers are a class of evanescent wave technology that can be used to measure changes in refractive index at the laser surface. These sensors are highly attractive for biosensing applications as they provide a sensitive platform for the label-free detection of a range of analytes, possibly in real-time, and they can be multiplexed for the detection of a suite of different analytes from a single test sample. The simple implementation of DFB lasers for sensing also means that they can be packaged into a compact sensing platform; this is especially true of DFB lasers incorporating an organic semiconductor as the gain layer where optical pumping may be performed with a compact source, such as a laser diode. In addition, organic semiconductor based DFB lasers have the potential for improved sensitivity relative to other organic DFB lasers (such as dye-doped) as the refractive index of organic semiconductors is generally higher, which leads to an increase in the interaction of the laser mode with the analyte binding region at the laser surface.

In this thesis, the first demonstration of an organic semiconductor (oligofluorene truxene (T3)) DFB laser for biosensing applications is described. Sensor development is focused on the ultimate aim of incorporating a T3 DFB laser into a compact and portable high-throughput sensing platform for the detection of cardiac biomarkers, Apolipoprotein B100, C-reactive protein and B-type natriuretic peptide in particular. Detection of these biomarkers is to be achieved via functionalisation of the T3 surface with oligonucleotide based probes.

The structure of the T3 DFB laser is optimised experimentally and theoretically by tuning the gain layer thickness to maximise sensitivity to changes in refractive index at the laser surface, such as the binding of an analyte. The optimised laser sensor has a laser threshold of 30 μJ.cm^{-2}/6 kW.cm^{-2} (5 ns pulse duration) which makes optical pumping with a laser diode a possibility.

The sensing potential of the DFB laser is shown via the detection of bulk solution refractive index changes and the addition of biomolecules to the laser surface, where a bulk sensitivity of 22 nm per refractive index unit is observed. The specific biosensing potential of the laser is highlighted through the functionalisation of the laser surface with biotin molecules and the subsequent detection of the complementary protein, avidin. The lowest limit of avidin detection achieved is 1 μg.mL^{-1}; at this level of sensitivity, the current T3 laser is expected to be able to detect the larger and more abundant of two of the three cardiac biomarker targets, ApoB and CRP. The effects of structural changes to device sensitivity are modelled theoretically and demonstrate that detection

of BNP may be achieved through the addition of a high-index cladding layer, a technique currently used for dye-doped DFB lasers.

The first demonstration of a DFB laser used for reversible sensing is also presented in this thesis. Through the use of desthiobiotin, a biotin analogue, reversible avidin detection is performed. A reversible biosensor may be of particular interest for applications where a large number of repeated measurements are required, and may be prohibitive to the use of single-use, disposable sensors.

Finally, functionalisation of the DFB laser with oligonucleotide probes is described. Several different techniques are explored for immobilisation of oligonucleotide probes on the T3 surface, with click chemistry and sulfhydryl linkage chemistries showing the most promise.

Acknowledgements

First and foremost I would like to thank my three supervisors Dr. Nicolas Laurand, Dr. Glenn Burley and Prof. Martin Dawson. Each of you were instrumental in the success of this project and supported my academic and professional development. In particular, I would like to thank Dr. Laurand for his time and patience during the knowledge transfer process relating to DFB laser theory and modelling. You have a canny ability to explain things in a clear and simple manner and I could not have asked for a better supervisor. Thanks to Dr. Burley for answering my many 'stupid' chemistry questions and his good humour whilst translating chemistry into a language I could understand. Thanks also to Prof. Dawson for your support throughout the project and your words of wisdom and guidance. Guidance on the clinical focus of this project was provided by Prof. Chris Packard so thank you for your interesting and useful discussions.

Many in the Institute of Photonics have helped me through my Eng.D journey. Special thanks goes to Dr. Johannes Herrnsdorf for getting me started with DFB lasers and by making my life significantly easier with your Matlab functions which I used on an almost daily basis. Thanks also to Dr. Benoit Guilhabert for teaching me the laser fabrication and various other things. Thanks to Ewan Mulhern, Sharon Kelly, Paul Hynd, Dr. Keith Mathieson, Dr. Jennifer Hastie and Prof. Alan Kemp who have also helped me in one way or another.

I am also grateful to Dr. Ishwar Singh and Dr. Sara De Ornellas for their help during oligo functionalisation amongst other things.

Finally, I would like to thank my partner Dr. Richard Crozier. Your help with Matlab and LaTeX was invaluable and saved me a lot of grief. My Eng.D may have seemed like a relatively straight-forward (and brief) process in comparison to your own, but I never would have done it without your love and support.

Contents

List of Figures

List of Schemes

List of Tables

Abbreviations

AFM	**A**tomic **F**orce **M**icroscopy
ApoB	**A**polipoprotein **B**100
AU	**A**rbitrary **U**nits
BBEHP-PPV	Poly[2,5-**b**is(2',5'-**b**is(2"-**e**thyl**h**exyloxy)-**p**henyl)-**p**-**p**henylene **v**inylene
BCN	**Bic**ycle(6.1.0)**n**onyne
BNP	**B**-type **N**atriuretic **P**eptide
BSA	**B**ovine **S**erum **A**lbumin
CCD	**C**harge **C**oupled **D**evice
Ck-MB	**C**reatine **K**inase **M**yocardial **B**and
CVD	**C**ardio**v**ascular **D**isease
CRP	**C**-**R**eactive **P**rotein
DCM	**Dic**hloro**m**ethane
DFB	**D**istributed **F**eed**b**ack
DI	**D**e**i**onised
DMSO	**Di**methyl**s**ulf**o**xide
DNA	**D**eoxyribo**n**ucleic **A**cid
DTT	**Di**thio**t**hreitol
ECG	**E**lectro**c**ardio**g**raphy
ELISA	**E**nzyme **L**inked **I**mmunosorbant **A**ssay
F8BD	Poly[(9,9-dioctyl-**f**luorenyl -2,7-diyl)-co-(1,4-**b**enzo-2,1',3-thia**d**iazole)]
FRET	**F**luorescence **R**essonance **E**nergy **T**ransfer
FWHM	**F**ull **W**idth **H**alf **M**aximum
HPLC	**H**igh **P**erformance **L**iquid **C**hromatography
IgG	**I**mmuno**g**lobulin **G**
InGaN	**I**ndium **G**allium **N**itride

kDa	**K**illo **Da**ltons
kRPM	**K**illo **R**evolutions **P**er **M**inute
LED	**L**ight **E**mitting **D**iode
M	**M**olar
MEH-PPV	Poly(2-**m**ethoxy-5-(2'-**e**thyl**h**exloxy)-**p**-**p**henylene **v**inylene
MI	**M**yocardial **I**nfarction
MiRNA	**Mi**cro **R**ibo**n**ucleic **A**cid
$\mathbf{M}_W$	**M**olecular **W**eight
NHS	**N**-**h**ydroxy**s**uccinimidyl
mRNA	**M**essenger **R**ibose **N**ucleic **A**cid
Nn:YAG	**N**eodymium **Y**ttrium **A**luminium **G**arnet
NT-proBNP	**N**-terminal **p**ro-**BNP**
PAH	**P**oly(**a**llylamine **h**ydrochloride)
PBS	**P**hosphate **B**uffered **S**aline
PEI	**P**oly(**e**thylene**i**mine)
pI	**I**soelectric **P**oint
PL	**P**oly **L**ysine
PMMA	**P**oly**m**ethyl**m**eth**a**crylate
PMT	**P**hoto**m**ultiplier **T**ube
POC	**P**oint **o**f **C**are
PPL	**P**oly **P**henylalanine **L**ysine
PEG	**P**oly**e**thylene **G**lycol
PPV	**P**oly **P**henylene **V**inylene
PSS	**P**oly(**s**odium 4-**s**tyrenesulfonate)
RIU	**R**efractive **I**ndex **U**nit
SERS	**S**urface **E**nhanced **R**aman **S**pectroscopy
SMCC	**S**uccinimidyl-4-(N-**m**aleimidomethyl)**c**yclohexane-**c**arboxylate
SPDP	N-**s**uccinimidyl 3-(2-**p**yridyl**d**ithio)**p**ropionate
SPR	**S**urface **P**lasmon **R**esonance
SS	**S**ingle **S**tranded
T3	**O**ligoflurene **T**ruxene
TCA	**T**ri**c**hloroacetic **A**cid
TCEP	**T**ris(2-**c**arboxy**e**thyl)**p**hosphine

TE	**T**ransverse **E**lectric
TM	**T**ransverse **M**agnetic
TNF-α	**T**umor **N**ecrosis **F**actor-α
UV	**U**ltra**v**iolet

For Richard, my hero.

Part I

Introduction

Chapter 1

Point of care medical diagnostics

Point of care (POC) testing is defined by the College of American Pathologists as being any test designed to be used at or near the site where the patient is located, does not require permanent dedicated space, and does not use the facilities of the clinical laboratory. A POC device is defined by the Medicines and Healthcare Products Agency as being any device or instrument that may be used to produce test results in the POC setting.

The use of POC diagnostics in healthcare is commonplace nowadays with urine dipstick tests, blood glucose meters and blood gas analysers likely to be found in every UK hospital and many GP surgeries [1]. POC testing is not a new concept, the first POC test dating back to 1945 with the introduction of a test for the presence of glucose in the urine [2]. This simple test involved mixing a tablet containing a number of different reagents with a urine sample; in the presence of glucose the solution changed colour from blue to green to orange. The glucose concentration could be estimated by visually comparing the colour of the solution to a colour chart provided with the test kit, as shown in Figure 1.1a. The continued research into POC glucose testing led to the introduction of the first qualitative blood glucose test in 1965 [3] with the more sophisticated quantitative tests that followed leading to the battery powered, hand-held, easy to use devices widely used today, as shown in Figure 1.1b [4]. Glucose POC testing paved the way for the development of POC devices for assessment of a wide variety of biochemical markers used in patient diagnosis and monitoring. The key objective of POC testing is to obtain results for a particular investigation quickly so that the most appropriate treatment regimen can be implemented. Therefore, one of the areas where POC testing has been widely adopted is in cardiovascular disease (CVD), and in particular, assessment of patients experiencing an acute cardiac event such as a myocardial infarction (MI). Establishing a diagnosis in patients with chest

pain as early as possible is extremely important as an untreated MI has a high risk of mortality and immediate treatment is linked to a significantly improved prognosis [5, 6]. However, establishing a diagnosis can be difficult, especially in patients with non-definitive electrocardiography (ECG) results. POC testing of a range of biomarkers associated with certain CVD events can be used to help determine a diagnosis within minutes.

1.1 Thesis objective

The aim of the work encompassed within this thesis was to develop and optimise a compact, modular and cost-effective optical diagnostic sensing system that can detect biomarkers in blood serum. The sensor is a plastic organic semiconductor distributed feedback (DFB) laser. DFB laser biosensors measure the change in refractive index at the laser surface. Therefore, by functionalising the laser with probe molecules, the specific binding of biomolecules to the laser surface can be detected and quantified. Organic DFB lasers are simple in their implementation and fabrication and they can be incorporated into compact, portable sensing systems through the use of a laser diode excitation source (with potential for pumping with InGaN laser diodes which are mass produced and therefore very cost effective) and a miniature spectrometer for collection and analysis of laser emission. These properties make DFB lasers an attractive transducer for biosensing applications.

The DFB laser sensor can be used in principle to specifically detect any analyte that will bind to a probe molecule. However, detection of cardiac biomarkers was the focus for demonstration of the sensing potential of the DFB laser system as there is an unmet need for a cardiac biosensor that can rapidly detect a wide range of cardiac biomarkers simultaneously with high sensitivity and specificity. Biomarker detection was to be focused on three particular cardiac biomarkers, B-type Natriuretic Peptide (BNP), Apolipoprotein B100 (ApoB) and C-reactive Protein (CRP). These three biomarkers are indicative of the presence of cardiac disease and can inform clinical treatment and patient prognosis and will allow the detection limits of the DFB laser sensor to be explored as BNP, CRP and ApoB are expressed at low (>100 pg.mL^{-1}) [7], moderate (>0.01 mg.mL^{-1}) [8] and high (>1 mg.mL^{-1}) [9] levels respectively.

This thesis presents the progress in the development of the DFB laser biosensing system. Optimisation of the DFB laser structure was performed and the non-specific detection of refractive index changes at the laser surface was demonstrated through exposure of the laser to bulk solutions and adsorption of biopolymer layers to the laser surface. Following this, the specific biosensing capability of the laser was shown via the detection

of a protein, with a limit of detection of 1 μg.mL^{-1}. Reversible biosensing was also demonstrated, highlighting the potential for the sensor's use not just in clinical diagnostics settings but also in other fields such as drug discovery where the large number of measurements required make the use of single-use biosensors impracticable. Finally, functionalisation of the DFB laser with nucleic acid probes is demonstrated, paving the way towards cardiac biomarker detection.

1.1.1 Thesis aims and outline

The aims of this thesis are:

- Development and optimisation of the organic semiconductor DFB laser for biosensing
- Demonstration of non-specific refractive index sensing
- Demonstration of non-specific detection of the presence of material on the laser surface
- Demonstration of specific biomolecule detection
- Functionalisation of the laser surface with nucleic acid probes and detection of nucleic acid target molecules
- Cardiac biomarker detection

As an introduction to Chapter 1, an overview of the benefits of POC testing in CVD, alongside a summary of the POC technologies used in CVD biomarker testing, is provided. The remainder of the chapter introduces the operation of DFB lasers and the motivation for pursuing an all-organic approach to DFB laser biosensing. A literature review of DFB laser biosensing is also presented here. Chapter 2 explains the physics of DFB laser sensing and introduces the numerical model used to characterise the laser sensors. In Chapter 3, the optimisation and characterisation of the organic DFB lasers for biosensing is described alongside demonstration of non-specific sensing. Specific biomolecule detection and reversible biosensing results are presented in Chapter 4. Early attempts at nucleic acid detection and future development are the subject of Chapter 5. Finally, concluding remarks are provided in Chapter 6.

(a) (b)

FIGURE 1.1: Photographs of (a) a Clinitest glucose testing kit (www.tudiabetes.org) and (b) a modern glucose testing device (www.francoischarron.com).

1.2 Point of care testing in cardiovascular disease

Measurement of the levels of circulating cardiac biomarkers are used extensively in the assessment of CVD patients. For example, a diagnosis of acute MI in a patient presenting chest pain and other symptoms suggestive of a MI can only be established if that patient also has elevated levels of cardiac troponin I or creatine kinase myocardial band isoensyme (Ck-MB) [10]. The main advantage of POC testing over the use of the traditional clinical biochemistry laboratory is the significant reduction in the turnaround time for results. POC devices are capable of providing results within minutes whereas sending blood samples to a centralised laboratory and return of results can take upwards of an hour [11]. The rapid provision of results facilitated by POC testing speeds up the decision-making and patient management process which has been shown to have a positive effect on the patient outcome [5, 6].

There are many different POC devices available for detection of an increasing number of biomarkers deemed to have diagnostic potential in the CVD setting. Table 1.1 lists some of the POC tests that have a CE mark and the biomarkers they detect. There are many other POC devices available, in the US for example, but the aim is to provide an overview of the capabilities of those commercially available and this subset covers the most established devices. There are a number of different transduction methods employed by POC devices, described in more detail below, but the principle of biomarker detection is essentially very similar. Biomarker detection is achieved through use of an immunoassay. An immunoassay is a highly sensitive and specific test used to determine the concentration of an analyte in a solution through the use of capture antibodies [18]. Implementation of an immunoassay may take a number of different formats but a common method

POC device	**Biomarkers**	**Assay time**	**Detection method**	**Multiplexing capability**
i-STAT [12] (Abbot Point of Care)	Troponin I CK-MB BNP	≈10 min.	Amperometric	No
Triage MeterPro [13] (Alere)	Troponin I Myoglobin CK-MB	≈15 min.	Fluorescence intensity	Yes
Cobas h232 [14] (Roche Diagnostics Ltd.)	Troponin I Myoglobin CK-MB NT-ProBNP	8 - 12 min.	Fluorescence intensity	No
Decision Point [15] (Nexus Dx)	Troponin I Myoglobin CK-MB	≈15 min.	Chemiluminometric	No*
RAMP Reader [16] (Response Biomedical Corp.)	Troponin I Myoglobin CK-MB NT-ProBNP	≈15 min.	Fluorescence intensity	No
Stratus CS Acute Care Diagnostics System [17] (Siemens)	Troponin I Myoglobin CK-MB NT-ProBNP	14 min.	Fluorescence intensity	No

TABLE 1.1: Summary of the POC devices for cardiac biomarker detection available in the UK. *In the UK there are three separate devices for each biomarker, but a multiplexed version is available in the US, as shown in Figure 1.6. Fluorescence intensity, chemiluminometric and amperometric sensing is described in more detail in Sections 1.2.1.1, 1.2.1.2 and 1.2.2.1 respectively.

used is to anchor antibodies, that will bind specifically to the antigen (or biomarker) of interest, to a solid surface. Upon passing a test solution containing the biomarker of interest over the immobilised antibodies, the biomarker will bind to the antibody. Commonly, a second antibody is then washed over the antibody-biomarker conjugate and binds to the biomarker resulting in an antibody-biomarker-antibody structure. This kind of immunoassay is known as a sandwich assay and the detection sequence is shown in Figure 1.2. The second antibody may be labelled with a fluorescent dye or an enzyme that will induce a colour change in the test solution thereby facilitating a quantitative measurement of the biomarker concentration through, for example, spectrofluorometry or spectrophotometry respectively.

As mentioned, immunoassays allow for highly sensitive and specific detection of a range of biomarkers and enzyme-linked immunosorbant assays (ELISA) are often the gold-standard for antigen detection in disease diagnosis. Antibodies do however have a number of limitations which in turn will limit the technologies that rely upon them for biomarker detection. One of the biggest drawbacks with antibodies is their production.

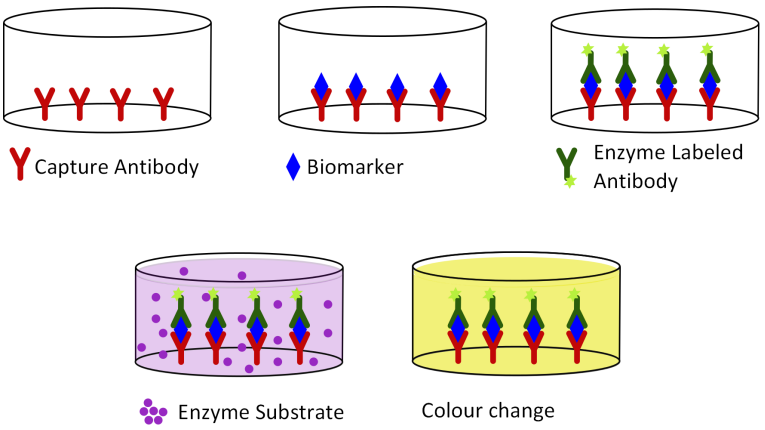

FIGURE 1.2: The steps involved in a sandwich immunoassay. A substrate is functionalised with a capture antibody and is exposed to a solution containing the target biomolecule. Binding of the biomolecule to the capture antibody occurs. A secondary antibody, labelled with an enzyme, for example, is washed over the substrate and binds with the biomarker, forming the sandwich structure. A solution containing a substrate that will be catalysed by the enzyme is added. This results in a reaction which induces a colour change in the solution which can be detected and indicates the presence of the biomarker.

Antibodies are proteins produced by cells, therefore production of antibodies relies on developing cell cultures to produce the antibody of interest. Cell culture assays are labour intensive and expensive and have the inherent risk of contamination of the cell line with viral or bacterial agents, which may affect or prevent antibody production. Furthermore, variations between cell culture batches can result in differences between the antibodies produced [19]. As is the case for most proteins, antibodies are susceptible to denaturing when exposed to temperature fluctuations. Therefore, antibodies must be kept in cold storage and they tend to have a limited shelf-life. These properties therefore dictate the conditions for the use of the POC tests listed in Table 1.1.

An alternative to antibody based detection is the use of nucleic acid based probes as depicted in Figure 1.3. The complementary binding between two single stranded oligonucleotides (oligos) is known as hybridisation. During hybridisation, binding occurs between adenine and thymine (or uracil in the case of RNA) and guanine and cytosine nucleotides. The formation of hydrogen bonds between complementary bases is very specific and means that hybridisation will only occur between complementary single stranded oligos. Single stranded oligos can be used for the detection of circulating messenger RNA (mRNA), the instructions for production of protein biomarkers. Or aptamers, folded single stranded oligos that bind molecular targets such as proteins, can be used. Nucleic acid based probes overcome many of the disadvantages associated with antibodies whilst maintaining excellent sensitivity and specificity [19]. For example, aptamers are chemically synthesised in a process that can be automated and is therefore cost effective relative to antibody production. The production method also

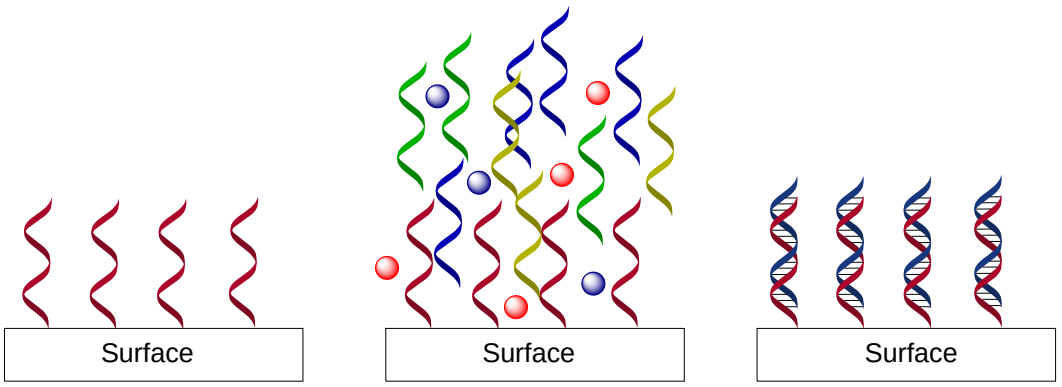

FIGURE 1.3: Nucelic acid oligos can be used to detect the complementary oligo. For example, a surface functionalised with a single stranded oligonucleotides (red ribbons), as shown on the left, can be exposed to a test sample containing a range of oligos, complementary (blue) and non-complementary (yellow and green), and other biomolecules (red and blue spheres), shown in the centre. Only complementary oligonucleotides will hybridise for specific detection, as shown on the right. Oligo hybridisation may be detected though a variety of means, e.g. via the addition of a fluorophore to the complementary oligo.

ensures little or no variation from batch to batch. Aptamers are also more thermally robust [19], therefore storage of POC tests is more flexible and the POC tests could be used in remote, hot climates, something that would be problematic for current antibody based POC technologies. Development of new POC devices would benefit from the use of nucleic acid based detection which would simplify the implementation of POC devices in the traditional hospital setting but also in other settings, such as a GP surgery, where there may not be cold storage facilities in place, for example.

The sandwich assay, used by all of the currently available POC devices for CVD, itself has associated advantages and disadvantages for biomarker detection. The sandwich assay incorporates two-step detection, the first is the binding between the biomarker and the target antibody and the second is the binding between the secondary antibody and the biomarker. This two-stage binding helps to maximise the specificity of the assay. However, the two-step binding process will take longer than single-step binding and will result in an increase in the time to obtain results. Each of the POC devices listed in Table 1.1 take >10 minutes and most >15 minutes to generate their results. This turnaround time is a significant improvement on the time-scales involved with centralised testing, as mentioned previously, but a test that could provide results in 2-3 minutes, whilst maintaining sensitivity and specificity, would provide clinicians with biomarker levels almost immediately [20]. Furthermore, a device capable of providing results in 2-3 minutes could be used during a General Practice (GP) visit for screening of patients or for measuring the level of certain biomarkers over a period of time. A test taking 15 minutes would be towards the upper limit or beyond the average time-scale for a standard GP visit.

As each of the currently available POC devices for CVD use antibodies for biomarker detection, the differences between each of the devices is predominantly dependent on their detection methodologies and implementation. A brief summary of the differences in operation between each of the POC devices listed in Table 1.1 is given below to highlight the strengths and weaknesses of each of the technologies.

1.2.1 Optical detection

Optical immunoassays are regarded as the 'gold standard' in antigen detection due to their unrivalled sensitivity [21]. Optical techniques also often do not require any preparation of the sample (such as the addition of fluorescent markers, etc., to the analyte) and detection of analytes is 'label-free'. There are many optical technologies available for biomarker detection with many being used in clinical biochemistry measurements [21–23]. Some of the most sensitive techniques utilise surface plasmon resonance (SPR) or surface enhanced Raman spectroscopy (SERS) and can detect the binding of single molecules [24–26]. However, these technologies are notoriously difficult to miniaturise and simplify for POC use. Therefore, only those devices suitable for POC use, as defined at the start of Chapter 1, are discussed further in the remainder of Section 1.2.

1.2.1.1 Fluorescence intensity

The majority of the commercially available POC devices for cardiac biomarker detection use fluorescence intensity measurements to quantify the target biomarker concentration in a blood or serum sample. Each of the fluorescence intensity POC devices listed in Table 1.1 achieve biomarker quantification through different means although the hardware required for the excitation of the fluorescent dyes, such as a laser diode or light emitting diode (LED), and a means of light collection such as a photomultiplier tube (PMT), are broadly similar. Fluorescence based cardiac biomarker detection has been demonstrated using either a single fluorescence label or pairs of fluorophores for Förster resonance energy transfer (FRET) [27].

The Triage Meter® system uses a pair of proprietary fluorophores for a FRET based measurement. FRET is the non-radiative transfer of excitation energy from a donor fluorophore to an acceptor fluorophore when the two fluorophores are in close proximity to one another and the donor emission spectrum overlaps with the acceptor absorption spectrum. Following excitation of the donor fluorophore, the excitation energy can be transferred to the excited state of the acceptor fluorophore, leading to fluorescence emission from the latter. The Triage Meter system uses capture and secondary antibodies labelled with latex particles containing donor and acceptor fluorophores respectively.

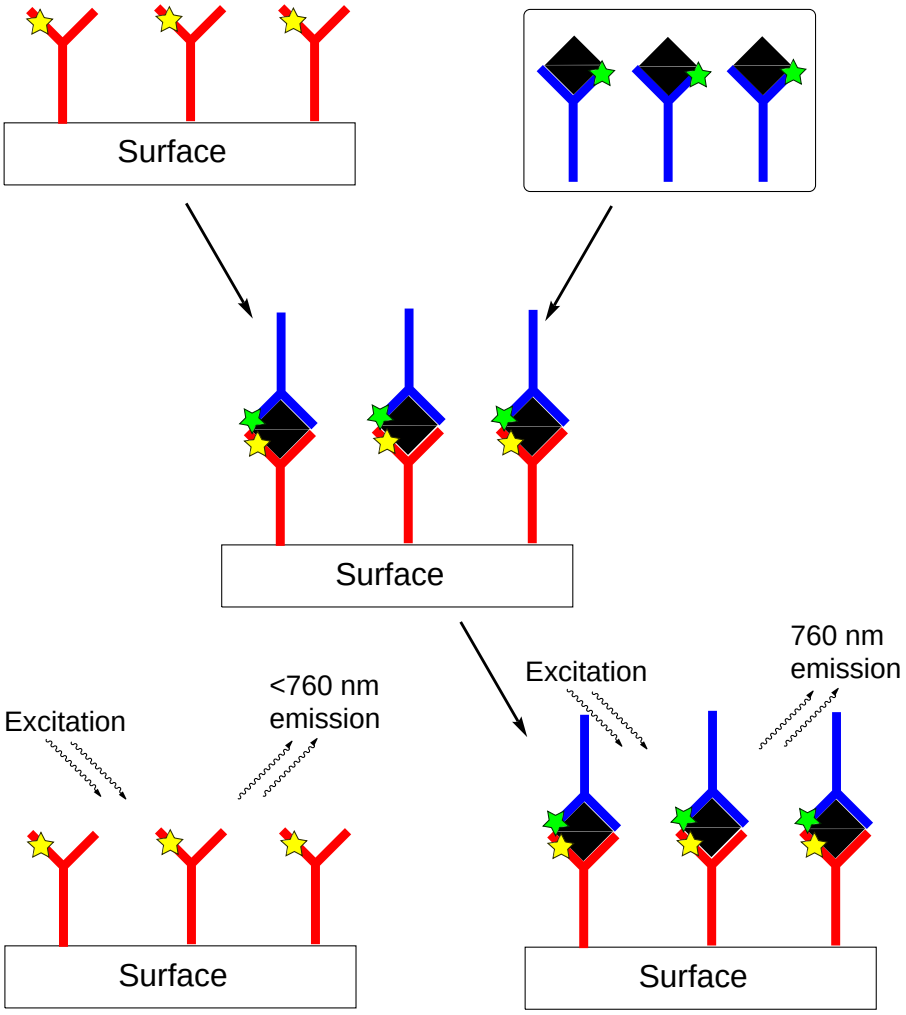

FIGURE 1.4: A probe antibody labelled with a donor fluorophore (yellow star) is immobilised on a test strip (top left). The blood sample containing the target biomolecule (black rhombus) is mixed with a secondary antibody containing an acceptor fluorophore (green star, top left). Addition of the blood sample to the test strip results in the specific coupling of the biomolecule to the probe antibody. As the donor-acceptor fluorophore pair are in close proximity to one another, upon excitation of the donor fluorophore, energy is transferred to the acceptor resulting in fluorescence emission from the acceptor. In the presence of the biomarker, fluorescence emission occurs at a wavelength of 760 nm, in the absence of the biomarker, emission is <760 nm.

The secondary antibody is mixed with the blood sample within the test chip. If the biomarker to be detected is present, the secondary antibody will bind to the biomarker. The mixture flows along the test chip to the detection region where the capture antibody is immobilised. Upon binding of the biomarker-antibody conjugate to complete the sandwich assay, the donor fluorophore is excited by a laser diode at 670 nm and the 760 nm emission from the acceptor fluorophore is collected using a photo-multiplier tube. The biomarker concentration is determined by comparing the fluorescence emission intensity to a calibration curve stored in the device. A schematic of the FRET principle used in the Triage Meter system is shown in Figure 1.4.

The remaining fluorescence intensity based devices use a single fluorescent particle in their biomarker quantification. The Stratus CS® and RAMP Reader® devices use a biomarker captive method similar to that of the Triage Meter system. Each test chip has a detection region where the capture antibody is immobilised. The Stratus CS device uses Starburst [28, 29] dendrimers to enhance immobilisation of the capture antibody to a glass substrate. In each system, the blood sample is mixed with the secondary antibody; secondary antibodies are labelled with either alkaline phosphatase (Stratus CS) or a fluorescently labelled latex bead (RAMP Reader). The biomarker-antibody solution is washed over the detection region where the biomarker binds to the capture antibody. In the Stratus CS system, a substrate solution will also be passed through the detection region. The reaction of the substrate with the alkaline phosphatase results in a fluorescent product, the intensity of which corresponds to the concentration of enzyme labelled antibody, and therefore, the biomarker present. The RAMP Reader measurement is based on the detection of fluorescence emission upon excitation of the fluorescently labelled antibody with UV light, the intensity of which is directly related to the biomarker concentration.

The final device in this category makes use of the high affinity binding between biotin and streptavidin, a coupling reaction widely used in the life-sciences (see Section 4.1)[14]. The capture antibody is labelled with a biotin molecule and the secondary antibody with a gold nanoparticle. The blood sample is added to the reaction chamber containing both the capture and secondary antibodies, therefore, in the presence of the biomarker of interest, the sandwich structure is formed. The reaction mixture is passed over the detection region which has been labelled with streptavidin. The biotin labelled antibody will bind with the streptavidin, immobilising the sandwich structure within the detection region. The gold nanoparticle has strong light absorbing properties, therefore an inverse intensity measurement can be used to determine the biomarker concentration. A schematic of biomarker detection is shown in Figure 1.5.

Fluorescence intensity based POC devices for cardiac biomarkers are used throughout hospitals in the UK [30, 31]. They can provide highly sensitive and specific results for a range of clinically useful biomarkers in a time scale of approximately 15 minutes. To date, only the Triage Meter system can provide multiplexed cardiac biomarker assessment. However, the FRET based detection system that allows multiplexing also results in an increase in device cost, relative to single fluorophore based detection, through the requirement for filters and an increase in the cost of each assay due to the additional fluorophore. However, even the use of a single fluorophore and the other reagents increases the cost of the assay relative to label free approaches. Also, the methods based on a

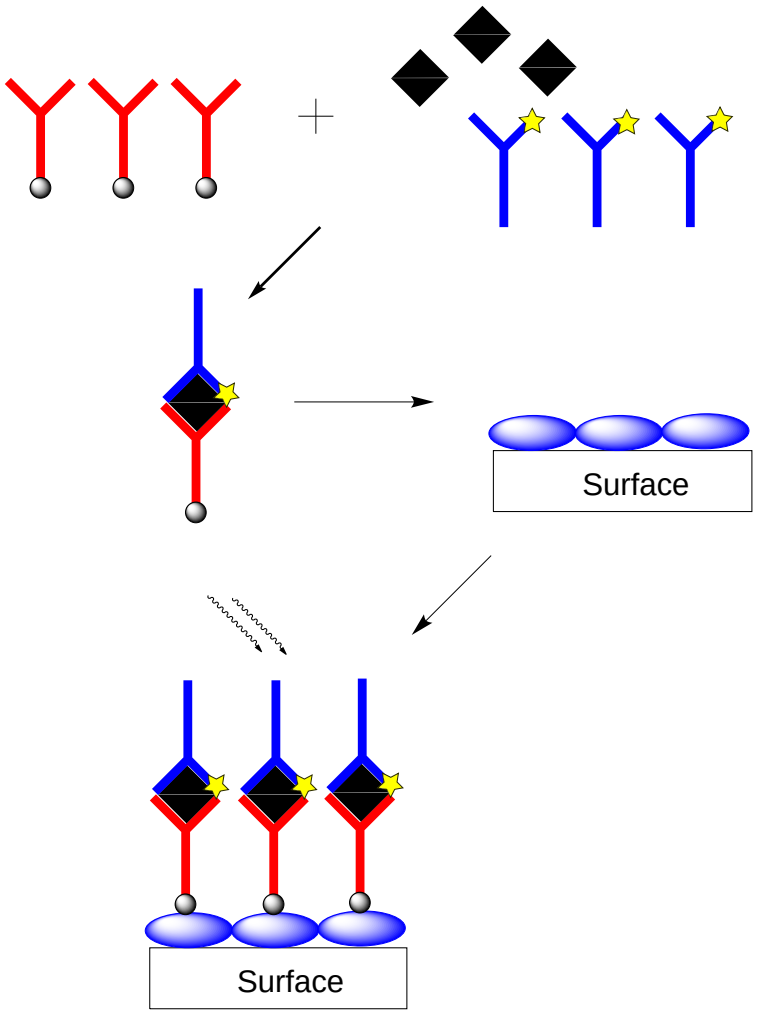

FIGURE 1.5: The capture antibody (red), labelled with a biotin molecule (black sphere), is mixed with the blood sample and the secondary antibody (blue) which is labelled with a gold molecule (yellow star). Upon mixing of the antibodies with the biomarker (black rhombus) in the blood sample, the sandwich antibody structure is formed. This structure migrates along the test strip to the detection area where there is a surface functionalised with streptavidin molecules where the biotin labelled sandwich structure is immobilised. The gold molecule strongly absorbs any incident light therefore quantification of the biomarker can be achieved by measuring light absorbance.

single fluorophore require the inclusion of wash steps to ensure that any unbound fluorescent material is removed prior to performing the intensity measurement, increasing assay times.

1.2.1.2 Chemiluminescence

Chemiluminescence immunoassays are one of the most widely researched immunoassays and are the basis of some of the most simple POC devices, including the home pregnancy test [32]. Chemiluminescence is the emission of light or a colour change that is

induced by a chemical reaction [27]. As described previously, many chemiluminescence immunoassays operate via a visible colour change.

The Decision Point® POC device for cardiac biomarkers operates and looks somewhat similar to a home pregnancy test (Figure 1.6). The blood sample is added to a region of the test strip containing secondary antibodies which bind to particular biomarkers. The biomarker-antibody solution migrates via capillary action through the test strip to the detection region which has been labelled with capture antibodies. The coupling of the biomarker-antibody conjugate to the capture antibody results in a visible colour change within the detection region, visible as a solid red line when the biomarker concentration is above a pre-determined cut-off concentration.

(a) (b)

FIGURE 1.6: Photograph of (a) the Decision Point device (www.emsworld.com) and (b) a home pregnancy test (www.elisa-antibody.com).

The Decision Point cardiac biomarker test is very simple to use and is significantly more portable than other optical POC devices as it does not require the hardware to 'read' the optical output. However, it is not possible to obtain an exact measure of the biomarker concentration resulting in only semi-quantitative results. There is also no advantage in terms of the turnaround time for test results. A multiplexed test that allows simultaneous assessment of a range of cardiac biomarkers has been developed by the manufacturer of the Decision Point but this has not been CE marked and is therefore not available in the UK.

1.2.2 Electrochemical detection

Electrochemical immunoassays have been researched extensively, resulting in many POC devices based on electrical transduction methods being commercialised, one of the best

known examples being the glucose meter as mentioned previously. Electrochemical immunosensors generate an electrical signal upon a specific immunoreaction. There are a number of different forms the generated electrical signal can take with amperometric, impediometric and potentiometric signal detection having been demonstrated previously [33]. Electrochemical based immunosensors have some advantages over optical based systems. For example, electrochemical detection is generally more amenable to miniaturisation than optical systems due to the wide availability of microfabricated electrochemical transducers. Of the POC devices listed in Table 1.1, the i-STAT® is the only quantitative device available in a hand-held format. Electrochemical detection is also independent of the optical properties of the reaction media, something that may have to be considered for optical systems.

Of the electrochemical POC devices available for cardiac biomarker assessment, only the i-STAT is currently available in the UK. The operation of this amperometric device is briefly summarised below.

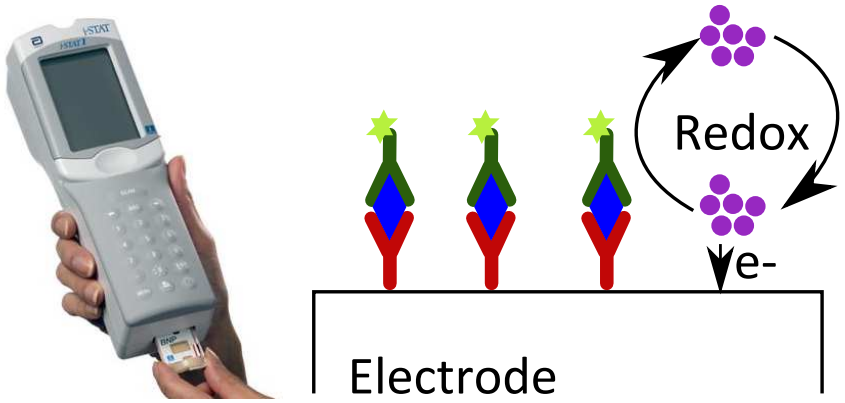

(a) (b)

FIGURE 1.7: Photograph of (a) the hand-held i-STAT (poct.co.uk) and (b) a schematic of current generation for amperometric based detection. Sandwich immunoassay provides specific coupling of antigen to an antibody functionalised electrode. An enzyme on the secondary antibody catalyses a redox reaction in a substrate solution, resulting in the flow of electrons to the electrode.

1.2.2.1 Amperometric

Amperometric sensors measure the current generated due to an electron transfer reaction (redox) at the surface of an electrode. The i-STAT, like all of the other immunoassay techniques described, uses a sandwich immunoassay and specifically a two-site ELISA method for biomarker detection [12]. The working electrode in the i-STAT is a silicon chip that is functionalised with a capture antibody specific to a particular biomarker. A second area of the electrode contains an antibody-alkaline phosphatase enzyme conjugate

specific to a different part of the chosen biomarker. Upon the addition of a blood sample to the silicon chip, the secondary antibody-enzyme conjugate is dissolved in the sample allowing the secondary antibody to bind with any biomarker present in the sample. The biomarker is then captured on the antibody functionalised electrode resulting in the characteristic sandwich structure. A substrate fluid added to the chip, after a 7 minute incubation period, results in a redox reaction catalysed by the alkaline phosphatase enzyme. The exchange of electrons is detected as a change in current at the electrode and is a measure of the number of bound secondary antibodies and therefore, biomarker concentration.

1.2.3 Requirements of the 'ideal' cardiac biomarker POC device

The adoption of POC testing in CVD has been expedited by the need to diagnose and treat patients as quickly as possible. Despite many POC devices being commercially available for the detection of cardiac biomarkers, a POC test with all of the desirable characteristics e.g. fast, high throughput, high sensitivity and specificity, highly multiplexed, etc., is not yet available [20]. CVD is a complex array of diseases and in order to fully understand an individual's disease, several different biomarker levels need to be considered. Therefore, one of the most desirable qualities for a POC device is the ability to multiplex and provide information simultaneously on a suite of biomarkers. The majority of devices can only assess single biomarkers. The Triage Meter system is the exception of those listed in Table 1.1 as this device is multiplexed for the detection of Troponin I, Myoglobin and CK-MB. These three biomarkers are useful for the diagnosis of various forms of CVD but only Myoglobin levels increase in the first 1-3 hours after a cardiac event and the specificity of Myoglobin to cardiac damage is low. Therefore, a diagnostic test with increased multiplexing capability, to include assays for the detection of additional biomarkers, such as BNP (the levels of which rise **before** a cardiac event [34]), would be beneficial.

A reduction in the cost of biomarker assays would also make POC testing a more attractive option for healthcare providers. Currently, all cardiac POC technologies use antibody based immunoassays for biomarker detection. As mentioned previously, antibody production is inefficient and expensive and the cold storage requirements limit the use of the technology. Therefore, alternative assay formats utilising nucleic acid based detection of mRNA or proteins would open up the possibility for cheaper biomarker tests with wider applications.

Another contributing factor to the cost of current biomarker assays is the cost of reagents (fluorophores, enzymes, etc.) used to generate the device signal. Although each of the

technologies listed in Table 1.1 allows "label-free" biomarker detection in the sense that there is no processing of the blood sample required, labels are instead incorporated into the immunoassay. Removing the requirement for additional labels altogether would reduce the cost per test.

Finally, the turnaround time for results (≈15 minutes) is a vast improvement on the time-scales involved with centralised testing. A further reduction in the assay times would allow diagnosis and treatment decisions to be made in a more timely manner and may open up the possibility for new settings in which to use POC devices. For example, if turnaround times were of the order of 2-3 minutes, biomarker screening and monitoring may take place within a routine GP appointment or paramedics could perform diagnostic tests and administer treatment en-route to the hospital in emergency situations.

A novel biosensor that incorporates the qualities mentioned above would be desirable for the next generation of cardiac POC devices. Such a biosensor is the subject of this thesis and is introduced in the remainder of this chapter.

1.3 Distributed feedback laser sensors

Organic DFB laser sensors are a type of evanescent wave refractive index sensor. There are many different kinds of evanescent wave sensors [35–37] but DFB lasers have several attributes that make them particularly well suited for the development of a label-free POC biosensor. For example, DFB lasers generate and output, normal to the sensor surface, their own coherent light for sensing making implementation simple and without the need for the stringent optical alignment, which is required for some other optical detection platforms [38, 39]. And lasers can also be fabricated through solution processing and soft material patterning, enabling large scale production [40, 41]. In this section, the operation and properties of DFB lasers will be described and a review of DFB laser biosensors in the literature will be presented.

1.3.1 DFB laser operation

DFB lasers do not have the typical laser resonator geometry consisting of a cavity enclosed by mirrors. Instead, feedback, necessary for laser oscillation, is provided by the use of a wavelength-scale periodic structure that diffracts the light. Excitation of the gain material is required for light production. For organic lasers, this is achieved by optically pumping the gain material. There are various different DFB laser structures

but the simplest example is that of a slab waveguide with a one-dimensional periodic grating pattern within the plane of the waveguide, as shown in Figure 1.8.

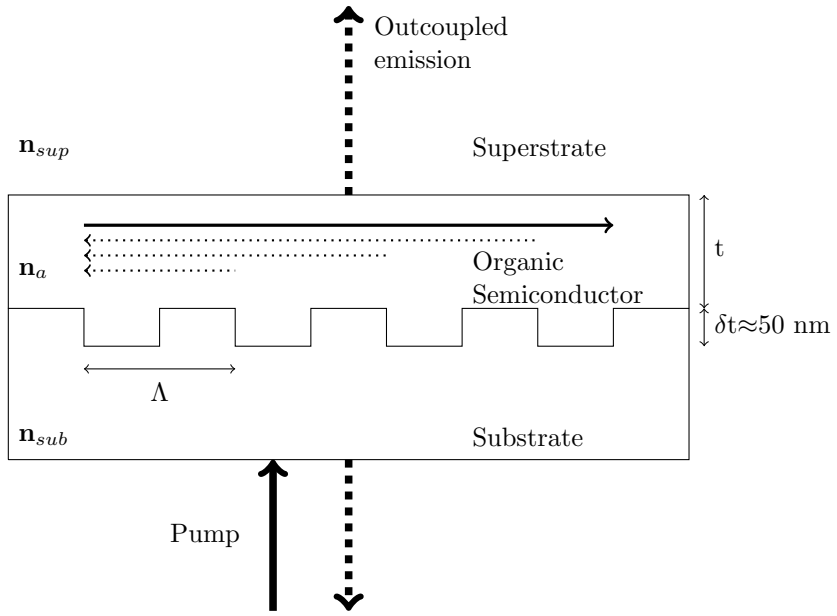

FIGURE 1.8: Schematic side-view cross-section illustration of a three layer DFB laser. The thick and dotted lines within the structure represent the guided 2nd order mode and feedback from successive periods of the grating respectively.

The laser consists of a three-layer planar waveguide with a thin, high-index gain layer of thickness, t, and refractive index, n_a, deposited on top of a substrate of refractive, n_{sub}, which has been imprinted with the periodic nanostructure. The third layer represents the medium in contact with the laser surface and is defined as the superstrate layer with refractive index, n_{sup}. Light propagating in the high-index gain layer is scattered by the grating structure. Scattered light can combine constructively to create a "Bragg-scattered" wave which will have some new direction. The emission from a DFB laser is governed by the Bragg equation, Eq. 1.1, where m is an integer that represents the order of diffraction, λ is the wavelength of the light, n_{eff} is the effective refractive index of the laser mode (which is a function of the refractive indices of each of the waveguide layers and the gain layer thickness) and Λ is the grating period.

$$m\lambda = 2n_{eff}\Lambda \tag{1.1}$$

The direction of out-coupled light is dependent on the order of diffraction of the grating structure. The majority of DFB lasers used for biosensing applications use a second order diffraction grating, as counter-propagating modes couple through the second order of diffraction while the first order couples waves vertically out of the laser structure as shown in Figure 1.8. The out-coupled laser emission wavelength is the parameter

of interest in biosensing applications and emission normal to the laser surface enables simple collection of this light signal. The biosensing principle is explained below.

1.3.2 DFB lasers for biosensing

For biosensing applications, the surface of the DFB laser must be functionalised with probe molecules that will specifically bind to a particular biomarker (target molecules). Functionalisation of the laser surface can be achieved via various means (specific examples are provided in Section 4.2) and the probe molecule may be an antibody, nucleic acid oligo, etc. Upon functionalisation of the DFB laser surface with an oligo, for example, the laser will have an emission wavelength of x nm (Figure 1.9). If the laser is exposed to a test solution, such as a blood sample, that contains the target oligo, hybridisation of the two complementary oligos occurs. A blood sample will contain a range of other biomolecules in addition to the target biomarker and this therefore, is why functionalisation of the DFB laser surface is necessary. Binding the target biomolecule to the probe molecule means that the target biomolecules remains immobilised on the laser surface while all of the other biomolecules are washed off of the surface. The addition of the target oligo to the laser surface results in a change in the superstrate refractive index which in turn alters the effective refractive index of the laser mode, causing a change in the emission wavelength ($x + \Delta x$ nm). The change in the laser emission wavelength (Δx nm) can be attributed to the binding of the target oligo and the magnitude of Δx nm corresponds to the density of the target oligo present on the laser surface. Therefore, a quantitative measurement of target biomarker concentration in a solution (such as blood) can be determined.

1.4 DFB laser gain materials

The laser gain medium is the material required for generation and amplification of photons. A generic laser material with four energy levels can be used to explain the light amplification process, as shown in Figure 1.10a. An electron in the ground energy state (E_0) is excited to a higher energy level (E_3) by an incident photon (absorption). This electron falls (non-radiatively) to a lower excited energy level (E_2). The electron may decay to a lower lying energy level of its own accord, emitting a photon with an energy equal to the difference between the electrons initial and final states and with a random direction and phase (spontaneous emission). Or, if the electron interacts with an electromagnetic wave with a particular wavelength (i.e. E_2-E_1), while in the excited state, it may make the transition to a lower energy level (E_1), releasing a photon with the same phase, frequency and direction as the excitation photon in the process

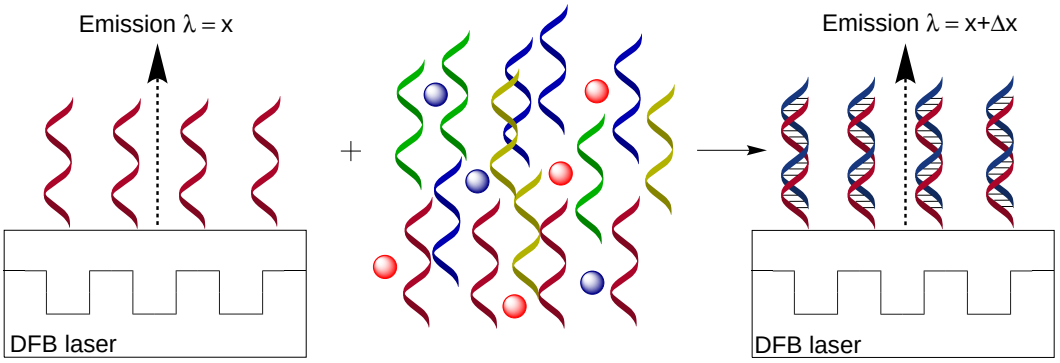

FIGURE 1.9: A DFB laser functionalised with a probe molecule, e.g. nucleic acid oligo (red ribbon), has a emission wavelength of x nm. The DFB laser is exposed to a test solution containing the complementary oligo (blue ribbon) and other molecules. Only the complementary target oligo will hybridise with the probe oligo. The addition of the target oligo to the laser surface results in a change in the refractive index of the superstrate and the effective refractive index of the laser mode causing the emission wavelength to change to x+Δx. The shift in wavelength, Δx, can be calculated by subtracting the emission wavelength of the laser before and after exposure of the laser to the test solution. The reasons why a positive shift in wavelength is expected are outlined in Chapter 2.

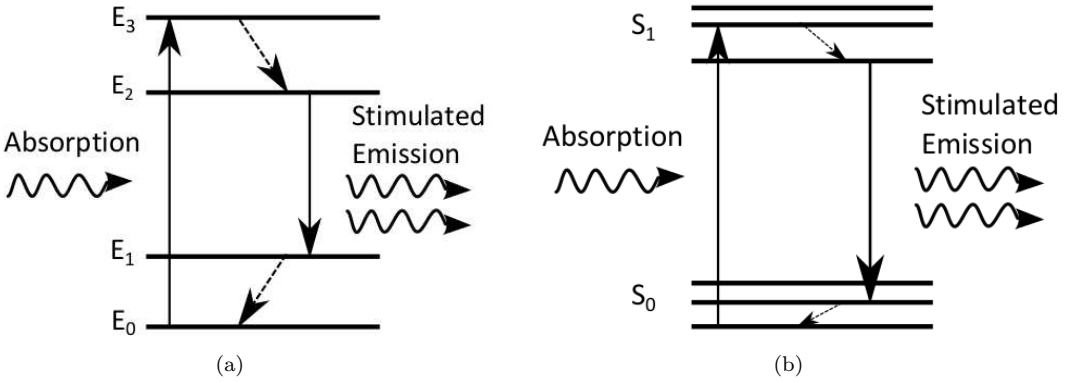

FIGURE 1.10: Jablonski diagram illustrating (a) the energy levels and transitions for a generic four level laser gain material and (b) a typical organic light emitter. Solid, wavy and dashed lines represent radiative, non-radiative and incident/emitted photons respectively.

(stimulated emission). The electron then decays non-radiatively back to the ground state. In order to ensure there is more stimulated emission than absorption there has to be more electrons in an excited state than in the E_1 level, i.e. a population inversion. The four level system allows for a population inversion between the E_2 and E_1 energy levels where stimulated emission occurs. The choice of gain material is fundamental as it has an effect on all laser characteristics such as wavelength, lasing threshold, stability, lifetime, etc.

DFB lasers for biosensing applications have so far been made exclusively from organic materials; either dyes or conjugated polymers and oligomers (also referred to as organic

semiconductors). There are important differences between the laser characteristics of dye based and organic semiconductor lasers, described in more detail below, but the physics of the stimulated emission process is similar. Organic gain media can be broadly represented by a four level system where transitions occur between the ground state and excited singlet state energy levels, shown in Figure 1.10b. Singlet states are so called because the unpaired electrons of an excited molecule have anti-parallel spins and a spin quantum number of S=0 and, therefore, a multiplicity of 2S+1=0. Non-radiative transitions correspond to internal conversion between vibrational levels (transition from a singlet state to a triplet state (electron spins are parallel)) and stimulated emission takes place between the lowest vibrational level of the first excited state and the vibrational level of the ground state. Also, all of the organic DFB laser biosensors to date are optically pumped under pulsed rather than continuous wave conditions. Continuous wave excitation leads to an increase in non-radiative decay from intersystem crossing, for example [42]. Pulsed pumping of organic semiconductor DFB lasers is straightforward due to their relatively low lasing threshold. And, as compact pulsed sources are available, operating under pulsed conditions will not have a negative effect on the development of a compact DFB laser sensing system.

1.4.1 Dyes

The first organic DFB laser demonstrated for biosensing applications had a dye-doped gain material [43]. Dyes are attractive gain materials as they have broad spectra and can be tuned across the visible spectrum [44]. One important difference between dyes and semiconductor gain materials is the difference in quantum yield of neat films. When dye molecules are in close proximity to one another, as happens in the solid state, radiative emission can be quenched through non-radiative relaxation of excited electrons [44]. Therefore, dyes tend to be incorporated into a transparent matrix at a volume percentage of ≈10% rather than in the form of a neat films of dye molecules [43, 45]. This has implications for properties such as the laser threshold and refractive index of the gain material, both important considerations for DFB laser biosensors. There are a vast number of suitable dye molecules for laser gain media but the ones incorporated into DFB laser biosensors thus far include Rhodamine 590 [45], Coumarin 503 [43] and Pyromethene 597 [46], the structures of which are shown in Figure 1.11a, b and c.

1.4.2 Organic semiconductors

Organic semiconductors are conjugated molecules with overlapping molecular orbitals resulting in their characteristic semiconductor properties. There are different types of

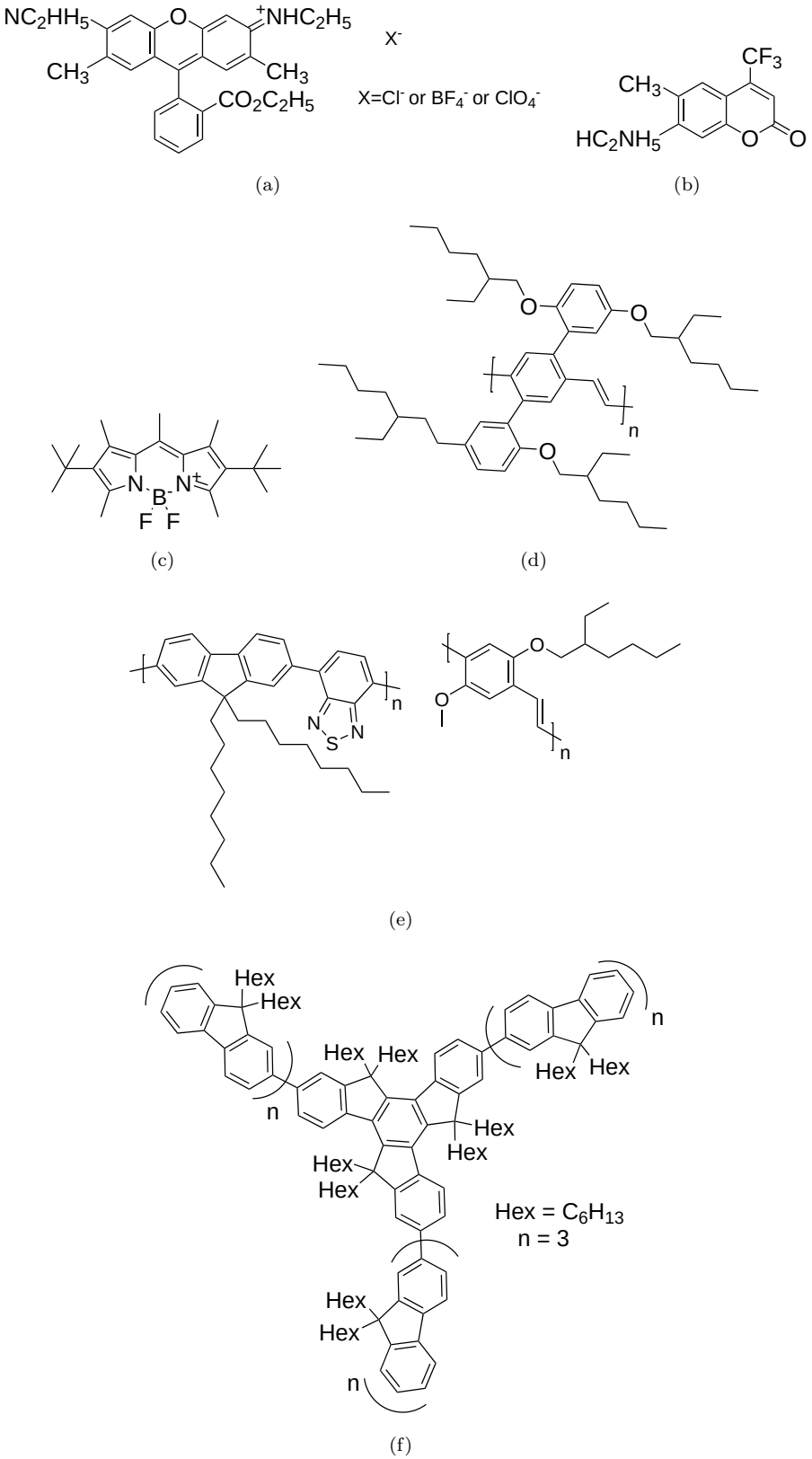

FIGURE 1.11: Chemical structures of (a) Rhodamine 590, (b) Coumarin 503, (c) Pyromethene 597, (d) BBEHP-PPV, (e) F8BT and MEH-PPV and (f) T3.

organic semiconductor used for lasing materials including polymers, conjugated dendrimers and spiro-compounds [44]. Conjugated polymers have been incorporated into DFB laser biosensors and their main properties are summarised below.

1.4.2.1 Conjugated polymers

Conjugated polymers are long chain-like molecules connected by alternating single and double bonds, resulting in electrons being free to move along the molecule [44]. Poly(phenylene vinylene) (PPV) [47, 48] and polyfluorenes [49] are two classes of conjugated polymer that have been subject to the greatest research. Example of conjugated polymers utilised in DFB laser sensors from the PPV family include poly[2,5-bis(2',5'-bis(2"-ethylhexyloxy)-phenyl)-p-phenylene vinylene] also known as BBEHP-PPV and (poly[(9,9-dioctyl- fluorenyl -2,7-diyl)- co -(1,4-benzo-2,1',3-thiadiazole)]/(poly(2-methoxy-5-(2'-ethylhexloxy)-p- phenylene vinylene) (F8BD/MEH-PPV) [50]. These structures are shown in Figure 1.11d and e respectively. The chemical design of conjugated polymers can be tailored to maximise the luminescence efficiency and chromophore density. For example, the polymer side chains can be chosen to prevent aggregation between repeating units, allowing high efficiencies to be maintained even in undiluted, neat films [44].

1.4.2.2 Macromolecules and oligomers

Oligomers are macromolecules composed of several subunits (rather than a potentially unlimited chain of molecules in the case of polymers), the oligofluorene arms of the tris(terfluorenyl)truxene (T3) are (Figure 1.11f) are good examples. Macromolecules used for laser gain materials often contain a central chromophore surrounded by conjugated branches and surface groups [44]. The optical properties of oligomers are similar to those of conjugated polymers. However, unlike the long chains of conjugated polymers, conjugated oligomers are discrete monodisperse macromolecules. A DFB laser has been demonstrated using T3 [51, 52] which is a conjugated oligomer (unbranched side groups). T3 is the gain material used for the DFB laser biosensor in this work, its specific material properties are described in Section 3.2.1. The structure of conjugated oligomers presents an interesting possibility for directly functionalising the oligomer arms with biomolecule targets which may lead to sensitivity advantages in biosensing applications.

1.5 Current state-of-the-art in organic DFB laser biosensors

Organic distributed feedback laser biosensors are a relatively new sensing format. The first demonstration of an organic DFB laser intended for label-free optical biosensing applications was in 2008 [43]. The biosensor was based on a one-dimensional, second order DFB laser with a gain material of Coumarin 503 doped polymethylmethacrylate (PMMA). The laser had an emission wavelength of around 500 nm when exposed to air and a threshold pump fluence of 180 μJ.cm^{-2} (10 ns pump duration). The bulk refractive index sensitivity was reported to be 16.6 nm/refractive index unit (RIU). Bulk sensitivity is a metric often used to compare the performance of DFB laser sensors and it is a useful means for comparing lasers with similar resonant wavelengths. However, it is useful to keep in mind that in biosensing applications, the analyte binding occurs at the sensor's surface and therefore the laser sensitivity for surface refractive index changes is of greater importance. Surface sensing was demonstrated via the detection of the non-specific adsorption of polyphenylalanine lysine (PPL), a protein based polyelectrolyte known to deposit a self-limited monolayer, corresponding to a shift in emission wavelength of 0.42 nm. The same group quickly followed up with the demonstration of a biosensor with a vastly improved bulk sensitivity [45]. This laser had a gain layer of SU-8 doped with Rhodamine 590, resulting in an emission wavelength around 590 nm in air. Bulk sensitivity was reported to be 99.58 nm/RIU for this device. Two factors can be attributed to the significant improvement in bulk sensitivity. The first is associated with the change in the gain material. The Coumarin doped PMMA has a refractive index of 1.48 and a resonant wavelength of 500 nm whereas Rhodamine doped SU-8 has a higher refractive index of 1.58 and a resonant wavelength of 590 nm. The sensitivity of the sensor is defined by the Bragg equation (Eq.1.1). As the Rhodamine dye results in a longer resonant wavelength the grating pitch is also longer; an increase in the grating pitch results in an increase in the shift in wavelength for bulk refractive index changes. However, a greater effect on the reported bulk sensitivity value can be attributed to the addition of a high index titanium dioxide (TiO_2) cladding layer on top of the gain layer. The presence of the TiO_2 layer will result in greater confinement of the electric field towards the TiO_2 layer, resulting in a greater overlap with the sensing region at the laser surface. While the additional TiO_2 layer does provide a marked increase in the DFB laser sensitivity, this is at the expense of an increase in the laser threshold of the device. The pump fluence threshold for the DFB laser with 30 nm TiO_2 layer was 850 μJ.cm^{-2} (170 μJ.cm^{-2} is the threshold for a Rhodamine laser without the TiO_2 layer [41] compared to 180 μJ.cm^{-2} for the Coumarin based laser). The laser threshold is an important consideration for the implementation of the technology as POC devices.

In order for DFB lasers to be miniaturised sufficiently for portable POC devices, a low lasing threshold is desirable to enable compact laser diode based pumping mechanisms.

Work has been done to optimise the TiO_2 layer to maximise detection sensitivities. The bulk sensitivity of a DFB laser with a gain layer of Pyromethene 597 doped Ormocomp with a TiO_2 layer was investigated for a range of TiO_2 thicknesses [46]. A TiO_2 layer thickness of 20 - 35 nm was found to be optimal for maximising bulk sensitivity, corresponding to a bulk sensitivity of 95 nm/RIU. The effect of TiO_2 thickness on laser threshold was not investigated, however in another paper the same authors investigated multilayer DFB lasers and they noted that the lowest lasing threshold occurs for lasers with a TiO_2 layer $\leq$20 nm [53]. This is because TiO_2 layers >20 nm in thickness result in stronger confinement of the laser mode towards the TiO_2 layer, therefore decreasing the overlap with the gain material, resulting in an increase in the lasing threshold. The strcture of the TiO_2 layer has also been the subject of investigation. A porous nanorod TiO_2 layer was shown to increase DFB laser biosensing capabilities [54]. In this study, the shift in wavelength for the adsorption of PPL to the laser surface was compared for a solid 30 nm TiO_2 layer and a nanorod layer of several thicknesses (22 nm, 30 nm, 67 nm and 90 nm respectively). An enhanced shift in wavelength was observed for all nanorod thicknesses relative to that of the 30 nm solid TiO_2 layer, with the greatest shift observed for the 90 nm nanorod layer. The porous TiO_2 layer increases the surface area for PPL adsorption, therefore resulting in a maximised shift in emission wavelength despite the reduction in the TiO_2 refractive index compared to that of a solid layer (1.82 compared to 2.10). A shift in wavelength approximately twice the magnitude of that for a solid 30 nm layer was noted for the 22 nm nanorod layer, therefore the use of a TiO_2 nanorod layer provides a good method of maximising the layer sensitivity whilst keeping the TiO_2 layer as thin as possible to prevent increasing the lasing threshold. However, one of the benefits of DFB lasers relative to other optical sensing techniques mentioned previously is their ease of fabrication. DFB lasers can be fabricated through solution processing and soft material patterning making them suitable for large scale production. For example, a horizontal dipping method, compatible with roll-based manufacturing, has been demonstrated for the fabrication of a uniform Rhodamine DFB laser over a large surface area [41]. The incorporation of a TiO_2 layer, solid or nanorod based, adds another step to the fabrication process and increases complexity.

Organic semiconductor DFB lasers are a relatively new addition to the DFB laser biosensor family, with the T3 DFB laser presented in this thesis being the first example of an organic semiconductor based DFB laser biosensor. As mentioned previously, organic semiconductors are much less prone to quenching than dyes, which makes the use of a dense solid-state film of 'neat' active material for the fabrication of lasers possible. The greater refractive index of such a neat thin film relative to that of a dye-doped polymer,

leads to greater confinement of the electric field within the gain layer, a greater overlap with the detection region at the laser surface and ultimately higher light matter interactions. Therefore, by utilising an organic semiconductor as the gain material rather than a dye-doped polymer, there is the potential to both match, if not improve upon, the sensitivity and resolution values and enhance the overall sensor characteristics. As the gain layer for organic semiconductors takes the form of a solid-state neat film, the lasing threshold tends to be lower than those of dye-doped lasers [43, 51]. A lower lasing threshold makes pumping with compact light sources, such as gallium nitride based laser diodes, a possibility as has already been demonstrated for organic semiconductor DFB lasers [55]. Laser diode based pumping will enable the miniaturisation of the DFB laser sensing system and if off-the-shelf components can be used, such as mass produced 'Blu-ray' diodes, it should also enable the technology to be competitively priced. It is for these reasons the potential of a T3 DFB laser was investigated for biosensing applications.

This thesis details the development of the first organic semiconductor DFB laser biosensor. Bulk and surface sensing and specific and reversible biomolecule detection results are presented in sections 3.5, 3.6, 4.4 and 4.5 respectively. Following the development of the T3 DFB laser biosensor, a second DFB laser biosensor incorporating an organic semiconductor gain layer has been reported in the literature. This laser has a gain material of F8BT/MEH-PPV, an emission wavelength of 630 nm and a lasing threshold of 92 nJ [50]. The laser structure consists of a low index UV-curable polymer imprinted with a second order diffraction grating pattern and the F8BT/MEH-PPV gain layer, which is 130 nm thick, directly on top. The bulk sensitivity of the device is said to be 154 nm/RIU, a significant increase relative to that of a dye-doped laser without the TiO_2 cladding layer (16.6 nm/RIU) [43]. As described previously, this will largely be due to the increase in grating pitch to accommodate the longer resonant wavelength of the semiconductor gain layer. However, the F8BT/MEH-PPV gain layer also has a higher refractive index (>1.8) relative to that of a dye-doped gain material (1.5 - 1.6) which plays a small part in increasing the bulk sensitivity but is much more significant for surface sensing.

As well as demonstrations of non-specific surface sensing, there have been several demonstrations of specific biosensing with organic DFB lasers. The first demonstration was in 2008 with the detection of an antibody (Human IgG) on a Rhodamine laser with a 30 nm TiO_2 layer functionalised with a layer of Protein A, a protein that has a binding site for IgG [45]. The minimum concentration of IgG detected was 3.2 nM which corresponded to a shift in wavelength of ≈0.05 nm. In 2012, the same group demonstrated the detection of TNF-α with a laser functionalised with a TNF-α antibody [38]. This time the Rhodamine laser had a TiO_2 thickness of 10 nm and the limit of detection for

TNF-α was 0.625 μg.mL^{-1}. At these levels of detection, and assuming the detection limits for these antigens would be comparable to other antigens, which may not necessarily be the case, these biosensors are within the diagnostic range of only a limited number of cardiac biomarkers such as C-reactive protein (>3 μg.mL^{-1} indicative of a high CVD risk). Therefore, an improvement in sensitivity will be required in order to target those biomarkers present at lower concentrations. Efforts have been directed at improving detection sensitivities through signal processing methods. Averages of multiple independent measurements and statistical methods have been shown to enable the detection of wavelength shifts as small as 1.5 pm [56]. However, the detection limit of the antibody (Rabbit IgG) on a protein A functionalised laser (10 nm TiO_2 cladding layer on a Rhodamine doped SU-8 gain layer) was 34 nM using these methods, which does not imply a large improvement in sensitivity relative to that of Human IgG detection mentioned previously. However, it should be noted that there is a difference in TiO_2 thickness which may affect sensitivity. The potential improvements in sensitivity, through the use of organic semiconductor gain materials, may open up the possibility for detection of a wider range of cardiac biomarkers.

A well-established biotin-avidin model was used for the demonstration of specific biodetection for the organic semiconductor based laser [50]. In this demonstration, a biotinylated hydrogel was covalently attached to the organic semiconductor gain layer for the detection of a range of avidin concentrations. The limit of detection for avidin was 25 μg.mL^{-1}. This is the first paper published on the F8BT/MEH-PPV based biosensor so one can only assume that work is ongoing to further improve their biosensing capabilities.

1.6 Summary

There are a number of POC devices for cardiac biomarker detection but the ideal system (fast, high sensitivity and specificity, highly multiplexed, portable, cost-effective, etc.) is not currently available. DFB lasers have demonstrated biosensing potential and provide a means for label-free, highly sensitive optical detection of biomarkers. One of the stand-out features of DFB lasers, in terms of POC applicability, is their capacity for multiplexing. The surface area of the active laser can be very small (μm - mm) therefore many DFB lasers can be incorporated into a single substrate, each one functionalised for the detection of a different biomarker. Current POC sensing is constrained by the limitations of antibody based detection. A nucleic acid approach would overcome many of the downsides associated with antibodies, as described, and may open up new areas for sensor use. It is proposed that an organic semiconductor based DFB laser biosensor

may be a suitable transducer for a multiplexed, nucleic acid based sensing platform for the detection of cardiac biomarkers. Therefore, this thesis explores the optimisation of a T3 based DFB laser for biosensing and its specific biomolecule detection capabilities.

References

[1] Tamas R Peredy and Robert D Powers. Bedside diagnostic testing of body fluids. *The American Journal of Emergency Medicine*, 15(4):400 – 407, 1997. ISSN 0735-6757. doi: http://dx.doi.org/10.1016/S0735-6757(97)90137-6. URL http://www.sciencedirect.com/science/article/pii/S0735675797901376.

[2] Alfred H. Free, Ernest C. Adams, Mary Lou Kercher, Helen M. Free, and Marion H. Cook. Simple specific test for urine glucose. *Clinical Chemistry*, 3(3):163–168, 1957. URL http://www.clinchem.org/content/3/3/163.abstract.

[3] Bert Walter. Dry reagent chemistries in clinical analysis. *Analytical Chemistry*, 55(4):498A–514A, 1983. doi: 10.1021/ac00255a001. URL http://pubs.acs.org/doi/abs/10.1021/ac00255a001. PMID: 6859537.

[4] S. F. Clarke and J. R. Foster. A history of blood glucose meters and their role in self-monitoring of diabetes mellitus. *British journal of biomedical science*, 69(2):83–93, 2012. URL http://search.proquest.com/docview/1033157924?accountid=14116. Date completed - 2012-08-28; Date created - 2012-08-09; Date revised - 2014-01-14; Last updated - 2014-01-15.

[5] Tobias Reichlin, Willibald Hochholzer, Stefano Bassetti, Stephan Steuer, Claudia Stelzig, Sabine Hartwiger, Stefan Biedert, Nora Schaub, Christine Buerge, Mihael Potocki, Markus Noveanu, Tobias Breidthardt, Raphael Twerenbold, Katrin Winkler, Roland Bingisser, and Christian Mueller. Early diagnosis of myocardial infarction with sensitive cardiac troponin assays. *New England Journal of Medicine*, 361(9):858–867, 2009. doi: 10.1056/NEJMoa0900428. URL http://www.nejm.org/doi/full/10.1056/NEJMoa0900428. PMID: 19710484.

[6] Till Keller, Tanja Zeller, Dirk Peetz, Stergios Tzikas, Alexander Roth, Ewa Czyz, Christoph Bickel, Stephan Baldus, Ascan Warnholtz, Meike Frhlich, Christoph R. Sinning, Medea S. Eleftheriadis, Philipp S. Wild, Renate B. Schnabel, Edith Lubos, Nicole Jachmann, Sabine Genth-Zotz, Felix Post, Viviane Nicaud, Laurence Tiret, Karl J. Lackner, Thomas F. Mnzel, and Stefan Blankenberg. Sensitive troponin i assay in early diagnosis of acute myocardial infarction. *New England Journal of Medicine*, 361(9):868–877, 2009. doi: 10.1056/NEJMoa0903515. URL http://www.nejm.org/doi/full/10.1056/NEJMoa0903515. PMID: 19710485.

[7] M.R Cowie, P Jourdain, A Maisel, U Dahlstrom, F Follath, R Isnard, A Luchner, T McDonagh, J Mair, M Nieminen, and G Francis. Clinical applications of b-type natriuretic peptide (bnp) testing. *European Heart Journal*, 24(19):1710–1718, 2003. doi: 10.1016/S0195-668X(03)00476-7. URL http://eurheartj.oxfordjournals.org/content/24/19/1710.abstract.

[8] Pai C. Kao, Shu-Chu Shiesh, and Ta-Jen Wu. Serum c-reactive protein as a marker for wellness assessment. *Annals of Clinical Laboratory Science*, 36(2):163–169, 2006. URL http://www.annclinlabsci.org/content/36/2/163.abstract.

[9] Greg Brown, John J. Albers, Lloyd D. Fisher, Susan M. Schaefer, Jiin-Tarng Lin, Cheryl Kaplan, Xue-Qiao Zhao, Brad D. Bisson, Virginia F. Fitzpatrick, and Harold T. Dodge. Regression of coronary artery disease as a result of intensive lipid-lowering therapy in men with high levels of apolipoprotein b. *New England Journal of Medicine*, 323(19):1289–1298, 1990. doi: 10.1056/NEJM199011083231901. URL http://www.nejm.org/doi/full/10.1056/NEJM199011083231901. PMID: 2215615.

[10] Elliott Antman, Jean-Pierre Bassand, Werner Klein, Magnus Ohman, Jose Luis Lopez Sendon, Lars Rydn, Maarten Simoons, and Michal Tendera. Myocardial infarction redefineda consensus document of the joint european society of cardiology/american college of cardiology committee for the redefinition of myocardial infarction: The joint european society of cardiology/ american college of cardiology committee. *Journal of the American College of Cardiology*, 36(3):959 – 969, 2000. ISSN 0735-1097. doi: http://dx.doi.org/10.1016/S0735-1097(00)00804-4. URL http://www.sciencedirect.com/science/article/pii/S0735109700008044.

[11] Fred S. Apple, Robert L. Jesse, L. Kristin Newby, Alan H.B. Wu, and Robert H. and Christenson. National academy of clinical biochemistry and ifcc committee for standardization of markers of cardiac damage laboratory medicine practice guidelines: Analytical issues for biochemical markers of acute coronary syndromes. *Clinical Chemistry*, 53(4):547–551, 2007. doi: 10.1373/clinchem.2006.084715. URL http://www.clinchem.org/content/53/4/547.short.

[12] Robert H. Christenson and Hassan M.E. Azzazy. Cardiac point of care testing: A focused review of current national academy of clinical biochemistry guidelines and measurement platforms. *Clinical Biochemistry*, 42(3):150 – 157, 2009. ISSN 0009-9120. doi: http://dx.doi.org/10.1016/j.clinbiochem.2008.09.105. URL http://www.sciencedirect.com/science/article/pii/S0009912008005122.

[13] Buechler KF, Dwyer BP, Noar B, Tadesse L, and Moi S. A fluorescence energy transfer detection system for immunoassays of biological samples. *Clinical Chemistry*, 32:5136, 1997.

[14] Ulrich Friess and Maik Stark. Cardiac markers: a clear cause for point-of-care testing. *Analytical and Bioanalytical Chemistry*, 393(5):1453–1462, 2009. ISSN 1618-2642. doi: 10.1007/s00216-008-2573-z. URL http://dx.doi.org/10.1007/s00216-008-2573-z.

[15] G. Jackowski. Method and device for diagnosing and distinguishing chest pain in early onset thereof, May 5 1998. URL http://www.google.com/patents/US5747274. US Patent 5,747,274.

[16] Lynn P. Cloney, Linda J. Spiller, Whalley K. Fong, Joanne E. Harris, and Paul C. Harris. Ramp: High accuracy from immunochromatographic assays by the use of internal control ratios. *Clinical Chemistry*, 49(10):1775–1777, 2003. doi: 10.1373/49.10.1775. URL http://www.clinchem.org/content/49/10/1775.short.

[17] Pratap Singh. Terminal groups in starburst dendrimers: activation and reactions with proteins. *Bioconjugate Chemistry*, 9(1):54–63, 1998. doi: 10.1021/bc970048a. URL http://pubs.acs.org/doi/abs/10.1021/bc970048a. PMID: 9460547.

[18] B.K. Van Weemen and A.H.W.M. Schuurs. Immunoassay using antigenenzyme conjugates. {*FEBS*} *Letters*, 15(3):232 – 236, 1971. ISSN 0014-5793. doi: http://dx.doi.org/10.1016/0014-5793(71)80319-8. URL http://www.sciencedirect.com/science/article/pii/0014579371803198.

[19] Anthony D Keefe, Supriya Pai, and Andrew Ellington. Aptamers as therapeutics. *Nature Reviews Drug Discovery*, 9(7):537–550, 2010.

[20] Madeleine H.E. Bruins Slot, Geert J.M.G. van der Heijden, Saskia D. Stelpstra, Arno W. Hoes, and Frans H. Rutten. Point-of-care tests in suspected acute myocardial infarction: A systematic review. *International Journal of Cardiology*, 168(6):5355 – 5362, 2013. ISSN 0167-5273. doi: http://dx.doi.org/10.1016/j.ijcard.2013.08.002. URL http://www.sciencedirect.com/science/article/pii/S0167527313015271.

[21] Mazher-Iqbal Mohammed and Marc P. Y. Desmulliez. Lab-on-a-chip based immunosensor principles and technologies for the detection of cardiac biomarkers: a review. *Lab Chip*, 11:569–595, 2011. doi: 10.1039/C0LC00204F. URL http://dx.doi.org/10.1039/C0LC00204F.

[22] Paul D'Orazio. Biosensors in clinical chemistry 2011 update. *Clinica Chimica Acta*, 412(1920): 1749 – 1761, 2011. ISSN 0009-8981. doi: http://dx.doi.org/10.1016/j.cca.2011.06.025. URL http://www.sciencedirect.com/science/article/pii/S0009898111003597.

[23] Brian Cunningham, Jean Qiu, Peter Li, and Bo Lin. Enhancing the surface sensitivity of colorimetric resonant optical biosensors. *Sensors and Actuators B: Chemical*, 87(2):365 – 370, 2002. ISSN 0925-4005. doi: 10.1016/S0925-4005(02)00273-3. URL http://www.sciencedirect.com/science/article/pii/S0925400502002733.

[24] Stefano Mariani and Maria Minunni. Surface plasmon resonance applications in clinical analysis. *Analytical and Bioanalytical Chemistry*, 406(9-10):2303–2323, 2014. ISSN 1618-2642. doi: 10.1007/s00216-014-7647-5. URL http://dx.doi.org/10.1007/s00216-014-7647-5.

[25] Bhavya Sharma, Renee R. Frontiera, Anne-Isabelle Henry, Emilie Ringe, and Richard P. Van Duyne. Sers: Materials, applications, and the future. *Materials Today*, 15(12):16 – 25, 2012. ISSN 1369-7021. doi: http://dx.doi.org/10.1016/S1369-7021(12)70017-2. URL http://www.sciencedirect.com/science/article/pii/S1369702112700172.

[26] Jiri Homola, Sinclair S. Yee, and Gnter Gauglitz. Surface plasmon resonance sensors: review. *Sensors and Actuators B: Chemical*, 54(12):3 – 15, 1999. ISSN 0925-4005. doi: 10.1016/S0925-4005(98)00321-9. URL http://www.sciencedirect.com/science/article/pii/S0925400598003219.

[27] J.R. Lakowicz. *Principles of Fluorescence Spectroscopy*. Springer, 2007. ISBN 9780387463124. URL http://books.google.co.uk/books?id=-PSybuLNxcAC.

[28] Donald A. Tomalia, Adel M. Naylor, and William A. Goddard. Starburst dendrimers: Molecular-level control of size, shape, surface chemistry, topology, and flexibility from atoms to macroscopic matter. *Angewandte Chemie International Edition in English*, 29(2):138–175, 1990. ISSN 1521-3773. doi: 10.1002/anie.199001381. URL http://dx.doi.org/10.1002/anie.199001381.

[29] Pratap Singh. Dendrimers and their applications in immunoassays and clinical diagnostics. *Biotechnology and Applied Biochemistry*, 48(1):1–9, 2007. ISSN 1470-8744. doi: 10.1042/BA20070019. URL http://dx.doi.org/10.1042/BA20070019.

[30] J Coates and C Walker. The value of admitting patients following a positive myoglobin using a rapid point of care triple cardiac panel test. *Emergency Medicine Journal*, 30(10):870–871, 2013. doi: 10.1136/emermed-2013-203113.11. URL http://emj.bmj.com/content/30/10/870.2.abstract.

[31] Alex Zaphiriou, Stephen Robb, Tarita Murray-Thomas, Gustavo Mendez, Kevin Fox, Theresa McDonagh, Suzanna M.C. Hardman, Henry J. Dargie, and Martin R. Cowie. The diagnostic accuracy of plasma bnp and ntprobnp in patients referred from primary care with suspected heart failure: Results of the uk natriuretic peptide study. *European Journal of Heart Failure*, 7(4):537–541,

2005. doi: 10.1016/j.ejheart.2005.01.022. URL http://eurjhf.oxfordjournals.org/content/7/4/537.abstract.

[32] C. Dodeigne, L. Thunus, and R. Lejeune. Chemiluminescence as diagnostic tool. a review. *Talanta*, 51(3):415 – 439, 2000. ISSN 0039-9140. doi: http://dx.doi.org/10.1016/S0039-9140(99)00294-5. URL http://www.sciencedirect.com/science/article/pii/S0039914099002945.

[33] Joseph Wang. Electrochemical biosensors: Towards point-of-care cancer diagnostics. *Biosensors and Bioelectronics*, 21(10):1887 – 1892, 2006. ISSN 0956-5663. doi: http://dx.doi.org/10.1016/j.bios.2005.10.027. URL http://www.sciencedirect.com/science/article/pii/S0956566305003441.

[34] Saihari Sadanandan, Christopher P. Cannon, Kasi Chekuri, Sabina A. Murphy, Peter M. DiBattiste, David A. Morrow, James A. de Lemos, Eugene Braunwald, and C. Michael Gibson. Association of elevated b-type natriuretic peptide levels with angiographic findings among patients with unstable angina and non-st-segment elevation myocardial infarction. *Journal of the American College of Cardiology*, 44(3):564 – 568, 2004. ISSN 0735-1097. doi: http://dx.doi.org/10.1016/j.jacc.2004.03.072. URL http://www.sciencedirect.com/science/article/pii/S0735109704009465.

[35] Martin Kristensen, Asger Krüger, Nathaniel Groothoff, Jaime García-Rupérez, Veronica Toccafondo, Javier García-Castelló, Maria Jose Ba nuls, Sergio Peransi-Llopis, and Angel Maquieira. Photonic crystal biosensor chip for label-free detection of bacteria. In *Optical Sensors*, page SWB1. Optical Society of America, 2011. URL http://www.opticsinfobase.org/abstract.cfm?URI=Sensors-2011-SWB1.

[36] Steven M. Shamah and Brian T. Cunningham. Label-free cell-based assays using photonic crystal optical biosensors. *Analyst*, 136:1090–1102, 2011. doi: 10.1039/C0AN00899K. URL http://dx.doi.org/10.1039/C0AN00899K.

[37] Martin Baaske and Frank Vollmer. Optical resonator biosensors: Molecular diagnostic and nanoparticle detection on an integrated platform. *ChemPhysChem*, 13(2):427–436, 2012. ISSN 1439-7641. doi: 10.1002/cphc.201100757. URL http://dx.doi.org/10.1002/cphc.201100757.

[38] Yafang Tan, Chun Ge, A. Chu, Meng Lu, W. Goldshlag, Cheng Sheng Huang, A. Pokhriyal, S. George, and B.T. Cunningham. Plastic-based distributed feedback laser biosensors in microplate format. *Sensors Journal, IEEE*, 12(5):1174 –1180, may 2012. ISSN 1530-437X. doi: 10.1109/JSEN.2011.2163933.

[39] F. Vollmer, D. Braun, A. Libchaber, M. Khoshsima, I. Teraoka, and S. Arnold. Protein detection by optical shift of a resonant microcavity. *Applied Physics Letters*, 80(21):4057 –4059, may 2002. ISSN 0003-6951. doi: 10.1063/1.1482797.

[40] Benoit Guilhabert, Nicolas Laurand, Johannes Herrnsdorf, Yujie Chen, Allan R Mackintosh, Alexander L Kanibolotsky, Erdan Gu, Peter J Skabara, R A Pethrick, and Martin D Dawson. Amplified spontaneous emission in free-standing membranes incorporating star-shaped monodisperse p-conjugated truxene oligomers. *Journal of Optics*, 12(3):035503, 2010. URL http://stacks.iop.org/2040-8986/12/i=3/a=035503.

[41] Chun Ge, Meng Lu, Xun Jian, Yafang Tan, and Brian T. Cunningham. Large-area organic distributed feedback laser fabricated by nanoreplica molding and horizontal dipping. *Opt. Express*, 18(12):12980–12991, Jun 2010. doi: 10.1364/OE.18.012980. URL http://www.opticsexpress.org/abstract.cfm?URI=oe-18-12-12980.

[42] Y. Wang. *Low Threshold Organic Semiconductor Lasers: Hybrid Optoelectronics and Applications as Explosive Sensors*. Springer Theses. Springer International Publishing, 2013. ISBN 9783319012667. URL http://books.google.co.uk/books?id=yJhKngEACAAJ.

[43] M. Lu, S. S. Choi, C. J. Wagner, J. G. Eden, and B. T. Cunningham. Label free biosensor incorporating a replica-molded, vertically emitting distributed feedback laser. *Applied Physics Letters*, 92(26):261502, 2008. ISSN 00036951. doi: DOI:10.1063/1.2913007. URL http://dx.doi.org/doi/10.1063/1.2913007.

[44] I. D. W. Samuel and G. A. Turnbull. Organic semiconductor lasers. *Chemical Reviews*, 107(4):1272–1295, 2007. doi: 10.1021/cr050152i. URL http://pubs.acs.org/doi/abs/10.1021/cr050152i.

[45] M. Lu, S. S. Choi, U. Irfan, and B. T. Cunningham. Plastic distributed feedback laser biosensor. *Applied Physics Letters*, 93(11):111113 –111113–3, sep 2008. ISSN 0003-6951. doi: 10.1063/1.2987484.

[46] Christoph Vannahme, Michael C. Leung, Frank Richter, Cameron L. C. Smith, Ptur G. Hermannsson, and Anders Kristensen. Nanoimprinted distributed feedback lasers comprising tio2 thin films: Design guidelines for high performance sensing. *Laser & Photonics Reviews*, 7(6):1036–1042, 2013. ISSN 1863-8899. doi: 10.1002/lpor.201300083. URL http://dx.doi.org/10.1002/lpor.201300083.

[47] JH Burroughes, DDC Bradley, AR Brown, RN Marks, K Mackay, RH Friend, PL Burns, and AB Holmes. Light-emitting-diodes based on conjugated polymers. *Nature*, 347(6293):539–541, OCT 11 1990. ISSN 0028-0836. doi: {10.1038/347539a0}.

[48] N Tessler, GJ Denton, and RH Friend. Lasing from conjugated-polymer microcavities. *NATURE*, 382(6593):695–697, AUG 22 1996. ISSN 0028-0836. doi: {10.1038/382695a0}.

[49] G. Heliotis, R. Xia, G.A. Turnbull, P. Andrew, W.L. Barnes, I.D.W. Samuel, and D.D.C. Bradley. Emission characteristics and performance comparison of polyfluorene lasers with one- and two-dimensional distributed feedback. *Advanced Functional Materials*, 14(1):91–97, 2004. ISSN 1616-3028. doi: 10.1002/adfm.200305504. URL http://dx.doi.org/10.1002/adfm.200305504.

[50] Esmaeil Heydari, Jens Buller, Erik Wischerhoff, Andr Laschewsky, Sebastian Dring, and Joachim Stumpe. Label-free biosensor based on an all-polymer dfb laser. *Advanced Optical Materials*, 2 (2):137–141, 2014. ISSN 2195-1071. doi: 10.1002/adom.201300454. URL http://dx.doi.org/10.1002/adom.201300454.

[51] A.-M. Haughey, B. Guilhabert, A.L. Kanibolotsky, P.J. Skabara, G.A. Burley, M.D. Dawson, and N. Laurand. An organic semiconductor laser based on star-shaped truxene-core oligomers for refractive index sensing. *Sensors and Actuators B: Chemical*, 185(0):132 – 139, 2013. ISSN 0925-4005. doi: http://dx.doi.org/10.1016/j.snb.2013.04.026. URL http://www.sciencedirect.com/science/article/pii/S0925400513004589.

[52] Anne-Marie Haughey, Benoit Guilhabert, Alexander L Kanibolotsky, Peter J Skabara, Martin D Dawson, Glenn A Burley, and Nicolas Laurand. An oligofluorene truxene based distributed feedback laser for biosensing applications. *Biosensors and Bioelectronics*, 54(0):679 – 686, 2014. ISSN 0956-5663. doi: http://dx.doi.org/10.1016/j.bios.2013.11.054. URL http://www.sciencedirect.com/science/article/pii/S0956566313008440.

[53] Christoph Vannahme, Cameron L. C. Smith, Mads Brokner Christiansen, and Anders Kristensen. Emission wavelength of multilayer distributed feedback dye lasers. *Applied Physics Letters*, 101(15): 151123, 2012. doi: 10.1063/1.4759131. URL `http://link.aip.org/link/?APL/101/151123/1`.

[54] Chun Ge, Meng Lu, Wei Zhang, and Brian T. Cunningham. Distributed feedback laser biosensor incorporating a titanium dioxide nanorod surface. *Applied Physics Letters*, 96(16):163702, 2010. doi: http://dx.doi.org/10.1063/1.3394259. URL `http://scitation.aip.org/content/aip/journal/apl/96/16/10.1063/1.3394259`.

[55] T. Riedl, T. Rabe, H.-H. Johannes, W. Kowalsky, J. Wang, T. Weimann, P. Hinze, B. Nehls, T. Farrell, and U. Scherf. Tunable organic thin-film laser pumped by an inorganic violet diode laser. *Applied Physics Letters*, 88(24):241116 –241116–3, jun 2006. ISSN 0003-6951. doi: 10.1063/1.2211947.

[56] Yafang Tan, A. Chu, Meng Lu, and B.T. Cunningham. Distributed feedback laser biosensor noise reduction. *Sensors Journal, IEEE*, 13(5):1972–1978, May 2013. ISSN 1530-437X. doi: 10.1109/JSEN.2013.2244591.

Chapter 2

Models for DFB laser design and optimisation

A biosensor consists of two elements, a transducer and a biorecognition component. The transducer converts a positive biorecognition event into a detectable signal, such as a shift in laser emission wavelength in the case of a DFB laser biosensor. And the biorecognition element enables specific biomolecule immobilisation on the transducer for sensing. This means that the performance of a biosensor depends on the characteristics of both the transducer and the method used for specific biorecognition of a molecule. For a DFB laser biosensor, the transducer characteristics are determined by the properties of the device structure and specific biorecognition is achieved through functionalisation of the laser surface to enable binding of certain biomolecules. Optimisation of both the DFB laser device structure and the surface functionalisation must be performed in order to maximise the sensitivity and specificity of the sensor. In chapters 4 and 5, the methods used to confer functionality to the laser surface for specific biomolecule detection are presented and discussed. The aim of this chapter is to explain the theoretical approach used to model and optimise the structural parameters of the device to achieve maximum sensing of molecules present on the laser surface.

2.0.1 Motivation for theoretical modelling of device structures

DFB laser biosensors operate via the detection of small refractive index perturbations at the laser surface, resulting from e.g. the binding of a biomolecule. As described in the previous chapter, changes to the refractive index of the superstrate, which may be a bulk solution or an adsorbed layer of molecules, alter the effective refractive index profile of the laser mode which results in a shift in resonant wavelength. Therefore, the

sensitivity of the device to adsorption of any biomolecules, not considering the effect of biofunctionalisation of the laser surface, is linked to the magnitude of the resonance shift and the inherent resonance bandwidth, i.e. the laser emission linewidth, which essentially determines the device resolution (minimum detectable shift in wavelength). In order to optimise the sensitivity of the device, the magnitude of the resonance shift must be maximised, e.g. by extending the interaction of the optical wave with the biosensing region, while simultaneously minimising the resonance linewidth. The interaction of the optical wave with the biosensing region is linked to the overlap of the laser mode with this region. The steps taken to minimise the laser emission linewidth are described in Section 3.3. Increasing the optical wave intensity within the biodetection region can be achieved through structural changes to the laser, and therefore in designing the device structure it is important to understand how the physical properties of the device affect the resonant laser mode and its interaction with the biosensing region. Modelling the response of the laser to structural changes is an efficient way to optimise the laser and provide a focus for experimental modifications to the device. Furthermore, a model can also be used to estimate the response of the laser to biomolecules of varying size/density, enabling predictions of which biomolecules the laser may be able to detect.

The effective refractive index of DFB laser modes can be determined by solving Maxwell's equations as described by a number of numerical models [1–4]. In designing a DFB laser biosensor, it is inevitable that the device structure will incorporate several layers, as depicted in Figure 2.1, including the laser gain material, a biorecognition layer of probe molecules, and a biomolecule layer consisting of analyte and buffer. Therefore, the model used to describe the T3 DFB lasers is based on a modified waveguide approach where a thin-film transfer matrix method is used to solve Maxwell's equations across the boundaries of the different layers of the laser structure [5]. The model enables the determination of the transverse profile of the laser mode (and the effective refractive index), which can be used to determine the interaction of the laser mode with the different regions of the DFB laser structure. One of the advantages of using the matrix formalism is that the transfer matrix allows electromagnetic fields to be traced throughout a multilayer stack. The model used in this work is described in Section 2.2. First, the DFB laser parameters that can be optimised are discussed.

2.1 Device parameters

A schematic of a DFB laser indicating its various parameters was shown in Figure 1.8. The device parameters that can be modified include:

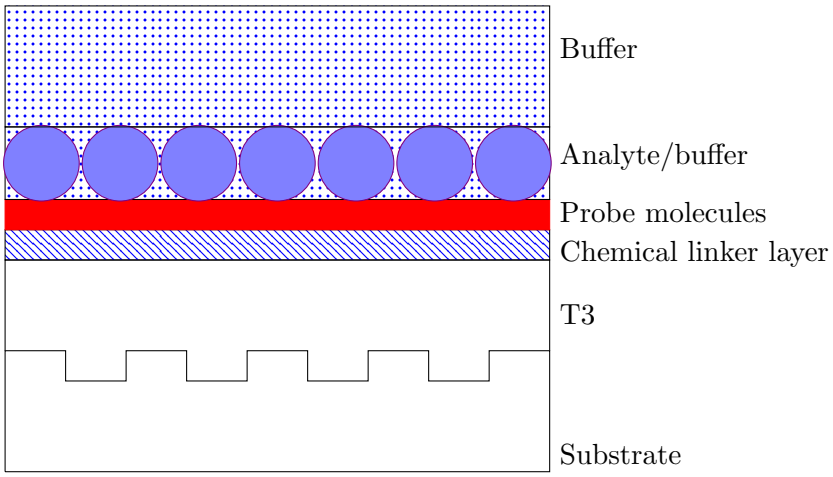

FIGURE 2.1: Schematic of the layers in a typical T3 DFB laser biosensor. Note that this Figure is not to scale.

- Grating period, Λ, and modulation depth, δt
- Gain layer refractive index, n_a
- Substrate refractive index, n_{sub}
- Gain layer thickness, t

Altering any of the parameters listed above will have an effect on the laser emission wavelength and/or the laser threshold. Each of these parameters, and their effect on biosensing, are discussed in more detail in Section 2.3.

2.2 Details of the model

A multilayer transfer matrix model based on [5] was used for numerical evaluation of the modes of DFB laser structures. The main points of the model are described here. The model outputs the effective refractive indices for the TE_0 laser mode, the expected shift in wavelength for both bulk and surface refractive index sensing, the mode profile and the overlap of the laser mode intensity profile with the various layers of a DFB laser.

2.2.1 The wave equation

A plane wave (incident on the DFB laser structure as represented in Figure 2.2, left) is considered for the derivation of the transfer matrix of the DFB laser structure. The latter is used to determine the laser mode as explained in Section 2.2.2. The laser gain layer and any other layers adjacent to the gain layer (with layer layer 1 being the topmost

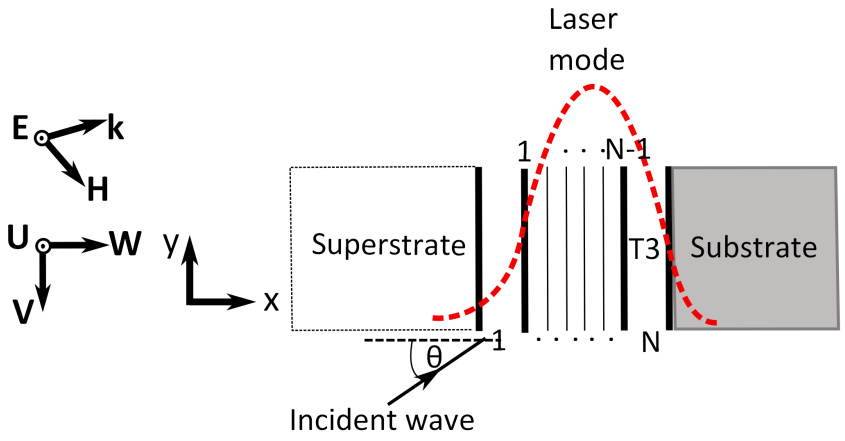

FIGURE 2.2: Multilayer stack of N thin films bounded by semi-infinite substrate and superstrate layers. The incident plane waves (shown on the left) are used to derive the transfer matrix of the multilayer structure. The laser mode (TE_0 wave) is guided in the multilayer structure along the y direction, i.e. has evanescent tails in the substrate and superstrate. Characteristics of this mode can be calculated from the elements of the transfer matrix.

layer adjacent to the superstrate and layer N being the T3 layer) are enclosed between semi-infinite superstrate and substrate layers. The boundaries between layers 1 to N are numbered 1 to N-1. The direction cosines are given by $\alpha = ncos\theta = (n^2 - \beta^2)^{1/2}$ and $\beta = nsin\theta$ as indicated in Figure 2.2, and where β is the propagation constant.

T3 DFB lasers fabricated for the experimental work presented in this thesis oscillate on the fundamental TE_0 mode and therefore the model is designed to solve for the TE_0 mode only, although it can equally be applied to other modes, including TM modes, due to the interchangeable nature of the components of Maxwell's equations. The plane of incidence is the xy plane and the interfaces between the layers of the DFB laser are parallel to the yz plane. Therefore the only material variation for the stack of layers occurs in the x direction, as shown in Figure 2.2. For a TE wave, E_x and E_y, and therefore H_z, are equal to zero, and Maxwell's equations in a waveguide reduce to the following six equations where ϵ, μ, ω and c represent dielectric permittivity, magnetic permeability, angular frequency and the speed of light respectively, and time dependence ($e^{-i\omega t}$) is assumed.

$$\frac{\partial H_y}{\partial x} - \frac{\partial H_x}{\partial y} + \frac{i\varepsilon\omega}{c} E_z = 0 \tag{2.1a}$$

$$\frac{\partial H_z}{\partial y} - \frac{\partial H_y}{\partial z} = 0 \tag{2.1b}$$

$$\frac{\partial H_x}{\partial z} - \frac{\partial H_z}{\partial x} = 0 \tag{2.1c}$$

$$\frac{i\omega\mu}{c} H_z = 0 \tag{2.1d}$$

$$\frac{\partial E_z}{\partial y} - \frac{i\omega\mu}{c} H_x = 0 \tag{2.1e}$$

$$\frac{\partial E_z}{\partial x} + \frac{i\omega\mu}{c} H_y = 0 \tag{2.1f}$$

H_x, H_y and E_z are functions of x and y only. Therefore, using equations 2.1a, e and f, H_y and H_x can be eliminated to provide a wave equation as a function of E_z only, Eq. 2.2.

$$\frac{\partial^2 E_z}{\partial x^2} + \frac{\partial^2 E_z}{\partial y^2} + \frac{\omega^2 \varepsilon \mu}{c^2} E_z = \frac{d(\ln \mu)}{dx} \frac{\partial E_z}{\partial x} \tag{2.2}$$

The solution of the wave equation, Eq. 2.2, can be found by separating the variables dependent on x and y using a trial solution that is the product of two functions, one involving x and the other involving y. $E_z(x, y) = Y(y)U(x)$ is the trial solution that is substituted into Eq. 2.2 and results in Eq. 2.3.

$$\frac{1}{X}\frac{d^2X}{dx^2} + \frac{\omega^2 \varepsilon \mu}{c^2} - \frac{d(ln\mu)}{dx}\frac{1}{X}\frac{dX}{dx} = -\frac{1}{U}\frac{d^2U}{dy^2} \tag{2.3}$$

As the left hand side and right hand side of Eq. 2.3 are dependent on x and y respectively, each side of the equation can be set equal to a constant and the solution to the wave equation therefore takes the form of $X(x)e^{ik(\beta y)-i\omega t}$, where k is the wave vector. Expressions for E_z, H_y and H_x are given by:

$$E_z = U(x)e^{i(k\beta y - \omega t)} \tag{2.4a}$$

$$H_y = V(x)e^{i(k\beta y - \omega t)} \tag{2.4b}$$

$$H_x = W(x)e^{i(k\beta y - \omega t)} \tag{2.4c}$$

The relationship between the amplitudes of the field components, $U(x)$, $V(x)$ and $W(x)$, is given by inserting Eq. 2.4a-c into Eq. 2.1a, 2.1e and 2.1f, resulting in Eq. 2.5a-c, where transverse electric field γ ($\gamma = \frac{ncos\theta}{z_0}$) in non-magnetic media and can be defined as $\gamma = \frac{\alpha}{c\mu}$.

$$V = \frac{\gamma}{ik\alpha}\frac{dU}{dx} \tag{2.5a}$$

$$W = \frac{\beta\gamma}{\alpha}U \tag{2.5b}$$

$$U = \frac{1}{ik\gamma\alpha}\frac{dV}{dx} \tag{2.5c}$$

At the boundary between two adjacent layers the tangential components of the electric and magnetic fields must be continuous. The tangential field components U and V are continuous whereas W, the amplitude of the component normal to the boundary between the layers, is proportional to U. Therefore, the total field can be specified using the pair of simultaneous equations for U and V given in Eq. 2.6.

$$\frac{dU}{dx} = \frac{ik\alpha}{\gamma}V \tag{2.6a}$$

$$\frac{dV}{dx} = ik\gamma\alpha U \tag{2.6b}$$

Elimination between Eq. 2.6a and b gives the second-order linear differential equations for U and V, Eq. 2.7.

$$\frac{d^2U}{dx^2} + k^2\alpha^2 U = 0 \tag{2.7a}$$

$$\frac{d^2V}{dx^2} + k^2\alpha^2 V = 0 \tag{2.7b}$$

2.2.2 The transfer matrix

The solutions to the differential equations involving the field amplitudes U and V can be conveniently expressed in matrix notation. As the functions $U(x)$ and $V(x)$ each satisfy a second-order linear differential equation, Eq. 2.7a and b, U and V may each be expressed as a linear combination of two solutions, say U_1 and U_2 and V_1 and V_2. These solutions must be coupled by the first order differential equations, Eq. 2.5a and c, resulting in Eq. 2.8a and b.

$$\begin{cases} \frac{dU_1}{dx} = \frac{ik\alpha}{\gamma}V_1 \\ \frac{dV_1}{dx} = ik\gamma\alpha U_1 \end{cases} \tag{2.8a}$$

$$\begin{cases} \frac{dU_2}{dx} = \frac{ik\alpha}{\gamma}V_2 \\ \frac{dV_2}{dx} = ik\gamma\alpha U_2 \end{cases} \tag{2.8b}$$

Inspection of Eq. 2.8 suggests that $\frac{d}{dx}(U_1V_2 - U_2V_1) = 0$, which resembles the determinant of a matrix, Eq. 2.9, and implies that the determinant of any two arbitrary solutions of Eq. 2.8 is a constant.

$$D = \begin{vmatrix} U_1 & V_1 \\ U_2 & V_2 \end{vmatrix} \tag{2.9}$$

If the particular solutions for the four matrix elements are chosen such that $U_1 = f(x)$, $U_2 = F(x)$, $V_1 = g(x)$ and $V_2 = G(x)$ where $f(0) = G(0) = 0$ and $F(0) = g(0) = 1$, then the solutions with $U(0) = U_0$ and $V(0) = V_0$ may be expressed in matrix notation, $\mathbf{Q} = \mathbf{NQ_0}$ where $\mathbf{Q}$, $\mathbf{N}$ and $\mathbf{Q}_0$ are given by Eq. 2.10.

$$\mathbf{Q} = \begin{vmatrix} U(x) \\ V(x) \end{vmatrix} \qquad \mathbf{Q_0} = \begin{vmatrix} U_0 \\ V_0 \end{vmatrix} \qquad \mathbf{N} = \begin{vmatrix} F(x) & f(x) \\ G(x) & g(x) \end{vmatrix} \tag{2.10}$$

The determinant of $\mathbf{N}$ is a constant and the value of the constant can be found using $|\mathbf{M}| = Fg - fG = 1$ and expressing U_0 and V_0 as functions of $U(x)$ and $V(x)$ such that $\mathbf{Q}_0 = \mathbf{MQ}$, where $\mathbf{M}$ is given by Eq. 2.11.

$$\mathbf{M} = \begin{vmatrix} g(x) & -f(x) \\ -G(x) & F(x) \end{vmatrix} \qquad |\mathbf{M}| = 1 \tag{2.11}$$

Matrix $\mathbf{M}$ relates the field amplitudes U and V at a position along the x axis, say x_n, to a second position, say x_{n-1}. As the knowledge of U and V is sufficient to describe the field of a wave propagating through the layers of the DFB laser, the properties of the layers need only be described by an appropriate unimodular matrix $\mathbf{M}$. The particular components of matrix $\mathbf{M}$ for the stack of N layers between the substrate and superstrate of the DFB lasers can be found, using Eq. 2.5 and the particular solutions noted previously, to give matrix $\mathbf{M}_n$ in Eq. 2.12 where Φ is the phase thickness of the layer and and is given by $\Phi_n = k\alpha_n(x_n - x_{n-1})$.

$$\mathbf{M}_n = \begin{pmatrix} cos\Phi_n & \frac{-i}{\gamma_n} sin\Phi_n \\ -i\gamma_n sin\Phi_n & cos\Phi_n \end{pmatrix} \tag{2.12}$$

Each of the N layers of the multilayer stack is described by a matrix resembling Eq. 2.12. The transfer matrix ($\mathbf{M}$) combining all of the N layers is given by the product of each of the matrices for the respective individual layers, Eq. 2.13.

$$\mathbf{M} = \prod_{n=1}^{N} \begin{pmatrix} m_{11} & m_{12} \\ m_{21} & m_{22} \end{pmatrix} \tag{2.13}$$

When the propagation constant β is real and the layers of the DFB laser have real refractive indices, the diagonal elements m_{11} and m_{22} of the transfer matrix are real and the off-diagonal elements m_{12} and m_{21} are imaginary. Eq. 2.13 can generally be used to determine the reflection and transmission of the structure in the case of waves incident on the multilayer stack. However, Eq. 2.13 also enables determination of the guided modes, i.e. the waves that are guided inside the multilayer structure in the y direction. In the DFB laser model presented here, the lowest order waveguided modes represent the laser mode (it overlaps the gain region, propagates in the y direction and interacts with the grating resulting in the feedback required for laser emission).

A wave propagating within the stack of N layers, as depicted in Figure 2.2, is confined between the substrate and superstrate layers by total internal reflection. For waveguided fields, the transfer matrix describing the stack of N layers must relate the field at the boundary between the superstrate and the layer N=1 to the field at the boundary between the T3 layer and the substrate. Therefore the fields at the stack boundaries are required to satisfy Eq. 2.14, where the subscripts $_{sub}$ and $_{sup}$ represent the substrate and superstrate respectively.

$$\begin{pmatrix} U_{sup} \\ V_{sup} \end{pmatrix} = \mathbf{M} \begin{pmatrix} U_{sub} \\ V_{sub} \end{pmatrix} \tag{2.14}$$

As the laser modes guided within the DFB laser are bound between the semi-infinite substrate and superstrate layers, the field amplitudes decay exponentially along the x direction, as shown in Figure 2.2, giving rise to the complex evanescent waves in the superstrate (and the substrate) that are used for sensing. The waves are negative-going in the substrate and positive-going in the superstrate (radiation condition) such that $U = U_{sup}e^{(-ik\alpha_{sup}x)}$ and $U = U_{sub}e^{(ik\alpha_{sub}(x-x_{sub}))}$, respectively. For waveguided modes α_{sup} and α_{sub} are imaginary.

Positive and negative travelling waves are distinguished from the total field by use of the notation U^+ and V^+ and are represented by Eq. 2.15.

$$\begin{pmatrix} U^+ \\ V^+ \end{pmatrix} = \begin{pmatrix} 1 \\ \gamma \end{pmatrix} U^+ \qquad \begin{pmatrix} U^- \\ V^- \end{pmatrix} = \begin{pmatrix} 1 \\ -\gamma \end{pmatrix} U^- \tag{2.15}$$

Using the notation in Eq. 2.15 and Eq. 2.14, results in Eq. 2.16.

$$\begin{pmatrix} 1 \\ -\gamma_{sup} \end{pmatrix} U_{sup} = \mathbf{M} \begin{pmatrix} 1 \\ \gamma_{sub} \end{pmatrix} U_{sub} \tag{2.16}$$

Solving Eq. 2.16 results in the modal-dispersion function ($\chi(\beta)$)for bound modes and is given by Eq. 2.17.

$$\chi(\beta) = \gamma_{sup} m_{11} + \gamma_{sup}\gamma_{sub} m_{12} + m_{21} + \gamma_{sub} m_{22} = 0 \tag{2.17}$$

Eq. 2.17 can be solved numerically for the propagation constant, β, which is equivalent to the effective refractive index of the laser mode in the case of the DFB laser described in Figure 2.2. Each solution of Eq. 2.17 corresponds to a waveguided mode, with the highest solution representing the lowest order waveguided mode (shown in Figure 2.3 for multilayer DFB lasers). An overview of the steps involved in the model used to characterise the DFB lasers is provided in the next section.

2.2.3 The multilayer DFB laser model

The multilayer model was first developed in Mathcad® by Dr N. Laurand with aspects of it converted into Matlab® by AM. Haughey to reduce computation time.

2.2.3.1 Calculation of the effective refractive index of the TE_0 mode

Calculation of the effective refractive index of the TE_0 mode propagating through a stack of N layers first requires that the matrices describing the properties of the layers, Eq. 2.12, are defined for each of the N layers. The product of these matrices is then used to produce the dispersion relation, Eq. 2.17. The amplitudes of the fields tangential to the layer interfaces are continuous across the layer interface and, therefore, the dispersion relation must be solved to satisfy this boundary condition. To do this, the 'fminsearch' function in Matlab was used to find the value of β satisfying Eq. 2.17, starting from an initial value of β, chosen to be close to the refractive index of the gain layer. The calculation of the effective refractive index can be performed for a range of scenarios, e.g. for detection of a thin layer of material adsorbing to the laser surface. In this case, the predicted shift in wavelength is calculated by taking the difference between the effective refractive indices of the laser mode with and without the adsorbed layer and using the Bragg equation, Eq. 1.1, to convert this into a value for wavelength. Two example plots of the output from the model for the modal dispersion function are shown in Figure 2.3.

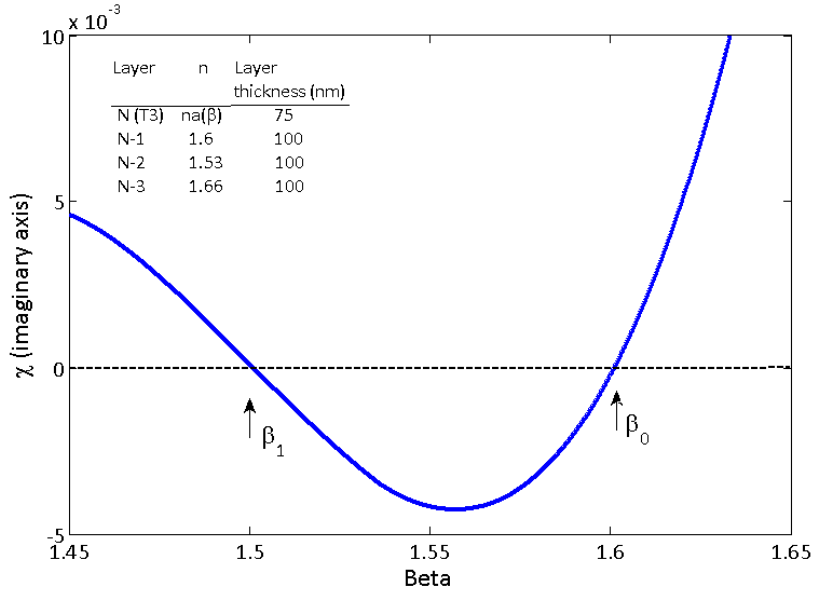

(a)

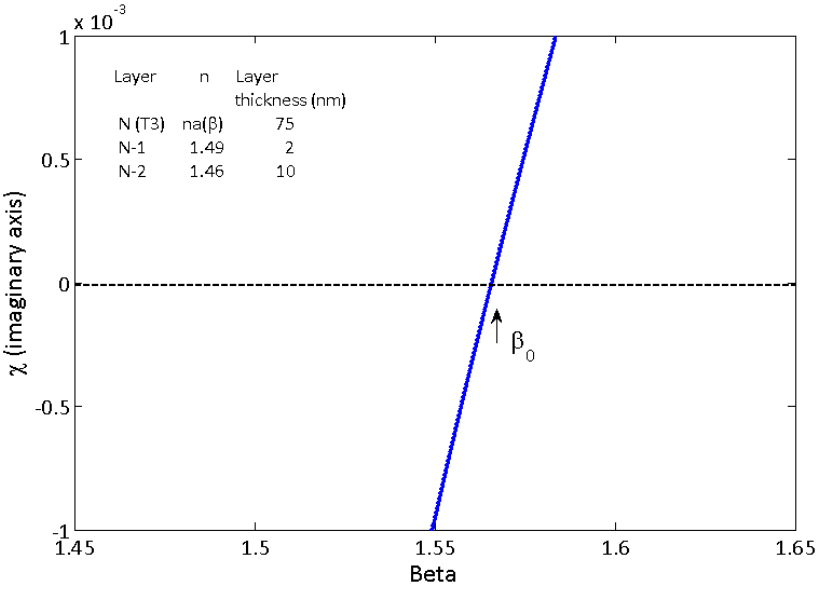

(b)

FIGURE 2.3: The modal dispersion function $\chi(\beta)$ versus the propagation constant β for TE modes. (a) was plotted for a four layer system (T3 layer and three arbitrary layers) to demonstrate that a thick DFB laser structure supports multiple modes. The TE_0 and TE_1 modes are shown. (b) was plotted for a three layer system (T3 layer, a thin chemical linker layer and a thin biolayer). This structure supports the TE_0 mode only. In each case the lowest order mode corresponds to the TE_0 laser mode. The layer parameters are shown on each Figure.

The calculation of the effective refractive index was performed using Matlab and a summary of the inputs, and typical values in brackets, for the model when calculating the effective refractive index is provided below:

- n_{sup}, (1.35)
- Cauchy constants for n_{sub}, (1.52)
- λ_{Bragg}, (430 nm)
- Grating period, (277 nm)
- Thickness of each of the N layers, (T3≈70 nm, variable thicknesses for other layers)
- Index of each of the N layers, (biolayer 1.40, polyelectrolyte layer 1.49)
- Constants for n_a, Eq. 2.24, (1.81)
- β (initial guess of n_{eff}, 1.60)
- z_0, impedance of free space

2.2.3.2 Calculation of the intensity mode profile and overlap with the DFB laser structure

Once the effective refractive index of the TE_0 mode is found, the field distribution throughout the DFB laser structure and the stack of N layers can be traced. To do this, one of the field amplitudes may be arbitrarily chosen at one point and Eq. 2.18 can be used to calculate the field amplitudes at other points of the structure relative to the initial chosen amplitude.

$$\begin{pmatrix} U_{n-1} \\ V_{n-1} \end{pmatrix} = \mathbf{M}_n \begin{pmatrix} U_n \\ V_n \end{pmatrix} \tag{2.18}$$

To calculate the mode profile through a stack of N layers the amplitude U was chosen to be 1 at the interface between the substrate and the gain layer. As mentioned previously, the gain layer is defined as layer N. Therefore, the interface between the topmost layer and the superstrate is the interface 1. As the variation of the stack of layers is in the x direction, and to simplify the notation in Mathcad/Matlab, the number of layers was re-defined as X with the interface between the superstrate and the topmost layer being set to 0. Therefore, once U_n and V_n are known, Eq. 2.18 can be used to determine U and V at any position along the x axis.

Knowing the amplitudes at each of the layer interfaces, the mode profile, $E(x)$, is calculated through the DFB laser structure and the X layers using Eq. 2.19 where $U(x) = E(x)$ for the TE mode.

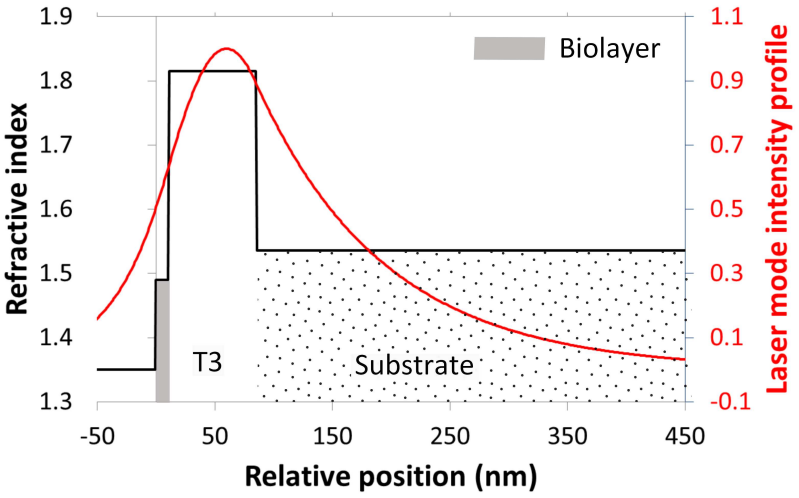

FIGURE 2.4: Laser mode intensity profile for a T3 laser with a 10 nm thick biolayer at the surface.

$$E(x) = U_n cos[k\alpha_n(x - x_n)] + \frac{i}{\gamma_n} sin[k\alpha_n(x - x_n)] \tag{2.19}$$

The resulting mode profile can be plotted against the refractive index of the structure and stack of layers, as shown in the example in Figure 2.4.

The laser mode field intensity is proportional to the square of the field amplitude and the contribution to the field for a particular layer can be found using Eq. 2.20. Eq. 2.20 is an example of the calculation of the laser mode intensity overlap for a biomolecule layer on the laser surface, that extends from x=0 to x=10 nm, where Γ_{bio} is the overlap with the biomolecule layer.

$$\Gamma_{bio} = \frac{\int_0^{10} |E(x)|^2 \, dx}{\int_{-\infty}^{+\infty} |E(x)|^2 \, dx} \tag{2.20}$$

2.2.4 Model for biomolecule binding

Biosensing with the DFB laser involves functionalising the laser surface with probe molecules that will specifically bind to particular target biomolecules. The multilayer slab waveguide model described in Section 2.2.3 can be extended to take into account the effective refractive indices of the laser mode for biolayers of differing densities, i.e. representing the difference in the number of target biomolecules on the laser surface after exposure to biomolecule solutions of varying concentrations. The coupling reaction between a probe and target biomolecule follows a Langmuir relationship with the number of bound target biomolecules increasing linearly with increasing numbers of target

biomolecules in the vicinity of the functionalised surface until saturation of the probe binding sites, with target molecules, occurs. The biolayer formed is a combination of the target biomolecule and buffer and therefore, the refractive index of the biolayer is a function of the index of the biomolecule and the buffer. The relationship between the biomolecule concentration and the biolayer refractive index is given by Eq. 2.21 where ϵ_1, ϵ_2 and ϵ_{av} are the dielectric permitivity of the buffer, biomolecule and biolayer average respectively and p represents the fraction of bound target biomolecules and is unity when the biolayer consists only of biomolecules [6].

$$(1-p)\frac{\epsilon_1-\epsilon_{av}}{\epsilon_1+2\epsilon_{av}}+p\frac{\epsilon_2-\epsilon_{av}}{\epsilon_2+2\epsilon_{av}}=0 \tag{2.21}$$

The value of p is related to the concentration of the target biomolecule solution via Eq. 2.22, where x is the concentration of the biomolecule solution, B represents saturation of the available binding sites and is set equal to 1 and K is the dissociation constant which is the number of target biomolecules bound to half of the available probe molecules, i.e. when an equilibrium between the available binding sites plus target biomolecules and biomolecule bound binding sites is equal.

$$p(x)=B\frac{x}{K+x} \tag{2.22}$$

To incorporate the dependence of the refractive index of the biolayer on the biomolecule concentration into the multilayer waveguide model, the refractive index of the biolayer, $n_{bio}(p)$ was calculated by solving Eq. 2.21 for the value of ϵ_{av} and then substituting the solution, $\epsilon(p)$, into Eq. 2.23. The effective refractive index, which was therefore a function of p, was calculated as described in Section 2.2.3. The value of the effective refractive index of the laser mode, for a biolayer with varying ratios of biomolecule to buffer, was then determined for specific values of biomolecule concentration.

$$n_{bio}(p)=\sqrt{\epsilon(p)} \tag{2.23}$$

2.3 Effect of optimisation of device parameters on biosensing performance

The various parameters of a DFB laser device were highlighted previously (Figure 2.1). Several of these parameters are dependent on the choice of gain material. For example, for optimised laser performance (e.g. low threshold operation), the grating period is set

by the Bragg relation (Eq. 1.1) where λ is the wavelength of maximum gain, Λ is the grating period and n_{eff} is the effective refractive index of the laser mode. On first glance at Eq. 1.1 it is apparent that operating at a longer wavelength, and therefore a higher grating period, will result in a greater shift in wavelength for changes to the effective refractive index of the laser mode. And, as discussed in Section 1.5, in the case of bulk sensing this is true. Figure 2.5 shows theoretical wavelength shift values, using the model detailed in Section 2.2, for bulk (n_{sup}=1.35) and surface (10-nm layer, n_{sup}=1.49) sensing for an optimised DFB laser with the following parameters: λ=430 nm, Λ=277 nm, n_{sub} ≈1.5, n_a ≈1.8 and t=75 nm. These parameters for an optimised T3 DFB laser were also used for calculation of the data in Figures 2.6 and 2.7. In the case of bulk sensing, the shift in wavelength is calculated from the difference in emission wavelength when the laser is exposed to a bulk solution and with the laser exposed to air. For surface sensing, the example of a 10 nm biolayer is given. The shift in wavelength is therefore calculated by subtracting the wavelength of laser emission without an additional 10 nm biolayer from the emission wavelength with the 10 nm biolayer. The difference in bulk sensing between a laser operating at a wavelength of 430 nm (the T3 wavelength value) and 600 nm (wavelength close to that of typical dye-doped DFB laser sensors) is 0.9 nm (34% increase). However, the same enhancement effect is not observed in the case of surface sensing, as shown in Figure 2.5. For detection of a 10-nm 'biolayer' on the laser surface, the difference in the magnitude of the shift in wavelength between lasers operating at 430 nm and 600 nm is only 0.07 nm (13% increase), and for a thinner biolayer this difference would be even smaller. As mentioned previously, in order to maximise the sensitivity of a DFB laser for biosensing, the intensity of the laser mode within the biodetection region must be maximised. A previous study investigating different configurations of photonic crystal biosensors found that the intensity of the optical wave within a biodetection region of 25 nm for an operating wavelength of 375 nm was almost double that of a similar device operating at a wavelength of 780 nm [7]. Therefore, any gain in the magnitude of the shift in wavelength achieved via operating at a longer wavelength was offset by the reduction in the overlap of the laser mode within the biodetection region for surface sensing. When the overlap of the laser mode with the biodetection region is modelled for a T3 laser and a hypothetical 'T3-like' laser with same refractive index characteristics but at a longer wavelength of 590 nm (grating period of 384 nm) with a 10 nm biolayer (n=1.49), the overlap of the biodetection region for the T3 laser was 3% whereas the overlap of the 590 nm T3 laser was <1%. Therefore, throughout optimisation of the T3 DFB lasers for biosensing, the grating period was fixed at 277 nm. The grating modulation depth was also fixed (50 nm) and its effect on device sensitivity was not considered during the modelling process. As the modulation depth can influence aspects such as the laser threshold, this may be a parameter that warrants further investigation in the future [8].

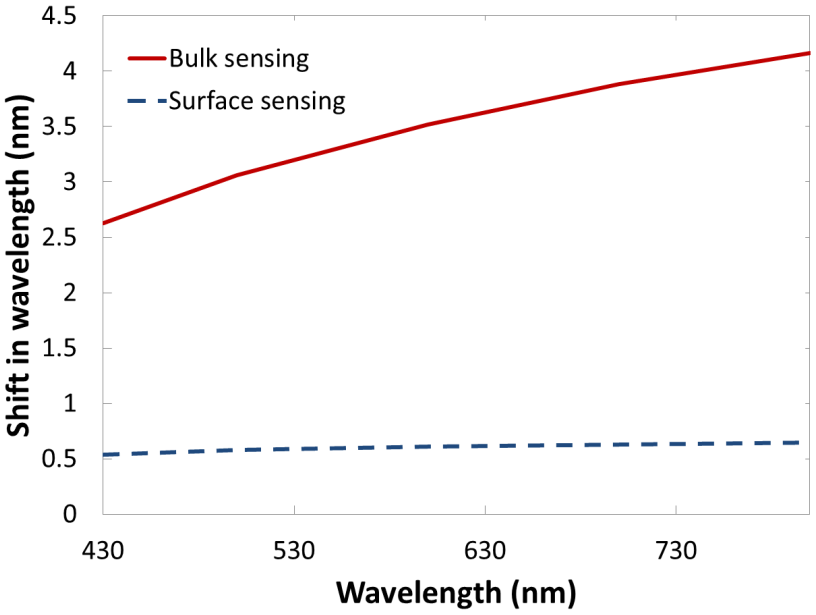

FIGURE 2.5: Surface (n=1.49) and bulk (n=1.35) sensing predictions as a function of laser wavelength.

2.3.1 Gain layer refractive index

As the gain layer refractive index is a property of the gain material there is little room to modify this parameter and the refractive index of the T3 layer was therefore 'fixed' during modelling. However, the magnitude of the refractive index of the T3 material is not a constant and varies with respect to the laser wavelength due to dispersion effects. The influence of dispersion on the T3 refractive index was taken into consideration during modelling of the lasers. The refractive index of dispersion for T3 has previously been published [9] and is described by equation 2.24 where A and B are constants given by 1.7385 and 9.511x10^8 nm respectively.

$$n_a(n_{eff}) = A + 2Be^{\frac{(n_{eff}\Lambda)}{18.1467}} \tag{2.24}$$

When modelling the response of dye-doped laser sensors, dispersion relationships were not available and therefore the refractive index was simply defined by the values in the literature.

2.3.2 Substrate refractive index

The transverse intensity profile of the DFB laser mode is governed by the refractive indices of the constituent layers. The laser mode is drawn towards higher index layers and, therefore, a low index substrate (preferably close to the index of the superstrate)

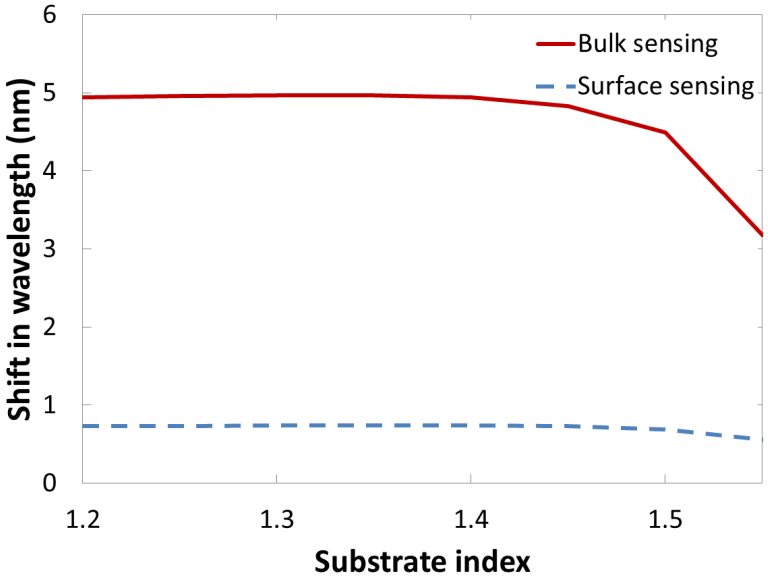

FIGURE 2.6: Surface (n=1.49) and bulk (n=1.35) sensing predictions as a function of substrate index.

is desirable in order to maximise the laser mode overlap with the biodetection region at the laser surface. Previous research has shown this to be the case theoretically and experimentally [7].

The material used as the substrate for T3 lasers was Norland 65, a photocurable optical epoxy that has a refractive index of ≈1.5 at a wavelength of 430 nm [10]. This material is very easy to work with and is cured using UV illumination in a very short time period (<1 minute). There are other optical epoxies available with a lower refractive index (indices of 1.3 are widely available) but these materials will only cure when they are protected from exposure to air, i.e. curing must take place in an inert atmosphere, such as nitrogen [10]. This requirement increases the complexity of DFB laser fabrication and therefore low index materials were not used in the experimental optimisation of the T3 laser sensors.

Figure 2.6 shows the theoretical effect of reducing the refractive index of the substrate from 1.55 to 1.2 on bulk and surface sensing. The difference in the magnitude of the shift in wavelength for bulk sensing (n=1.35) between a substrate index of 1.5 and 1.3 is 0.48 nm (11% increase) which is only a modest difference in comparison to the effect of changing the grating period, for example. The same difference in substrate index results in a 0.05 nm (7% increase) change in the wavelength shift for surface sensing of a 10 nm biolayer (n=1.49). Therefore, the potential improvement in the sensitivity of surface sensing did not justify the added complexity of working with a lower index substrate material. Although small, a wavelength shift of 0.05 nm may be significant in terms of

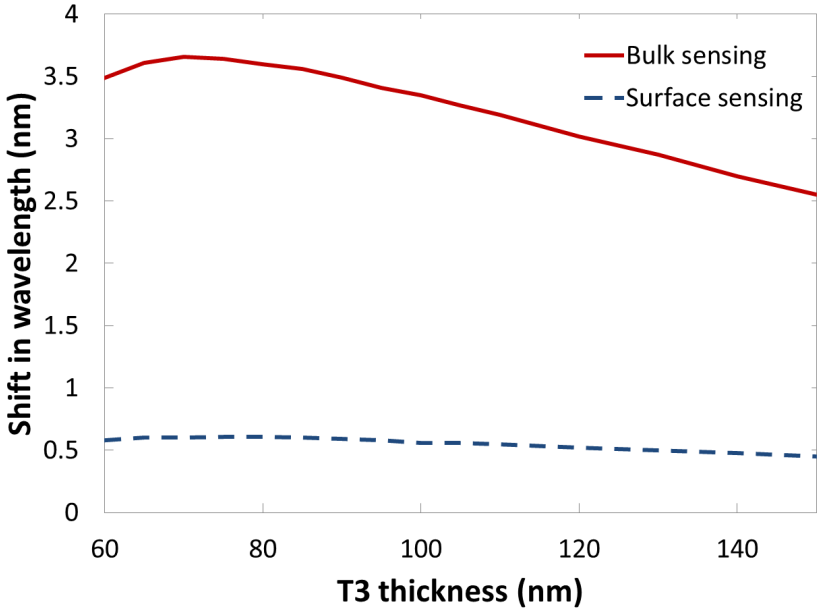

FIGURE 2.7: Surface (n=1.49) and bulk (n=1.35) sensing predictions as a function of gain layer thickness.

biosensing, and therefore reducing the substrate index of the T3 lasers to better match that of the superstrate index may be something worth investigating in future.

The refractive index of the substrate was therefore a fixed parameter when modelling the T3 lasers. The effect of dispersion on the refractive index of the substrate was taken into consideration using Cauchy's equation (Eq. 2.25), as supplied by Norland Products, where A, B and C are the constants 1.50631, 5435.62 nm^2 and 2.77798x10^7 nm^4 respectively. When modelling other devices, such as dye-doped lasers, the stated literature values for the substrate indices were used, these values did not represent any dispersion effects.

$$n_{sub}(n_{eff}\Lambda) = A + \frac{B}{(n_{eff}\Lambda)^2} + \frac{C}{(n_{eff}\Lambda)^4} \tag{2.25}$$

2.3.3 Gain layer thickness

The thickness of the region between the laser substrate and superstrate influences the effective refractive index of the laser mode and, subsequently, the laser wavelength and sensitivity. Therefore, it is necessary to optimise the thickness of the T3 gain layer in order to achieve the maximum shift in wavelength for changes to the superstrate index. A minimum gain layer thickness (expected to be in the region of 50-60 nm) is required in order to support the laser mode, but beyond this minimum 'cut-off' thickness

a thinner gain layer results in a greater shift in emission wavelength per unit change to the superstrate refractive index.

Figure 2.7 shows how the thickness of the T3 layer affects bulk and surface sensing. It is obvious from the bulk sensing results that there is a maximum shift in wavelength around a thickness of 70 nm, but there is also a maximum shift in wavelength occurring for a T3 thickness of 75 nm in the surface sensing plot. The thickness of the T3 layer can be easily controlled during fabrication of the lasers and this was therefore explored experimentally and is described in Section 3.3.1. During modelling of the T3 lasers, the thickness of the gain layer can be defined to represent the experimental thickness of the lasers or it can be varied in order to maximise the theoretical sensitivity of the laser.

During modelling, the overall effect of the grating depth on the laser modes is neglected and the thickness of the gain layer is an 'average' thickness to take into account of the modulation depth of the grating. The model is shown to accurately predict experimental data.

2.4 Validation of the model

The modelling techniques described in this chapter have been validated through comparison of the predicted model outputs with experimental data. One of the outputs from the multilayer DFB laser model is the effective refractive index of the TE_0 mode for a given laser structure. As the effective refractive index is coupled to the emission wavelength of a DFB laser via the Bragg equation, Eq. 1.1, the simplest method for testing the accuracy of the model is to compare the emission wavelength values predicted by the model to those observed through experiment. The effective refractive indices of the laser mode, as mentioned in Chapter 1, is a function of the DFB laser structure. Therefore, modification of the gain layer thickness has a marked effect on the emission wavelength of the laser, and the shift in wavelength resulting from bulk or surface sensing, as discussed in Section 2.1.3. Experimental optimisation of the gain layer thickness for maximising bulk and surface sensing, discussed further in Section 3.3.1, was performed and the observed shift in wavelength upon exposure of the laser to water is plotted alongside the operational wavelength of the laser when exposed to air, i.e. air is the superstrate layer, in Figure 2.8. These predicted values from the model are also included in Figure 2.8.

Multiple wavelength and shift measurements (i.e. the difference between emission wavelengths with the laser superstrate being air and water) were recorded, at different positions on the laser surface, for each of the lasers fabricated to have a different gain

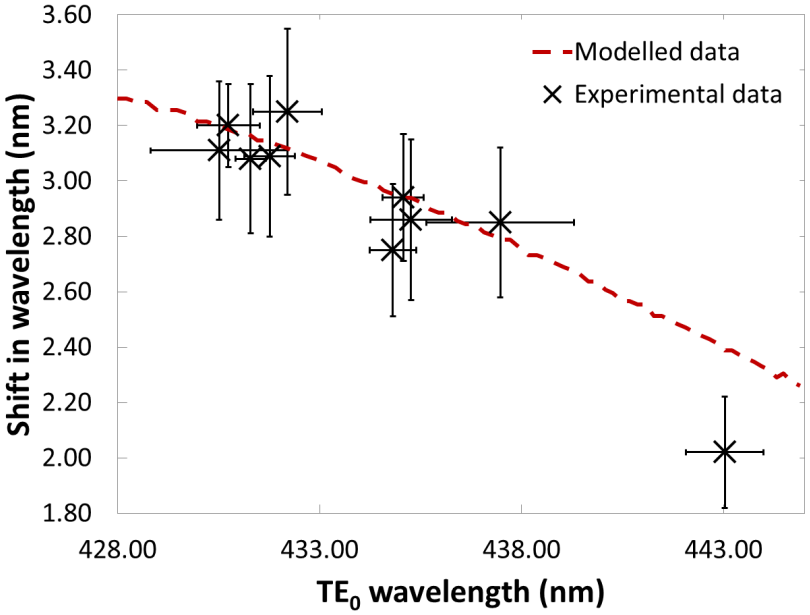

FIGURE 2.8: Comparison of experimental and modelled values of the operational wavelength in air versus the shift in wavelength of a laser immersed in water.

layer thickness. The experimental data in Figure 2.8 represents mean values ± standard deviations. Lasers fabricated with a thicker gain layer have higher effective refractive indices as a higher proportion of the laser mode intensity profile exists within the gain layer, resulting in a longer operational wavelength. Figure 2.8 demonstrates agreement between the experimental and modelled data with the only data point being far from the predicted value resulting from the laser with the thickest gain layer. The gain layer thickness is controlled via the spin coating speed used to deposit the laser material, discussed further in Section 3.1, and therefore slower spin coating speeds result in a thicker layer. Variation in layer thickness can be greater for lasers fabricated at slower spin coating speeds due to the additional effect of evaporation of the gain layer solvent which has a bigger influence at slower spin coating speeds. Overall, the agreement between the theoretical and experimental values indicated that the model could be used to predict the expected shift in wavelength upon exposure of the laser to a bulk solution. Modelled surface sensing was also performed, for which results presented in Section 3.5, with predicted results shown to demonstrate good agreement with experimental data.

The accuracy of the predicted overlap values can be inferred from the experimental data. For example, the laser threshold, which is discussed in Section 3.3, was observed to be twice the value with the laser exposed to air as it was when immersed in water. This can be explained as the laser mode intensity profile being raised closer to the DFB laser surface when immersed in water due to the effect of the increased superstrate index of water, relative to that of air, on the effective refractive index of the laser mode. This in turn results in an increase of the overlap of the laser mode with the gain layer when

the laser is immersed in water and, therefore, a higher modal gain. When the overlap of the laser mode was modelled for a laser exposed to air and water, as shown in Figure 2.9, the overlap was predicted to be 31% in water and 23% in air, which is consistent with the theoretical explanation and the experimental threshold measurements. Further comparisons between the predicted overlap of the laser mode with the various layers of the DFB laser structures are presented throughout this thesis. The correlation between the theoretical description of the lasers and the experimental results suggests that the model can be used to describe the interaction of the laser mode with the DFB laser structure.

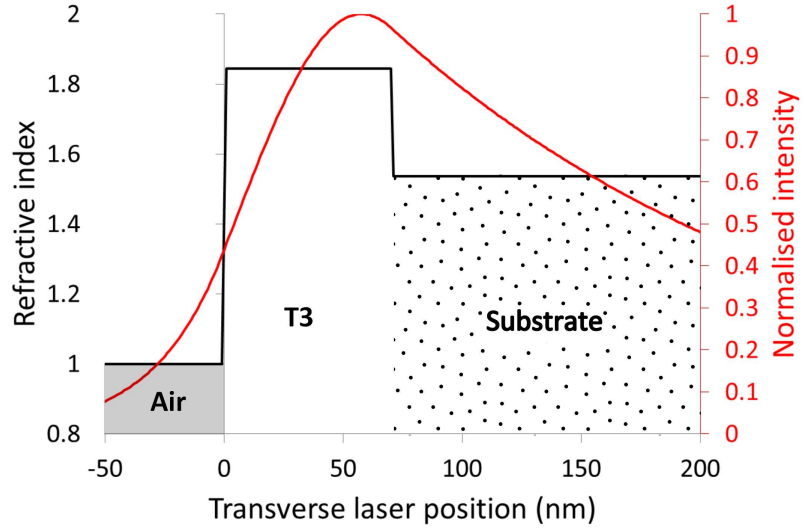

(a)

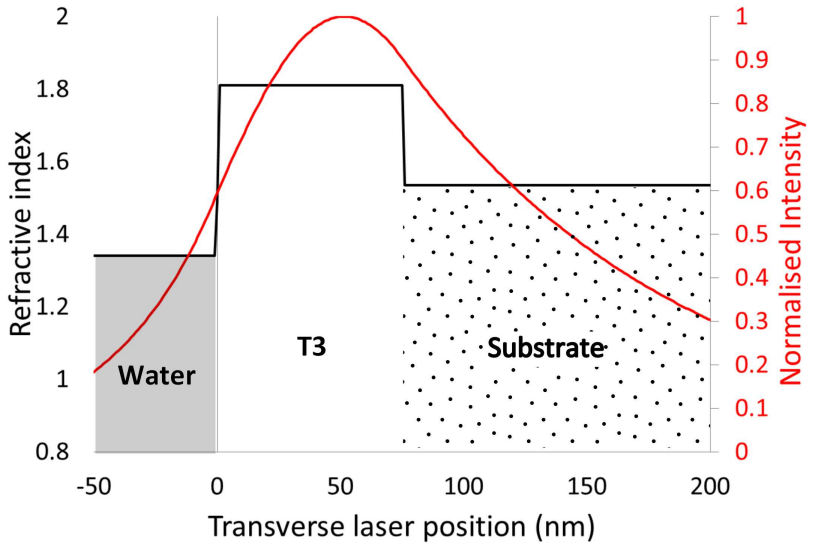

(b)

FIGURE 2.9: Laser mode intensity profile for (a) a T3 laser exposed to air and (b) water.

The values predicted by the multilayer DFB laser model modified to consider the effect of biomolecule binding to the laser surface were also compared to experimental data. Good agreement between the modelled and experimental data was observed indicating that the model can be used to predict binding events at the laser surface if the dissociation constant is known for the probe and target molecule interaction. This may be useful for future development of the laser sensor for predicting the expected sensing response to biomarker detection.

2.5 Summary

In this chapter, a theoretical description of the model of the DFB lasers was provided. The model is used to predict the effective refractive index of the TE_0 laser mode, and therefore the shift of emission wavelength in sensing events, the mode profile and the overlap of the laser mode with the various layers. A modification to the multilayer DFB model in order to incorporate the Langmuir behaviour of the probe-target biomolecule interaction was also described. The predicted values for each of the models were shown to correlate well with experimental data indicating that the theoretical models can be used to predict how structural changes to the DFB lasers will affect the response of the lasers to sensing applications and can therefore be used to help optimise the structure for maximum biosensing sensitivity.

The models are used to relate the experimental results back to the theory governing DFB lasers throughout the reminder of this thesis and to make predictions about the biosensing potential of the T3 DFB lasers.

References

[1] Cameron L. C. Smith, Johan U. Lind, Claus H. Nielsen, Mads B. Christiansen, Thomas Buss, Niels B. Larsen, and Anders Kristensen. Enhanced transduction of photonic crystal dye lasers for gas sensing via swelling polymer film. *Opt. Lett.*, 36(8):1392–1394, Apr 2011. doi: 10.1364/OL.36.001392. URL `http://ol.osa.org/abstract.cfm?URI=ol-36-8-1392`.

[2] Christoph Vannahme, Michael C. Leung, Frank Richter, Cameron L. C. Smith, Ptur G. Hermannsson, and Anders Kristensen. Nanoimprinted distributed feedback lasers comprising tio2 thin films: Design guidelines for high performance sensing. *Laser & Photonics Reviews*, 7(6):1036–1042, 2013. ISSN 1863-8899. doi: 10.1002/lpor.201300083. URL `http://dx.doi.org/10.1002/lpor.201300083`.

[3] P. K. Tien. Light waves in thin films and integrated optics. *Appl. Opt.*, 10(11):2395–2413, Nov 1971. doi: 10.1364/AO.10.002395. URL `http://ao.osa.org/abstract.cfm?URI=ao-10-11-2395`.

[4] H. Kogelnik. An introduction to integrated optics. *Microwave Theory and Techniques, IEEE Transactions on*, 23(1):2–16, 1975. ISSN 0018-9480. doi: 10.1109/TMTT.1975.1128500.

[5] John Chilwell and Ian Hodgkinson. Thin-films field-transfer matrix theory of planar multilayer waveguides and reflection from prism-loaded waveguides. *J. Opt. Soc. Am. A*, 1(7):742–753, Jul 1984. doi: 10.1364/JOSAA.1.000742. URL `http://josaa.osa.org/abstract.cfm?URI=josaa-1-7-742`.

[6] E. Stefan Kooij, Herbert Wormeester, E. A. Martijn Brouwer, Esther van Vroonhoven, Arend van Silfhout, and Bene Poelsema. Optical characterization of thin colloidal gold films by spectroscopic ellipsometry. *Langmuir*, 18(11):4401–4413, 2002. doi: 10.1021/la0256127. URL `http://pubs.acs.org/doi/abs/10.1021/la0256127`.

[7] Ian D. Block, Nikhil Ganesh, Meng Lu, and B.T. Cunningham. A sensitivity model for predicting photonic crystal biosensor performance. *Sensors Journal, IEEE*, 8(3):274–280, March 2008. ISSN 1530-437X. doi: 10.1109/JSEN.2008.917127.

[8] Justin R. Lawrence, Graham A. Turnbull, and Ifor D. W. Samuel. Polymer laser fabricated by a simple micromolding process. *Applied Physics Letters*, 82(23):4023–4025, 2003. doi: http://dx.doi.org/10.1063/1.1579858. URL `http://scitation.aip.org/content/aip/journal/apl/82/23/10.1063/1.1579858`.

[9] Georgios Tsiminis, Yue Wang, Paul E. Shaw, Alexander L. Kanibolotsky, Igor F. Perepichka, Martin D. Dawson, Peter J. Skabara, Graham A. Turnbull, and Ifor D. W. Samuel. Low-threshold organic laser based on an oligofluorene truxene with low optical losses. *Applied Physics Letters*, 94 (24):243304 –243304–3, jun 2009. ISSN 0003-6951. doi: 10.1063/1.3152782.

[10] March 2013. URL https://www.norlandprod.com/techrpts/chemresit.html.

Part II

Results

Chapter 3

Laser characterisation and non-specific sensing

The previous chapter provided an explanation of the numerical model used to assess the response of DFB laser sensors for refractive index sensing and gave a general overview of how changes to the device structure affect surface and bulk sensing. This chapter introduces the experimental optimisation and testing of the DFB laser sensors. In Sections 3.1 - 3.3, the fabrication, characterisation and optimisation, including comparison to the theoretical model, are described. The second part concentrates on demonstration of refractive index sensing. In Section 3.4, bulk refractive index sensing (detecting refractive index changes in solutions used to immerse the laser) experimental results are given. And surface sensing results - the detection of the addition of molecules to the laser surface - are provided in Section 3.5. Experimental results are also compared to predicted values from the model.

3.1 The sensing concept

As described in Chapters 1 and 2, the concept of sensing with DFB lasers is very simple. The wavelength of emission from the laser changes based on variations of the refractive index of the superstrate, e.g. biomolecules binding to the laser surface will induce a shift in the emission wavelength. Many optical sensing technologies are based on the detection of small refractive index changes [1–4]. These technologies are typically very high resolution, with some capable of single molecule detection [2], and also tend to have a high Q-factor. Q-factor is defined as the ratio of resonance linewidth and wavelength, in the case of DFB lasers. Ideally, both the shift in wavelength and the resolution will be maximised to obtain high sensitivity. Many of the current sensing technologies with

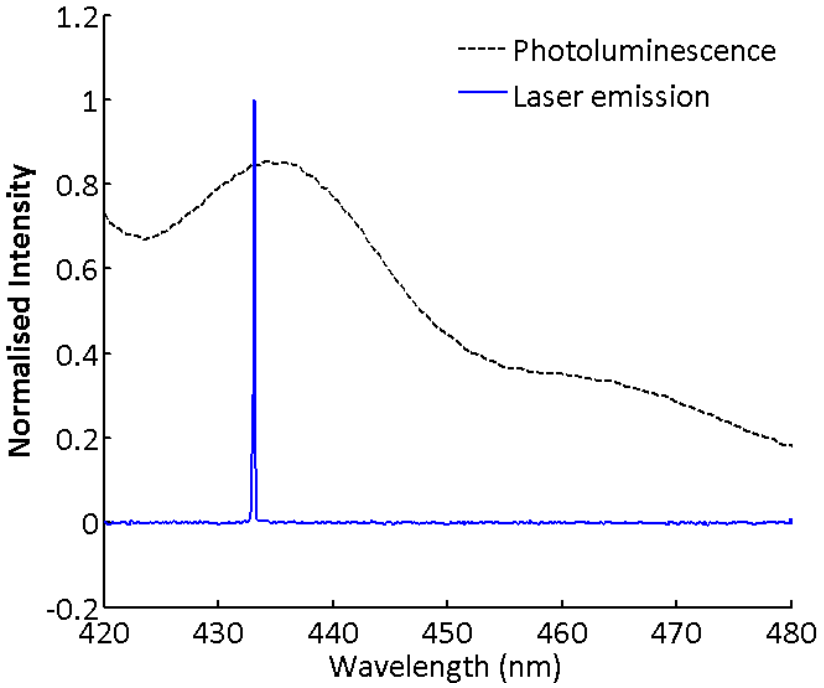

FIGURE 3.1: Emission spectrum of a T3 laser above and below the laser threshold.

high Q-factors generally achieve their higher resolution at the expense of sensitivity, i.e. a reduction in the magnitude of the shift in wavelength per refractive index unit. DFB lasers are 'active cavity' sensors that enable both high sensitivity and resolution through stimulated emission, resulting in narrow resonances for single mode emission [5], as shown in Figure 3.1 of the emission spectrum of a T3 laser above and below the lasing threshold. Although DFB lasers have a Q-factor that is generally lower than that of a micro-resonator, for example, this is compensated by the fact that spectrally narrow laser emission leads to high resolution and small changes in refractive index result in large shift in the emission wavelength, relative to the wavelength shifts observed for some passive optical sensors [2]. A table of Q-factor and sensitivity (wavelength shift/RIU) is provided in Section 3.5.2 for various refractive index biosensors to allow a comparison between the different technologies.

3.2 Laser fabrication

One of the key advantages of organic DFB lasers for sensing applications is their ease of fabrication. Lasers are fabricated entirely through soft material patterning of the substrate and solution processing of the gain layer, processes that are scalable for industrial production [6, 7]. The properties of the organic semiconductor material, oligofluorene truxene, used as the gain material for the DFB lasers presented in Section 1.4 are described in more detail here.

3.2.1 Oligofluorene truxene

Oligofluorene truxenes are star-shaped macromolecules. The structure for T3 shown previously in Figure 1.11f is reproduced in Figure 3.2a. Star-shaped oligomers have been of great interest over the past 20 years, especially for optoelectronic applications such as light emitting diodes [8]. Monodisperse star-shaped oligomers have high photoluminescence quantum yields in both solution (0.83) and the solid-state (0.60) and form low loss waveguiding films when deposited from solution [6–8], both of which are ideal properties for a laser gain material. The molecule itself consists of a truxene core with three arms of repeat fluorene units. In this case, the number of fluorene units per arm is three, hence the term "T3" used to reference the material. T3 macromolecules are efficiently excited with light in the 350 - 390 nm range and emit in the 420 - 450 nm range (3.2b). T3 has a refractive index of ≈1.81 at 430 nm which is higher than that of typical dye-doped polymer gain materials (≈1.5). A high index is beneficial for refractive index sensing applications and a T3 DFB laser demonstrates improved surface sensing capabilities relative to that of a dye-doped DFB laser (Section 5.2).

3.2.2 Laser fabrication

A DFB laser structure identical to those used in the experimental work was shown in Figure 1.8. The laser fabrication process is depicted in Figure 3.3. The diffraction grating within the substrate layer was obtained by replicating a silica master grating into Norland 65 optical epoxy (Norland Products Inc). The master grating had a period and modulation depth of 276 nm and 50 nm, respectively, and is shown in Figure 3.4a. Norland 65 is a curable epoxy, this means that it contains chemical groups that are initiated by exposure to a source of energy. In this case the material is photocurable so upon exposure to UV radiation, the thermosetting material produces a stable, highly cross-linked polymer. For grating fabrication, the epoxy was drop-coated onto the master grating surface and a 15x15 mm^2 commercially available acetate sheet of 0.1-mm thickness was placed on top of the epoxy which was subsequently photocured with a UV lamp (exposure dose ≈30 $J.cm^{-2}$, spectrum centred at 370 nm) for 50 s. Care must be taken when adding the acetate sheet to the epoxy drop in order to not produce a substrate containing bubbles, which may affect the spectral quality of the laser emission. After curing, the grating-imprinted epoxy was peeled from the master grating, cut to size if required, and cured under the UV lamp for a further 60 minutes. A photograph of an epoxy imprinted grating is shown in Figure 3.4b.

The T3 oligomer solution was prepared by adding T3 to toluene (Fisher Scientific) at a concentration of 20 $mg.mL^{-1}$. The solution was vortexed briefly to ensure the T3 was

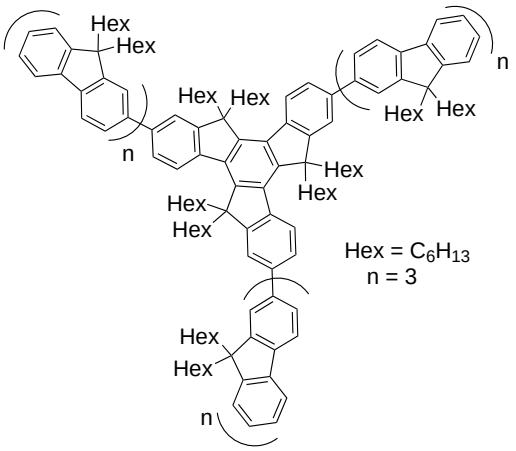

(a)

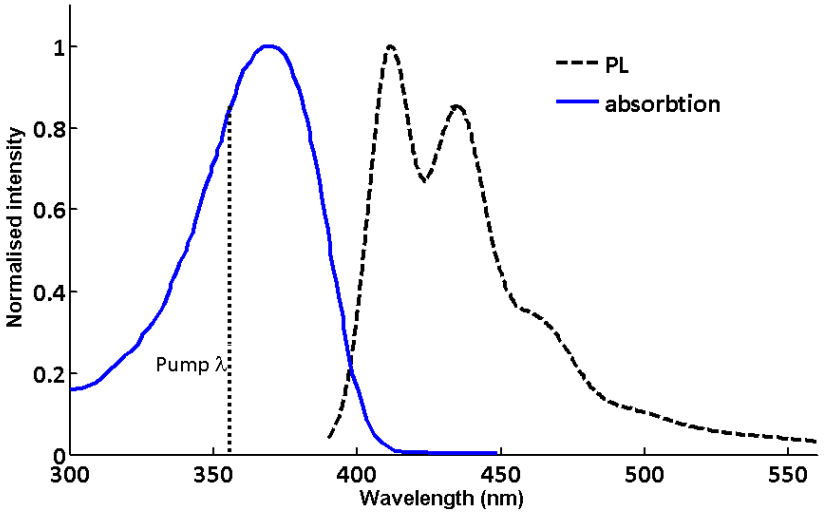

(b)

FIGURE 3.2: (a) Chemical structure of T3 and (b) absorbance and photoluminescence spectra of T3.

completely dissolved. Prior to spin coating, the substrate was taped to a piece of glass to provide a solid support for the substrate and to ensure that it was held flat for spin coating. 20 μL of solution was spin-coated on the surface of the grating imprinted epoxy at 3.2 krpm for 90 s. The Norland 65 supplier states that toluene does not degrade or have any negative effect on the cured epoxy structure, e.g. it does not cause the grating to swell [9]. This standardised fabrication process results in single mode (TE_0) DFB laser structures for >95% of devices. Spin coating of the T3 layer is not feasible for large scale production of laser devices. 'Horizontal dipping' is a process that has been used to fabricate similar laser structures over a relatively large surface area [7] and could replace the spin-coating step described here. In addition, room-temperature nanoimprint lithography could provide a method of patterning the T3 layer directly with a grating structure and simplifying the fabrication further [10, 11].

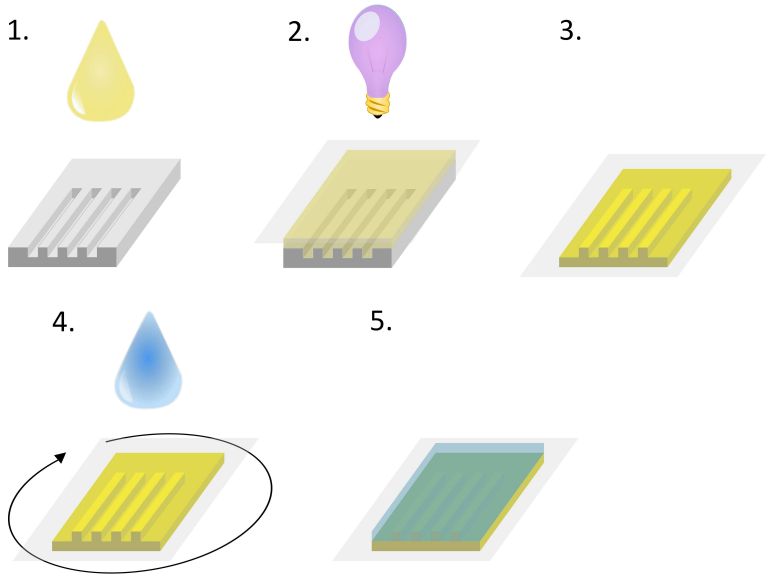

FIGURE 3.3: Steps for DFB laser fabrication. (1) Optical epoxy is drop-coated onto a the silica master grating and (2) cured for 50 s under the UV lamp. (3) The grating imprinted substrate is peeled from the master grating and (4) post cured before spin coating the T3 gain layer. (5) The DFB laser is ready for use.

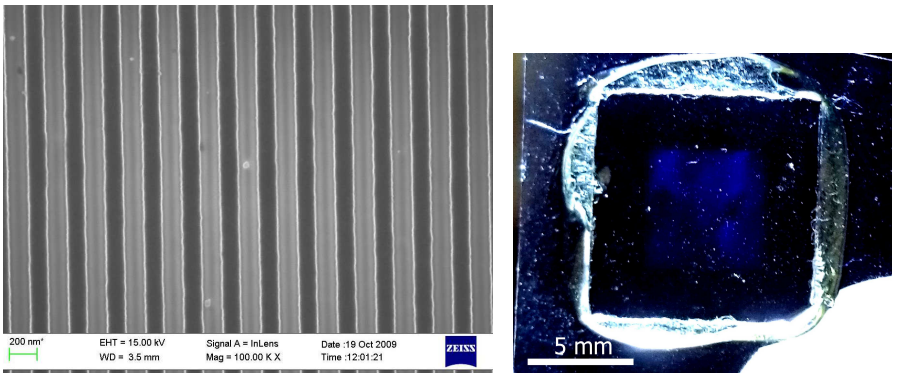

(a) (b)

FIGURE 3.4: (a) SEM of silica master grating and (b) photograph of a grating imprinted substrate prior to the addition of the T3 layer.

3.3 Optical set-up

Over the course of the experimental work, the optical set-up evolved to meet the need to use ever smaller solution volumes as the materials used for sensing became more expensive. The three main experimental set-ups are described here.

For non-specific experimental sensing work a large (dimensions 55x24x56 mm, 25 mL) cuvette, purchased from Starna, was used to house the laser and allow for immersion of the laser in solutions, as shown in Figure 3.5a. The DFB laser was taped to an inner face of the cuvette using Kapton polyimide film (Agar Scientific) so that the T3 surface

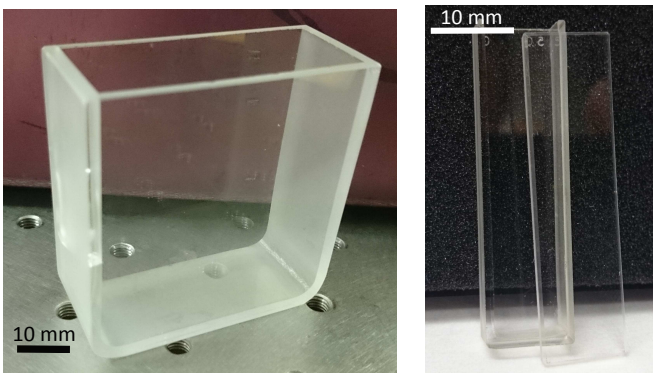

(a) (b)

FIGURE 3.5: Photographs of (a) the large cuvette and (b) the demountable cuvette.

was exposed to the solvent within the cuvette. Measurements of the emission from the DFB laser were performed by photopumping the DFB laser through the cuvette, with a Photonic Solutions frequency-tripled, Q switched Nd:YAG laser with 355 nm wavelength pulses (5 ns pulse duration and linewidth of 12 pm) at 10 Hz repetition rate. The large cuvette was held in place with a custom made mount, at an angle of approximately 45^o to the surface normal. An angle of 45^o was chosen purely to simplify the collection of the laser emission and to negate the need for filters to cut the pump. The energy of the pump was controlled using a quarter-waveplate followed by a polariser and a neutral density filter wheel (Figure 3.6). A dichroic mirror was used to filter any remaining green (frequency-doubled, 532 nm) components out of the laser emission. The laser was pumped through the substrate to avoid the added complications of pumping through the solution in the cuvette. For the same reason, emission from the DFB laser was collected through the substrate. Outcoupled emission was collected via a 50-μm-core optical fibre, positioned normal to the cuvette surface at a distance of ≈20 mm, as shown in Figure 3.6. The other end of the fibre was directly plugged into a grating-coupled (10 μm slit) Avantes (AvaSpec 2048) CCD spectrometer channel covering 420 - 653 nm with spectral resolution of 0.06 nm.

3.3.1 Surface and specific sensing - demountable cuvette

For demonstration of detection of analytes at the sensor surface, a cuvette with a smaller volume (≈1.5 mL) was used, see Figure 3.5b. The cuvette was custom made by Comar Optics to have an internal width (or pathlength) of 5 mm to accommodate the "height" of the DFB lasers (≈1 mm). The outer length and width of the cuvette were 45 and 12.5 mm respectively. When the grating imprinted substrates were fabricated, the size of the substrate was determined by the dimensions of the master grating, which was roughly 10 mm square, as the epoxy spread over the area of the master grating. As

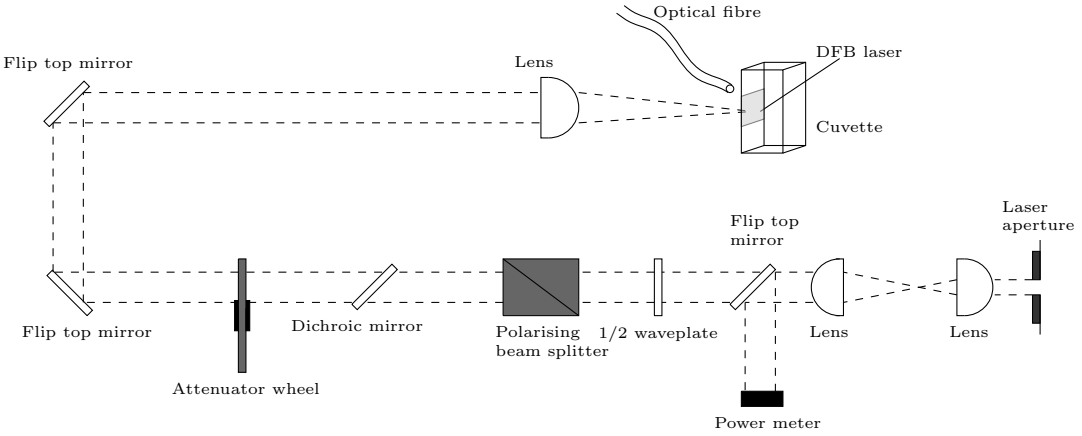

FIGURE 3.6: Schematic of the optical set-up. The pump is attenuated before being focused by a 125 mm focal length lens through the cuvette onto the laser substrate.

the inner dimensions of the demountable cuvette were <10 mm, the lasers had to be trimmed to size along two parallel sides. This was done by cutting the substrate prior to post-curing with scissors. The grating itself is situated within the centre of the substrate and has a surface area of ≈25 mm^2, therefore, it is possible to trim the substrate without disrupting the grating structure. The width of the cuvette meant that tape could not be used to fix the laser in place. Instead, the grating imprinted substrate was fixed to the flat face of the demountable cuvette, prior to spin coating the T3 gain layer, with Norland 65 and cured for 2 minutes. The T3 was then spin coated in the usual way but without the need to fix the substrate to a glass support. The optical set-up using the demountable cuvette was the same as that shown in Figure 3.6, with a modified holder made to accommodate the smaller cuvette and hold the two pieces of the cuvette firmly together.

3.3.2 Specific sensing - 24 well microtiter plate

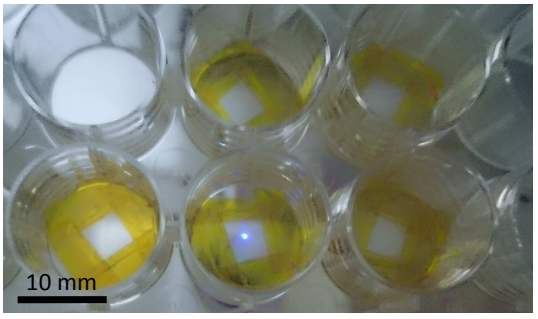

FIGURE 3.7: Photograph of T3 lasers taped within the 24 well mictotiter plate.

As specific biosensing developed to include more expensive biomolecules, such as nucleic acids probes, the experimental solution volumes had to be decreased further. To achieve

this, the experimental set-up was modified to facilitate the use of a 24 well microtiter plate (Figure 3.7). The diameter of the wells (16 mm) was large enough to allow trimmed lasers to be taped to the bottom of the well but also reduced the required solution volume to just over 300 μL. When lasers were housed in the microtiter plate, they were trimmed so that there was a border of $\approx$1 mm around the central grating structure before spin coating the T3 layer as described in Section 3.1.2. As the surface area of the lasers were smaller than those described in Section 3.1.2 the volume of T3 solution added during spin coating was reduced from 20 μL to 15 μL. This had no effect on the thickness of the T3 layer (confirmed by no change in emission wavelength).

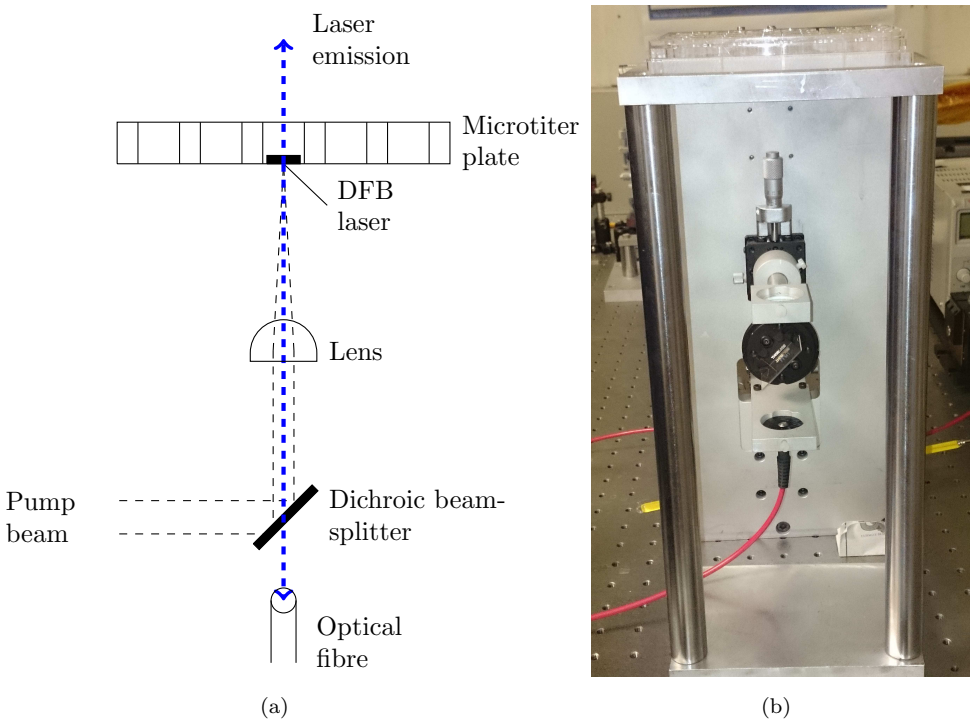

FIGURE 3.8: Optical set-up when using the microtiter plate. A dichroic beam-splitter is used to divert the pump through a 125 mm lens onto the bottom of the plate. DFB laser emission is collected after passing the beam-splitter by a 50-μm-core optical fibre. (a) Schematic and (b) photograph.

In order to incorporate the microtiter plate into the optical set-up, the set-up shown in Figure 3.6 had to be modified. A schematic and a photograph of the modified set-up are shown in Figure 3.8. The optics used for attenuation of the pump beam remained unchanged from the previous set-up so are not shown. DFB lasers were pumped through the plate and epoxy, normal to the laser plane (Figure 3.8). A dichroic beam-splitter, positioned at 45^o to the incoming pump beam, was used to direct the pump through a lens and onto the laser within the plate, and to cut any of the pump beam when collecting emission from the DFB laser with the same optical fibre/spectrometer mentioned previously.

A custom plate holder was made which allowed the plate to be moved to position the pump spot at a particular location within the laser. This was later modified to allow accurate x-y translation of the plate to allow for movement and relocation of the plate to a specified location.

3.4 Optical characterisation

The pump spot was focused onto the grating using a 125 mm focal length lens to have a minimum focal area of 4x10^{-3} mm^2. Reducing the focal area from 60x10^{-3} mm^2 (with a 50 cm focal length lens) to 4x10^{-3} mm^2 reduced the DFB laser emission linewidth from 0.20 nm to below the resolution of the spectrometer (0.13 nm), as shown in figures 3.9a, b and c. It is expected that the reduction in pump spot size helps to minimise the number of lateral modes that can oscillate and are known to affect the linewidth [12]. The central wavelength and linewidth for each of the spectra shown in Figure 3.9, and indeed all spectra presented in this thesis, were obtained using a Matlab function, 'peakdecomposition', which fits a Gaussian lineshape to the experimental data [13]. The goal of the peakdecomposition function is to minimise the residual function (essentially the difference between the Gaussian function and the data) and, therefore, a plot of the residual of the fit is also produced with each fitted spectra. As the linewidth of laser emission was at, or below, the resolution of the spectrometer, spectra were fitted using only two or three data points above the noise. The limited number of data points used for fitting may lead to fitting error, however, fitting the data was considered to provide the best estimate of the central wavelength and linewidth within the spectrometer limitations [7]. The resolution of the spectrometer used can be improved upon. For example, compact spectrometers with a resolution of 0.02 nm within the spectral range of the T3 lasers are available. Furthermore, the footprint of such spectrometers is small (dimensions of 15x10x5 cm^3) making them a suitable off-the-shelf option for incorporation into a compact, portable sensing system.

3.4.1 Gain layer thickness optimisation

As mentioned in Section 2.1, the device parameters that can be modified to optimise the sensing performance of the DFB laser are the substrate refractive index, the grating pitch and the thickness of the T3 layer. The capacity to vary the substrate index is limited by the photocurable optical epoxies available and their properties. Generally, low index epoxies (n<1.4) require that curing is performed in an inert atmosphere, as mentioned in Section 2.1.2, and therefore this parameter was not considered as part of the experimental work. The grating pitch is also constrained by the T3 wavelength and

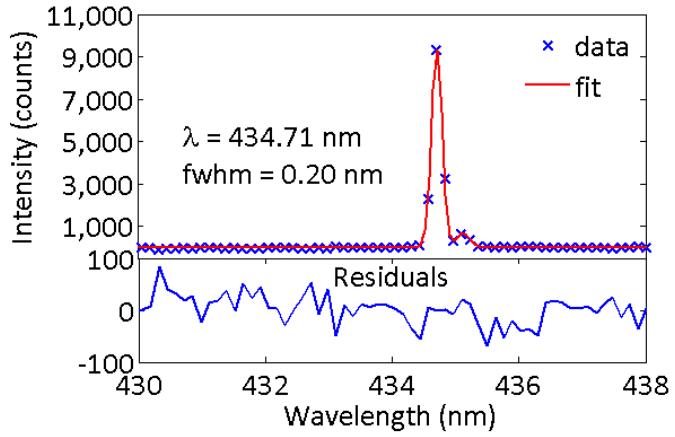

(a)

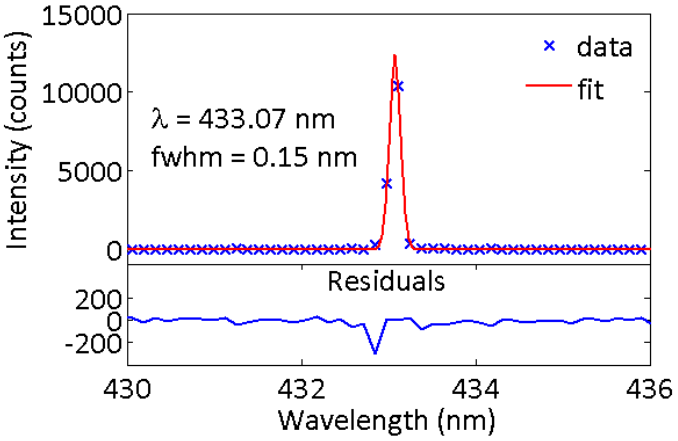

(b)

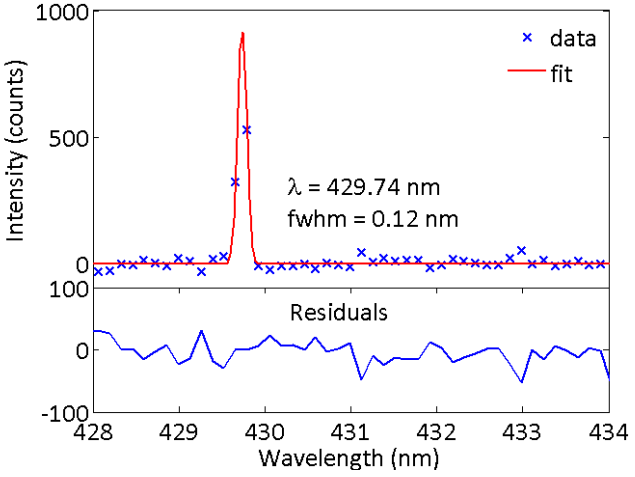

(c)

FIGURE 3.9: Demonstration of the reduction in laser emission linewidth to below the resolution of the spectrometer by reducing the pump spot area. A 500 mm, 250 mm and 125 mm focal length lens was used to focus the pump spot in (a), (b) and (c), respectively.

the available master gratings, therefore this parameter was fixed for the experimental work. Optimisation of the gain layer thickness was shown to have a marked effect on the bulk sensitivity of the DFB laser and a relatively large (±0.16 nm) influence on the sensitivity of surface sensing, see Figure 2.7. As the thickness of the gain layer could be easily controlled by modifying the spin coating speed of T3 deposition, an experimental study of the effect of gain layer thickness was performed in order to obtain single transverse mode operation and maximise the shift in wavelength per unit change in superstrate refractive index. Experimental data was also compared to predicted values from the model.

The spin coating speeds used to deposit the T3 gain layer ranged from 0.5 to 3.5 krpm. The emission wavelength of these lasers was previously plotted against the shift in wavelength upon immersion in water (Figure 2.8). These results demonstrated that a thinner gain layer resulted in a greater shift in wavelength upon immersion of the laser in water. A minimum gain layer thickness (expected to be in the region of 50 - 60 nm) is required in order to support the laser mode but beyond this minimum "cut-off", maximum sensitivity is achieved.

The shift in wavelength versus truxene thickness/emission wavelength in air was modelled and is plotted alongside the experimental data in Figure 3.10. The largest shift in wavelength upon exposure of the laser to DI water occurred for the lasers with the shortest emission wavelengths which corresponded to lasers with a thinner truxene layer. This can be explained by considering the effect of the gain layer thickness on the overall effective refractive index and position of the laser mode within the device. The effective refractive index of a DFB laser is dependent on the refractive indices of n_{sub}, n_a and n_{sup} and the thickness of the gain layer. A thick (>100 nm), high index gain layer will lead to a large overlap of the laser mode with the gain layer, which is useful for minimising the laser threshold, but at the expense of a reduction in overlap with the superstrate, and therefore, a reduction in the overall bulk sensitivity. Incidentally, the model predicted that the largest overlap of the TE_0 mode with the superstrate occurs for a gain layer thickness of 76 nm (13.2 % when the superstrate is water), resulting in the maximum shift in wavelength observed for a T3 layer of this thickness. The theoretical wavelength versus shift in wavelength plot replicated the experimental data. The model predicted a maximum shift of 3.30 nm for a refractive index change corresponding to the air to water transition, as shown in the plateau region of the plot in Figure 3.10. The model also predicts that this maximum response to refractive index changes occurs for a T3 layer thickness of around 65 - 75 nm.

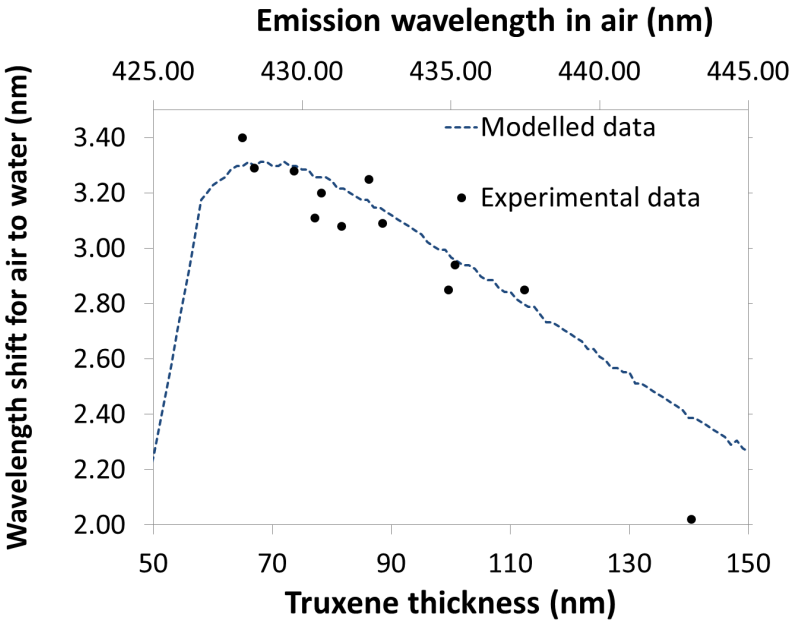

FIGURE 3.10: The shift in wavelength and emission wavelength in air for lasers fabricated with a range of truxene thicknesses is plotted. Theoretical thickness, emission wavelength and wavelength shifts are also plotted.

3.4.2 Measurement of T3 gain layer thickness

The thickness of the T3 gain layer was measured experimentally using atomic force microscopy (AFM) in order to compare to the predicted optimal thickness provided by the model. Lasers spin coated at a speed of 3.2 krpm consistently provided the maximum shift in wavelength when immersed in water compared to other speeds. Therefore, the thickness of the T3 layer produced at this speed was measured alongside layers expected to be thicker.

To measure the T3 thickness, T3 (20 μL) was spin coated onto a 100 mm^2 glass coverslip at three different speeds, 1, 2 and 3.2 krpm. A score was made through the T3 layer with the pointed tip of a pair of tweezers the length of the coverslip. Very little pressure was applied in order to ensure that the glass substrate was not scratched. The AFM tip was positioned to the left of the "scratch" and was scanned across the void to the other side. An example profile of a T3 layer is shown in Figure 3.11. It should be noted that the surface area of the glass had to be representative of the surface area of the grating; if the surface area of the glass was larger than that of a typical grating, as was the case in Figure 3.11 (coverslip area was 625 mm^2, spin coating speed of 2 krpm) a thinner gain layer resulted. Using the 100 mm^2 glass, six profiles across the scratch were recorded at different positions along the length of the scratch. The height of the flat T3 surface, either side of the scratch, was noted and the average values are provided in Table 3.1.

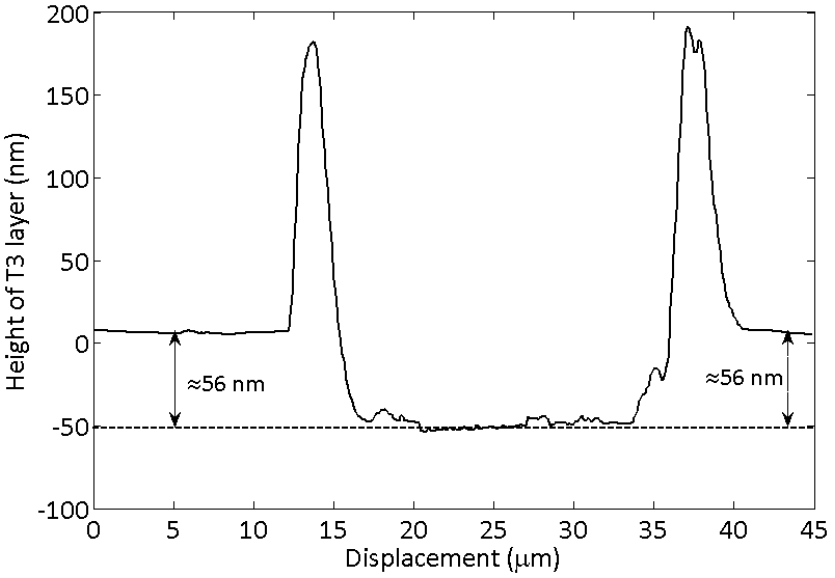

FIGURE 3.11: AFM measurement of T3 thickness.

Spin speed (krpm)	**Average T3 thickness (nm)**
1	174±11
2	83±11
3.2	71±9

TABLE 3.1: AFM thickness measurements of the T3 spin coated onto glass.

It is expected that the thickness of the T3 layer may be slightly different when spin coated onto the substrate due to the grating features and the different properties of the surface. However, the model predicts that a DFB laser with a gain layer thickness of 70 nm will have an emission wavelength of 431.62 nm in air and demonstrate a shift of 3.30 nm when immersed in water, which agrees well with experimental (mean wavelength of 430.74±0.77 nm and a mean shift of 3.33±0.07 nm in water) values. A gain layer thickness of 70 nm is within the range resulting in the maximum shift in wavelength for the index change from air to water and, therefore, all subsequent lasers were fabricated to have a gain layer of this thickness.

3.4.3 Laser threshold

Optimisation of the DFB laser threshold was not one of the aims of this work and therefore threshold measurements were not made routinely. However, the threshold was measured for a number of lasers and is expected to be representative of all laser sensors fabricated. A brief explanation of the threshold measurement is provided here.

DFB laser are known to have a "soft threshold". This means that when pumped close to the threshold for optical gain there is a graded increase in the laser emission intensity

rather than a well defined sharp threshold [13]. The soft threshold is an effect of the contribution of amplified spontaneous emission to the emission intensity when below the laser threshold. The laser threshold can be determined by recording the laser intensity (I_{laser}) corresponding to a range of pump energies (E_p) until saturation of the intensity occurs (I_{sat}). These experimental parameters can be inserted into Eq. 3.1 to obtain the pump threshold for optical gain (E_{th}). In Eq. 3.1, κ is a dimensionless parameter that accounts for the coupling of spontaneous emission into the laser mode [13]. A higher value of κ accounts for greater coupling of unsaturated stimulated emission which decreases the contrast between the emission intensity below and above laser threshold, hence the soft threshold. Eq. 3.1 was fitted to the threshold measurement data using a Matlab function, 'softthreshold', which treats I_{sat} as a linear parameter while minimising the other parameters [13]. An example of a threshold fit is given in Figure 3.12.

$$I_{laser} = \frac{I_{sat}\kappa\frac{E_p}{E_{th}}}{1 + \frac{I_{laser}}{I_{sat}} - \frac{E_p}{E_{th}}} \tag{3.1}$$

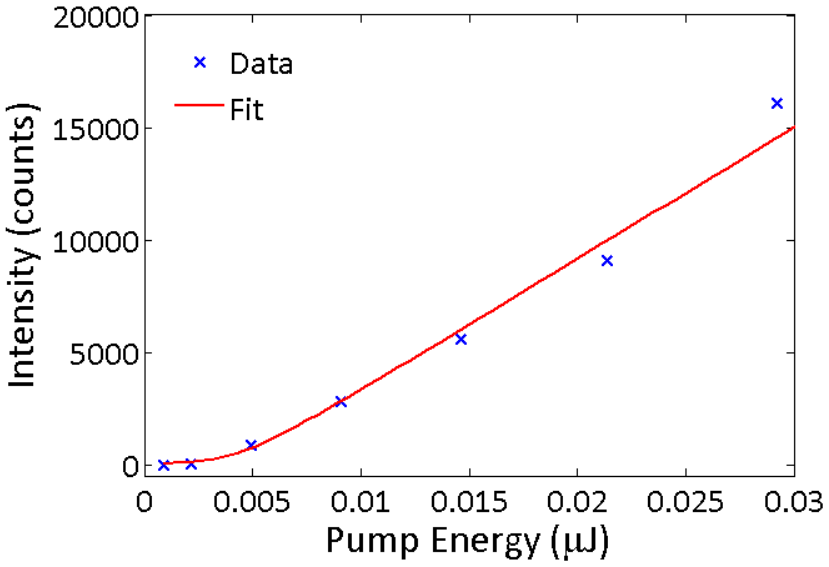

FIGURE 3.12: Example threshold measurement for a typical T3 laser. A threshold of 60 μJ.cm^{-2} is observed when the laser is exposed to air. The fit parameters were: κ=8.14x10^{-12}, I$_{sat}$=4.11x10^3 counts, E$_p$=<0.05 μJ, resulting in a E$_{th}$=5 nJ (a second ND filter was used for this measurement to halve the pump intensity, but this is not accounted for in the fitted data).

T3 DFB lasers typically have a threshold fluence of approximately 60 μJ.cm^{-2} (energy of 2.5 nJ) when the superstrate is air. The laser threshold decreases with increasing superstrate refractive index and is approximately 30 μJ.cm^{-2} when immersed in DI water. The decrease in threshold can be attributed to the increased superstrate index drawing the laser mode closer to the device surface, resulting in a greater overlap with the gain region and therefore a higher modal gain. The overlap of the laser mode with

gain layer was modelled with air and water as the superstrate and predicted an overlap of 23 % and 31 % in air and water, respectively, which corroborates the experimental results.

The DFB laser threshold is an important consideration for the miniaturisation of the technology and use as a POC device. The threshold fluence in water corresponds to a power density of the order of 6 kW.cm^{-2}. Therefore it is expected that optical pumping may be achieved with a "Blu-ray" gallium nitride laser diode, assuming the gain material absorption can be matched to the diode wavelength, as has already been demonstrated for other organic lasers [14]. There is also scope for LED pumping if the threshold can be reduced further [15].

3.4.4 Properties of laser emission

FIGURE 3.13: Photograph of the emission from a T3 DFB laser. Coherent laser emission is observed in the central section of the fan shaped beam with diffracted amplified spontaneous emission accounting for the four extended beams extending from the central region.

When pumped above threshold, the DFB laser demonstrates fan-shaped emission as shown in Figure 3.13. With a gain layer thickness of ≈70 nm, all lasers tend to oscillate on the fundamental TE_0 mode, i.e. the laser mode is polarised parallel to the grating, with a wavelength around 430 nm when exposed to air and with a linewidth below the resolution of the spectrometer (Figure 3.9a). The spectral linewidth of the laser remains narrow, even after functionalisation of the laser surface with other molecules (Figure 3.9b), where a laser has been functionalised with a monolayer of polyelectrolyte and biotin and subsequently used for avidin sensing. This is important for sensing applications as the sensor will have to be functionalised with molecules in order to

specifically detect target biomarkers, and the sensitivity of the device is dependent on the linewidth of the laser emission.

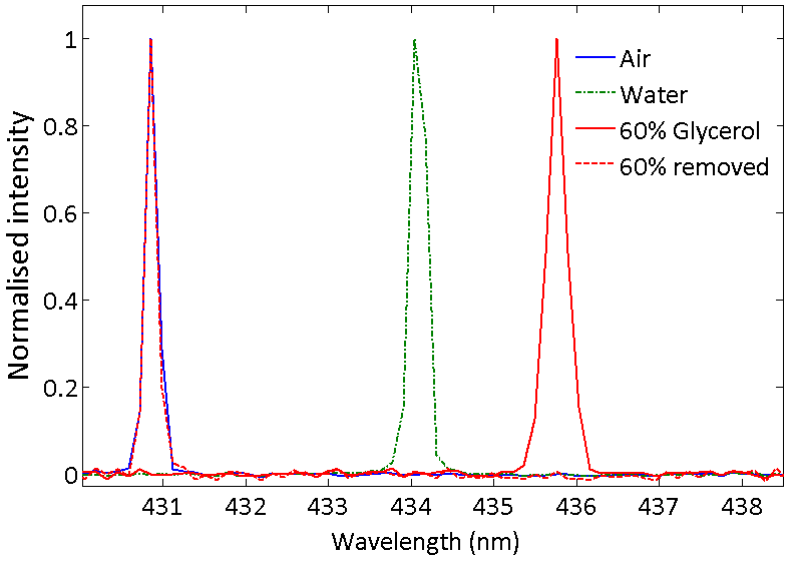

(a)

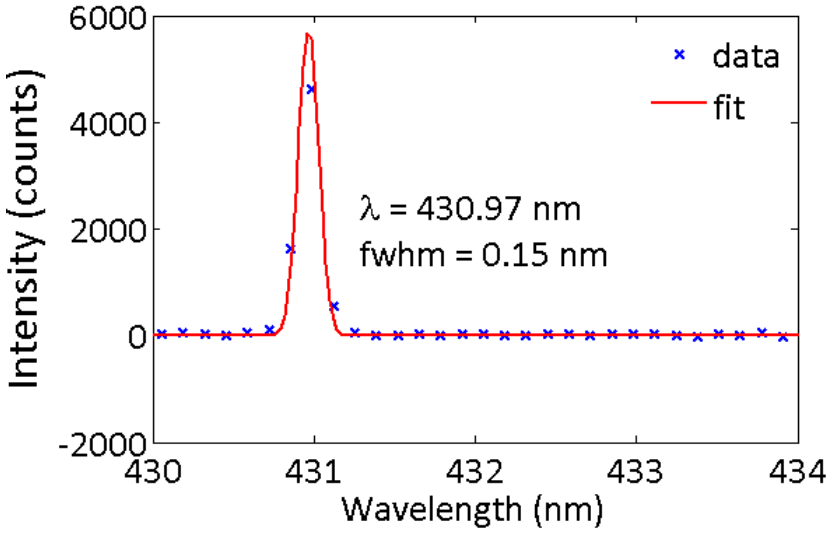

(b)

FIGURE 3.14: (a) T3 laser emission in air, before and after immersion in water and glycerol solutions, and solution. The wavelength and linewidth remains constant over the time of the bulk sensing experiment with glycerol. (b) The linewidth also remains narrow after functionalisation of the laser with polyelectrolyte, biotin and avidin.

Investigation of the operational laser lifetime was not within the remit of this work but it is an important consideration for the performance of DFB lasers as sensors. The lifetime of T3 DFB lasers identical to those found in this thesis have previously been reported [16]. Lifetime measurements indicated that when submerged in water and pumped with a fluence ≈250 times that of the threshold fluence, lasers remained operational beyond exposure to 10,000 pulses corresponding to a period of time >15 minutes. During sensing

measurements, the laser is pumped for approximately 5 s per measurement and therefore, at the pulse fluence mentioned, this would allow for >200 measurements to be made at one particular location on the laser. In reality, lasers are pumped at a far lower fluence, closer to that of the laser threshold, and therefore the estimate of 200 measurements is greatly underestimated. Although there is a slight decrease in emission intensity with prolonged pumping, the emission wavelength does not change. For example, the emission wavelength for a laser exposed to air, and then a number of different glycerol solutions (described further in Section 3.4) before a final measurement in air, is shown to remain constant despite 16 measurements being made in the interim (Figure 3.14a). Wavelength stability, along with linewidth stability, is paramount if the laser is to be used for sensing applications.

3.5 Bulk refractive index sensing

Differentiation of solutions with different refractive indices was the method chosen to investigate the bulk sensing potential of the T3 DFB lasers and to provide a means of comparison to other DFB laser sensors for biosensing applications. The solution used for the experimental work was glycerol and this solution was chosen for reasons now discussed. The T3 gain layer is deposited via a toluene/T3 solution, therefore solvents miscible to toluene can affect this layer. For example, when a T3 laser was immersed in methanol, there was a blueshift in the emission wavelength rather than the expected redshift due to the increased refractive index (≈1.33) relative to that of air (Figure 3.15).

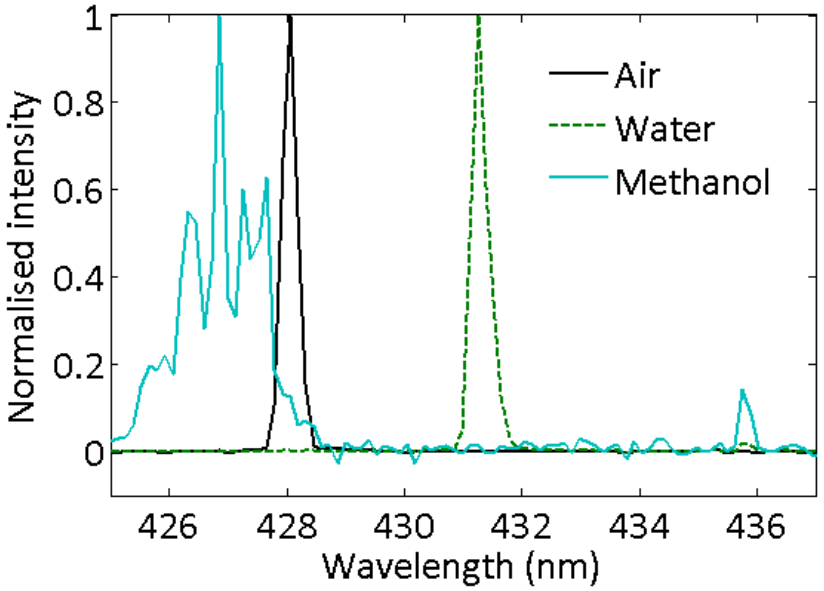

FIGURE 3.15: Laser emission from a T3 DFB laser exposed to air, water and methanol, respectively.

It is expected that the methanol solvates the T3 layer, resulting in a decrease in the gain layer thickness and the corresponding blueshift in wavelength. Figure 3.15 also shows that the single mode peak decomposes into a broad multi-peaked spectrum in methanol solution with the peaks indicating significant variations in the gain layer thickness over the surface area of the pump spot. Therefore, only solutions that do not affect the T3 gain layer could be used to demonstrate bulk refractive index sensing. Glycerol was also shown to not "stick" to the laser surface. Therefore, no glycerol deposits built up on the laser between measurements which would have affected subsequent bulk measurements. A similar experiment was also performed using polyethylene glycol (PEG) but the refractive indices of the PEG solutions are not known as precisely as the glycerol solutions and the results are broadly similar (data not shown).

3.5.1 Experimental methods

Glycerol solutions of varying concentrations, and therefore of differing refractive indices, were created by serially diluting 60% (v/v) glycerol in DI water down to a 5% solution. A T3 laser was taped into the large cuvette as per the previous set-up (Figure 3.6). A set of air-water-air emission spectra were recorded before adding the 5% glycerol solution to the cuvette and recording the spectra. The 5% glycerol solution was removed and the emission wavelength returned to the 'air' wavelength before the next glycerol solution was added to the cuvette. This process was repeated for all glycerol concentrations and the emission wavelength returned to the air wavelength upon solution removal each time, indicating no glycerol residue remaining on the laser surface. The measurements were repeated for excitation at different positions within the DFB laser sensor and for a number of different lasers.

3.5.2 Bulk sensing results

The redshift in wavelength across all of the glycerol solutions in Figure 3.16a is approximately linear and corresponds to a bulk refractive index sensitivity of 22 nm/RIU when the refractive indices of 5% and 60% glycerol are assumed to be 1.35 and 1.43, respectively [17]. The mean shift in wavelength, and associated standard deviation, are plotted in Figure 3.16b alongside the values predicted by the model for each glycerol solution. Wavelength shift data was collected from several positions on one laser and from several different lasers. Due to the nature of the laser fabrication, there can be small variations in the gain layer thickness at different positions within one laser, and therefore between lasers. These small changes in gain layer thickness affect the magnitude of the shift in wavelength upon immersion of the laser in glycerol solution (as

shown for water in Figure 3.10), i.e. resulting in differences in the magnitude of the shift produced per unit change in refractive index. In order to minimise the effect on small variations in gain layer thickness on the shift in wavelength due to bulk refractive index changes, the emission wavelength of the laser exposed to water was subtracted from wavelengths recorded with the laser immersed in glycerol. Therefore, the values shown in Figure 3.16b are the difference in the wavelength for the laser immersed in each of the glycerol solutions minus the emission wavelength of the laser immersed in water. The predicted wavelength shift values closely match the experimental values for each of the different solutions, providing further validation of the theoretical model.

The bulk sensitivity values for dye-doped lasers were previously noted in Section 1.5 to be ≈17 nm/RIU for a Coumarin based laser (wavelength of ≈500 nm) and ≈100 nm/RIU for a Rhodamine laser (wavelength of ≈590 nm) capped with a high index TiO_2 layer. The improvement in performance of the T3 laser relative to that of the Coumarin laser is predominantly due to the higher refractive index of the T3 gain layer. A higher index gain layer causes the laser mode to reside higher in the device structure, i.e. greater overlap with the gain layer, which also results in a greater overlap with the superstrate and hence greater sensitivity. Furthermore, the bulk sensitivity of the Coumarin based laser is 'enhanced' relative to the T3 laser due to the longer emission wavelength, as mentioned in Section 1.5. A fairer comparison between the two lasers is to take the ratio of the shift in wavelength ($\Delta\lambda$) per RIU to the emission wavelength (λ). The ratio is 3.4% for a Coumarin laser and 5.1% for a T3 laser, further indicating the improves sensitivity of the T3 laser relative to that of a dye-doped laser without a TiO_2 cladding layer. The addition of a TiO_2 layer atop a T3 laser is expected to result in an improvement in the bulk sensitivity. However, as the surface sensing capabilities of the laser are more indicative of the usefulness of the laser as a biosensor, only the effect of an additional TiO_2 layer for surface sensing was modelled. This is discussed in more detail in Chapter 5.

Table 3.2 provides sensitivity and Q-factor details of several refractive index biosensor technologies. As mentioned previously, both high sensitivity and resolution are desirable properties for a biosensor, therefore, ideally both the Q-factor and sensitivity will be maximised. As shown in Table 3.2, technologies with a high resolution tend to have a lower sensitivity. One of the benefits of DFB laser biosensors is the possibility for relatively high resolution through narrow linewidth laser emission and a high sensitivity to bulk refractive index changes, coupled with ease of fabrication and implementation.

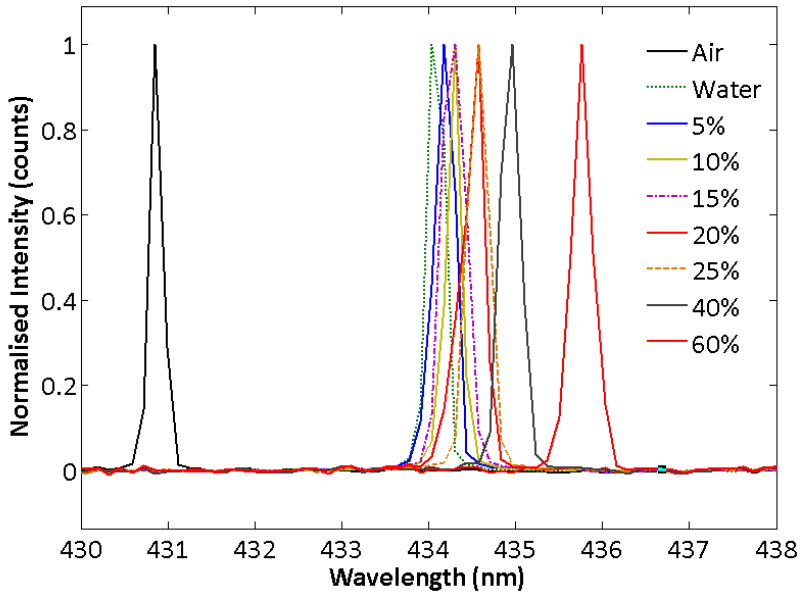

(a)

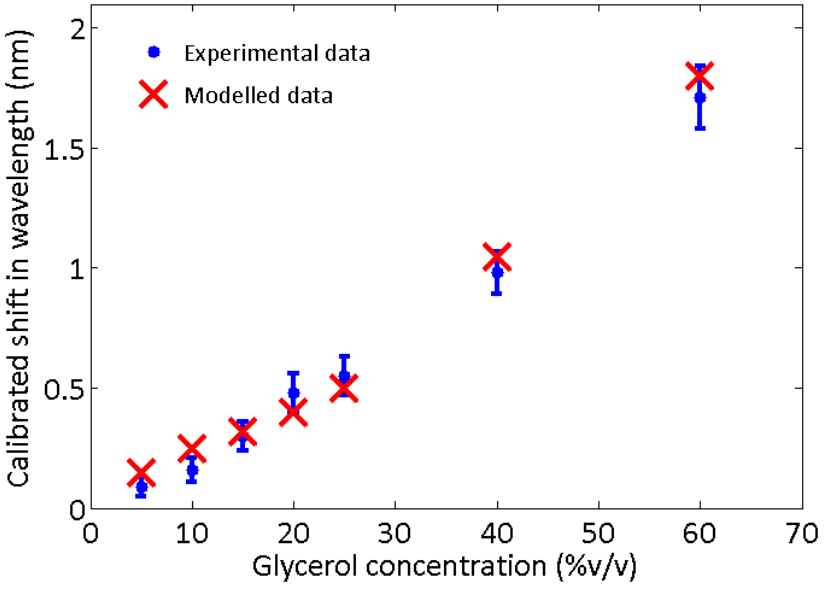

(b)

FIGURE 3.16: (a) Redshift in lasing wavelength with increasing glycerol concentration. (b) Comparison of experimental and theoretical shift for increasing glycerol concentration. Error bars indicate the standard deviation between the shift in wavelength observed for each glycerol concentration for different positions within a single laser sensor and between different laser sensors.

3.6 Surface sensing

The ability of the laser to detect the presence of analytes bound to the sensor surface is more representative of the laser's performance as a biosensor. In biosensing applications, a probe molecule will traditionally be bound to the sensor surface and will be used to

Technology	Q-factor	Wavelength shift/RIU (nm)
DFB laser (T3)	3580	22
DFB laser (Dye-doped [5])	10000	100
SPR [18]	40	13000
Ring resonator [19]	12000	140
Microsphere [19]	10000000	20

TABLE 3.2: Q-factor and sensitivity values for a range of refractive index biosensor technologies.

specifically capture the biomarker of interest for detection (Section 1.5). As this is the intended application of the T3 laser sensor, it is necessary to demonstrate firstly, that the presence of an analyte at the laser surface can be detected and secondly, that specific biomolecule detection is possible. Specific biomolecule detection is the topic of the next chapter. For surface sensing, the non-specific adsorption of polyelectrolyte layers to the laser surface were measured. Polyelectrolytes are charged polymers that have been well characterised and are known to form a self-limiting nanolayer when deposited from solution. The properties of the solution, such as the salt concentration, can be used to control the thickness of the deposited nanolayer [20]. When alternately charged polyelectolytes are used, it is possible to build a stack of layers on a substrate, as shown in Figure 3.17. Generally, the initial layers of such a stack will be thinner than subsequent layers, with a plateau thickness being reached around the sixth anionic/cationic layer. The polyelectrolytes used in the following experiments are expected to have a refractive indices of 1.49 and a thickness of 4-5 nm [20].

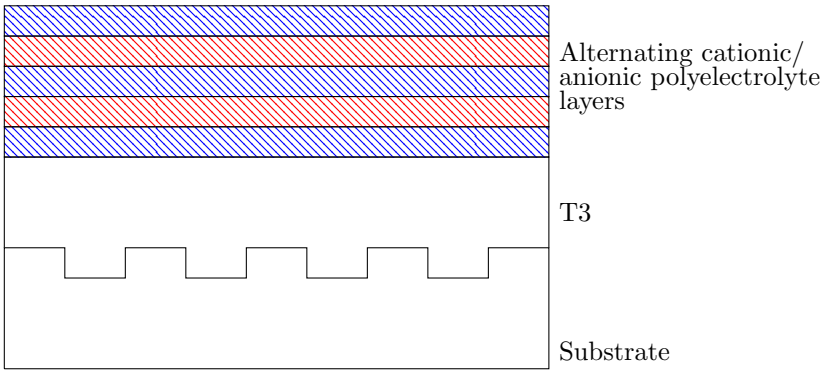

FIGURE 3.17: Schematic representing the build-up of polyelectrolyte layers on the laser surface.

3.6.1 Experimental methods

The polyelectrolytes used for the investigation into surface sensing were Poly(ethylen-eimine) (PEI), Poly(allylamine hydrochloride) (PAH) and Poly(sodium 4-styrenesulfonate)

(PSS), chemical structures, as shown in Figure 3.18. Solutions of anionic PSS (M_W = 70,000) and cationic PAH (M_W= 58,000) and branched-PEI (M_W = 60,000) were prepared without further purification in 0.9 M pH 7 NaCl (all Sigma Aldrich) to a concentration of 5 mg.mL^{-1}. The demountable cuvette was used for these experiments. Emission spectra in air, water and NaCl were recorded before adding the PEI solution to the cuvette. The solution was left in the cuvette for 10 minutes and spectra were recorded every 30 s. The PEI solution was removed and the cuvette and laser sensor were washed twice with NaCl solution. Five sets of PSS-PAH layers were then formed on the laser surface following the same protocol as for the PEI adsorption with two NaCl washes between each new layer. Figure 3.19a shows the wavelength shift relative to the shift due to NaCl solution for each of the polyelectrolyte layers with time.

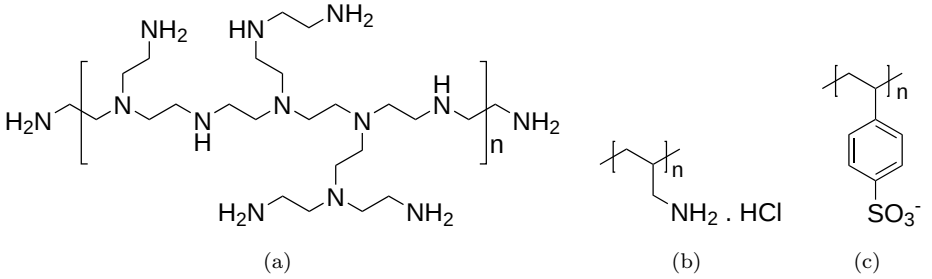

FIGURE 3.18: Chemical structures of (a) PEI, (b) PAH, and (c) PSS, respectively.

PEI is a relatively toxic polyelectrolyte, but it was initially included as the protocol used was taken from the literature [21]. As both PEI and PAH are positively charged, it was expected that the PEI layer may be replaced with an initial PAH layer. Therefore, the experiment was repeated excluding PEI. Also, as the emission wavelength remains relatively constant during the 10 minute incubation in solution, the incubation time was reduced to five minutes for each solution, with spectra recorded every 30 s.

3.6.2 Surface sensing results

The adsorption of nano-layers on the laser was performed in order to investigate the capability of detecting the non-specific adsorption of molecules at the laser surface. The results shown in Figure 3.19 demonstrate that the T3 sensor is indeed sensitive enough to detect the addition of each adsorbed nano-layer. In both Figure 3.19a and b, the addition of each polyelectrolyte layer is resolved. The polyelectrolytes are expected to deposit nano-layers with a thickness of 4-5 nm (with slightly thinner layers for the initial six layers). Therefore, Figure 3.19 shows that the laser is sensitive to adsorption of nano-layers relatively far from the sensor surface, as the effective sensing area extends to >40 nm in Figure 3.19a and >70 nm in Figure 3.19b. Retained sensitivity at some distance from the immediate vicinity of the laser surface will be useful when functionalised layers

are constructed on the laser surface in order to facilitate specific adsorption/binding events.

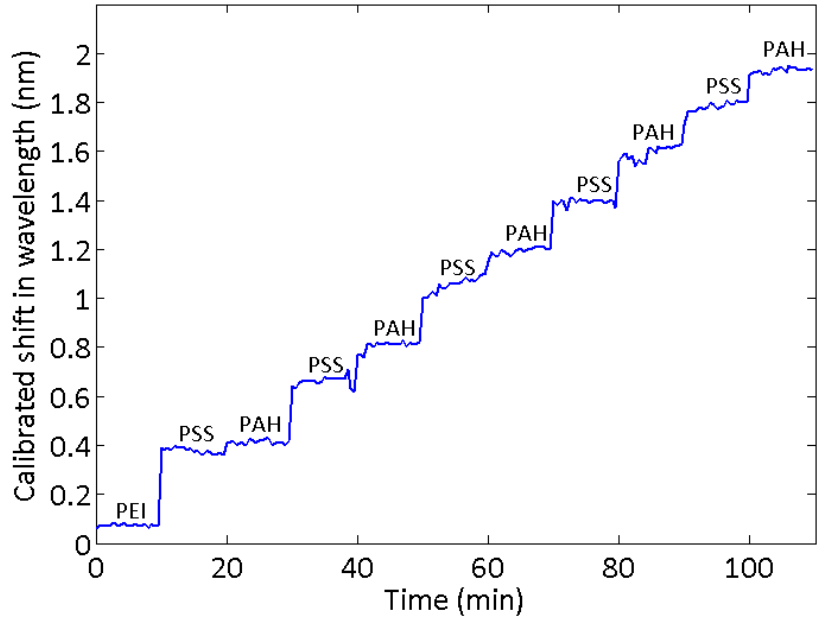

(a)

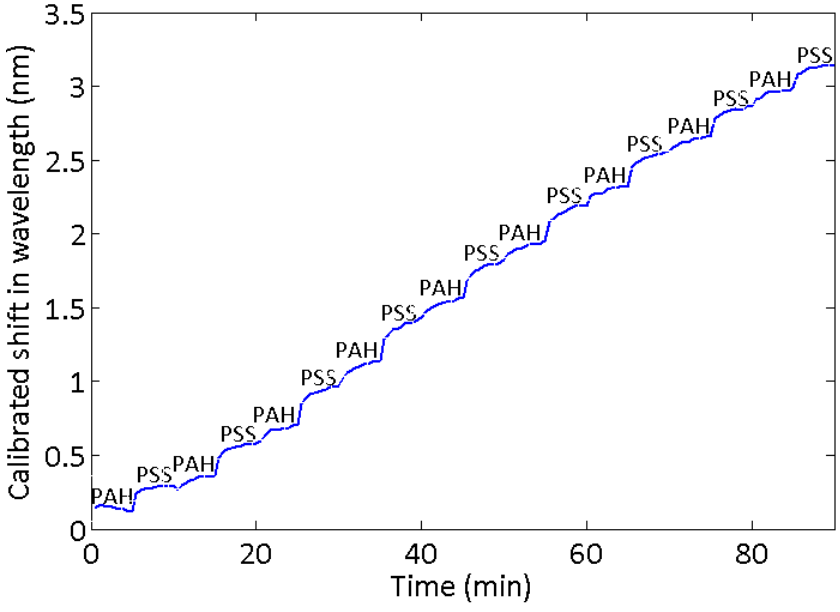

(b)

FIGURE 3.19: Adsorption of alternatively charged polyelectrolyte layers (a) with and (b) without an initial PEI layer.

The mean shift in wavelength values are re-plotted in Figure 3.20 against the thickness of the polyelectrolyte stack, alongside predicted shift values produced by the theoretical model for a given polyelectrolyte layer thickness. In the model, the refractive index of each layer and the superstrate (NaCl solution) was set to 1.49 and 1.35, respectively.

In order to compare the experimental and theoretical values, the thickness of the polyelectrolyte layers has to be defined. In Figure 3.20a, the experimental data is plotted with an assumed constant layer thickness of 5 nm (blue x) and with the layer thickness assumed to vary for the initial six layers before an equilibrium of 5 nm is reached (black +), as suggested by previous polyelectrolyte studies [20]. The general trend of the modelled data in Figure 3.20a corresponds with both sets of assumptions, but better fits the data when the initial six layers are assumed to be less than 5 nm. Figure 3.20b shows the mean wavelength shift for each of the polyelectrolyte layers, without the initial PEI layer, and the predicted values from the model.

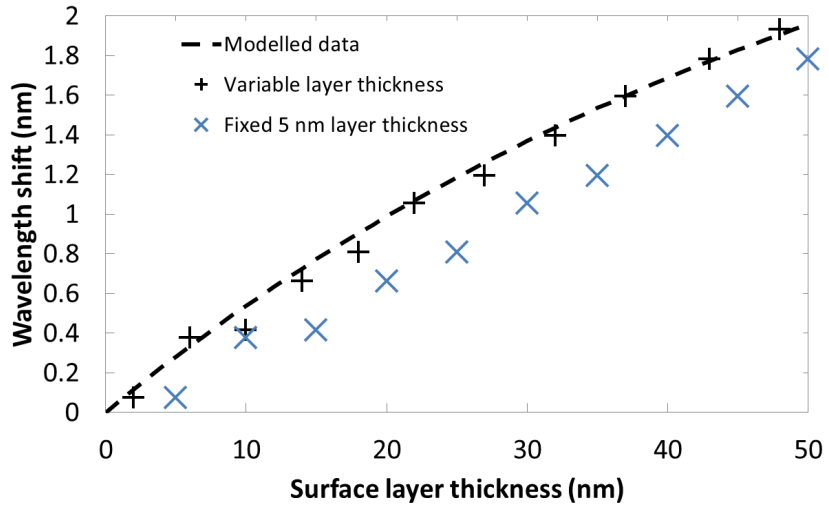

(a)

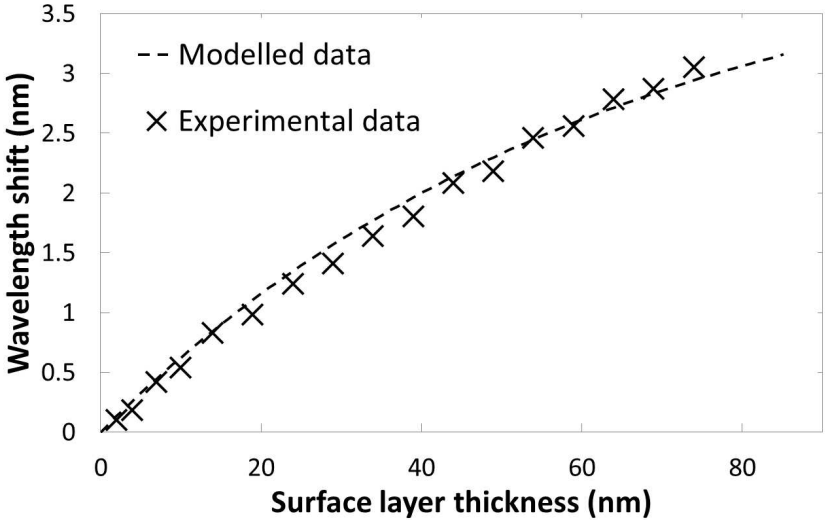

(b)

FIGURE 3.20: Comparison of experimental and modelled data for the adsorption of polyelectrolytes (a) with and (b) without an initial PEI layer.

3.6.2.1 Surface sensing resolution

Using the surface sensing data it is possible to estimate the thickness of the thinnest detectable nano-layer with a T3 DFB laser. To do this it is necessary to first define the resolution or the minimum detectable change in refractive index. The resolution of the sensor is characterised by the inherent noise of the sensor. To measure the noise the laser, multiple measurements of the emission spectra can be recorded in a steady state i.e. when there is no intentional change of refractive index occurring at the sensor surface. The noise is defined as the standard deviation, σ, of all of the recorded measurements. A signal is commonly defined to be detectable if it has a magnitude at or above 3σ [22]. The minimum detectable shift in emission wavelength for the T3 lasers has been found to be 0.06 nm, which is limited by the resolution of the spectrometer being used.

In Figure 3.20b the polyelectrolyte stack thickness is ≈70 nm. There is the potential to detect additional layers beyond this thickness as the magnitude of the shift in wavelength for the final layer added was 0.18 nm, three times that of the minimum detectable shift. Figure 3.20b shows that after the initial six adsorbed polyelectrolyte layers, the shift in wavelength is roughly linear. Within the refractive index range of 1.3 - 1.5, which is expected to encompass the indices for biosensing, the shift in wavelength is expected to be linear with respect to index. The shift in wavelength for layers 7 to 18 are re-plotted in Figure 3.21 and fitted with a straight line. The slope of the wavelength shift per nm of adsorbed material is 3.8 %. This suggests that the T3 laser can detect thicknesss of adsorbed material from the nm scale up to several tens of nm. Furthermore, a shift of 0.06 nm, the resolution limit, corresponds to a nanolayer thickness of ≈2 nm. This analysis can be extrapolated to suggest which biomarkers the T3 laser may be able to detect. For example, a 'size' of 2 nm equates to proteins with a molecular weight of ≈5 kDa [23]. Assuming the protein to be detected formed a complete homogeneous layer over the laser surface, the laser has the potential to detect biomarkers of this size. Many cardiac biomarkers are relatively large (>20 kDa), such as CRP and Troponin I, and therefore with its current sensitivity and resolution the DFB laser may be able to detect these biomarkers [24, 25]. BNP, a biomarker identified to be of great use in predicting a cardiac event as mentioned previously, has a molecular weight of 3.5 kDa, just under the current estimated limit of detection [26]. However, there is the potential to improve the resolution and sensitivity of the T3 sensing platform through improvements in the instrumentation, such as the spectrometer, and in the DFB laser structure, such as inclusion of the high index TiO_2 cladding layer.

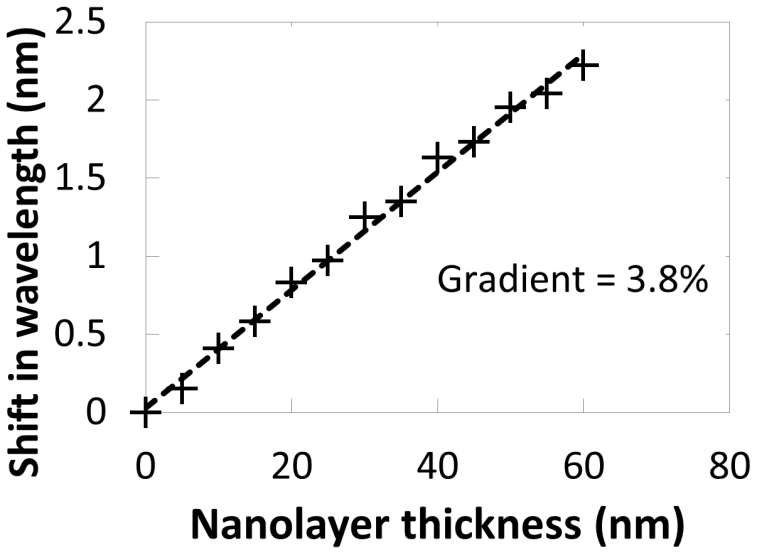

FIGURE 3.21: Shift in laser wavelength versus adsorbed nanolayer thickness.

3.7 Summary

In this chapter, the potential of organic semiconductor DFB lasers for refractive index sensing has been demonstrated. The fabrication of the T3 lasers is achieved entirely through solution processing and soft material patterning and it has been suggested how the fabrication process may be modified to enable commercial scale production. The lasers have also been shown to have excellent stability and a threshold that puts pumping with miniaturised sources, such as laser diodes, within reach. The optimisation of the gain layer thickness to maximise the shift in emission wavelength per unit change in refractive index was demonstrated experimentally and theoretically and the sensing capability of such lasers was presented.

T3 lasers have a bulk sensitivity of 22 nm/RIU and a $\Delta\lambda/\lambda$ ratio of 5.1% which improves upon the 17 nm/RIU (3.4%) achieved with the equivalent dye-doped DFB laser sensor. The non-specific surface sensing potential of the T3 laser was also demonstrated and experimental results were shown to correlate well with values predicted by the theoretical model presented in Chapter 2. The layer-by-layer deposition of polyelectrolytes not only provides a demonstration of surface sensing but also provides a means for further functionalisation of the laser surface with probes to enable specific biomolecule detection - the ultimate aim of this thesis.

References

[1] Jiri Homola, Sinclair S. Yee, and Gnter Gauglitz. Surface plasmon resonance sensors: review. *Sensors and Actuators B: Chemical*, 54(12):3 – 15, 1999. ISSN 0925-4005. doi: 10.1016/S0925-4005(98)00321-9. URL http://www.sciencedirect.com/science/article/pii/S0925400598003219.

[2] Martin Baaske and Frank Vollmer. Optical resonator biosensors: Molecular diagnostic and nanoparticle detection on an integrated platform. *ChemPhysChem*, 13(2):427–436, 2012. ISSN 1439-7641. doi: 10.1002/cphc.201100757. URL http://dx.doi.org/10.1002/cphc.201100757.

[3] Martin Kristensen, Asger Krüger, Nathaniel Groothoff, Jaime García-Rupérez, Veronica Toccafondo, Javier García-Castelló, Maria Jose Ba nuls, Sergio Peransi-Llopis, and Angel Maquieira. Photonic crystal biosensor chip for label-free detection of bacteria. In *Optical Sensors*, page SWB1. Optical Society of America, 2011. URL http://www.opticsinfobase.org/abstract.cfm?URI=Sensors-2011-SWB1.

[4] Steven M. Shamah and Brian T. Cunningham. Label-free cell-based assays using photonic crystal optical biosensors. *Analyst*, 136:1090–1102, 2011. doi: 10.1039/C0AN00899K. URL http://dx.doi.org/10.1039/C0AN00899K.

[5] Yafang Tan, Chun Ge, A. Chu, Meng Lu, W. Goldshlag, Cheng Sheng Huang, A. Pokhriyal, S. George, and B.T. Cunningham. Plastic-based distributed feedback laser biosensors in microplate format. *Sensors Journal, IEEE*, 12(5):1174 –1180, 2012. ISSN 1530-437X. doi: 10.1109/JSEN.2011.2163933.

[6] Benoit Guilhabert, Nicolas Laurand, Johannes Herrnsdorf, Yujie Chen, Allan R Mackintosh, Alexander L Kanibolotsky, Erdan Gu, Peter J Skabara, R A Pethrick, and Martin D Dawson. Amplified spontaneous emission in free-standing membranes incorporating star-shaped monodisperse p-conjugated truxene oligomers. *Journal of Optics*, 12(3):035503, 2010. URL http://stacks.iop.org/2040-8986/12/i=3/a=035503.

[7] Chun Ge, Meng Lu, Xun Jian, Yafang Tan, and Brian T. Cunningham. Large-area organic distributed feedback laser fabricated by nanoreplica molding and horizontal dipping. *Optics Express*, 18(12):12980–12991, 2010. doi: 10.1364/OE.18.012980. URL http://www.opticsexpress.org/abstract.cfm?URI=oe-18-12-12980.

[8] Alexander L. Kanibolotsky, Rory Berridge, Peter J. Skabara, Igor F. Perepichka, Donal D. C. Bradley, and Mattijs Koeberg. Synthesis and properties of monodisperse oligofluorene-functionalized truxenes - highly fluorescent star-shaped architectures. *Journal of the American Chemical Society*, 126(42):13695–13702, 2004. doi: 10.1021/ja039228n. URL http://pubs.acs.org/doi/abs/10.1021/ja039228n. PMID: 15493927.

[9] March 2013. URL https://www.norlandprod.com/techrpts/chemresit.html.

[10] Dario Pisignano, Luana Persano, Paolo Visconti, Roberto Cingolani, Giuseppe Gigli, Giovanna Barbarella, and Laura Favaretto. Oligomer-based organic distributed feedback lasers by room-temperature nanoimprint lithography. *Applied Physics Letters*, 83(13):2545–2547, 2003. doi: 10.1063/1.1613362. URL http://link.aip.org/link/?APL/83/2545/1.

[11] Elisa Mele, Andrea Camposeo, Ripalta Stabile, Pompilio Del Carro, Francesca Di Benedetto, Luana Persano, Roberto Cingolani, and Dario Pisignano. Polymeric distributed feedback lasers by room-temperature nanoimprint lithography. *Applied Physics Letters*, 89(13):131109, 2006. doi: 10.1063/1.2357116. URL http://link.aip.org/link/?APL/89/131109/1.

[12] S. Riechel, U. Lemmer, J. Feldmann, T. Benstem, W. Kowalsky, U. Scherf, A. Gombert, and V. Wittwer. Laser modes in organic solid-state distributed feedback lasers. *Applied Physics B: Lasers and Optics*, 71:897–900, 2000. ISSN 0946-2171. URL http://dx.doi.org/10.1007/s003400000467. 10.1007/s003400000467.

[13] Johannes Herrnsdorf. *Organic Lasers and Nanostructured Organic Films for Hybrid Integration.* PhD thesis, University of Strathclyde, Glasgow, Nov. 2012.

[14] T. Riedl, T. Rabe, H.-H. Johannes, W. Kowalsky, J. Wang, T. Weimann, P. Hinze, B. Nehls, T. Farrell, and U. Scherf. Tunable organic thin-film laser pumped by an inorganic violet diode laser. *Applied Physics Letters*, 88(24):241116 –241116–3, 2006. ISSN 0003-6951. doi: 10.1063/1.2211947.

[15] Y. Yang, G. A. Turnbull, and I. D. W. Samuel. Hybrid optoelectronics: A polymer laser pumped by a nitride light-emitting diode. *Applied Physics Letters*, 92(16):163306, 2008. doi: 10.1063/1.2912433. URL http://link.aip.org/link/?APL/92/163306/1.

[16] C. Foucher, B. Guilhabert, A. L. Kanibolotsky, P. J. Skabara, N. Laurand, and M. D. Dawson. *Optical materials express*, 3(5):584–597, 2013. ISSN 2159-3930.

[17] J.R. Krivacic and D.W. Urry. Ultraviolet and visible refractive indices of spectroquality solvents: Ii. aqueous solutions of polyhydroxy solutes. *Analytical Biochemistry*, 43(1):240 – 246, 1971. ISSN 0003-2697. doi: 10.1016/0003-2697(71)90129-1. URL http://www.sciencedirect.com/science/article/pii/0003269771901291.

[18] Zongfu Yu and Shanhui Fan. Extraordinarily high spectral sensitivity in refractive index sensors using multiple optical modes. *Opt. Express*, 19(11):10029–10040, May 2011. doi: 10.1364/OE.19.010029. URL http://www.opticsexpress.org/abstract.cfm?URI=oe-19-11-10029.

[19] Xudong Fan, Ian M. White, Siyka I. Shopova, Hongying Zhu, Jonathan D. Suter, and Yuze Sun. Sensitive optical biosensors for unlabeled targets: A review. *Analytica Chimica Acta*, 620(12):8 – 26, 2008. ISSN 0003-2670. doi: http://dx.doi.org/10.1016/j.aca.2008.05.022. URL http://www.sciencedirect.com/science/article/pii/S0003267008009343.

[20] G. Ladam, P. Schaad, J. C. Voegel, P. Schaaf, G. Decher, and F. Cuisinier. In situ determination of the structural properties of initially deposited polyelectrolyte multilayers. *Langmuir*, 16(3):1249–1255, 2000. doi: 10.1021/la990650k. URL http://pubs.acs.org/doi/abs/10.1021/la990650k.

[21] M. Lu, S. S. Choi, U. Irfan, and B. T. Cunningham. Plastic distributed feedback laser biosensor. *Applied Physics Letters*, 93(11):111113 –111113–3, 2008. ISSN 0003-6951. doi: 10.1063/1.2987484.

[22] B.T. Cunningham. Label-free optical biosensors: An introduction. pages 1–28. Cambridge University Press, 2009.

[23] Harold P. Erickson. Size and shape of protein molecules at the nanometer level determined by sedimentation, gel filtration, and electron microscopy. *Biological Procedures Online*, 11, 2009. URL `http://www.springerprotocols.com/Abstract/doi/10.1007/s12575-009-9008-x`.

[24] Irving Kushner and Jo Anne Somerville. Estimation of the molecular size of c-reactive protein and cx-reactive protein in serum. *Biochimica et Biophysica Acta (BBA) - Protein Structure*, 207 (1):105 – 114, 1970. ISSN 0005-2795. doi: http://dx.doi.org/10.1016/0005-2795(70)90140-6. URL `http://www.sciencedirect.com/science/article/pii/0005279570901406`.

[25] Alan H.B. Wu. Cardiac troponin: Friend of the cardiac physician, foe to the cardiac patient? *Circulation*, 114(16):1673–1675, 2006. doi: 10.1161/CIRCULATIONAHA.106.652123. URL `http://circ.ahajournals.org/content/114/16/1673.short`.

[26] Karina R. Seferian, Natalia N. Tamm, Alexander G. Semenov, Kadriya S. Mukharyamova, Anastasya A. Tolstaya, Ekaterina V. Koshkina, Andrei N. Kara, Mihail I. Krasnoselsky, Fred S. Apple, Tatiana V. Esakova, Vladimir L. Filatov, and Alexey G. Katrukha. The brain natriuretic peptide (bnp) precursor is the major immunoreactive form of bnp in patients with heart failure. *Clinical Chemistry*, 53(5):866–873, 2007. doi: 10.1373/clinchem.2006.076141. URL `http://www.clinchem.org/content/53/5/866.abstract`.

Chapter 4

Specific and reversible biomolecule detection

Chapter 3 demonstrated the bulk and surface sensing capability of the laser through detecting changes in the refractive indices of bulk solution and the adsorption of material onto the laser surface. In the case of surface sensing, the transduction event was the addition of a thin polyelectrolyte layer to the laser surface resulting in a change in the emission wavelength. Although it was possible to say conclusively that there had been an addition of material to the laser surface, taken to be the polyelectrolyte layer, it was not possible to identify what the material was simply from the shift in wavelength (Section 3.5). For example, a similar shift in wavelength may be observed for a layer of protein or polymer. In order to use the DFB laser for biosensing applications, the surface of the sensor must have the ability to selectively immobilise certain biomolecules to the surface, whilst at the same time preventing the non-specific attachment of other materials and molecules that may also produce a shift in wavelength and contribute to background noise and false positive results. The sensor surface must be functionalised with a probe molecule that will bind exclusively to the CVD biomarker of interest. The probe may also be designed to simultaneously prevent the non-specific attachment of other blood components to the sensor surface or a secondary process may be used to block the surface to non-specific adsorption, as shown in Figure 4.1.

In this chapter, we aim to demonstrate the specific biosensing potential of the T3 DFB laser. There are many different strategies available for the functionalisation of the sensor surface with one molecule for the detection of another. The method chosen to confer specific biomolecule attachment at the laser surface will depend on a number of considerations such as: the nature of the target biomolecule (e.g. oligonucleotides, protein, etc.), the properties of the probe molecule and the feasibility for attachment of linker

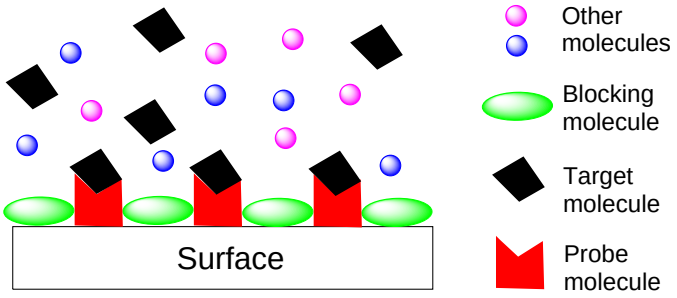

FIGURE 4.1: A surface functionalised with a probe molecule can specifically bind a chosen target molecule. Other molecules or chemistries can be used to block the surface to adsorption of other molecules that may be present alongside the target molecule, preventing any non-specific adsorption and false positive results.

molecules which may be required to tether the probe to the surface whilst maintaining specificity and affinity for the target molecule, the effect of orientation on the sensitivity and selectivity of the probe molecule, etc. [1]. The method chosen to facilitate biomolecule detection at the laser surface is crucial to the performance of the laser as a biosensor as it will ultimately determine the sensitivity of the device, i.e. the minimum detectable concentration of a biomarker which therefore dictates the biomarkers that can be detected within a clinically useful range. Section 1.2 highlighted that there are a number of advantages in a nucleic acid based approach to biosensing relative to that of an antibody based approach. These include ease of synthesis and less stringent storage requirements [2]. It was therefore our intention to demonstrate functionalisation of the DFB laser surface with nucleic acid probes for the specific detection of three CVD biomarkers. However, prior to focusing on this challenge, proof-of-principle specific biomolecule detection with a model system provides a means of identifying the best functionalisation approach for the T3 surface. The model system used was the biotin-avidin interaction [3], which is widely used in life science and biotechnology applications and is discussed in more detail here.

The aims of this chapter are, firstly, to demonstrate the specific detection of avidin via a biotin functionalised surface. Biotinylation of the DFB laser can be achieved through a number of means, therefore the method resulting in the best sensitivity and specificity results must be identified. Secondly, we aim to demonstrate the reversible nature of avidin sensing. And thirdly, we aim to investigate the potential interference of blood components. Albumin is a protein present in large quantities in the blood, that is known

to readily adsorb non-specifically to surfaces. Therefore, the non-specific adsorption of albumin on the T3 surface was investigated, as well as its effect on specific avidin sensing.

4.1 The biotin-streptavidin interaction

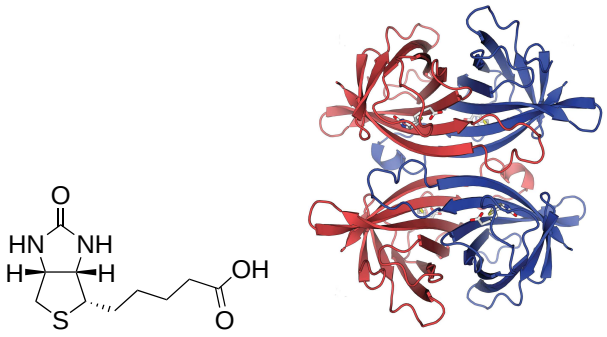

(a) (b)

FIGURE 4.2: (a) Chemical structure of biotin. (b) Ribbon diagram of avidin, from [4].

The biotin-avidin system is the interaction between avidin, a protein found in the egg-whites of birds, reptiles and amphibians with biotin, a small molecule (M_W 244.3 Da) found in minute quantities in all living cells and is also known as vitamin H [3]. The relevant structures are shown in Figure 4.2. A similar protein, streptavidin, derived from the bacterium Streptomyces avidinii, can be used as an alternative to avidin. The interaction between avidin and biotin is thought to represent a natural defence mechanism, arising from the fact that biotinylated enzymes are required for the growth of bacteria and by binding with avidin, the biotinylated enzyme is inactivated, therefore inhibiting the growth of the bacteria [5]. The avidin-biotin interaction is the strongest known non-covalent interaction, with a binding affinity of 10^{-15} M and also displays a number of other useful characteristics for biosensing applications. For example, the high affinity ensures that once the avidin-biotin interaction has taken place, the conjugation is very difficult to break and is not disturbed by extremes in pH, temperature, organic solvents and other denaturing agents [6]. Both avidin and streptavidin are exceptionally stable molecules and their capacity for binding biotin is maintained even after being subjected to harsh reaction conditions [6]. There are many similarities between avidin and streptavidin. Both are composed of four subunits that will each bind a single biotin molecule and their affinity for biotin is the same. However, there are some important differences between the two (Table 4.1) [5], which has implications for the development of a surface sensing assay. The most pronounced difference between the two is that at a pH of $\approx$7.5 avidin is positively charged whereas streptavidin is neutral. These differences in isoelectric point (pI), i.e. the pH at which a particular molecule or surface carries no

net electrical charge, can have an effect on the non-specific adsorption potential which may be beneficial if a negatively charged surface is to be functionalised with avidin or detrimental if non-specific adsorption is to be keep to a minimum.

	Avidin	**Streptavidin**
Molecular weight	67000 kDa	53000 kDa
Isoelectric point (pI)	10 - 10.5	6.8 - 7.5
Biotin affinity	10^{-15} M	10^{-15} M
Non-specific binding	High	Low
No. biotin binding sites	4	4
Avidin specificity	Low	High

TABLE 4.1: Comparison of avidin and streptavidin properties [5].

The properties of the biotin binding proteins, noted in Table 4.1, make the system suitable for a range of applications including detection, purification and retrieval assays [7–9]. For detection assays, the intended use with the DFB laser, the avidin-biotin interaction can be used in a number of different ways. One example was presented in Section 1.2.1.1 when describing the Cobas POC device. In this example, a streptavidin functionalised surface was used to immobilise a biotinylated antibody to a detection region where an antigen measurement could take place, as depicted in Figure 1.5. For the purposes of proof-of-principle specific biomolecule detection with the T3 laser, either molecule, biotin or avidin, could be the probe/target. When the experimental work was initiated the intention was to immobilise biotin on the laser surface for the detection of streptavidin as it was assumed that detection of a large molecule binding to a smaller molecule may be more straight-forward than vice versa. Functionalisation of the laser surface with biotin can be achieved using a number of different methods. These methods predominantly fall under two broad categories: physical adsorption and covalent attachment.

4.2 Methods of surface functionalisation

Surface functionalisation with probe molecules can be achieved using physical adsorption, covalent immobilisation and entrapment in a support material such as a polymer matrix [1], as depicted in Figure 4.3. When choosing the immobilisation technique to use in a biosensing assay, the key consideration is to balance the sensitivity, specificity and the availability of the binding site to the target biomolecule and to prevent any structural changes, or denaturing, of the probe which may by detrimental for the binding reaction with the target biomolecule. Specific biosensing using a wide range of surface functionalisation strategies has been demonstrated in commercially available

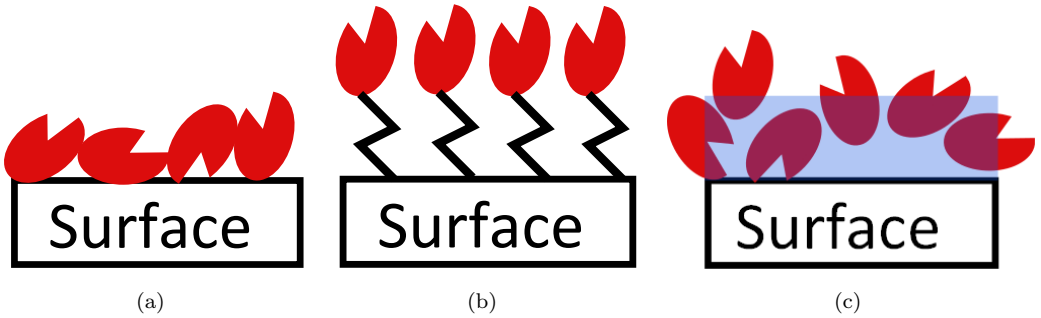

FIGURE 4.3: (a) The options available for immobilisation of biomolecules on a surface: adsorption, (b) covalent attachment and (c) entrapment in a matrix.

systems, producing sensing platforms with excellent sensitivity and specificity [10–12]. However, functionalisation of an organic semiconductor based DFB laser for biosensing has never been demonstrated. In this work, both physical adsorption and covalent immobilisation methods were considered. These methods are discussed in more detail for functionalisation of the DFB laser surface with biotin (via a biotinylated bovine serum albumin (BSA) protein) or avidin, but can be equally applied to other probe types such as antibodies and oligonucleotides.

4.2.1 Physical adsorption

Physical adsorption of a molecule to a surface arises due to forces between the molecule and the surface. The main driving forces for protein attachment are the interactions between hydrophobic regions of the protein and the surface and electrostatic interactions [1]. A typical protein will have numerous different properties over its surface area; there will likely be hydrophobic regions and other areas with a positive and/or negative charge, as depicted in Figure 4.4. For hydrophobic interactions, hydrophobic regions of the protein surface will interact with hydrophobic areas on the surface due to the thermodynamic driving force to reduce the net hydrophobic surface area of the protein-surface system exposed to the solvent [13]. Generally, a hydrophobic surface will adsorb proteins more strongly than a neutrally charged hydrophilic surface and will therefore result in a greater number of adsorbed molecules [13, 14]. Greater adsorption of molecules may be a benefit or a hindrance. Improvements in sensitivity may be achieved through adsorption of more of the target proteins although this may be offset by reduced specificity if the adsorption of other proteins is also increased.

Electrostatic interaction between charged groups on the protein surface and charged regions of the surface also leads to adsorption. The electrostatic properties of the protein and the surface are functions of the solvent pH and the ionic strength and, therefore, electrostatic interactions can be minimised or encouraged by tuning the properties of

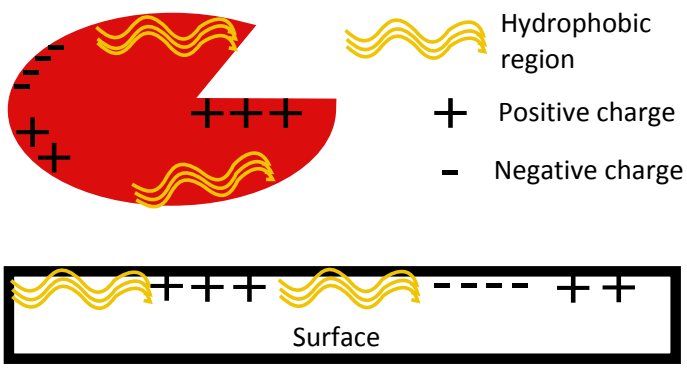

FIGURE 4.4: Surface properties of a typical protein and its interaction with a surface.

the solvent. For example, if it is desirable to minimise electrostatic attractions, the solvent pH can be matched to the isoelectric point of the protein and the ionic strength of the solvent can be increased to help mask charged groups [1]. Protein adsorption also depends on the concentration of protein in solution and the time the solution is in contact with the surface. At low concentration, there may not be sufficient molecules on the surface in a set time period for adsorption to occur. Also, for proteins that do adsorb at low concentrations, the extra space available to the protein molecules may encourage them to maximise the number of binding interactions and this can make the probability of the protein undergoing conformational changes greater [1, 15]. On the other hand, a high concentration means that adsorbed proteins will be surrounded by other proteins. This reduces the space available to maximise surface interactions and therefore decreases the likeliness of conformational changes occurring, but also reduces the strength of the interaction between the protein and the surface, making desorption of the protein more likely [15].

Physical adsorption of a biomolecule to a surface will often involve a combination of both hydrophobic and electrostatic interactions. The T3 laser surface is neutral and hydrophobic and has been shown to non-specifically adsorb proteins such as BSA and lambda DNA. Therefore, non-specific adsorption of either biotinylated BSA or avidin was a viable option for functionalisation of the laser surface (Section 4.3).

Non-specific functionalisation of a surface with biomolecules can be a simple and efficient process. If there are no intermediate steps required for preparation of the surface, the surface can simply be incubated in the protein solution for a set period of time. This can reduce the overall time and reagents required for a biodetection assay. In some cases, the thickness of the protein layer can be controlled via the solvent conditions as was mentioned for the polyelectrolyte layers in Section 3.5 [16, 17]. However, the random nature of the protein adsorption can lead to potential drawbacks for this method of functionalisation. Loss of a biomolecules specific binding capacity for a target biomolecule is the greatest disadvantage of non-specific adsorption. This can occur due

to conformational changes and/or due to the orientation of the molecule at the surface [1], which can lead to availability of the binding site being inhibited as illustrated in Figure 4.3a. Reproducible results can also be difficult to achieve with a non-specific adsorption approach due to the variability in adsorption from assay to assay. Furthermore, adsorption to a surface is also reversible which may mean that surface functionalisation may not withstand the wash steps required in most biosensing assays [1]. It is this lack of control over the orientation of the molecule, resulting in compromised availability of the binding site, and the reversible nature of surface functionalisation that spurred research into alternative methods of more permanent surface functionalisation protocols, specifically, the covalent attachment of biomolecules to a surface.

4.2.2 Covalent attachment

Covalent attachment of biomolecules to a surface can be achieved using functional groups present on the surface that will form covalent bonds with the biomolecule, either directly or indirectly via a linker molecule or vice versa. Chemists have identified and devised a number of strategies for biofunctionalisation of surfaces and these will be discussed in more detail in the following sections.

Unlike non-specific adsorption, functionalisation of a surface using covalent binding is not a random process. The density and orientation of the biomolecule can be controlled through the solution conditions and the design of the linker groups on the surface/biomolecule that will take part in covalent binding [1]. This control allows the surface functionalisation to take place in a reproducible way. Control of the density of the biomolecule layer on the surface is necessary as a balance must be achieved between the maximum number of available biomolecule binding sites and the prevention of any steric hindrance reducing the functionality of those binding sites [1, 18]. Also, if the position of functional groups on the biomolecule are known, or designed, it is possible to ensure that the binding site is available to the target biomolecule, which is not possible with non-specific adsorption. Another advantage of covalent attachment is the strength of the binding between the biomolecule and the surface. As the bond is strong, washing will not result in removal of bound molecules from the surface. This can lead to a reduction in background noise as a more aggressive wash protocol can be implemented to remove any unbound or non-specifically bound material from the surface [19].

The disadvantages of covalent attachment are greatly outweighed by the many advantages. An increase in the number of surface functionalisation steps and more reagents is an acceptable compromise if the resulting biodetection assay shows better reproducibility and stability. The main disadvantage is the time it can take to find, and optimise,

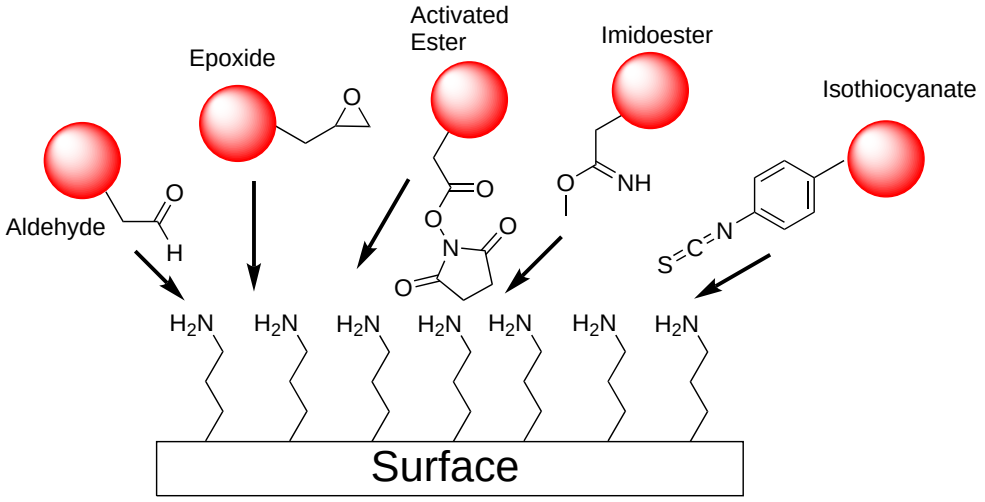

FIGURE 4.5: A number of chemical groups can form bonds with amino groups including aldehyde, activated ester, epoxide, imidoester and isothiocyanate groups. The red sphere represents any biomolecule that can be functionalised with the various amino reactive groups.

the binding chemistry for a particular application. This requires detailed knowledge of chemical interactions and, in our experience, a degree of trial and error. However, there are a number of standard protocols and commercially available linker products that can help simplify this process. Three of the most widely used chemical interactions used for covalent binding are described below.

4.2.2.1 Amine functionalisation

Many surface functionalisation strategies for covalent attachment of biomolecules rely on the use of primary amino groups (-NH_2) [20]. There are ample amine-base coupling chemistries available, many of which are suitable for use in aqueous conditions which is the preferred environment for many biomolecules. Most proteins have lysine residues which have amino groups on their surface. These can be used to cross-link them to a surface [1]. Figure 4.5 highlights several of the amine coupling options available for biomolecule (red sphere) surface functionalisation. Only activated ester-amine (N-hydroxysuccinimidyl (NHS)-amine) coupling was used for the experimental work presented in this chapter therefore, an overview of the mechanisms involved in this method is provided below.

4.2.2.1.1 Activated ester bioconjugation

NHS esters, are reactive groups formed by carbodiimide-activation or carboxylate molecules [1, 21, 22]. Many biomolecules can be purchased pre-functionalised with an NHS-ester

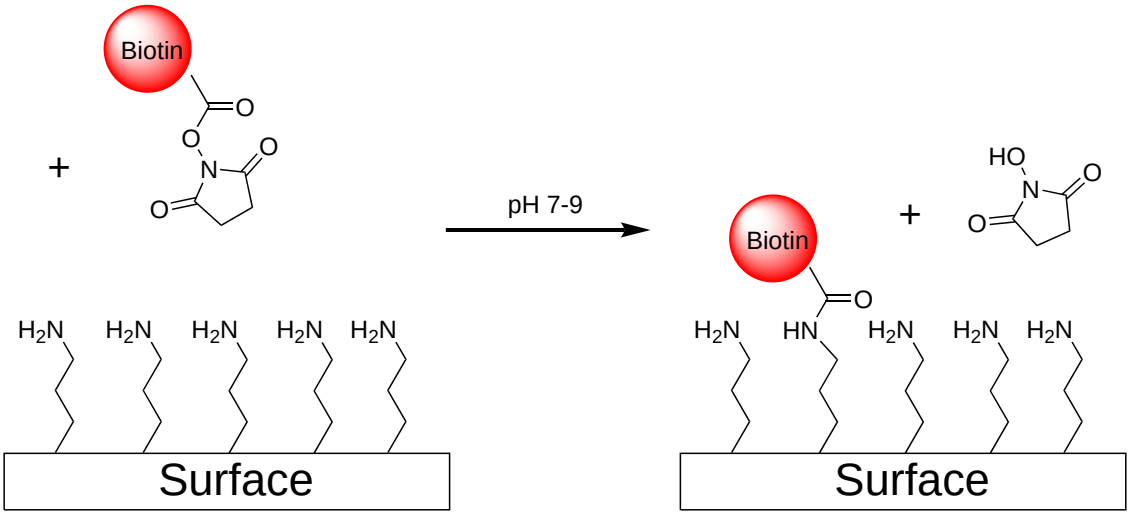

SCHEME 4.1: Schematic representing the amine coupling of biotin functionalised with an activated ester group to the laser surface.

group or NHS-ester cross-linkers are widely available. NHS-ester groups react with primary amines in aqueous solutions within a pH range of 7-9, to produce stable amide bonds, N-hydroxysuccinimide (NHS) is released as a by-product [1]. The reaction is represented by the schematic in Scheme 4.1. The formation of amide bonds is quick (≈30 minutes) and can be performed at room temperature. The water solubility of the NHS-ester can also be improved with the addition of a sulfonate (-SO_3) group on the NHS ring [23]. This addition has no effect on the reaction chemistry, as sulfo-NHS is released as the reaction by-product. These properties, and the fact that the reaction can be performed under physiological conditions, make this method of amine coupling a good option for immobilisation of biomolecules on a surface and there are many examples of this approach being used for the surface functionalisation of biosensors [24–26]. In this work, NHS-biotin was used to functionalise the DFB laser surface for the specific detection of avidin, described in more detail in Section 4.4.2.

4.2.2.2 Sulfhydryl functionalisation

Covalent coupling of biomolecules using thiol (-SH) groups is a method used for the surface functionalisation of many biosensors [1, 27, 28]. Thiol coupling can be a good alternative for surface functionalisation when the use of amine groups is not appropriate. For example, many proteins will contain several amine groups on their surface and therefore it can be difficult to control the orientation of a protein when immobilising it on the surfave via an amine reactive linker. As proteins contain fewer thiol groups, linking the molecule to the surface via thiol groups can provide a better option for controlling the orientation of the immobilised protein. Thiol groups are very reactive to a number of

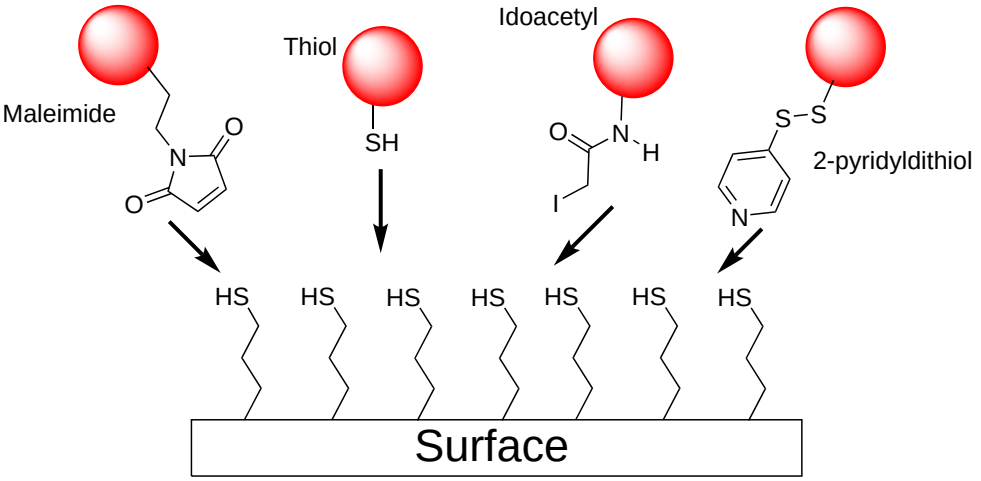

FIGURE 4.6: A number of chemical groups can form bonds with sulfhydryl groups including thiol, maleimide, idoacetyl and pyridyldithiol groups. The red sphere represents any biomolecule that can be functionalised with the various amino reactive groups.

other chemical groups, as highlighted in Figure 4.6, and can produce very stable bonds in aqueous solutions. Due to the high reactivity of thiol groups, these groups are often protected [29], and a de-protection step is therefore required before thiol coupling can take place. One of the simplest methods of thiol based immobilisation is to react a thiol group on a biomolecule directly with a thiol functionalised surface via the formation of a disulfide bond. However, if the surface does not contain thiol groups, as was the case for the T3 laser surface, other cross-linker chemistries are available for secondary functionalisation of the surface. For example, amine-sulfhydryl and amine-pyridylthiol cross-linkers can be used to immobilise a biomolecule to an amine functionalised surface via a thiol group on the molecule. These are only two possibilities for thiol coupling, and others are shown in Figure 4.6, but as these were the linker chemistries used for the experimental work presented in Chapter 5, they are described in more detail here.

4.2.2.2.1 Maleimide-activated bioconjugation

A maleimide group will react with sulfhydryl or amine groups depending on the pH of the solvent [30]. Within a pH range of 6.5-7.5, maleimide will react selectively with sulfhydryl groups to form an irreversible, and therefore very stable, thioether linkage. At a pH of >8.5, the maleimide may couple with amine groups, however, at this pH the maleimide group is prone to hydrolysis which will render it inactive. Therefore, the methods discussed in Section 4.2.2.1 are preferable for amine coupling.

There are maleimide-amine cross-linkers readily available for the attachment of biomolecules with sulfhydryl groups to an amine functionalised surface, an example of this reaction is shown in Scheme 4.2. In the experimental work presented in Chapter 5, an

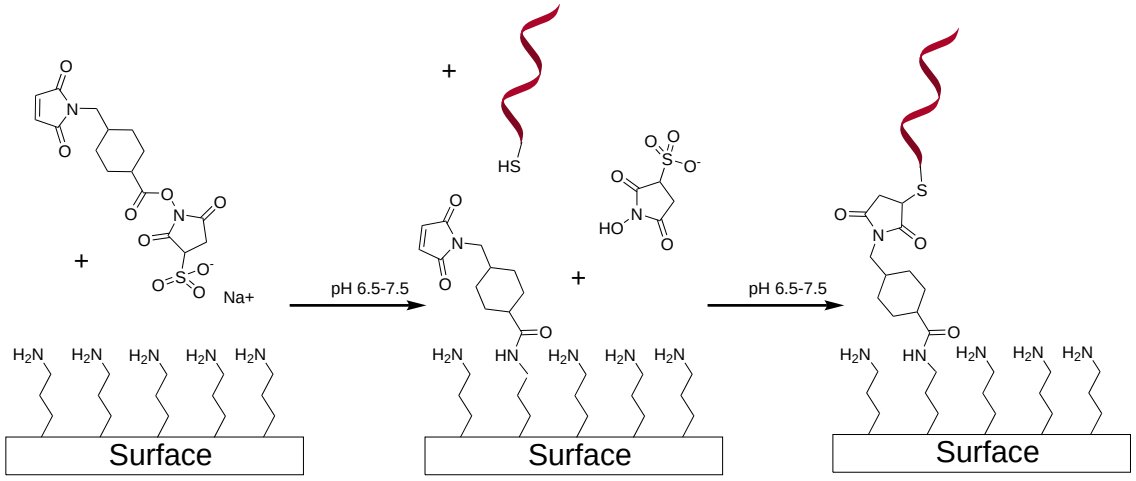

SCHEME 4.2: Schematic representing the NHS-maleimide linker used to couple thiol labelled DNA (ribbon) to an amine functionalised surface. The NHS-maleimide linker is first used to functionalise the laser surface with maleimide groups via an NHS reaction with the amine groups on the surface. Thiol modified oligo can then be coupled to the maleimide.

attempt was made to couple a thiol-modified oligonucleotide to the T3 DFB laser surface. Bioconjugation via maleimide/amine groups can take place in aqueous solutions at room temperature and a pH of around 7.5, ideal conditions for nucleic acid probes. The main drawbacks with maleimide functionalisation is the instability of maleimide in solution over time and, more generally, the need to de-protect thiol groups prior to maleimide activation. These factors lead to the requirement that only fresh maleimide solutions be used for cross-linking applications. Furthermore, additional steps are required to de-protect any thiol modified biomolecules and to remove any de-protection agents, which themselves can react with the maleimide group, prior to the reaction (although this step is required for all sulfhydryl reactions involving protected thiol groups and is not exclusive to the maleimide reaction).

4.2.2.2.2 Pyridyl disulfide bioconjugation

An alternative to the maleimide functional group for thiol reactions is the pyridyldithio group [1, 31]. The pyridyldithio group will also react with sulfhydryl groups via the formation of a disulfide bond (Scheme 4.3). Like the maleimide reaction, this reaction can also take place in aqueous solutions with a pH in the range of 7-8. The main differentiation between the sulfhydryl reactions with maleimide and pyridyldithio groups is that the maleimide reaction is irreversible whereas the disulfide bond formed via the pyridyldithio reaction can be cleaved, providing the potential for reversible surface functionalisation [31]. Pyridyldithio cross-linkers are commercially available and can be used to bioconjugate thiol modified biomolecules to an amine functionalised surface. As with

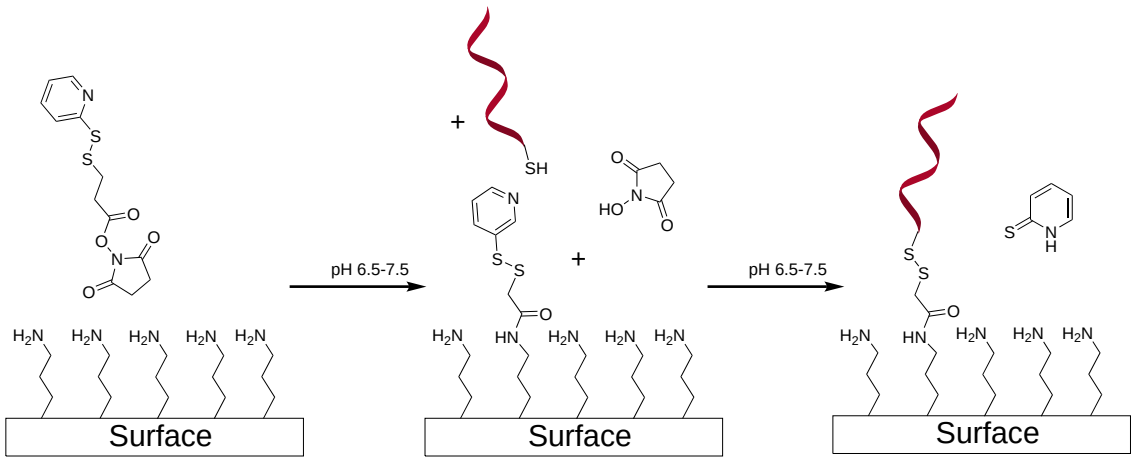

SCHEME 4.3: Schematic representing the NHS-pyridyldithiol linker used to couple thiol labelled DNA (ribbon) to an amine functionalised surface. The NHS-pyridyldithiol linker is first used to functionalise the laser surface with pyridyldithiol groups via an NHS reaction with the amine groups on the surface. Thiol modified oligo can then be coupled to the pyridyldithiol.

maleimide groups, the pyridyldithio group is unstable in solution and therefore cannot be stored, requiring that fresh solutions be made for each reaction. A pyridyldithio-NHS corsslinker was used for experimental work investigating functionalisation of the laser surface with a thiol modified biomolecule, details are provided in Chapter 5.

4.2.2.3 Bioorthogonal bioconjugation

'Bioorthogonal conjugation' is a term used to describe a reaction that proceeds under physiological conditions and takes place between two components that are non-interacting (orthogonal) to the functionality of a biological system [32]. The coupling chemistries mentioned so far, e.g. amine-activated ester, thiol-maleimide, etc., cannot be considered to represent bioorthogonal reactions as competing chemical groups present on proteins, nucleic acids and other biomolecules would interfere with the reaction [32]. One class of reactions that are bioorthogonal are 'click' reactions. 'Click Chemistry' is a term that was introduced at the turn of the 21st century to describe reactions that are simple to perform, can be carried out in water based solvents, are efficient (high yield), create easily removed by-products and are very specific [33]. There are many examples of the use of click chemistry for attachment of oligonucleotide probes to surfaces in the literature and it is a widely used method due to the properties cited above [34–36].

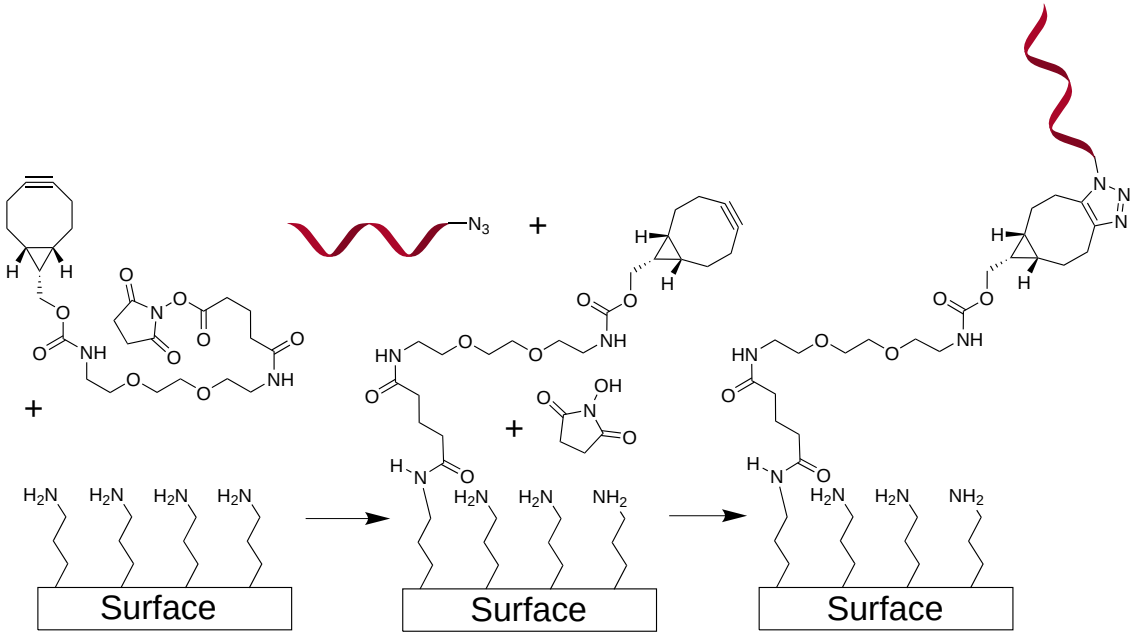

SCHEME 4.4: Schematic representing the NHS-BCN and azide-polyT surface functionalisation reaction. The amine functionalised surface is exposed to alkyne-NHS in the first instance to immobilise the alkyne on the laser surface. Azide modified polyT (ribbon) is then added to the surface via the 'click' reaction between the alkyne and azide, resulting in immobilisation of the polyT oligo on the laser surface.

4.2.2.3.1 The azide-alkyne click reaction

The reaction between azide and alkyne groups satisfies the requirements of both bioorthonanality and click reactions. Historically, the azide-alkyne reaction was catalysed by copper(I) [37], but as copper was toxic to many biological systems an alternative method involving the use of cyclooctynes was developed [38]. This was known as 'copper-free' click chemistry. A wide variety of cyclooctyne reagents, including bifunctional linker molecules, can be purchased for click reactions. And azide modified oligos can be commercially sourced or synthesised in house relatively simply. In this work, a bifunctional linker molecule containing a cyclooctyne and an NHS group at either end was used to selectively couple azide modified DNA to the laser surface, as represented in Scheme 4.4. The experimental methods and results are described in detail in Section 5.1.2.

The remainder of this chapter focuses on the experimental results obtained to demonstrate the specific biosensing capabilities of the T3 DFB laser sensor. First, an overview of our initial attempt at surface functionalisation via the non-specific adsorption of biotinylated BSA (bioBSA) and subsequent detection of streptavidin is provided. Following that, the methods used to covalently link biotin to the sensor surface are described and presented alongside specific albumin sensing results. The final two sections provide details on a demonstration of the multi-use potential of the sensor and an investigation into the effect of non-specific adsorption of albumin on specific biomolecule detection.

4.3 Initial attempts at surface functionalisation

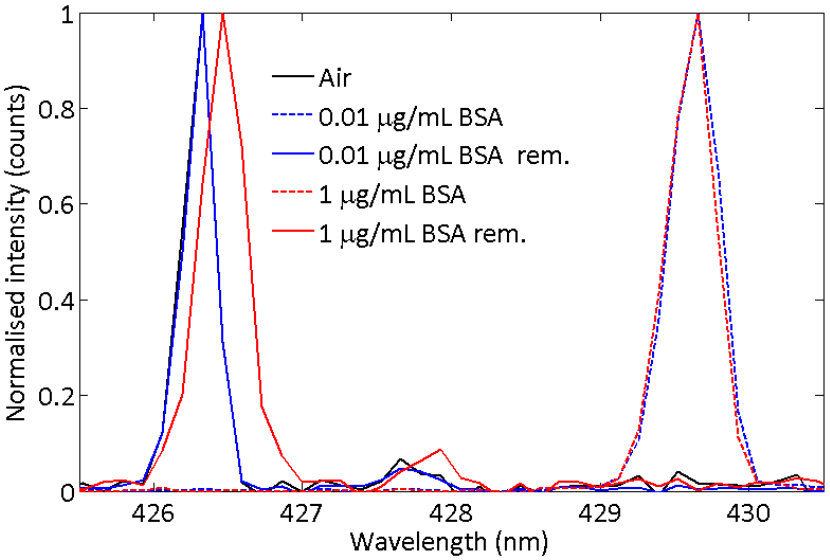

FIGURE 4.7: Non-specific adsorption of BSA to the T3 laser surface. Adsorption of BSA is shown to occur at a concentration of 1 μg.mL but not at a lower concentration of 0.01 μg.mL as the laser wavelength returns to the air wavelength upon removal of the BSA solution.

As mentioned in Section 4.1, the the interaction between biotin and avidin/streptavidin was chosen as a model system to show specific biosensing with the T3 DFB laser. As BSA was known to bind non-specifically to the laser surface (Figure 4.7) initial surface functionalisation attempts focused on immobilising bioBSA (BSA conjugated to a biotin molecule) to the laser surface for the specific detection of streptavidin. This is a method that has been widely reported as a means of functionalising a surface with biotin [39, 40].

Functionalisation of the laser with bioBSA was performed by immersing the laser, fixed within the demountable cuvette as described in Section 3.2, in a bioBSA solution (25 μg.mL in 10 mM PBS) for two minutes. This resulted in a shift in wavelength of 0.16 nm upon the removal of the bioBSA and PBS wash solutions, i.e. with the laser exposed to air. For the same measurement but with the laser immersed in PBS, the relative shift in wavelength due to bioBSA adsorption was 0.11 nm (Figure 4.8a). When these measurements were made, it was assumed that the best method of recording the shift in wavelength would be upon removal of all test and wash solutions. However, it soon became apparent that upon the addition of biomolecules to the laser surface, the hydrophobicity of the laser surface was diminished and the wetting of the surface caused interference with biosensing results recorded in air. Therefore, the shift due to bioBSA adsorption to the laser surface recorded in solution is expected to provide a more accurate measurement relative to that recorded in air. Functionalisation of the laser surface with bioBSA resulted in variable solution measurement of the shift in wavelength due

to bioBSA molecule adsorption (0.27±0.24 nm over four measurements). Even when the variable nature of non-specific adsorption is taken into consideration, this level of variability seemed extreme. Perhaps not surprisingly, streptavidin sensing results for bioBSA functionalised lasers also showed a high degree of variability, although these measurements were also compounded by the fact that the wavelength shift measurements were recorded with the laser exposed to air rather than solution, therefore surface wetting was also a factor. For streptavidin sensing, a range of streptavidin solutions (1 - 100000 ng.mL^{-1}) were prepared in 10 mM PBS. The laser was exposed to each streptavidin solution in turn for ≈1 minute, starting with the 1 ng.mL^{-1} solution, with PBS wash steps between each of the different concentrations. An example of streptavidin sensing results are shown in Figure 4.8b.

The results in Figure 4.8b suggest that there is no detectable streptavidin binding to the biotinylated laser surface for the lowest four streptavidin concentrations, which span three orders of magnitude. The final streptavidin solution tested, with a concentration of 0.1 mg.mL^{-1}, results in a shift in wavelength of 3.28 nm relative to the wavelength in air post bioBSA functionalisation. The magnitude of this shift is predominantly an effect of surface wetting which makes it impossible to determine the shift due to streptavidin binding to the laser surface without additional solution measurements.

When this work was performed it was concluded that biotin-streptavidin coupling was not being detected towards the lower end of the concentration range. This was surprising considering the affinity between biotin and streptavidin, as mentioned previously, and the size of the streptavidin molecules (dimensions of ≈5x5x4 nm [41]). It was thought that the non-specific adsorption of bioBSA resulted in a relatively low number of biotin molecules on the surface, perhaps in a non-homogeneous fashion, and/or a low availability of the biotin molecules on the laser surface for streptavidin coupling as has been reported [42]. In hindsight, it is likely that the measurements being recorded in air, rather than in solution, may have been a major factor in the lack of sensing results as a small degree of surface wetting may have masked the effect of any streptavidin binding, resulting in the 'constant' shift in wavelength noted for the lowest streptavidin concentrations measured, as in Figure 4.8b. However, it is apparent that the variability of the bioBSA adsorption, which was measured in solution as well as in air, did not provide a good basis for further reproducible sensing measurements. Therefore, covalent attachment of biotin to the laser surface was performed which improved the reproducibility of biotin functionalisation, and subsequent detection of avidin.

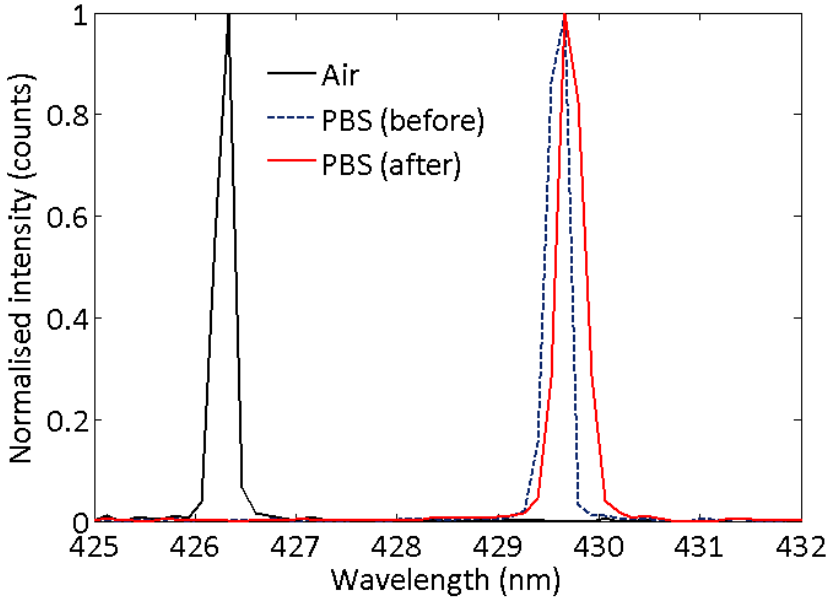

(a)

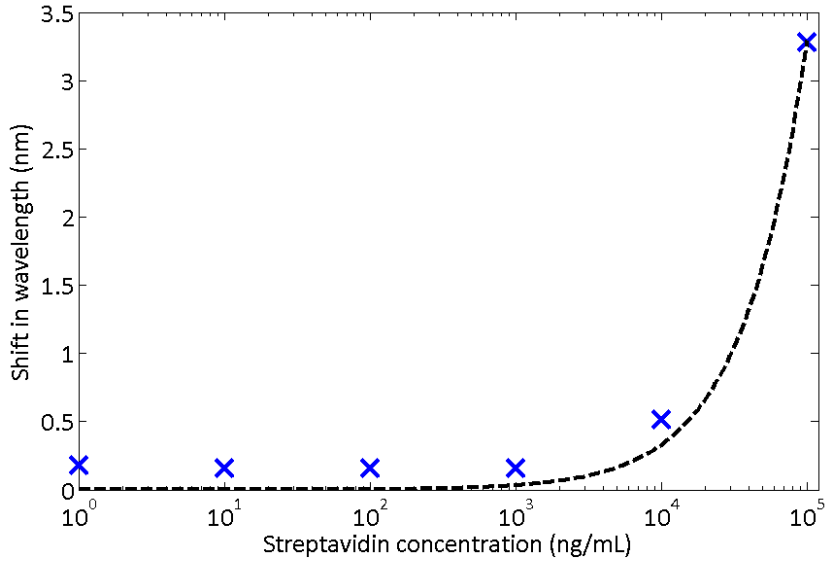

(b)

FIGURE 4.8: (a) Adsorption of bioBSA to the laser surface results in a shift in wavelength of 0.11 nm. (b) Shift in wavelength due to specific detection of streptavidin with a bioBSA functionalised laser. The data is fitted with Eq. 4.1, discussed in Section 4.4.2.

4.4 Specific avidin detection

The T3 laser gain layer was said in the previous section to be hydrophobic and that there was no net surface charge. The T3 surface also contains no functional groups that would enable covalent attachment of biotin, as shown in the chemical structure of T3 in Figure 3.2a. Therefore, in order to covalently immobilise biotin to the surface, the

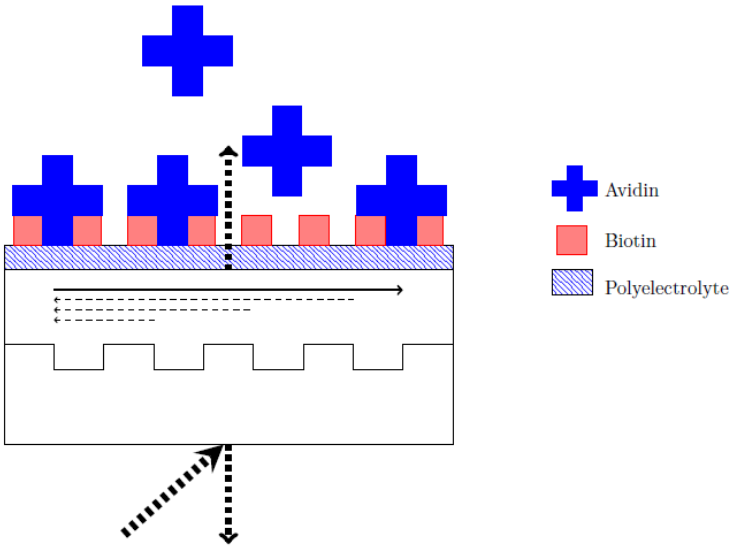

FIGURE 4.9: Schematic of polyelectrolyte and biotin functionalisation of the DFB laser for specific detection of avidin.

T3 surface must first be functionalised with chemical groups appropriate for reacting with the complementary covalent linker. As the non-specific surface sensing results, see Section 3.5, demonstrated the successful and stable adsorption of polyelectrolyte to the sensor surface, adsorption of a polyelectrolyte layer was the method chosen to provide surface functional groups for the covalent coupling of biotin, as represented in Figure 4.9.

PEI, the polyelectrolyte used previously, contains branched amine functional groups as shown in Figure 4.10a, therefore, amine coupling was the surface chemistry used for biotin functionalisation of the surface. As well as PEI, a second polyelectrolyte, polyphenylalanine lysine (PPL), was also tested in order to determine the polyelectrolyte layer resulting in the most effective biotin functionalisation, measured via the lowest detectable avidin concentration. PPL contains an aromatic group and it was hypothesised that the aromatic phenylalanine group on the PPL may participate in non-covalent π-π interactions with the aromatic groups within the arms of the T3 molecule, resulting in a more homogeneous polyelectrolyte layer in comparison to the adsorption of PEI. To test this hypothesis, poly-l-lysine (PL) was also used to provide amine functionality to the laser surface and the avidin sensing results from layers functionalised with each of the three polyelectrolytes were compared.

4.4.1 Experimental methods

The polyelectrolytes used to provide the amine functionality to the DFB laser surface were PPL (M_W 20000 - 50000), PL (M_W 30000 - 70000) and PEI (M_W 750000)(Sigma

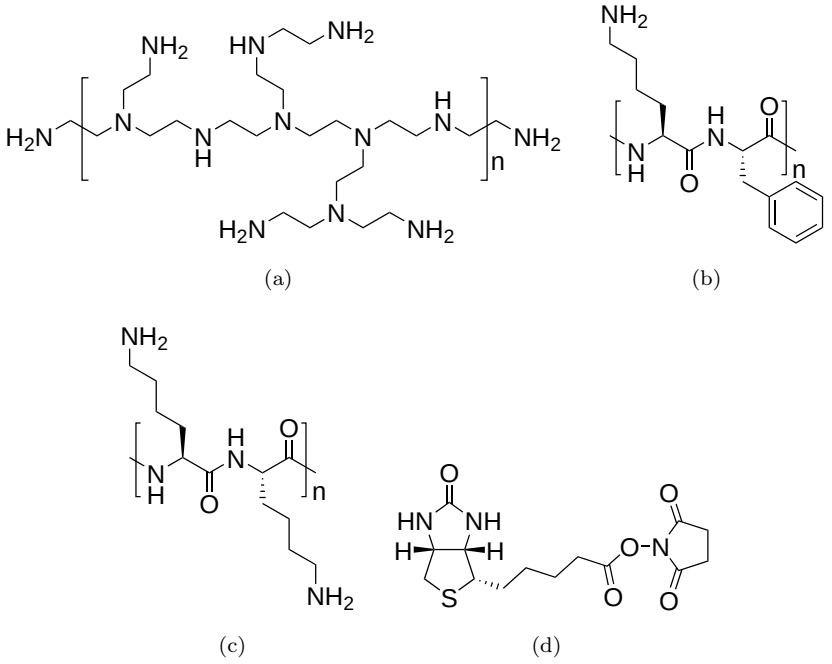

FIGURE 4.10: Chemical structures of (a) PEI, (b) PPL, (c) PL and (d) NHS-biotin.

Aldrich), the chemical structures of which are shown in Figure 4.10. The demountable cuvette was used for this experimental work, therefore, and lasers were fabricated as described in Section 3.1.

Polyelectrolyte functionalised surfaces were achieved using similar protocols reported in the literature [43, 44]. PEI was prepared in 0.9 M sodium chloride (NaCl) to a concentration of 5 mg.mL^{-1}. The laser sensor was washed with 0.9 M NaCl before immersing the laser in PEI solution for 10 minutes. After removal of the PEI solution, the sensor was washed with NaCl and then 10 mM pH 7.4 PBS. The emission wavelength from the sensor, whilst immersed in PBS, was recorded. Water soluble biotin functionalised with an amine reactive NHS group (sulfosuccinimidobiotin, NHS-biotin), structure shown in Figure 4.10d, was dissolved in 10 mM PBS to a concentration of 0.2 mg.mL^{-1} (0.82 mM), was added to the cuvette for 20 minutes, which was considered sufficient time for amine coupling to take place. The emission wavelength was recorded upon adding and prior to removal of the biotin solution. The NHS-biotin solution was removed and the cuvette and laser was washed with PBS before recording the emission wavelength in PBS. A dilution series of Avidin (1-500000 ng.mL^{-1} (14.9 pM - 7.50 μM)) in 10 mM PBS was used to determine the limit of detection of the T3 biosensor. The biotin concentration was chosen to be in excess of the highest avidin concentration to ensure the availability of sufficient biotin binding sites. The emission wavelength was recorded upon immersion of the sensor in avidin solution and after 20 minutes, just prior to removal of the solution. The sensor was washed with PBS and the final emission wavelength

recorded in PBS. This process was repeated, with a different laser sensor, for each of the avidin concentrations.

This general protocol was used for the fabrication of the T3 lasers with PPL or PL in place of PEI. PPL and PL solutions were at a concentration of 1 mg.mL^{-1} in 10 mM PBS and therefore NaCl washes and measurements were replaced by PBS.

All polyelectrolyte adsorption, biotin functionalisation and avidin binding measurements were performed with the laser immersed in PBS solution after a wash step with PBS to remove any unbound molecules that may be present on the laser surface. Wavelength shift measurements for the addition of molecules to the surface were obtained by subtracting the emission wavelength recorded in PBS prior to immersion in the solution containing the biomolecules to be deposited, from the emission wavelength in PBS post immersion. This relative shift in wavelength is caused by the change in the effective refractive index of the laser mode due to the presence of biomolecules on the laser surface.

4.4.2 Specific avidin detection results

4.4.2.1 PEI functionalisation

Branched PEI was previously used as the base monolayer for stacking of alternately charged polyelectrolytes and was therefore the initial polyelectrolyte chosen to investigate biotin functionalisation [45]. The primary amine groups of PEI enabled facile functionalisation with the activated ester of NHS-biotin. A number of DFB laser sensors were functionalised with PEI and biotin and the average relative shift in emission wavelength (with the non-functionalised laser as reference), attributed to biotin covalently linked to the sensor surface, was 0.17±0.07 nm. Each of these sensors were subsequently exposed to an avidin solution over a range of concentrations. The relative shifts in emission wavelength after exposure to each avidin concentration are shown in Figure 4.11. Avidin coupling follows Langmuir adsorption as described previously in Section 2.2.4 and Figure 4.11 depicts a typical sigmoidal concentration curve, representing an increasing response to increasing avidin concentrations until all of the available biotin binding sites are saturated. The binding of avidin to the biotinylated surface is not simply an adsorption reaction, therefore, to consider the binding affinity ($[\mathrm{A}] + [\mathrm{B}] \underset{\mathrm{K}_d}{\overset{\mathrm{K}_a}{\rightleftharpoons}} [\mathrm{AB}]$, where A, B, K_a and K_d represent avidin, biotin, association constant and dissociation constant respectively) between the surface bound biotin and the avidin in solution, Eq. 4.1, was used to fit the specific binding data [46].

$$y = \frac{B_{max}.x}{K_d + x} \tag{4.1}$$

Eq. 4.1 is often used to describe enzyme kinetics where a substrate binds irreversibly to an enzyme in solution [46] but it can also be used to describe protein binding reactions such as the biotin-avidin interaction, where y is the relative shift in wavelength corresponding to avidin binding to sensor surface, B_{max} represents the maximum relative shift in wavelength, which is directly proportional to the maximum binding capacity of the biotin functionalised sensor, x is the avidin concentration and K_d is the dissociation constant that represents the avidin concentration for which the number of avidin molecules bound to the sensor surface results in a shift of $B_{max}/2$. Since the avidin-biotin interaction does not involve a catalytic step, the calculation of the association and dissociation constant follows a Langmuir relationship, described in Section 2.2.4. The avidin limit of detection for a PEI-biotin functionalised DFB laser sensor was ≈5 μg.mL^{-1} with a dissociation constant of 2.0^{-7} M, the R-squared value for the fit to the data was 0.83.

In order to test the specificity of avidin detection, an avidin binding assay was performed on a DFB laser sensor functionalised with PEI alone. As PEI is cationic, it was expected that positively charged avidin would not non-specifically adsorb to the PEI layer as it should be repelled by electrostatic forces. A 100 μg.mL^{-1} avidin solution, chosen as it results in a maximum shift in wavelength for a biotin coated sensor, produced a negative shift in wavelength (-0.12 nm). This relatively large negative shift is presumably due to the extra immersion of the laser sensor in various solutions which may remove more unbound PEI than the standard single wash. The negative shift in wavelength indicates that avidin does not bind to the surface of a PEI coated laser in the absence of subsequent biotin functionalisation, therefore avidin binding to a PEI-biotin functionalised sensor is specific.

4.4.2.2 PPL functionalisation

As mentioned previously, PPL was investigated as an alternative polyelectrolyte layer to PEI as it contains an aromatic phenylalanine group which was hypothesised to improve the coverage of the laser surface with polyelectrolyte, and therefore improve biotin coupling and increase the number of biotin binding sites. Aromatic rings, such as those in phenylalanine and T3, are known to demonstrate a type of intermolecular attraction to one another, often referred to a π-stacking or π-π interactions

Replacing the initial PEI base layer with PPL resulted in an average relative shift in emission wavelength, due to biotin binding to the PPL coated surface, of 0.28±0.09 nm.

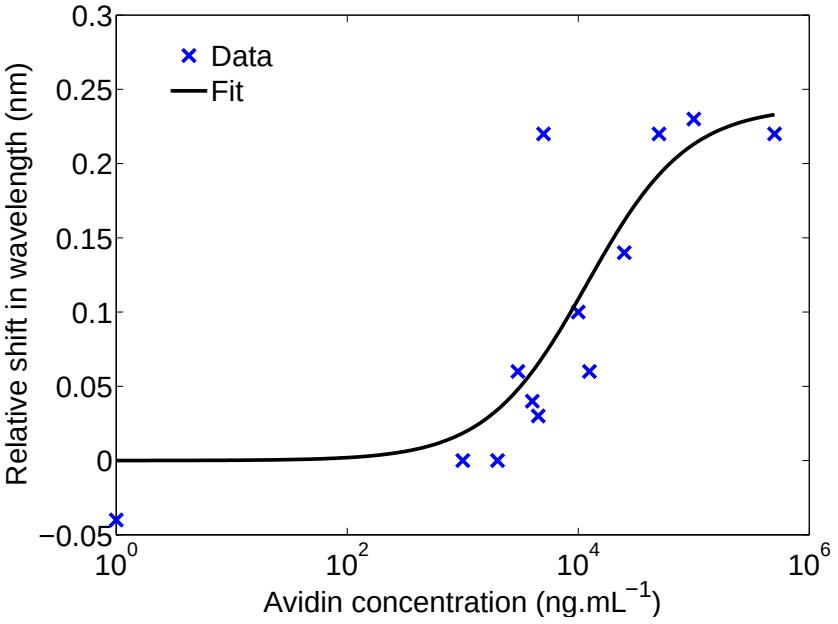

FIGURE 4.11: Specific avidin detection with PEI providing amine functionality for biotin coupling.

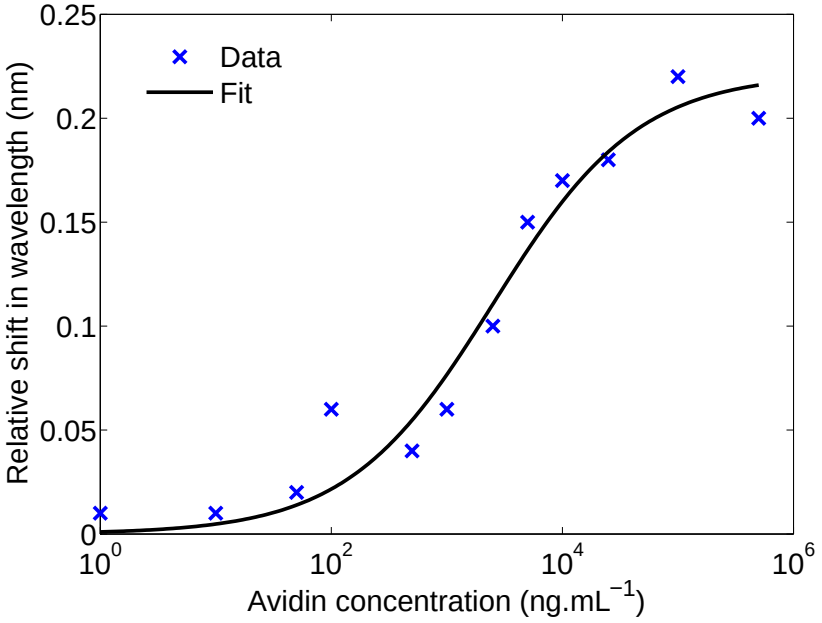

FIGURE 4.12: Specific avidin detection with PPL providing amine functionality for biotin coupling.

Figure 4.12 shows the relative shift in wavelength for each avidin concentration for PPL-biotin functionalised sensors. There was an improvement in the fit to the data, relative to the fit of data for a PEI-biotin coated sensor, with an R-squared value of 0.98. The avidin limit of detection for a PPL-biotin functionalised laser sensor was $\approx$1 μg.mL^{-1}, which is almost five times lower than the avidin limit of detection for a laser sensor with PEI as the initial monolayer and the corresponding dissociation constant was 3.6^{-8} M.

The specificity of avidin binding was investigated by immersing a PPL functionalised laser in a 25 μg.mL^{-1} avidin solution. This concentration was at the saturation point of avidin detection for a PPL-biotin functionalised sensor. As for the PEI control, there was a negative (-0.17 nm) shift in emission wavelength upon removal of the avidin solution, indicative of specific binding to the biotin-functionalised monolayer.

4.4.2.3 PL functionalisation

In order to test the hypothesis that the order of magnitude improvement in the limit of detection of avidin when PPL was used in place of PEI was due to the π-stacking of the phenyl substituents of the phenylalanine groups on the T3 surface, PPL was replaced with PL. The relative shift in emission wavelength for biotin binding at the surface of a PL functionalised sensor was significantly lower than that for a PEI and PPL functionalised sensor, at 0.07$\pm$0.07 nm. In addition, there was a significant increase in the variability of the shift in wavelength produced by biotin binding. The variability in biotin binding may be because the initial PL layer may not be a confluent, uniform monolayer for each sensor, therefore reducing the density of available amine binding sites which in turn results in a marked increase in variability from sensor to sensor. The avidin detection data for a PL-biotin functionalised sensor is shown in Figure 4.13 where the avidin limit of detection was $\approx$50 μg.mL^{-1}, an order of magnitude higher than the avidin limit of detection when the sensor was functionalised with PEI and two orders of magnitude higher than when PPL was used. The associated dissociation constant was 6.9^{-7} M. The data also produced a poor fit to Eq. 4.1, with an R-squared value of 0.80, and a decrease in the dynamic range for avidin detection.

4.4.2.4 Comparison of the effect of adsorption on specific avidin sensing

Functionalisation of the sensor with PPL resulted in the lowest avidin limit of detection; the results are summarised in Table 4.2. A base layer of PEI resulted in an order of magnitude increase in avidin limit of detection, relative to that of PPL, at 1 μg.mL^{-1} and a limit of detection of 50 μg.mL^{-1} when PL was used. The differences in the limit of detection values correlate with the relative shift in emission wavelength attributed to biotin coupling. A redshift in emission wavelength is a result of an increase in the effective refractive index of the sensor, as described in Eq. 1.1. Therefore, the area density of biotin molecules bound to the sensor surface correlates to the magnitude of the relative shift in wavelength detected, i.e. higher levels of biotin coupling result in a greater redshift in emission wavelength. The greatest relative shift in emission wavelength for biotin coupling, 0.28$\pm$0.09 nm, was observed when PPL was used as the

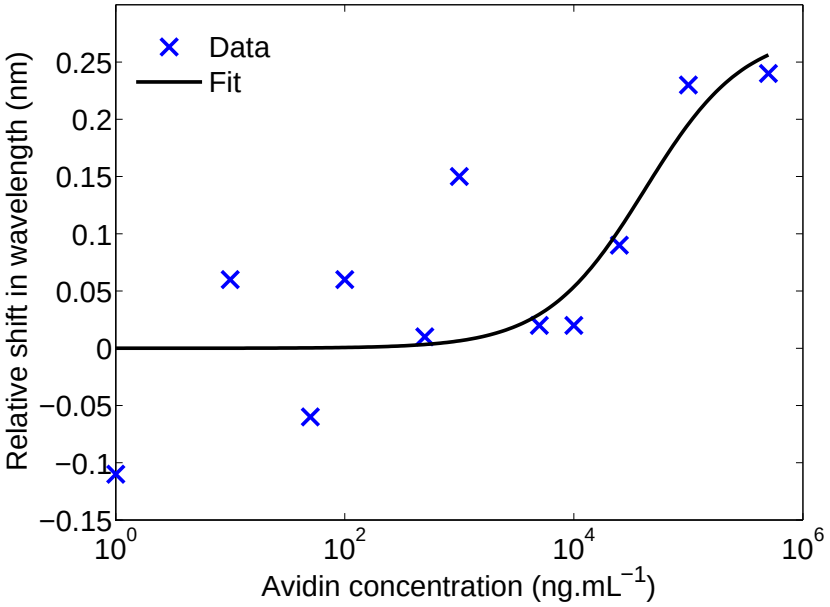

FIGURE 4.13: Specific avidin detection with PL providing amine functionality for biotin coupling.

base polyelectrolyte layer and the smallest shift, 0.07±0.07 nm, was observed when PL was used. Therefore, it is reasonable to infer that the sensor surface is functionalised with the greatest number of biotin molecules when PPL is used as the polyelectrolyte base layer.

Polyelectrolyte	**Relative shift in wavelength for biotin coupling (nm)**	**Avidin limit of detection (μg.mL^{-1})**	**Dissociation const. (M)**
PEI	0.17±0.07	5	2.0^{-7}
PPL	0.28±0.09	1	3.6^{-8}
PL	0.07±0.07	50	6.9^{-7}

TABLE 4.2: Relative shift in wavelength due to biotin coupling to sensors functionalised with PEI, PPL or PL, the corresponding avidin limit of detection for each of those sensors and the dissociation constants extracted from the fit to the data (Eq. 4.1).

4.4.2.5 Comparison of T3 DFB laser specific biosensing with dye-doped DFB lasers

The aim of T3 DFB laser sensor surface functionalisation is to develop a sensor that can be used for the specific detection of biomolecules, such as cardiac biomarkers. In Chapter 1, an overview of the specific sensing capabilities of dye-doped DFB lasers was provided. To recapitulate, specific biomolecule detection has been demonstrated with Rhodamine based DFB lasers. TNF-α and Human IgG antibody detection was reported with detection limits of 0.6 μg.mL^{-1} and ≈0.5 μg.mL^{-1} respectively [49, 50]. It is difficult to make a direct comparison between avidin detection and TNFα/IgG

detection due to the differences in the nature of the binding assays, such as binding affinity, etc., but the avidin detection limit of 1 μg.mL is of a similar magnitude to the detection limits for the dye-doped lasers. It should be noted that the Rhodamine based lasers incorporate a TiO_2 cladding layer on top of the dye gain layer, which serves to increase the overlap of the laser mode with the biomolecule sensing region and therefore improves the sensitivity of those lasers relative to lasers without the TiO_2 cladding layer. When a T3 DFB laser is modelled with a similar TiO_2 layer, the limit of detection for specific avidin binding decreases by over half, suggesting that there may be some benefit in the inclusion of a similar cladding layer atop the T3 gain layer surface. This is discussed further in Chapter 5.

4.4.2.6 Avidin sensing results predicted by the theoretical model

In order to determine how well the experimental specific sensing results align with what is predicted theoretically, the sensing results for PPL-biotin functionalised lasers were compared to modelled values using the modified multilayer slab waveguide model (Chapter 2). The avidin sensing data presented in previous sections were fitted using Eq. 4.1 which describes the biotin-avidin interaction and corresponds to Langmuir adsorption. By assuming a Langmuir relationship for avidin binding to the biotinylated laser, the refractive index of the avidin layer can be modelled by solving Eq. 4.2, Eq. 4.3 and Eq. 4.4 (reproductions of Eq. 2.21, Eq. 2.22 and Eq. 2.23 respectively) as described in Chapter 2, where ϵ_1, ϵ_2 and ϵ_{av} are the dielectric permitivity of the buffer, biomolecule and biolayer average, p represents the fraction of bound target biomolecules and is dependent on the avidin concentration, x, and B represents saturation of the available binding sites and is set equal to 1.

$$(1-p)\frac{\epsilon_1-\epsilon_{av}}{\epsilon_1+2\epsilon_{av}}+p\frac{\epsilon_2-\epsilon_{av}}{\epsilon_2+2\epsilon_{av}}=0 \tag{4.2}$$

$$p(x)=B\frac{x}{K+x} \tag{4.3}$$

$$n_{bio}(p)=\sqrt{\epsilon(p)} \tag{4.4}$$

The model inputs are the refractive indices and thickness of the T3, PPL and biotin layers, the refractive indices of the avidin molecules and the PBS buffer, and the avidin concentration. By solving Eq. 4.2 for each avidin concentration, the refractive index of the avidin layer (composed of avidin molecules and buffer) can be determined and used

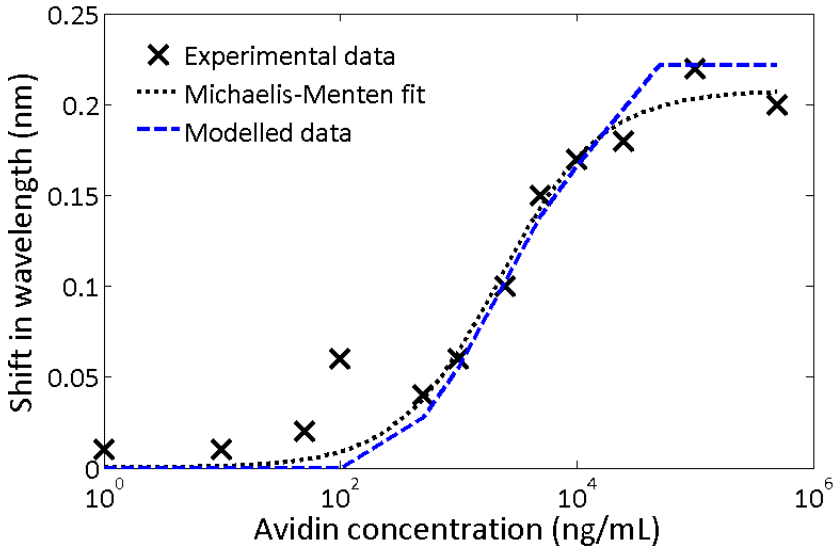

FIGURE 4.14: Experimental and modelled data for the specific detection of avidin on a PPL-biotin functionalised T3 laser.

to calculate the magnitude of the shift in wavelength resulting from the presence of the avidin layer. Figure 4.14 shows the experimental avidin sensing data from Figure 4.12, plotted alongside the expected theoretical data produced by the model.

As Figure 4.14 shows, the modelled data closely follows the experimental data. The fit to the data provides a dissociation constant of $3.6\text{x}10^{-8}$ M which is lower than that provided by the model at $4.5\text{x}10^{-8}$ M, demonstrating excellent agreement between the modelled and experimental data. Modelling the response of the laser to biomolecule binding will be very useful in the future development of the DFB laser biosensor as it provides an indication of the magnitude of the shift expected for an array of different biomolecules. The effect of modifications to the laser structure on biosensing can also be probed using the model and is discussed for the inclusion of a TiO_2 cladding layer on the T3 surface in Section 5.2.

4.5 Reversible avidin detection - multi-use sensor?

In medical applications, biosensors tend to be single-use, disposable devices. For those cardiac biosensing devices described in Chapter 1, the biosensor element that comes into contact with the test solution is disposable. There are obvious reasons why this is the case in terms of maintaining the sterility of the test strip and the simplicity for the end user. However, there are occasions where a re-usable biosensor may be beneficial. For example, a re-usable sensor will be an attractive sensing platform in applications where large numbers of measurements (hundreds or thousands) are required in order to generate statistically significant data sets, such as in environmental monitoring and food

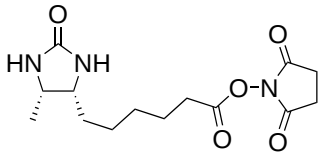

FIGURE 4.15: Structure of NHS-desthiobiotin.

safety [51, 52], where the costs involved in using a single-use sensor may be prohibitive. Therefore, the multi-use potential of the T3 DFB laser was investigated.

The interaction between avidin and biotin is one of the strongest known non-covalent interactions and only harsh reaction conditions, such as extremes of pH and temperature, will result in the release of a biotin bound avidin molecule. Therefore, under physiological reaction conditions, avidin binding is essentially irreversible. However, an analogue to biotin exists that binds less tightly to avidin. This analogue is desthiobiotin, the structure of which is shown in Figure 4.15 [53]. Desthiobiotin has a binding affinity to avidin of 10^{11} M^{-1} (biotin is 10^{15} M^{-1}). Therefore, as a desthiobiotin bound avidin molecule will have a stronger attraction to biotin, it was expected that avidin would be released from a desthiobiotin functionalised surface when in the presence of biotin [54]. To test this hypothesis, desthiobiotin was used in place of biotin to functionalise the laser surface and specific avidin sensing was performed. The reversible nature of avidin sensing was probed by exposing a desthiobiotin-avidin surface to biotin and the re-usability of the DFB laser was investigated.

4.5.1 Experimental methods

T3 DFB lasers were functionalised with PPL and desthiobiotin as described in Section 4.4.1 for a PPL functionalised sensor. To prepare the NHS-desthiobiotin solution, NHS-desthiobiotin was dissolved in dimethyl sulfoxide (DMSO); this is necessary as NHS-desthiobiotin is not water soluble. DMSO was tested with the T3 lasers and was shown to have no effect, up to a concentration of 10%, on the T3 surface, which was initially a concern given the response of the laser upon exposure to methanol. NHS-desthiobiotin, in DMSO, was added to 10 mM PBS to a concentration of 0.2 $mg.mL^{-1}$, with a final DMSO concentration of 2% v/v.

10 mM PBS solution was used for all wash steps prior to and following immersion of the sensor in avidin/biotin. The relative shift in emission wavelength for the demonstration of reversible avidin sensing and for determining the avidin limit of detection was obtained as described in Section 4.4.1.

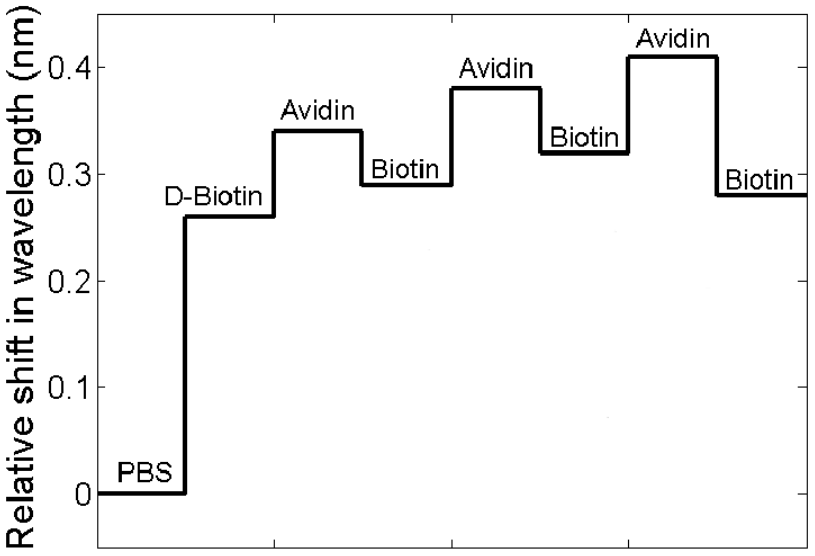

(a)

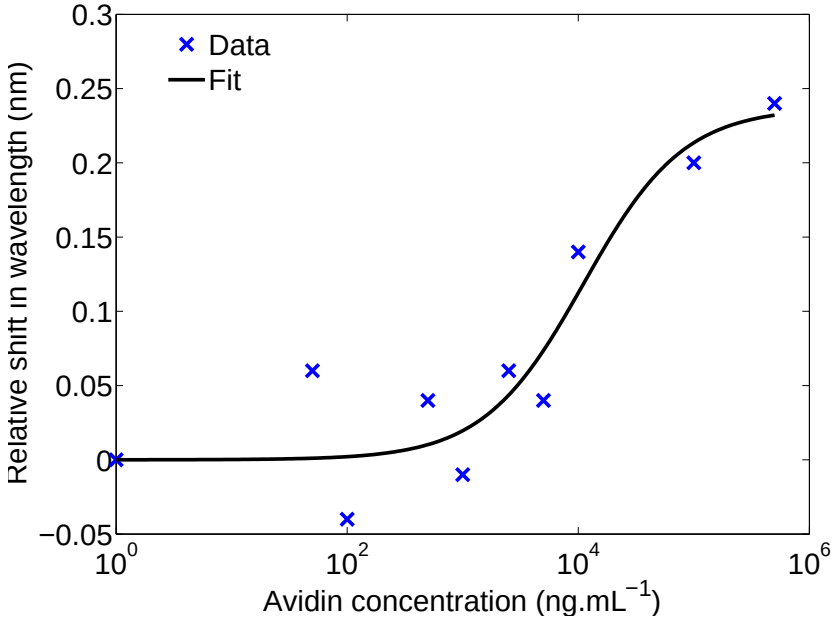

(b)

FIGURE 4.16: (a) Repeated avidin sensing and regeneration of the surface, via exposure to biotin, and (b) specific avidin detection with a PPL-desthiobiotin functionalised laser.

4.5.2 Reversible sensing results

As the lowest avidin limit of detection was achieved for a laser functionalised with an initial layer of PPL, PPL was the polyelectrolyte used to investigate the capacity of reversible binding of desthiobiotin-avidin binding using the T3 DFB lasers. Figure 4.16a shows the reversibility of avidin coupling to desthiobiotin. Relative shifts in wavelength of 0.08, 0.09 and 0.09 nm were observed after each exposure to avidin solution (10 μg.mL^{-1}), respectively. Upon removal of avidin solution and a PBS wash, the sensor

was immersed in a biotin solution (0.2 mg.mL^{-1}) where the associated relative shifts in wavelength after exposure to the biotin solutions were -0.05, -0.06 and -0.13 nm, respectively. Figure 4.16a clearly shows that most of the avidin bound to the desthiobiotin functionalised sensor was removed after immersion in the biotin solution and that avidin binding to the desthiobiotin layer was reproducible. When biotin was used in place of desthiobiotin, the addition of biotin after avidin binding resulted in no change in the emission wavelength from the sensor, indicating that there was no removal of avidin from the sensor and no detectable biotin binding.

As the binding affinity between a desthiobiotin functionalised surface and avidin is lower than that of a biotin functionalised surface, it was expected that the limit of detection for avidin binding would be higher. To test this hypothesis, the avidin detection assay was also performed using a PPL-desthiobiotin functionalised sensor. Figure 4.16b shows the relative shift in wavelength for each avidin concentration for PPL-desthiobiotin functionalised sensors. The average relative shift in wavelength due to desthiobiotin binding to the PPL surface was 0.14±0.08 nm. The data in Figure 4.16b was fitted to the Eq. 4.1 and an R-squared value of 0.94 was observed. The limit of detection for a PPL-desthiobiotin functionalised sensor was 2.5 μg.mL^{-1}, between that of a PEI-biotin and PPL-biotin functionalised sensor and the dissociation constant was 1.8^{-7} M. Therefore, specific and reversible avidin detection can be achieved through the replacement of biotin with desthiobiotin for the functionalisation of the laser sensor. Also, not surprisingly, due to the reduced affinity between desthiobiotin and avidin, the avidin limit of detection was lower than that of a PPL-biotin functionalised laser.

4.6 Non-specific adsorption investigation

The difference between the surface sensing results presented in Chapter 3 and the avidin sensing results in this chapter is the specificity of the reaction between the laser surface and the avidin molecules. Adsorption of all molecules to the laser surface will result in a shift of the laser emission wavelength. Therefore binding of all molecules except the target must be prevented to minimise false positive binding results. To investigate the specificity of avidin detection with the PPL-biotin functionalised laser, binding assays were preformed in the presence of BSA. Albumin is a protein found at concentrations within the range of 3.5-5 mg.mL^{-1} [55] in healthy individuals, and therefore it has the potential to interfere with specific biomarker detection in serological solutions.

To determine the effect of non-specific adsorption to the laser surface, PPL and PPL-biotin functionalised lasers were exposed to different concentrations of BSA solutions.

The effect of BSA on avidin sensing was also investigated by performing a competition assay with BSA solutions spiked with a known concentration of avidin in order to compare avidin detection with and without the presence of BSA.

4.6.1 Experimental methods

The non-specific adsorption of BSA to a PPL and PPL-biotin functionalised sensor was investigated for four BSA concentrations (1, 10, 500 and 50000 μg.mL^{-1}). BSA solutions were prepared in 10 mM PBS. Sensors were coated with PPL as previously described in Section 4.4.1. The emission wavelength with the sensor immersed in PBS was recorded. A BSA solution was then added to the cuvette and the emission wavelength recorded. After 20 minutes, the emission wavelength was recorded again before removing the BSA solution from the cuvette. The sensor was washed with PBS before a final emission wavelength was noted with the sensor immersed in PBS. This was repeated for each BSA concentration, with a new sensor for each measurement, and was performed in triplicate for each BSA concentration. The procedure was also repeated for a PPL-biotin functionalised sensor.

Competition assays using BSA and avidin were performed with a PPL-biotin functionalised laser sensor. A range of BSA concentrations (1 - 50000 μg.mL^{-1}), containing 2.5 μg.mL^{-1} avidin, were prepared in 10 mM PBS. The relative shift in wavelength due to BSA and/or avidin was determined in the same way as described for BSA.

4.6.2 Non-specific adsorption interference results

Figure 4.17a shows the mean response of the T3 sensor, functionalised with either PPL or PPL-biotin, after exposure to BSA solutions of varying concentrations. BSA has a pI of 4.7 and is thus negatively charged at pH 7.4. As a result, a significant redshift in emission wavelength was attributed to non-specific adsorption of BSA to the positively charged surface of a PPL coated laser. There was a reduction in the shift in wavelength across all BSA concentrations for PPL-biotin functionalised lasers, presumably as consequence of the biotin layer masking the positive charge of the underlying PPL layer. We assume that this suppresses the electrostatic attraction between the positively charged PPL and negative BSA, which in turn suppresses the non-specific adsorption of BSA to the sensor surface [56].

The effect of non-specific adsorption of BSA on specific avidin sensing with PPL-biotin functionalised sensor was investigated by performing a competition assay with BSA solutions. No increase in emission wavelength as a function of increasing BSA concentration

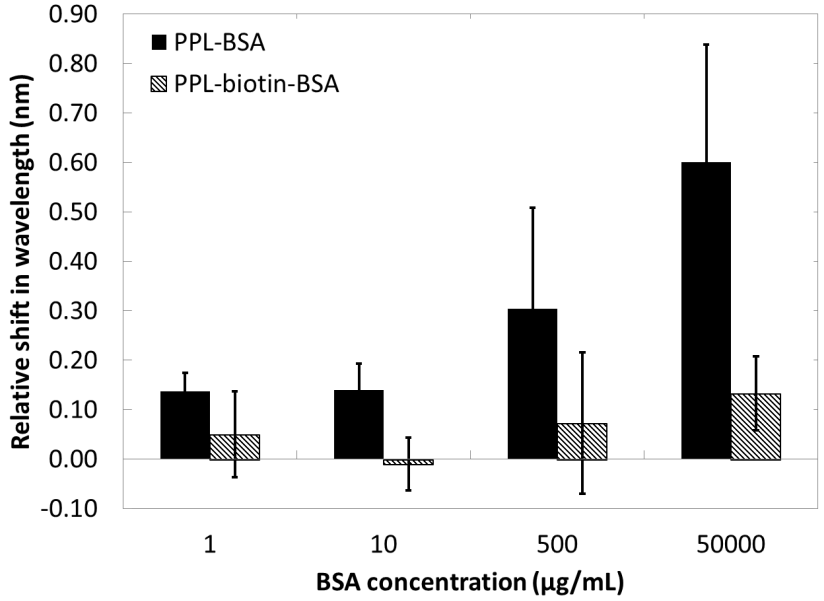

(a)

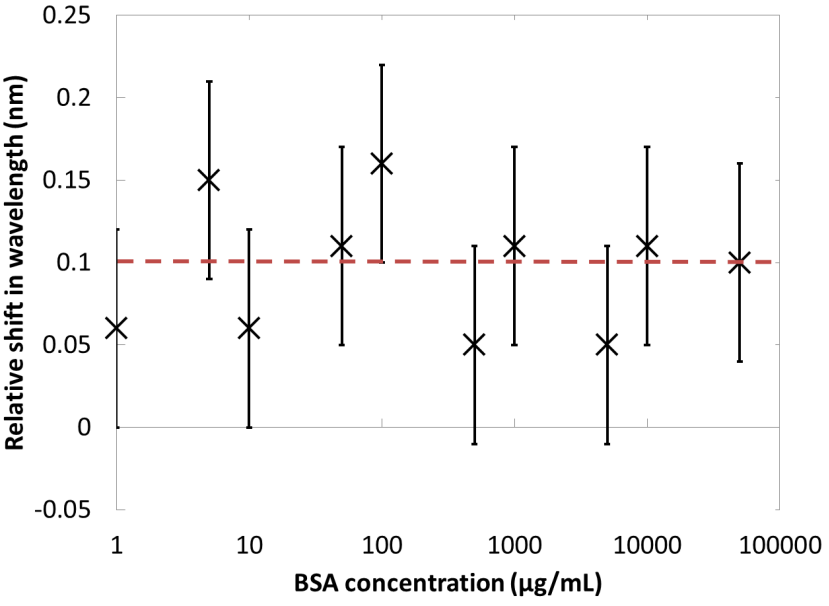

(b)

FIGURE 4.17: (a) Non-specific adsorption of BSA to PPL and PPL-biotin functionalised T3 lasers. (b) Avidin detection in the presence of BSA. The red dashed line represents the shift in wavelength due to avidin binding (2.5 μg.mL^{-1}) to a PPL-biotin functionalised laser.

was observed. The average shift in emission wavelength was 0.09±0.04 nm. These values correspond to the relative shifts in emission wavelengths observed for detection of 2.5 μg.mL^{-1} avidin with a PPL-biotin functionalised laser in the absence of BSA (Figure 4.12). It was therefore concluded that the presence of BSA did not affect the specific detection of avidin even at concentrations comparable to those found in serological samples, and that there was no detectable non-specific adsorption of BSA in the presence of avidin at a concentration of 2.5 μg.mL^{-1}. This is an important observation in downstream optimisation of the specificity of the DFB laser sensor for specific biosensing applications.

4.7 Summary

The specific biosensing potential of the T3 based laser biosensors was established through the use of the biotin-avidin interaction system. Three polyelectrolytes were investigated in order to verify which provided the maximum surface coverage with biotin molecules and when PPL was used, a minimum avidin concentration of 1 μg.mL^{-1} could be detected. Avidin detection with the biotinylated laser surface was shown to be specific and was not affected by the presence of albumin, an encouraging result since albumin is found in abundance in blood. The avidin detection limit is comparable to the detection limits for other DFB lasers used for biosensing and there is the potential to improve the sensitivity of the T3 laser further through modifications to the laser structure.

Finally, the first demonstration of reversible biosensing with a DFB laser was exhibited through replacement of biotin with desthiobiotin for reversible avidin coupling. A reusable sensor can be beneficial in a variety of industries, therefore indicating the potential of the T3 laser sensor for applications out-with clinical diagnostics.

References

[1] Vincent Dugas, Abdelhamid Elaissari, and Yves Chevalier. Surface sensitization techniques and recognition receptors immobilization on biosensors and microarrays. In Mohammed Zourob, editor, *Recognition Receptors in Biosensors*, pages 47–134. Springer New York, 2010. ISBN 978-1-4419-0918-3. doi: 10.1007/978-1-4419-0919-0_2. URL http://dx.doi.org/10.1007/978-1-4419-0919-0_2.

[2] Anthony D Keefe, Supriya Pai, and Andrew Ellington. Aptamers as therapeutics. *Nature Reviews Drug Discovery*, 9(7):537–550, 2010.

[3] N. Michael Green. volume 29 of *Advances in Protein Chemistry*, pages 85 – 133. Academic Press, 1975. doi: http://dx.doi.org/10.1016/S0065-3233(08)60411-8. URL http://www.sciencedirect.com/science/article/pii/S0065323308604118.

[4] Jenni Leppiniemi, Juha A. E. Mtt, Henrik Hammaren, Mikko Soikkeli, Mikko Laitaoja, Janne Jnis, Markku S. Kulomaa, and Vesa P. Hytnen. Bifunctional avidin with covalently modifiable ligand binding site. *PLoS ONE*, 6(1):e16576, 01 2011. doi: 10.1371/journal.pone.0016576. URL http://dx.doi.org/10.1371%2Fjournal.pone.0016576.

[5] E P Diamandis and T K Christopoulos. The biotin-(strept)avidin system: principles and applications in biotechnology. *Clinical Chemistry*, 37(5):625–36, 1991. URL http://www.clinchem.org/content/37/5/625.abstract.

[6] Eleftherios P. Diamandis and Robert C. Morton. Time-resolved fluorescence using a europium chelate of 4,7-bis-(chlorosulfopheny1)-1,10-phenanthroline-2,9-dicarboxylic acid (bcpda): Labeling procedures and applications in immunoassays. *Journal of Immunological Methods*, 112(1):43 – 52, 1988. ISSN 0022-1759. doi: http://dx.doi.org/10.1016/0022-1759(88)90031-2. URL http://www.sciencedirect.com/science/article/pii/0022175988900312.

[7] E.A. Gould, A. Buckley, and N. Cammack. Use of the biotin-streptavidin interaction to improve flavivirus detection by immunofluorescence and {ELISA} tests. *Journal of Virological Methods*, 11 (1):41 – 48, 1985. ISSN 0166-0934. doi: http://dx.doi.org/10.1016/0166-0934(85)90123-5. URL http://www.sciencedirect.com/science/article/pii/0166093485901235.

[8] Mark N. Bobrow, Thomas D. Harris, Krista J. Shaughnessy, and Gerald J. Litt. Catalyzed reporter deposition, a novel method of signal amplification application to immunoassays. *Journal of Immunological Methods*, 125(12):279 – 285, 1989. ISSN 0022-1759. doi: http://dx.doi.org/10.1016/0022-1759(89)90104-X. URL http://www.sciencedirect.com/science/article/pii/002217598990104X.

[9] K Hofmann, S W Wood, C C Brinton, J A Montibeller, and F M Finn. Iminobiotin affinity columns and their application to retrieval of streptavidin. *Proceedings of the National Academy of Sciences*, 77(8):4666–4668, 1980. URL http://www.pnas.org/content/77/8/4666.abstract.

[10] Mengsu Yang, Hellas C. M. Yau, and Hing Leung Chan. Adsorption kinetics and ligand-binding properties of thiol-modified double-stranded dna on a gold surface. *Langmuir*, 14(21):6121–6129, 1998. doi: 10.1021/la980577i. URL http://pubs.acs.org/doi/abs/10.1021/la980577i.

[11] Edy Wijaya, Cdric Lenaerts, Sophie Maricot, Juriy Hastanin, Serge Habraken, Jean-Pierre Vilcot, Rabah Boukherroub, and Sabine Szunerits. Surface plasmon resonance-based biosensors: From the development of different {SPR} structures to novel surface functionalization strategies. *Current Opinion in Solid State and Materials Science*, 15(5):208 – 224, 2011. ISSN 1359-0286. doi: http://dx.doi.org/10.1016/j.cossms.2011.05.001. URL http://www.sciencedirect.com/science/article/pii/S1359028611000325.

[12] Liviu Nicu and Thierry Lechl. Biosensors and tools for surface functionalization from the macro- to the nanoscale: The way forward. *Journal of Applied Physics*, 104(11):111101, 2008. doi: http://dx.doi.org/10.1063/1.2973147. URL http://scitation.aip.org/content/aip/journal/jap/104/11/10.1063/1.2973147.

[13] Christian F. Wertz and Maria M. Santore. Effect of surface hydrophobicity on adsorption and relaxation kinetics of albumin and fibrinogen: single-species and competitive behavior. *Langmuir*, 17(10):3006–3016, 2001. doi: 10.1021/la0017781. URL http://pubs.acs.org/doi/abs/10.1021/la0017781.

[14] Martin Malmsten. Formation of adsorbed protein layers. *Journal of Colloid and Interface Science*, 207(2):186 – 199, 1998. ISSN 0021-9797. doi: http://dx.doi.org/10.1006/jcis.1998.5763. URL http://www.sciencedirect.com/science/article/pii/S0021979798957630.

[15] Thorsten Fischer and Henry Hess. Materials chemistry challenges in the design of hybrid bionanodevices: supporting protein function within artificial environments. *J. Mater. Chem.*, 17:943–951, 2007. doi: 10.1039/B615278C. URL http://dx.doi.org/10.1039/B615278C.

[16] Johannes Schmitt, Torsten Gruenewald, Gero Decher, Peter S. Pershan, Kristian Kjaer, and Mathias Loesche. Internal structure of layer-by-layer adsorbed polyelectrolyte films: a neutron and x-ray reflectivity study. *Macromolecules*, 26(25):7058–7063, 1993. doi: 10.1021/ma00077a052. URL http://pubs.acs.org/doi/abs/10.1021/ma00077a052.

[17] Mathias Lsche, Johannes Schmitt, Gero Decher, Wim G. Bouwman, and Kristian Kjaer. Detailed structure of molecularly thin polyelectrolyte multilayer films on solid substrates as revealed by neutron reflectometry. *Macromolecules*, 31(25):8893–8906, 1998. doi: 10.1021/ma980910p. URL http://pubs.acs.org/doi/abs/10.1021/ma980910p.

[18] Thomas Schiestel, Herwig Brunner, and Gnter E.M. Tovar. Controlled surface functionalization of silica nanospheres by covalent conjugation reactions and preparation of high density streptavidin nanoparticles. *Journal of Nanoscience and Nanotechnology*, 4(5):504–511, 2004-05-01T00:00:00. doi: doi:10.1166/jnn.2004.079. URL http://www.ingentaconnect.com/content/asp/jnn/2004/00000004/00000005/art00006.

[19] Christophe Blaszykowski, Sonia Sheikh, and Michael Thompson. Surface chemistry to minimize fouling from blood-based fluids. *Chem. Soc. Rev.*, 41:5599–5612, 2012. doi: 10.1039/C2CS35170F. URL http://dx.doi.org/10.1039/C2CS35170F.

[20] Debasis Samanta and Amitabha Sarkar. Immobilization of bio-macromolecules on self-assembled monolayers: methods and sensor applications. *Chem. Soc. Rev.*, 40:2567–2592, 2011. doi: 10.1039/C0CS00056F. URL http://dx.doi.org/10.1039/C0CS00056F.

[21] Nikin Patel, Martyn C. Davies, Mark Hartshorne, Richard J. Heaton, Clive J. Roberts, Saul J. B. Tendler, and Philip M. Williams. Immobilization of protein molecules onto homogeneous and mixed carboxylate-terminated self-assembled monolayers. *Langmuir*, 13(24):6485–6490, 1997. doi: 10.1021/la970933h. URL http://pubs.acs.org/doi/abs/10.1021/la970933h.

[22] Pedro Cuatrecasas and Indu Parikh. Adsorbents for affinity chromatography. use of n-hydroxysuccinimide esters of agarose. *Biochemistry*, 11(12):2291–2299, 1972. doi: 10.1021/bi00762a013. URL http://pubs.acs.org/doi/abs/10.1021/bi00762a013.

[23] James V. Staros. N-hydroxysulfosuccinimide active esters: bis(n-hydroxysulfosuccinimide) esters of two dicarboxylic acids are hydrophilic, membrane-impermeant, protein cross-linkers. *Biochemistry*, 21(17):3950–3955, 1982. doi: 10.1021/bi00260a008. URL http://pubs.acs.org/doi/abs/10.1021/bi00260a008.

[24] Brian Cunningham, Bo Lin, Jean Qiu, Peter Li, Jane Pepper, and Brenda Hugh. A plastic colorimetric resonant optical biosensor for multiparallel detection of label-free biochemical interactions. *Sensors and Actuators B: Chemical*, 85(3):219 – 226, 2002. ISSN 0925-4005. doi: http://dx.doi.org/10.1016/S0925-4005(02)00111-9. URL http://www.sciencedirect.com/science/article/pii/S0925400502001119.

[25] V. Dumont, A.-C. Huet, I. Traynor, C. Elliott, and P. Delahaut. A surface plasmon resonance biosensor assay for the simultaneous determination of thiamphenicol, florefenicol, florefenicol amine and chloramphenicol residues in shrimps. *Analytica Chimica Acta*, 567(2):179 – 183, 2006. ISSN 0003-2670. doi: http://dx.doi.org/10.1016/j.aca.2006.03.028. URL http://www.sciencedirect.com/science/article/pii/S0003267006005587.

[26] Manihar Situmorang, J.Justin Gooding, D.Brynn Hibbert, and Donald Barnett. Electrodeposited polytyramine as an immobilisation matrix for enzyme biosensors. *Biosensors and Bioelectronics*, 13 (9):953 – 962, 1998. ISSN 0956-5663. doi: http://dx.doi.org/10.1016/S0956-5663(98)00033-5. URL http://www.sciencedirect.com/science/article/pii/S0956566398000335.

[27] Sami Ameur, Claude Martelet, Nicole Jaffrezic-Renault, and Jean-Marc Chovelon. Sensitive immunodetection through impedance measurements onto gold functionalized electrodes. *Applied Biochemistry and Biotechnology*, 89(2-3):161–170, 2000. ISSN 0273-2289. doi: 10.1385/ABAB:89:2-3:161. URL http://dx.doi.org/10.1385/ABAB%3A89%3A2-3%3A161.

[28] Benjamin T. Houseman, Ellen S. Gawalt, and Milan Mrksich. Maleimide-functionalized self-assembled monolayers for the preparation of peptide and carbohydrate biochips. *Langmuir*, 19 (5):1522–1531, 2003. doi: 10.1021/la0262304. URL http://pubs.acs.org/doi/abs/10.1021/la0262304.

[29] J. Jefferson Smith, David W. Conrad, Matthew J. Cuneo, and Homme W. Hellinga. Orthogonal site-specific protein modification by engineering reversible thiol protection mechanisms. *Protein Science*, 14(1):64–73, 2005. ISSN 1469-896X. doi: 10.1110/ps.04965405. URL http://dx.doi.org/10.1110/ps.04965405.

[30] G. Mattson, E. Conklin, S. Desai, G. Nielander, M.D. Savage, and S. Morgensen. A practical approach to crosslinking. *Molecular Biology Reports*, 17(3):167–183, 1993. ISSN 0301-4851. doi: 10.1007/BF00986726. URL http://dx.doi.org/10.1007/BF00986726.

[31] J Carlsson, H Drevin, and R Axn. Protein thiolation and reversible protein-protein conjugation. n-succinimidyl 3-(2-pyridyldithio)propionate, a new heterobifunctional reagent. *Biochem. J.*, 173 (3):723–737, 1978. URL http://www.biochemj.org/bj/173/bj1730723.htm.

[32] JeremyM. Baskin and CarolynR. Bertozzi. Bioorthogonal click chemistry: Covalent labeling in living systems. *QSAR Combinatorial Science*, 26(11-12):1211–1219, 2007. ISSN 1611-0218. doi: 10.1002/qsar.200740086. URL http://dx.doi.org/10.1002/qsar.200740086.

[33] Hartmuth C. Kolb, M. G. Finn, and K. Barry Sharpless. Click chemistry: Diverse chemical function from a few good reactions. *Angewandte Chemie International Edition*, 40(11):2004–2021, 2001. ISSN 1521-3773. doi: 10.1002/1521-3773(20010601)40:11⟨2004::AID-ANIE2004⟩3.0.CO;2-5. URL http://dx.doi.org/10.1002/1521-3773(20010601)40:11<2004::AID-ANIE2004>3.0.CO;2-5.

[34] Neal K. Devaraj, Gregory P. Miller, Wataru Ebina, Boyko Kakaradov, James P. Collman, Eric T. Kool, and Christopher E. D. Chidsey. Chemoselective covalent coupling of oligonucleotide probes to self-assembled monolayers. *Journal of the American Chemical Society*, 127(24):8600–8601, 2005. doi: 10.1021/ja051462l. URL http://pubs.acs.org/doi/abs/10.1021/ja0514621.

[35] Dorota I. Rozkiewicz, Johannes Gierlich, Glenn A. Burley, Katrin Gutsmiedl, Thomas Carell, Bart Jan Ravoo, and David N. Reinhoudt. Transfer printing of dna by click chemistry. *ChemBioChem*, 8(16):1997–2002, 2007. ISSN 1439-7633. doi: 10.1002/cbic.200700402. URL http://dx.doi.org/10.1002/cbic.200700402.

[36] Lu Chen, Hernn R. Rengifo, Cristian Grigoras, Xiaoxu Li, Zengmin Li, Jingyue Ju, and Jeffrey T. Koberstein. Spin-on end-functional diblock copolymers for quantitative dna immobilization. *Biomacromolecules*, 9(9):2345–2352, 2008. doi: 10.1021/bm800258g. URL http://pubs.acs.org/doi/abs/10.1021/bm800258g.

[37] Vsevolod V. Rostovtsev, Luke G. Green, Valery V. Fokin, and K. Barry Sharpless. A stepwise huisgen cycloaddition process: Copper(i)-catalyzed regioselective ligation of azides and terminal alkynes. *Angewandte Chemie*, 114(14):2708–2711, 2002. ISSN 1521-3757. doi: 10.1002/1521-3757(20020715)114:14⟨2708::AID-ANGE2708⟩3.0.CO;2-0. URL http://dx.doi.org/10.1002/1521-3757(20020715)114:14<2708::AID-ANGE2708>3.0.CO;2-0.

[38] EllenM. Sletten and CarolynR. Bertozzi. Bioorthogonal chemistry: Fishing for selectivity in a sea of functionality. *Angewandte Chemie International Edition*, 48(38):6974–6998, 2009. ISSN 1521-3773. doi: 10.1002/anie.200900942. URL http://dx.doi.org/10.1002/anie.200900942.

[39] F. Vollmer, D. Braun, A. Libchaber, M. Khoshsima, I. Teraoka, and S. Arnold. Protein detection by optical shift of a resonant microcavity. *Applied Physics Letters*, 80(21):4057 –4059, may 2002. ISSN 0003-6951. doi: 10.1063/1.1482797.

[40] Jrg Wiedenmann, Sergey Ivanchenko, Franz Oswald, Florian Schmitt, Carlheinz Rcker, Anya Salih, Klaus-Dieter Spindler, and G. Ulrich Nienhaus. Eosfp, a fluorescent marker protein with uv-inducible green-to-red fluorescence conversion. *Proceedings of the National Academy of Sciences of the United States of America*, 101(45):15905–15910, 2004. doi: 10.1073/pnas.0403668101. URL http://www.pnas.org/content/101/45/15905.abstract.

[41] W A Hendrickson, A Phler, J L Smith, Y Satow, E A Merritt, and R P Phizackerley. Crystal structure of core streptavidin determined from multiwavelength anomalous diffraction of synchrotron radiation. *Proceedings of the National Academy of Sciences*, 86(7):2190–2194, 1989. URL http://www.pnas.org/content/86/7/2190.abstract.

[42] G. Raschke, S. Kowarik, T. Franzl, C. Snnichsen, T. A. Klar, J. Feldmann, A. Nichtl, and K. Krzinger. Biomolecular recognition based on single gold nanoparticle light scattering. *Nano Letters*, 3(7):935–938, 2003. doi: 10.1021/nl034223+. URL `http://pubs.acs.org/doi/abs/10.1021/nl034223%2B`.

[43] Ali H. Al-Hakim and Roger Hull. *Nucleic Acids Res.*, 14(24):9965–9976, 1986. doi: 10.1093/nar/14.24.9965. URL `http://nar.oxfordjournals.org/content/14/24/9965.abstract`.

[44] Moon Suk Kim, Kwang Su Seo, Gilson Khang, and Hai Bang Lee. *Langmuir*, 21(9):4066–4070, 2005. doi: 10.1021/la046868a. URL `http://pubs.acs.org/doi/abs/10.1021/la046868a`.

[45] A.-M. Haughey, B. Guilhabert, A.L. Kanibolotsky, P.J. Skabara, G.A. Burley, M.D. Dawson, and N. Laurand. An organic semiconductor laser based on star-shaped truxene-core oligomers for refractive index sensing. *Sensors and Actuators B: Chemical*, 185(0):132 – 139, 2013. ISSN 0925-4005. doi: http://dx.doi.org/10.1016/j.snb.2013.04.026. URL `http://www.sciencedirect.com/science/article/pii/S0925400513004589`.

[46] Alan D. Attie and Ronald T. Raines. *J. Chem. Educ.*, 72(2):119, 1995. doi: 10.1021/ed072p119. URL `http://pubs.acs.org/doi/abs/10.1021/ed072p119`.

[47] Franco Cozzi, Francesco Ponzini, Rita Annunziata, Mauro Cinquini, and Jay S. Siegel. Polar interactions between stacked systems in fluorinated 1,8-diarylnaphthalenes: Importance of quadrupole moments in molecular recognition. *Angewandte Chemie International Edition in English*, 34(9):1019–1020, 1995. ISSN 1521-3773. doi: 10.1002/anie.199510191. URL `http://dx.doi.org/10.1002/anie.199510191`.

[48] Chelsea R. Martinez and Brent L. Iverson. Rethinking the term "pi-stacking". *Chem. Sci.*, 3:2191–2201, 2012. doi: 10.1039/C2SC20045G. URL `http://dx.doi.org/10.1039/C2SC20045G`.

[49] Yafang Tan, Chun Ge, A. Chu, Meng Lu, W. Goldshlag, Cheng Sheng Huang, A. Pokhriyal, S. George, and B.T. Cunningham. Plastic-based distributed feedback laser biosensors in microplate format. *Sensors Journal, IEEE*, 12(5):1174 –1180, may 2012. ISSN 1530-437X. doi: 10.1109/JSEN.2011.2163933.

[50] M. Lu, S. S. Choi, U. Irfan, and B. T. Cunningham. Plastic distributed feedback laser biosensor. *Applied Physics Letters*, 93(11):111113 –111113–3, sep 2008. ISSN 0003-6951. doi: 10.1063/1.2987484.

[51] K.R. Rogers and J.N. Lin. Biosensors for environmental monitoring. *Biosensors and Bioelectronics*, 7(5):317 – 321, 1992. ISSN 0956-5663. doi: http://dx.doi.org/10.1016/0956-5663(92)85026-7. URL `http://www.sciencedirect.com/science/article/pii/0956566392850267`.

[52] Evangelyn C. Alocilja and Stephen M. Radke. Market analysis of biosensors for food safety. *Biosensors and Bioelectronics*, 18(56):841 – 846, 2003. ISSN 0956-5663. doi: http://dx.doi.org/10.1016/S0956-5663(03)00009-5. URL `http://www.sciencedirect.com/science/article/pii/S0956566303000095`. Selected papers from the Seventh World Congress on Biosensors Kyoto, Japan 15-17 May 2002.

[53] Ngo Yin Wong, Hang Xing, Li Huey Tan, and Yi Lu. *J. Am. Chem. Soc.*, 135(8):2931–2934, 2013. doi: 10.1021/ja3122284. URL `http://pubs.acs.org/doi/abs/10.1021/ja3122284`.

[54] James D Hirsch, Leila Eslamizar, Brian J Filanoski, Nabi Malekzadeh, Rosaria P Haugland, Joseph M Beechem, and Richard P Haugland. *Anal. Biochem.*, 308(2):343 – 357, 2002. ISSN 0003-2697. doi: http://dx.doi.org/10.1016/S0003-2697(02)00201-4. URL `http://www.sciencedirect.com/science/article/pii/S0003269702002014`.

[55] John P. Doweiko and Dominic J. Nompleggi. Reviews: Role of albumin in human physiology and pathophysiology. *Journal of Parenteral and Enteral Nutrition*, 15(2):207–211, 1991. doi: 10.1177/0148607191015002207. URL `http://pen.sagepub.com/content/15/2/207.abstract`.

[56] Elissa H. Williams, John A. Schreifels, Mulpuri V. Rao, Albert V. Davydov, Vladimir P. Oleshko, Nancy J. Lin, Kristen L. Steffens, Sergiy Krylyuk, Kris A. Bertness, Amy K. Manocchi, and Yaroslav Koshka. *J. Mater. Res.*, 28:68–77, 1 2013. ISSN 2044-5326. doi: 10.1557/jmr.2012.283.

Chapter 5

Towards biomarker detection and outlook

Following the successful proof-of-principle demonstration of specific avidin detection with a biotin functionalised T3 DFB laser in Chapter 4, the natural progression of sensor development was to aim to specifically detect other target molecules bearing a closer resemblance to clinically useful cardiac biomarkers. As mentioned in Chapter 1, it was the intention to functionalise the laser surface with nucleic acid based probes, such as single stranded (ss) DNA or aptamers to avoid some of the problems associated with antibody based detection approaches. Therefore, an attempt was made to identify the best method for functionalisation of the laser surface with ssDNA and to detect hybridisation of the complementary DNA sequence. In this chapter, the experimental approaches tested for functionalisation of the sensor surface for DNA detection are outlined and a rationale for future work is provided.

In previous chapters, it has been highlighted that structural changes to the DFB laser structure may improve the surface sensing capabilities of the T3 laser sensor. In this chapter, these changes are discussed in more detail, in particular modelling results indicating the potential improvement in biomolecule detection sensitivity for the addition of a high index TiO_2 cladding layer atop of the T3 gain layer are presented. The implications on the potential cardiac biomarkers that may be detected pre- and post- structural changes to the DFB laser are also discussed.

Finally, as stated in Chapter 1, DFB laser sensor technology provides an opportunity to produce a very compact sensing platform through the use of miniaturised excitation sources and light collection. A rationale is provided outlining a potential route to miniaturisation of the current sensing system to realise this goal.

5.1 Oligonucleotide surface functionalisation strategies

There are numerous strategies available for nucleic acid based cardiac biomarker detection. As has been mentioned previously, aptamers can be used for the detection of proteins typically detected by antibody based immunoassays [1, 2]. Another approach is to directly detect the precursors to the proteins usually detected. mRNA are nucleic acid sequences that provide the 'instructions' for production of the protein biomarkers and, therefore, levels of mRNA in the blood cells will rise in parallel with cardiac protein biomarkers and can themselves be used as biomarkers [3]. mRNA does not circulate freely in the blood but instead resides within the blood cells and therefore a degree of sample preparation is required before measurement of mRNA levels can take place. This is a significant drawback for this approach of biomarker detection, relative to other methods. Another nucleic acid based approach, which is a relatively new field of research, is to detect microRNA (miRNA). miRNAs are small (≈22 nucleotide) non-coding RNAs that regulate gene expression and circulate freely in plasma. In cardiovascular disease, expression levels of some miRNAs have been shown to increase in response to a cardiac event and can therefore provide very specific information about a patient's condition and prognosis [4–6]. Each of these strategies have different biomarker targets but the approach used to functionalising the sensor surface with oligonucleotide probes is invariable. In each instance, the probe is a sequence of nucleotides immobilised on the sensor surface. Therefore, to demonstrate specific detection of a nucleic acid target, any simple oligo sequence can be used as a probe, which keeps costs low, while the surface functionalisation approach is optimised. Several different functionalisation methodologies were investigated with the T3 laser with varying degree of success. The methodologies used and the results obtained are presented and discussed below.

5.1.1 Biotinylated DNA

The successful detection of avidin presented in Section 4.4 provided a potentially quick and straightforward route to oligo functionalisation of the laser surface. As shown in Figure 4.8, avidin contains four biotin binding sites, with two on either side of the protein. Therefore, it was thought that a biotin labelled oligo could be immobilised on the laser surface via coupling to a layer of avidin molecules, as depicted in Figure 5.1.

Immobilisation of biotinylated oligos has previously been demonstrated successfully for other biosensing platforms [7]. The strength of the biotin-avidin interaction results in irreversible immobilisation, which is a desirable property for surface functionalisation. The approach taken to functionalise the T3 laser surface with an oligonucleotide sequence and the results are described here.

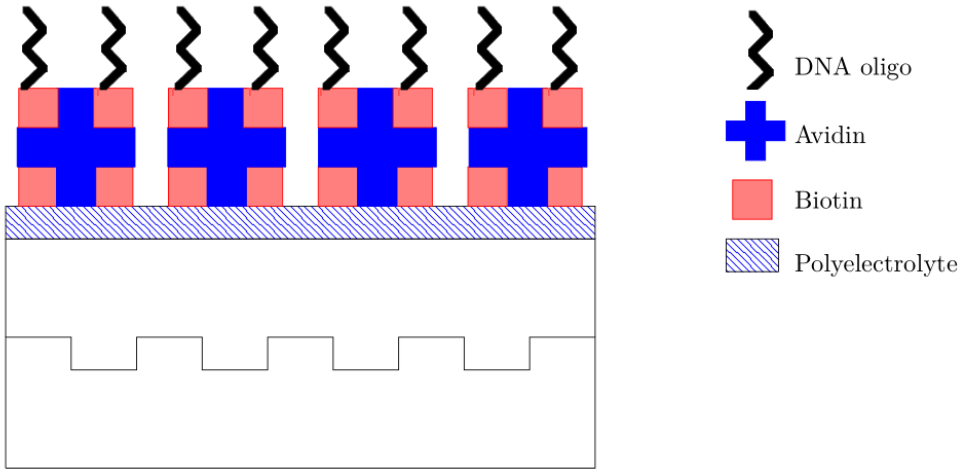

FIGURE 5.1: Schematic of PPL, biotin, avidin functionalised laser coupled with a biotinylated oligo.

5.1.1.1 Experimental methods

Prior to attempting to functionalise the T3 lasers with biotinylated DNA, the detection of biotin on lasers coated with layers of PPL, biotin and avidin was investigated. Functionalisation of the T3 laser surface with PPL (1 mg.mL^{-1}), biotin (0.2 mg.mL^{-1}), and avidin was performed as described in Section 4.4.1. Several different avidin concentrations (2.5, 10 and 100 μg.mL^{-1}) were used to form the avidin layer to see if it had any effect on biotin binding. These concentrations were chosen to provide a good coverage of the laser surface with avidin (2.5 μg.mL^{-1} is the concentration resulting in approximately half of the biotin binding sites being occupied). Avidin functionalised lasers were exposed to NHS-biotin solutions (0.2 mg.mL^{-1}, which was thought to be in excess to avidin) for 20 minutes. The final layer of biotin binding was determined by comparing the DFB laser wavelengths before and after exposure of the laser surface to the final biotin solution and any wash steps, as previously described for avidin sensing.

Biotin sensing was also repeated using biotin without the NHS group. In this case, two lasers were functionalised with avidin (10 μg.mL^{-1}) prior to exposure to the final biotin solution (0.2 mg.mL^{-1}, 20 minutes).

Sensing of a biotinylated oligonucleotide sequence with avidin coated lasers was also performed. The oligo used was a simple sequence of 5 thymine nucleotides (referred to as polyT), purchased from Biotez. The polyT oligo was synthesised with an amine group on the 5' terminal to allow biotinylation via reaction with NHS-biotin.

PolyT was purchased from Biotez in cartridges as shown in Figure 5.2. The oligo synthesis is performed by building up the oligo a nucleotide at a time on a solid resin

FIGURE 5.2: DNA is purchased in cartridges. A syringe can be inserted into the top (and bottom) of the cartridge to allow for functionalisation of the oligo within the cartridge.

support within the cartridge resulting in the final oligo tethered by one end to the solid support. The cartridge allows a syringe to be attached at either side so that solution can be injected into the cartridge, and removed, which facilitates functionalisation of the oligo within the cartridge. The polyT oligo was purchased with an amine group on the 5' terminal which was protected with a functional group to prevent any inadvertent reactions occurring. To de-protect the amine group, trichloroacetic acid (TCA) in dichloromethane (DCM) (3% w/v, 2 mL) was passed through the column three times. The cartridge, and oligo, was then washed with acetonitrile (2 mL) four times to remove any remaining TCA/DCM. Acetonitrile with 5% v/v triethylamine was injected into the cartridge and left for 2 minutes, before removing, to extract any by-products of the de-protection step, this was repeated four times. A second wash step with acetonitile was then performed and repeated four times.

NHS-biotin was prepared in dimethylformamide (DMF) to a concentration of 25 $mg.mL^{-1}$. The 1 mL solution was passed through the oligo cartridge ten times before leaving the solution in the cartridge for one hour to allow NHS-amine reaction to take place. This step was then repeated a second time. The cartridge was finally washed with DMF (2 mL) five times before a final wash with acetonitrile (2 mL), also five times, before attaching the cartridge to a vacuum for 30 minutes to dry.

To remove the biotin functionalised polyT from the resin support within the cartridge, methylamine in water (40% w/v) was added to the cartridge and heated to 65^{o}C for 30 minutes. When cooled, the oligo/methylamine solution was placed in an eppendorf and the methylamine was evaporated in a concentrator for 30 minutes at room temperature. Following this step the biotin functionalised polyT was ready for use.

Biotinylated polyT sensing was performed with three avidin coated lasers (two with an avidin concentration of 27 μg.mL^{-1} and one at 10 μg.mL^{-1}) using the same procedure described for biotin sensing in Section 4.4.1.

5.1.1.2 Biotinylated DNA surface functionalisation results

Functionalisation of the DFB laser surface with a simple oligonucleotide probe would demonstrate the potential for immobilisation of any DNA sequence on the laser and would provide an excellent start point to further explore detection of hybridisation events. In an attempt to understand whether the biotin-avidin bilayer could provide a way of capturing a biotinylated molecule, such as a DNA oligo, detection of biotin binding was investigated. Initially, NHS-biotin was used as the biotin source as it was readily available. However, biotin without the NHS group was also tested to rule out any potential effects, although unlikely, occurring due to the presence of the NHS group. Lasers functionalised with PPL, biotin and avidin, with a range of avidin layer densities, were exposed to biotin solutions (Table 5.1).

Avidin concentration (μg.mL^{-1})	**Shift in wavelength for biotin binding (nm)**	
	With NHS	Without NHS
2.5	0.01	
10	-0.02	0.06/-0.06
100	0	

TABLE 5.1: Detection of biotin binding on PPL-biotin-avidin functionalised lasers.

The magnitude of the shift values are small and do not suggest that biotin binding is being detected (recalling that a minimum shift of 0.06 nm indicates a positive result as mentioned in Section 4.4.2). The mean shift, combining the biotin results with and without the NHS group, was 0±0.04 nm. Biotin is a small molecule (M_W 244.3 kDa, dimensions of ≈ 0.53x1x2.2 nm) and therefore it is not expected to produce a large shift in wavelength upon binding to avidin. As avidin results in a shift in wavelength of ≈0.2 nm, and has a volume of ≈100 times that of biotin, one may expect to see no shift at all for biotin binding. However, the previous results for biotin functionalisation of the laser surface (0.28±0.09 nm, Section 4.4.2.2) demonstrated clearly that biotin binding was detected. This is most likely because a monolayer of biotin is expected to be more tightly packed due to the smaller size of biotin, meaning that there will be a lower ratio of buffer within the biotin layer, in comparison to an avidin monolayer. Assuming both biotin and avidin have a similar refractive index, the average refractive index of a biotin layer will be greater than that of an avidin layer. In the case of biotin binding to the deposited avidin layer, a dense biotin layer cannot be achieved as there are most

likely only two biotin binding sites available per avidin molecule. The greater volume of avidin will introduce space between biotin molecules that will be filled with buffer. When biotin binding is modelled (assuming biotin and avidin have the same refractive index of 1.46, which results in a predicted shift of 0.22 nm for a layer of avidin, Section 4.4.2.2) using the multilayer model, the predicted shift in wavelength for biotin binding to a PPL-biotin-avidin functionalised T3 laser was 0.08 nm. As the experimental biotin binding results are smaller, it suggests that either biotin coupling is not taking place or the biotin layer is not a dense, confluent layer. Due to the binding affinity between biotin and avidin it is very unlikely that binding of biotin to the avidin layer will not take place. Also, in Section 4.5, removal of avidin from a desthiobiotin functionalised laser was demonstrated. The biotin binding sites available in that instance to the biotin used to 'lift' avidin from the laser surface will be available for biotin coupling in this case. As the addition of an oligonucleotide to the biotin molecule increases the size of the overall molecule, coupling of biotinylated polyT with the avidin layer was attempted regardless of the inconclusive biotin sensing results.

Prior to performing the biotinylated polyT binding assay with the DFB laser, the coupling between NHS-biotin and the polyT oligo was explored by performing high-performance liquid chromatography (HPLC) measurements. HPLC measurements allow a comparison to be made between reaction components and can provide an indication of whether a reaction has taken place, i.e. if biotinylation of polyT was successful. HPLC involves passing the reaction components, in solvent, through a column filled with an adsorbent material, under high pressure. The individual reaction components will interact differently with the adsorbent material than the combined product of the reaction, with the difference being the time taken for each component/product to pass through the column. In an attempt to assess how successful the biotinylation of the polyT oligo was, HPLC measurements of the polyT and biotinylated polyT oligo were made, as well as water which was the buffer used for the polyT solutions. Figure 5.3 shows the HPLC spectra for the polyT and biotinylated polyT solutions after subtraction of the background signal from water.

There was a retention time difference of 7.6 minutes between the peaks for the biotinylated and unmodified polyT solutions indicating that the polyT oligo was successfully coupled with biotin. As there was no peak present at the same position as the polyT peak in the biotinylated polyT spectra, this suggests that all of the polyT present was biotinylated, which was expected since the concentration of NHS-biotin was in excess to that of the polyT oligo. Following the HPLC tests, three lasers functionalised with PPL, biotin and avidin were treated with biotinylated polyT for 20 minutes. The mean shift in wavelength after exposure of the laser to biotinylated polyT was -0.01$\pm$0.09 nm, again indicating that binding of the polyT was not detected.

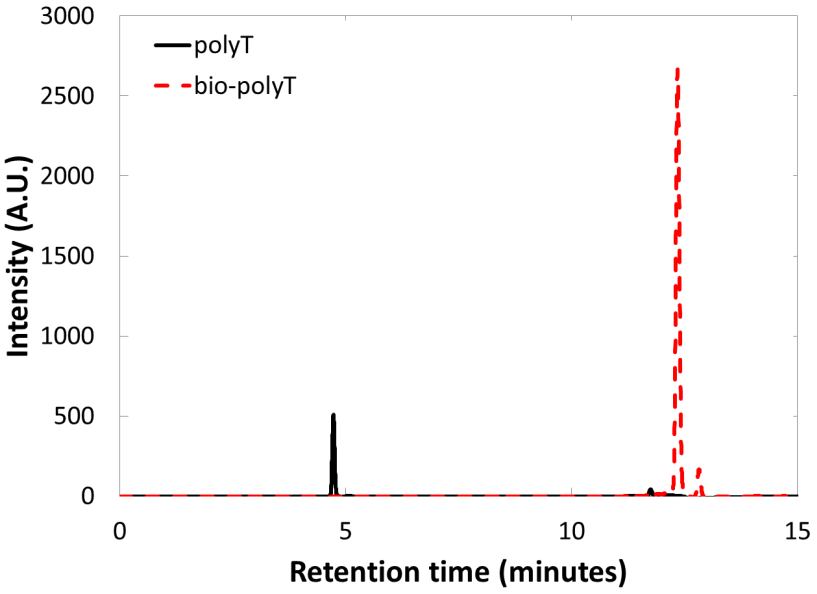

FIGURE 5.3: HPLC spectra of polyT and biotinylated polyT oligos after subtraction of the buffer background.

As mentioned previously, the biotin-avidin interaction is commonly used for surface functionalisation applications and there was no reason why secondary biotin-avidin interactions would not take place. It would be extremely unlikely given the reaction conditions that biotin-avidin binding did not take place. Therefore, why was biotin/biotinylated polyT binding not detected?

The structure of avidin, previously shown in Figure 4.2, is symmetric, consisting of two biotin binding sites expected to be available to further biotin binding following the deposition of the avidin layer on the biotin functionalised laser surface, i.e. the schematic in Figure 5.1 is likely to represent the orientation of many of the avidin molecules. However, studies investigating DNA surface functionalisation using a biotin-avidin-biotin method have shown that on average, the binding ratio of avidin to biotinylated DNA is ≈1.5 [8]. It is thought that a combination of electrostatic repulsion between the negatively charged oligos and steric hindrance prevents the efficient coupling of two biotinylated oligos per avidin molecule [8, 9]. Furthermore, as biotin is a significantly smaller molecule than avidin, even if two biotins coupled to every avidin molecule, a dense biotin layer would not be formed due to the separation introduced to the layer due to the increased dimensions of avidin. The resulting biotin layer would have a greater buffer content than a dense biotin layer, resulting in an overall reduction in the refractive index of that layer, which in turn translates into a reduced shift in wavelength attributed to a biotin/biotinylated polyT layer. Optimisation of the biotin-avidin immobilisation is likely to be possible. For example, introducing a linker molecule between biotin and the oligo may help to minimise steric hindrance and electrostatic effects. However, the

limiting factor of the number of available biotin binding sites on the avidin layer cannot be overcome, assuming full coverage of the laser surface was achieved with avidin, as expected. Therefore, in an attempt to improve the density of oligo probes on the DFB laser surface, two chemical coupling methods were investigated, click chemistry and sulfhydryl linkage.

5.1.2 Click chemistry

The click chemistry approach chosen for attachment of oligonucleotide probes to the T3 laser surface was based on 'copper-free' azide-alkyne coupling [10]. The laser surface was functionalised with a cyclooctyne group via amine-NHS coupling with the PPL layer and the polyT oligo was labelled with an azide group. The azide-alkyne reaction was depicted previously in Scheme 4.4 and the experimental methods are described below.

5.1.2.1 Experimental methods

The coupling of polyT to the laser surface was a two step process involving the immobilisation of the cyclooctyne group on the sensor surface before exposing the laser to the azide polyT. The cyclooctyne used was BCN N-hydroxysuccinimide ester II (Berry & Associates) which is a bifunctional molecule with an NHS group at one end and a cyclooctyne (BCN) group at the opposite end. As good surface coverage with biotin on a PPL coated laser was obtained with a NHS-biotin concentration of 0.2 $mg.mL^{-1}$, the same concentration was used for BCN-NHS treatment of the surface. BCN-NHS solution was prepared in a 10 mM PBS solution after first dissolving the BCN-NHS in DMSO, with a final DMSO concentration of 2% v/v. BCN functionalisation of the laser surface was achieved by immersing PPL coated lasers in BCN-NHS solution for 30 minutes. The shift in wavelength for BCN functionalisation was observed for six lasers.

The azide polyT used was the same oligo as for the biotin investigation in Section 5.1.1 and was functionalised on the 5' terminal with an azide group by Dr. Sara De Ornellas (Chemistry Department, University of Strathclyde). Three lasers were exposed to ≈0.3 mM solutions of azide polyT for two hours before washing with PBS and measuring any shift in wavelength due to polyT coupling using the same method as has been described previously (Section 4.4.2).

5.1.2.2 Click chemistry bioconjugation results

Functionalisation of the laser surface with BCN was successful. For the six lasers treated with BCN-NHS solution a mean redshift of 0.14±0.10 nm was observed. There was significant variation between the shift measurements for BCN functionalisation in comparison to the variation observed for biotin functionalisation of the PPL (Section 4.4.2.2). The non-specific adsorption of the PPL layer is likely to lead to variation in PPL layers between lasers, which may introduce some variability to further functionalisation via amine groups. However, in this instance, the variability was more likely to be an artefact of the laser itself. In our experience in making several hundreds of lasers, the quality (wavelength and intensity stability) of laser emission reduces as the raw T3 material ages. It is not known why this may be the case, but it may be that repeated exposure of the T3 to the environment, as T3 solution is prepared, may result in oxidation of the material, which may lead to the reduction in laser quality. This theory is purely speculative and the only action taken to counteract the observation was to aliquot the T3 material into smaller quantities so that repeated exposure of each batch to the environment was minimised. Regardless, six repeated measurements with BCN-NHS resulted in a redshift of the laser emission wavelength which does suggest that BCN functionalisation of the laser surface occurred.

Of the three lasers treated with azide polyT solution, wavelength shifts of 0.02, 0.05 and 0.19 nm were noted. The size of the polyT oligo is ≈2 nm (assuming a nucleotide size of 0.33 nm [11]) therefore, a shift of 0.19 nm for a layer of polyT is unlikely. Assuming the refractive index of biotin and polyT are similar [12], a shift in wavelength of around 0.08 nm would be expected, as described in Section 5.1.1.2, therefore it is likely that the shift of 0.19 nm was an anomalous result, perhaps an artefact of the laser stability issues mentioned previously. The wavelength shifts of 0.02 nm and 0.05 nm are small and so few measurements make it impossible to say with certainty whether polyT detection occurred. This was 'work in-progress' and future functionalisation investigations may wish to expand upon these initial results to determine whether the click reaction provides an efficient method for oligonucleotide functionalisation of the laser surface, and indeed if hybridisation of the complementary polyA oligo can be detected.

5.1.3 Sulfhydryl linkage

The final attempt at immobilisation of oligonucleotides on the laser surface made use of sulfhydryl chemistry [13]. As mentioned in Section 4.2.2.2, biomolecules labelled with thiol groups are often used with a thiol reactive linker molecule to couple biomolecules

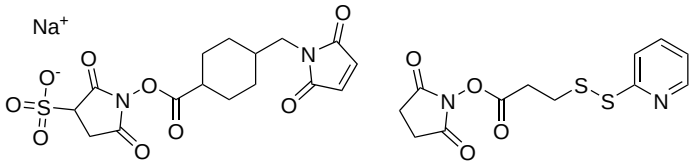

(a) (b)

FIGURE 5.4: (a) Chemical structues of sulfo-SMCC and (b) SPDP.

to a surface. The performance of two sulfhydryl linker molecules, sulfosuccinimidyl-4-(N-maleimidomethyl)cyclohexane-carboxylate (sulfo-SMCC) and N-succinimidyl 3-(2-pyridyldithio)propionate (SPDP), was investigated for coupling of thiol modified polyT oligo to the PPL functionalised laser surface.

Sulfo-SMCC and SPDP are bi-functional linkers with an amine reactive group at one end and a thiol reactive group, maleimide (sulfo-SMCC) and pyridyl disulfide (SPDP), at the opposite end. Therefore, both linker molecules can be used to couple a thiol modified oligo to a PPL functionalised laser surface. Sulfo-SMCC was used to investigate the coupling of a polyT oligo (12 thymines) modified with a thiol group on the 5' terminal and SPDP was used to investigate the coupling of a neutral peptide to the laser surface.

5.1.3.1 Experimental methods

5.1.3.1.1 Preparation of thiol modified polyT

Thiol modified polyT was purchased from Biotez. Prior to use of the polyT, the oligo must be separated from the solid resin support used during synthesis of the oligo, as described in Section 5.1.1.1, and the thiol protective group must be removed.

To remove the oligo from the resin, the contents of the cartridge were dissolved in methylamine (40% w/v in water, 1 mL) and heated to a temperature of 65 ^{o}C for 30 minutes. The solution was cooled to room temperature and placed in a concentrator for $\approx$30 minutes to remove the methylamine. The solid resin/oligo was washed three times with DI water and the eluted water/oligo solution was passed through a NAP-25 gravity flow column (Illustra), equilibrated with 10 mM PBS, to remove any small molecules from the oligo solution. The concentration of the de-salted oligo solution, 185 μM, was measured using a spectrophotomether (NanoDrop, Thermo Scientific).

To de-protect the thiol, either tris(2-carboxyethyl)phosphine (TCEP) or dithiothreitol (DTT) were used. The concentration of the reducing agent was 10 times that of the oligo solution and the reaction was performed by adding the reducing agent to the

oligo solution for 10 minutes before repeating the de-salting step with a second NAP-25 column.

In order to determine whether de-protection of the thiol group was successful, HPLC analysis was performed. Spectra for water, polyT pre and post de-salting, and polyT with TCEP were recorded.

5.1.3.1.2 SMCC laser surface coupling

The PPL binding capability of SMCC was investigated by immersing PPL coated lasers in SMCC (1 mg.mL^{-1}, in 10 mM PBS) for 30 minutes. The shift attributed to SMCC coupling was determined by taking the difference between PBS wavelength measurements before and after immersion of the laser in SMCC solution. This was repeated in triplicate.

5.1.3.1.3 PolyT functionalisation

Coupling of polyT (127 μg.mL^{-1}) to SMCC functionalised lasers was investigated by immersing SMCC functionalised lasers in polyT solution, initially for a period of 30 minutes. The effect of increasing the immersion time to two hours and overnight ($\approx$17 hours) was also established. The thiol reactivity of the maleimide group was also tested by immersing a SMCC functionalised laser in poly(ethylene glycol) (PEG) methyl ether thiol (0.2 mM, Sigma) for two hours.

Following the experimental tests with thiol modified PEG, it was queried whether the negative charge of the oligo backbone may prevent efficient thiol-maleimide coupling due to electrostatic repulsion. Therefore, coupling of a neutrally charged thiol modified peptide was investigated. The peptide was prepared by Dr. Sara De Ornellas and had a sequence of cysteine-glycine-(alanine-serine)$_4$. Coupling of the peptide to lasers coated with SMCC and SPDP was investigated. SMCC functionalisation of the lasers was achieved as described in Section 5.1.3.1. As SPDP was not water soluble, DMSO was used to first dissolve the SPDP before diluting with PBS to a concentration of 1 mg.mL^{-1}, and a final DMSO concentration of 2 % v/v. The method used for SMCC functionalisation of the laser was repeated for SPDP functionalisation. Peptide coupling was performed by immersing SMCC/SPDP functionalised lasers in peptide (0.5 mg.mL^{-1}) for two hours, before washing with PBS and determining the shift due to peptide coupling.

5.1.3.2 Sulfhydryl linkage surface functionalisation results

5.1.3.2.1 De-protection of thiol modified polyT

De-protection of the thiol group (i.e. breaking the disulfide bond) on the polyT was initially performed using TCEP. TCEP is a more powerful reducing agent than DTT and has better stability over a wider range of pH values. A significant advantage of TCEP is that it does not have to be removed prior to the thiol-sulfhydryl reaction taking place [14]. On the other hand, DTT contains a free thiol that may compete for the sulfhydryl reaction if it is not removed following de-protection. The main drawback of TCEP is that it is unstable in PBS, especially at neutral pH. However, the literature provided by the supplier suggest that if PBS is used, freshly made TCEP solutions should be effective for de-protection. As there are many examples of both reducing agents being used for de-protection of thiol modified oligos, it was thought that either could be used [15–17]. As TCEP removal was not required following de-protection of the thiol, and is therefore the simplest of the two methods, TCEP was the reducing agent used initially.

To determine if reduction of the disulfide was successful, HPLC analysis was used to differentiate between the polyT oligo pre and post thiol de-protection. Figures 5.5a and b show the HPLC spectra for the polyT, following de-salting, before and after the addition of freshly made TCEP to the polyT solution respectively. The difference between the spectra of the polyT before and after de-protection is clear, with the retention time for the de-protected thiol reduced by approximately five minutes. The retention times suggest that the products pre and post exposure to TCEP are different, with the difference thought to indicate the successful de-protection of the polyT thiol group.

5.1.3.2.2 SMCC-polyT coupling

The NHS-amine reaction had previously been tested extensively during biotin functionalisation of the laser surface. Regardless, to ensure that the SMCC coupled to the PPL layer on the laser surface as expected, the laser was exposed to SMCC solutions for 30 minutes. The shift in emission wavelengths for each of the three lasers tested are included in Table 5.2. The mean shift in wavelength, 0.15 ± 0.03 nm, suggested that functionalisation of the laser surface with SMCC was successful. Therefore, coupling of the polyT oligo via the thiol-maleimide reaction was attempted.

SMCC functionalised lasers were initially exposed to polyT solution for 30 minutes before increasing the incubation time to two hours, and then $\approx$17 hours (overnight), following inconclusive wavelength shift measurements. The wavelength shifts recorded for polyT

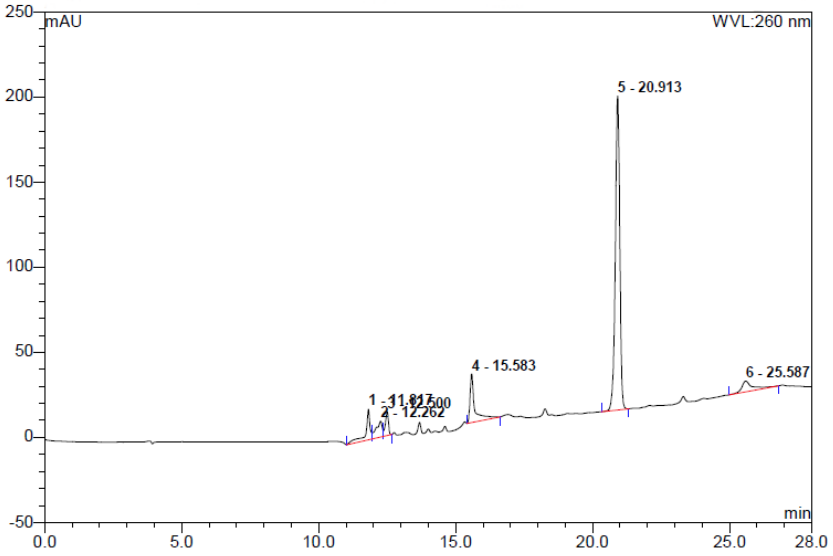

(a)

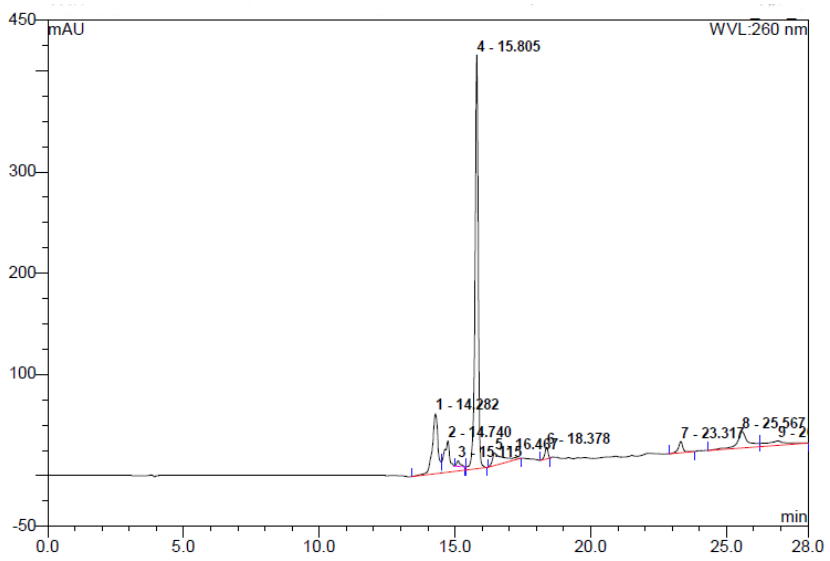

(b)

FIGURE 5.5: (a) HPLC spectra of polyT solution before and (b) after de-protection of the thiol group. Retention time (minutes) versus intensity (arbitrary units) is plotted. The highest intensity peaks account for the presence of the polyT before and after de-protection. Lower intensity peaks (intensity <100 mAU) arise from small molecules in the buffer solution.

coupling and the mean and standard deviations are included in Table 5.2. The wavelength shift values for each polyT incubation time are extremely variable and cannot be considered to reliably represent detection of polyT binding to the laser surface. Increasing the incubation time also appeared to make little difference to the coupling reaction. Following these results, and out of curiosity, a SMCC functionalised laser was immersed in a polyT solution prior to de-protection of the thiol group. The relatively small shifts recorded in Table 5.2 may suggest that there was little non-specific adsorption of the

	SMCC	**polyT**		
	30 min.	30 min.	2 hours	overnight
	0.18	0.02	-0.09	0.02
	0.12	-0.01	0.11	0.26
	0.14	-0.08	-0.11	0.01
mean±S.D.	0.15±0.03	-0.02±0.05	-0.03±0.12	0.10±0.14

TABLE 5.2: Wavelength shifts for SMCC functionalisation and polyT functionalisation for a range of immersion times. The final PBS wavelength measurements are given in brackets for comparison.

polyT to the SMCC functionalised laser. However, the disulfide polyT resulted in a shift of 0.31 nm, adding to the uncertainty in the thiol-maleimide reaction. The random nature of the results suggests that perhaps the de-protection step had not been successful as thought and/or the maleimide group was not freely available to couple with the thiol polyT. To test these hypotheses, a thiol modified PEG molecule was reacted with the SMCC functionalised laser surface to investigate the thiol-maleimide reaction and an alternative reducing agent, DTT, was used with the thiol modified polyT.

5.1.3.2.3 SMCC-thiolPEG reaction

The thiol modified PEG did not require a de-protection step prior to use. Two SMCC coated lasers were immersed in a thiolPEG solution for two hours and a third for ≈17 hours. The resulting wavelength shifts due to PEG binding were 0.07, 0.16 and 0.13 nm, respectively (mean of 0.12±0.05 nm). Although the variation between the results is still large, it was significantly lower than the variation observed for the polyT coupling and three relatively large redshifts suggest that PEG binding was being detected on the laser surface. Therefore, it was concluded that the maleimide was available for coupling to the thiol modified polyT oligos.

5.1.3.2.4 Disulfide reduction with DTT

The reduction of the disulfide bond on the polyT with DTT in the place of TCEP also appeared to provide more positive results. Three wavelength shifts of 0.18, 0.12 and 0.1 nm (mean of 0.13±0.04) nm were observed post immersion of SMCC functionalised lasers in polyT for two hours. Functionalisation of the laser surface with a single stranded oligo is only the first step towards demonstrating detection of DNA hybridisation events. Therefore, to test whether DNA hybridisation could be detected, the third of the SMCC-polyT functionalised lasers was immersed in a polyA (12 adenine's) solution (500 μM)

for ≈17 hours. The resulting shift in wavelength was a blueshift of 0.15 nm, indicating no polyA binding and perhaps removal of the polyT layer.

As mentioned previously in Section 4.2.2.2.1, the thiol-maleimide reaction is irreversible. Therefore, if this reaction was taking place between the thiol modified polyT and the SMCC, it should not be disrupted by the addition of the complementary polyA oligo. Furthermore, the strength of the amine-NHS reaction has been previously tested during avidin detection with biotin functionalised lasers. If there was any weakness in the NHS-amine bond for coupling of biotin to the PPL coated laser, reported in Section 1.42, a blueshift in wavelength would have been observed upon addition of the avidin solutions, as was the case for the desthiobiotin reversible coupling. Therefore, it is unlikely that addition of the polyA oligo was disrupting the bond between the PPL and the SMCC. This suggests that the thiol modified polyT is not coupling to the maleimide functionalised surface as expected for some as yet unknown reason. In addition, the fact that the thiol modified oligo, prior to de-protection, resulted in a shift in wavelength of 0.31 nm also casts doubt onto the positive results obtained after DTT de-protection.

In an attempt to understand if the negative charge of the oligo backbone was preventing the thiol-maleimide reaction, via electrostatic repulsion between oligo, a neutral thiol modified peptide was reacted with SMCC functionalised lasers. A second bi-functional linker, SPDP, was also used to coat lasers with a thiol reactive pyridyldithio group. The wavelength shifts observed for SMCC/SPDP and peptide coupling are presented in Tables 5.3 and 5.4.

Shift in wavelength (nm)		
Laser	**SMCC**	**Peptide**
1	0	0.03
2	0.11	0.05
3	0.13	0
4	-0.05	-0.05
mean±S.D.	0.05±0.09	0.01±0.04

TABLE 5.3: Wavelength shifts for SMCC and peptide binding to the PPL functionalised T3 laser surface.

The variability observed for SMCC coupling to the PPL layer was in contrast to the previous measurement of 0.15±0.03 nm (Section 5.1.3.2). The SMCC solution used was from the same stock solution used for the results in Section 5.1.3.2, that had been aliquoted and frozen. The literature provided by the SMCC supplier suggests using only fresh solutions, however, at the time it was thought that any degradation of the linker in solution would be prevented by freezing. The marked difference in the results for sulfo-SMCC coupling suggest that this may not have been the case and poor coverage

Shift in wavelength (nm)		
Laser	**SPDP**	**Peptide**
1	0.05	0.08
2	0.09	0.24
3	0.13	0.04
mean±S.D.	0.09±0.04	0.12±0.11

TABLE 5.4: Wavelength shifts for SPDP and peptide binding to the PPL functionalised T3 laser surface.

of the laser surface with functional maleimide groups would also be expected to lead to poor coupling of the neutral peptide, which was the case.

The results for SPDP were more encouraging. Redshifts for both SPDP and peptide coupling were observed although the variability for both results was still high. Like the PEG results presented in Section 5.1.3.2.3, exposure of the laser surface to the neutral peptide indicated that the peptide was binding to the maleimide coated surface. This perhaps indicates that charge may be having an effect on the functionalisation of the surface with thiol modified polyT.

5.1.4 Summary and outlook for oligonucleotide surface functionalisation

The initial steps towards oligo surface functionalisation of the T3 DFB laser have been described. Three approaches for immobilisation of a simple polyT oligo were investigated - immobilisation of biotinylated polyT via the biotin-avidin interaction, immobilisation of an azide functionalised polyT via a click reaction and immobilisation of thiol modified polyT via sulfhydryl chemistries. The avidin-biotinylated polyT approach resulted in no detection of biotin or biotinylated polyT, suggesting that the biotin/polyT layer formed was too sparse to result in a large enough change in the refractive index relative to that of the background buffer, which would make up a significant portion of a sparse biolayer. The density of any biotin/polyT layer was limited by the number of available biotin binding sites within the avidin layer, and as the concentration of avidin used to form that layer had previously been shown to represent saturation of the biotin binding sites, see Section 4.4.2.2, it is unlikely that the number of biotin binding sites within the avidin layer can be increased. In addition, the biotin-avidin interaction requires the formation of several layers on the laser surface prior to the addition of the probe oligo. A more efficient method would involve the addition of fewer additional layers. Therefore, chemical attachment of oligo probes is a more attractive option for surface

functionalisation and the potential to better control the density of probe molecules on the laser surface.

The two chemical approaches tested, click chemistry and sulfhydryl linkage, resulted in relatively uncertain results. The problems with the laser quality during the click reactions mean that ideally this experimental work will be repeated to obtain more reliable results. However, the results that were obtained for polyT functionalisation of the laser surface via the click reaction do suggest that this method warrants further investigation. It is suggested that repeating the experimental work presented and expanding to include the detection of the complementary polyA oligo would be a good starting point for further development of the laser functionalisation.

The results using the thiol polyT are very inconclusive and raise several questions about the thiol-sulfhydryl reaction. It is not clear whether the charge of the nucleic acid sequence is affecting the thiol-maleimide reaction and therefore requires further investigation. Positive thiol-sulfhydryl coupling was observed for the addition of PEG and peptide molecules to the surface which suggests that the charge of the oligo may be a factor. However, as both the PEG and peptide molecules could be used without requiring de-protection of the thiol group, there is still the possibility that the problem with the coupling of the polyT lies with the de-protection step of the thiol group. Going forward, it would be advisable to follow the polyT-sulfhydryl reaction with the HPLC in order to ascertain whether this reaction is occurring. There is also no reason why this reaction cannot be performed prior to addition to the laser surface. No attempt was made to optimise the reaction conditions so this in another aspect of the reaction that may warrant some attention. Surface functionalisation of sensors with oligonucleotide probes is commonplace for may sensing technologies, therefore, we are confident that an effective and reproducible method of functionalising the T3 laser surface with probes will be found. Unfortunately, as a reliable method for surface functionalisation was not found, detection of cardiac biomarkers remains a goal for future development.

5.2 Enhancement of biomolecule detection sensitivity

In Chapter 2 the DFB laser structure parameters and their effect on surface sensing were discussed. It was noted that the parameters not dependent on the gain layer material e.g. the substrate refractive index and the gain layer thickness, could be optimised to maximise the sensing capability of the DFB laser. The improvements in both bulk and surface sensing for tuning of the gain layer thickness was explored experimentally and theoretically in Chapters 2 and 3. The potential improvement in surface sensing by optimising the refractive index of the substrate, i.e. using a lower index material

more closely matched to the index of the superstrate, was modelled and was shown (Section 2.1.2) to result in an increase in the magnitude of the shift in wavelength for the detection of typical a 10 nm biolayer (n=1.49) of 0.05 nm. This corresponds to a 7% improvement in the biomolecule detection sensitivity relative to the T3 lasers presented in this thesis, where no attempt has been made to tune the index of the laser substrate. To realise this sensitivity enhancement, future development of the T3 DFB laser sensor may investigate the effect of tuning the substrate index experimentally, informed by the predictions from the model.

While reviewing the literature relating to DFB laser utilising a dye-doped gain material (Chapter 1) it was mentioned that a vast improvement in their sensitivity was achieved by the addition of a TiO_2 cladding layer to the surface of the gain material. Bulk surface sensing sensitivity of ≈17 nm/RIU was improved to ≈100 nm/RIU by the addition of a 20-35 nm TiO_2 layer. In terms of sensitivity improvement for surface sensing, the response of a dye-doped laser was modelled for different thickness of TiO_2 layer, a TiO_2 thickness of 25 nm results in an increase in the magnitude of the shift attributed to a 10 nm biolayer of 0.47 nm, which is a significant improvement. However, an advantage of using an organic semiconductor as the laser gain material, such as T3, is the higher refractive index associated with such materials relative to that of dye-doped materials, which are lower due to the dye content being restricted to prevent quenching. The higher gain layer refractive index of T3 means that the overlap of the laser mode with the biosensing region at the surface of the laser is greater than for the equivalent dye-doped laser without a TiO_2 layer, as shown in Figure 5.6. The addition of a 25 nm layer of TiO_2 to the dye-doped laser increased the surface sensing sensitivity of the dye-doped laser beyond that of the T3 laser and as the refractive index for the T3 gain material is higher than that of dye-doped material, the addition of a 25 nm TiO_2 cladding layer to the surface of the T3 laser does not increase the sensitivity beyond that of the TiO_2 clad dye-doped laser, as also shown in Figure 5.6.

However, the addition of a TiO_2 cladding layer can have an effect on the laser threshold. For the incorporation of DFB lasers into a portable sensing system, using a compact excitation source, the threshold of the laser is an important consideration, with a lower threshold enabling a wider choice of suitable pump sources. The lasing threshold is dependent on the overlap of the laser mode with the gain layer, with a greater gain layer overlap resulting in a lower lasing threshold. Previous studies have reported that the gain layer overlap for TE modes decreases for a TiO_2 thickness greater than 20 nm [18]. Therefore, a TiO_2 thickness <20 nm may be preferable to balance the increase in surface sensing sensitivity without compromising the laser threshold. The response of dye-doped and T3 DFB lasers with a TiO_2 cladding layer of varying thickness was modelled in response to detection of a 10 nm biolayer and is shown in Figure 5.7. The

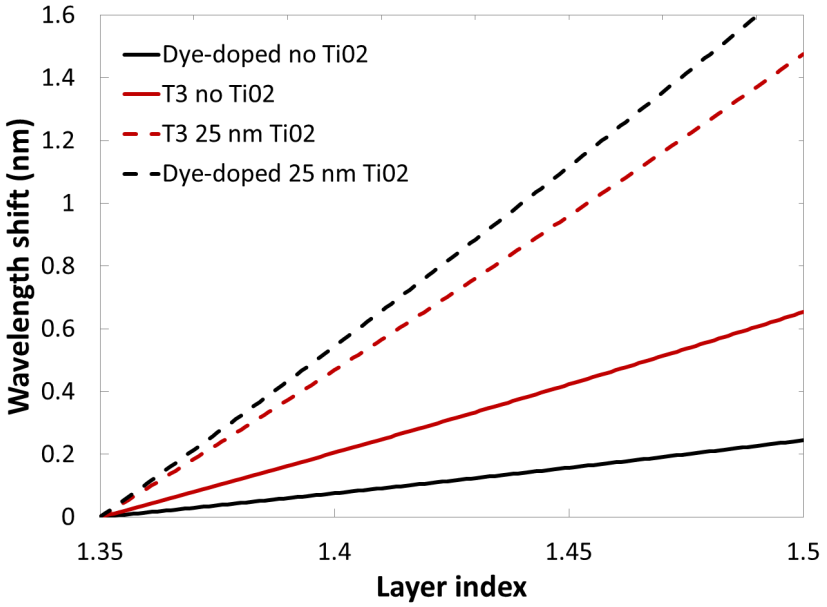

FIGURE 5.6: Modelled shift in wavelength for thin biolayer adsorption to truxene and typical dye-doped DFB laser, with and without a 25 nm TiO_2 cladding layer.

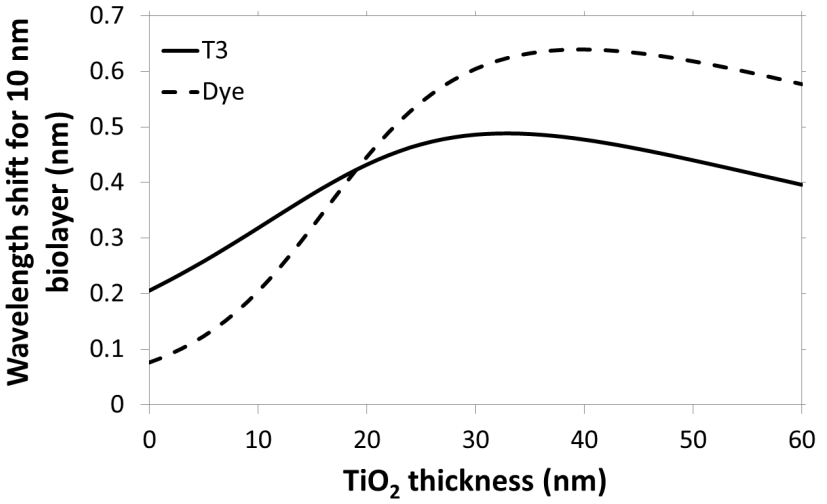

FIGURE 5.7: Modelled shift in wavelength for adsorption of the 10 nm biolayer to the surface of a truxene and a dye-doped laser for a range of different TiO_2 cladding layer thicknesses.

sensitivity of the dye-doped laser drops sharply for a TiO_2 layer with a thickness <20 nm, resulting in improved sensitivity with an equivalent T3 laser.

In terms of the improvement to surface sensing sensitivity of the T3 laser, the addition of a thin 10 nm TiO_2 cladding layer results in a 54% increase in the magnitude of the shift in wavelength attributed to the detection of a 10 nm biolayer relative to a T3 laser without the high index cladding layer. This is a very significant improvement in device sensitivity. The detection of avidin on a PPL-biotin functionalised laser was modelled (Figure 5.8) and was shown to result in a decrease in the avidin limit of

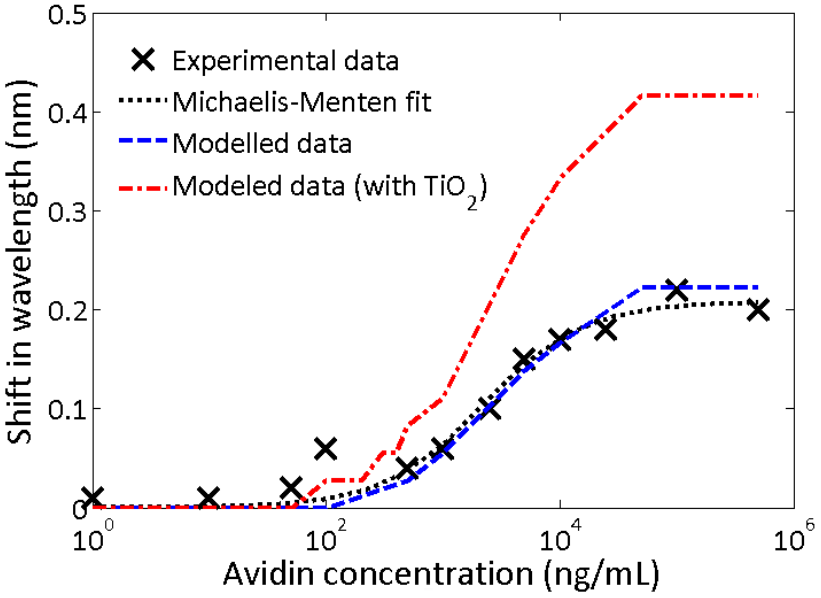

FIGURE 5.8: Experimental and modelled data for the specific detection of avidin on a biotin functionalised truxene laser. The smoothness of the curves is limited by the resolution of the calculation.

detection from 1 μg.mL^{-1} to 0.3 μg.mL^{-1}. In Chapter 3, the minimum thickness of a layer adsorbed to the T3 surface, with an index of 1.49 which is similar to that of many biomolecules [12], was determined to be 2 nm, corresponding to a shift in wavelength of 0.06 nm, which is the current minimum detectable shift in wavelength (limited by the resolution of the spectrometer). It was also noted in Chapter 3 that a layer thickness of 2 nm corresponds to a biomolecule with a molecular weight of ≈5 kDa [19]. The theoretical model predicts that a shift of 0.06 nm should be obtained for a biolayer thickness of 0.90 nm, therefore approximately half of the thickness extrapolated from the experimental data. For a T3 laser with a 10 nm TiO_2 cladding layer, the biolayer thickness corresponding to a wavelength shift of 0.06 nm is 0.60 nm. Therefore, if the same relationship between the theoretical and experimental predictions can be applied, an experimental layer thickness of 1.2 nm should be detected with a T3 laser topped with a TiO_2 layer of 10 nm. As shown in Figure 5.7, increasing the thickness of the TiO_2 layer up to 20 nm will increase the device sensitivity further. A 1-2 nm biolayer thickness would correspond to a biomolecule 'size' of ≈3 kDa. As mentioned in Chapter 3, many cardiac biomarkers, such as CRP and Troponin I, have a molecular weight >20 kDa therefore the T3 laser sensor could potentially detect these molecules without further improvements to the device sensitivity. Other cardiac biomarkers, such as BNP, are significantly smaller. BNP has a molecular weight of ≈3.5 kDa which puts it just below the current sensitivity levels of the T3 laser. However, the addition of a TiO_2 cladding layer would facilitate the detection of such small biomarkers, in theory at least.

The main drawback with incorporating a high index cladding layer into the DFB laser

structure is the added complexity to the device fabrication. One of the advantages of DFB laser technology over some other optical sensing platforms is the ease of manufacture of the lasers. As previously mentioned, organic DFB lasers can be fabricated entirely through solution processing and soft material patterning which makes then suitable for large scale manufacturing. The addition of a TiO_2 layer is typically achieved using ion beam or electron beam evaporation techniques to produce either a solid or nanostructured thin film [20–22]. Use of these techniques mean that the laser fabrication is no longer entirely solution based. However, these techniques are commonly used during fabrication of microelectronics and microsystem fabrication [23], and incorporation of a final step involving these processes is not too difficult to imagine for the mass production of DFB lasers. Therefore, future development of the T3 laser sensors may investigate the incorporation of a high index cladding layer (such as TiO_2, high index composites or spin on glass, for example) to achieve the best possible device sensitivities and to open up the potential to detect even the smallest of cardiac biomarkers. The results achieved to the T3 DFB laser can also be expected to apply for other high index organic semiconductor materials and possibly colloidal quantum dots [24, 25].

5.3 Miniaturisation of the DFB laser sensing platform

Finally, for the DFB laser sensors to be incorporated into a portable, POC, device, the pump laser and light collection hardware must be miniaturised. Miniaturisation of the spectrometer is straightforward as high resolution (0.02 nm FWHM) spectrometers are commercially available for the T3 spectral range from manufacturers such as Ocean Optics. Miniaturisation of the pump source is more of a challenge due to the absorption spectra of T3, which peaks around 375 nm. However, the T3 laser threshold ($\approx$6 kW.cm^{-2}, in solution) is close to the range of many off-the-shelf pulsed laser diode systems operating at 375 nm and therefore, finding a suitable miniaturised pump source should be possible. Use of other organic semiconductor materials, assuming a similar laser threshold, with a higher peak absorption wavelength may make this challenge easier. Figure 5.9 is a summary of reported organic DFB laser thresholds from [26]. It is expected that organic lasers with a threshold within the 0.1 to 10 kW.cm^{-2} energy and 20 - 100 ns pulse duration can be optically pumped with a laser diode.

Future development of the DFB laser sensing system may incorporate miniaturisation of the hardware using off-the-shelf components as suggested, or custom made technologies.

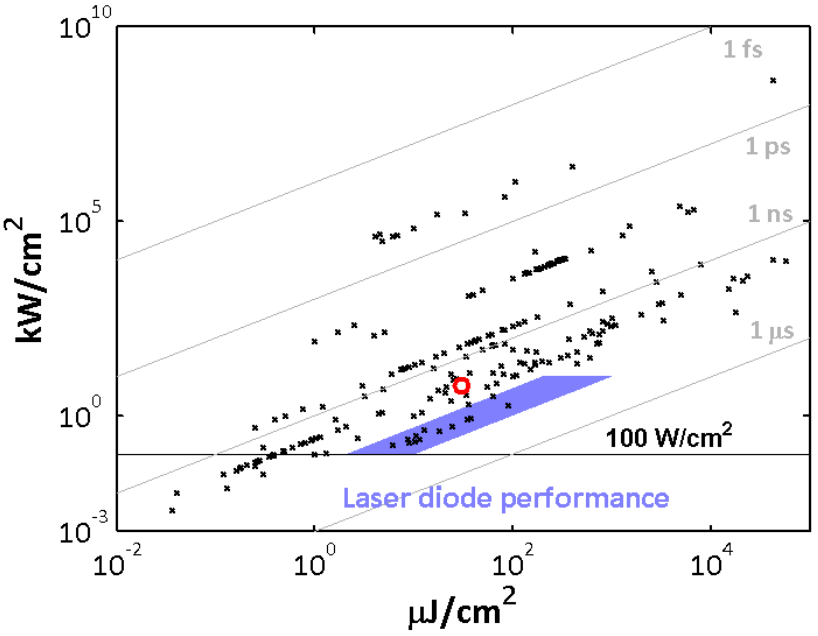

FIGURE 5.9: Summary of reported organic DFB laser thresholds. The red circle indicates the T3 DFB laser threshold when immersed in DI water. The blue area is an indication of capabilities of current GaN laser diode based measurements performed at the Institute of Photonics and extrapolation from characteristics of commercial devices (courtesy of Dr Johannes Herrnsdorf).

5.4 Summary

The surface functionalisation strategies used for the attachment of simple oligo probes were described. No method resulted in the demonstration of detection of the hybridisation of the complementary oligo. However, progress was made in identifying which methods warrant further investigation, namely click chemistry and sulfhydryl chemistry, and which questions need to be answered to understand the reactions involved in surface functionalisation.

Modelling of the T3 DFB lasers identified potential sensitivity improvements that may be achieved by tuning the refractive index of the substrate to match that of the superstrate and by investigating the possibility of incorporating a high index TiO_2 layer on the T3 surface. Realisation of potential sensitivity improvements increases the likelihood that the T3 laser sensor can be used to detect the smallest of cardiac biomarkers, such as BNP, upon determining a successful surface functionalisation strategy.

Finally, miniaturisation of the sensing platform should be relatively straightforward through the use of off-the-shelf components.

References

[1] Anjum Qureshi, Yasar Gurbuz, Saravan Kallempudi, and Javed H. Niazi. Label-free rna aptamer-based capacitive biosensor for the detection of c-reactive protein. *Phys. Chem. Chem. Phys.*, 12: 9176–9182, 2010. doi: 10.1039/C004133E. URL http://dx.doi.org/10.1039/C004133E.

[2] John G. Bruno, Alicia M. Richarte, and Taylor Phillips. Preliminary development of a {DNA} aptamer-magnetic bead capture electrochemiluminescence sandwich assay for brain natriuretic peptide. *Microchemical Journal*, 115(0):32 – 38, 2014. ISSN 0026-265X. doi: http://dx.doi.org/10.1016/j.microc.2014.02.003. URL http://www.sciencedirect.com/science/article/pii/S0026265X14000174.

[3] Vivian N. Silbiger, Andr D. Luchessi, Rosrio D.C. Hirata, Ldio G. Lima-Neto, Dbora Cavichioli, Angel Carracedo, Maria Brin, Joaqun Dopazo, Francisco Garca-Garca, Elizabete S. dos Santos, Rui F. Ramos, Marcelo F. Sampaio, Dikran Armaganijan, Amanda G.M.R. Sousa, and Mario H. Hirata. Novel genes detected by transcriptional profiling from whole-blood cells in patients with early onset of acute coronary syndrome. *Clinica Chimica Acta*, 421(0):184 – 190, 2013. ISSN 0009-8981. doi: http://dx.doi.org/10.1016/j.cca.2013.03.011. URL http://www.sciencedirect.com/science/article/pii/S0009898113001022.

[4] Rina Recchioni, Fiorella Marcheselli, Fabiola Olivieri, Stefano Ricci, Antonio Domenico Procopio, and Roberto Antonicelli. Conventional and novel diagnostic biomarkers of acute myocardial infarction: a promising role for circulating micrornas. *Biomarkers*, 18(7):547–558, 2013. doi: 10.3109/1354750X.2013.833294. URL http://dx.doi.org/10.3109/1354750X.2013.833294. PMID: 24025051.

[5] Joost P.G. Sluijter and Pieter A. Doevendans. Circulating microrna profiles for detection of peripheral arterial disease: Small new biomarkers for cardiovascular disease. *Circulation: Cardiovascular Genetics*, 6(5):441–443, 2013. doi: 10.1161/CIRCGENETICS.113.000344. URL http://circgenetics.ahajournals.org/content/6/5/441.short.

[6] Maarten F. Corsten, Robert Dennert, Sylvia Jochems, Tatiana Kuznetsova, Yvan Devaux, Leon Hofstra, Daniel R. Wagner, Jan A. Staessen, Stephane Heymans, and Blanche Schroen. Circulating microrna-208b and microrna-499 reflect myocardial damage in cardiovascular disease. *Circulation: Cardiovascular Genetics*, 3(6):499–506, 2010. doi: 10.1161/CIRCGENETICS.110.957415. URL http://circgenetics.ahajournals.org/content/3/6/499.abstract.

[7] Xiaojing Liu and Weihong Tan. A fiber-optic evanescent wave dna biosensor based on novel molecular beacons. *Analytical Chemistry*, 71(22):5054–5059, 1999. doi: 10.1021/ac990561c. URL http://pubs.acs.org/doi/abs/10.1021/ac990561c.

[8] Xiaodi Su, Ying-Ju Wu, Rudolf Robelek, and Wolfgang Knoll. Surface plasmon resonance spectroscopy and quartz crystal microbalance study of streptavidin film structure effects on biotinylated dna assembly and target dna hybridization. *Langmuir*, 21(1):348–353, 2005. doi: 10.1021/la047997u. URL http://pubs.acs.org/doi/abs/10.1021/la047997u.

[9] Charlotte Larsson, Michael Rodahl, and Fredrik Hk. Characterization of dna immobilization and subsequent hybridization on a 2d arrangement of streptavidin on a biotin-modified lipid bilayer supported on sio2. *Analytical Chemistry*, 75(19):5080–5087, 2003. doi: 10.1021/ac034269n. URL http://pubs.acs.org/doi/abs/10.1021/ac034269n.

[10] JeremyM. Baskin and CarolynR. Bertozzi. Bioorthogonal click chemistry: Covalent labeling in living systems. *QSAR Combinatorial Science*, 26(11-12):1211–1219, 2007. ISSN 1611-0218. doi: 10.1002/qsar.200740086. URL http://dx.doi.org/10.1002/qsar.200740086.

[11] Struther Arnott, R. Chandrasekaran, I.H. Hall, and L.C. Puigjaner. Heteronomous dna. *Nucleic Acids Research*, 11(12):4141–4155, 1983. doi: 10.1093/nar/11.12.4141. URL http://nar.oxfordjournals.org/content/11/12/4141.abstract.

[12] Linda Olofsson, Tomas Rindzevicius, Indriati Pfeiffer, Mikael Kll, and Fredrik Hk. Surface-based gold-nanoparticle sensor for specific and quantitative dna hybridization detection. *Langmuir*, 19 (24):10414–10419, 2003. doi: 10.1021/la0352927. URL http://pubs.acs.org/doi/abs/10.1021/la0352927.

[13] Vincent Dugas, Abdelhamid Elaissari, and Yves Chevalier. Surface sensitization techniques and recognition receptors immobilization on biosensors and microarrays. In Mohammed Zourob, editor, *Recognition Receptors in Biosensors*, pages 47–134. Springer New York, 2010. ISBN 978-1-4419-0918-3. doi: 10.1007/978-1-4419-0919-0_2. URL http://dx.doi.org/10.1007/978-1-4419-0919-0_2.

[14] Elise Burmeister Getz, Ming Xiao, Tania Chakrabarty, Roger Cooke, and Paul R. Selvin. A comparison between the sulfhydryl reductants tris(2-carboxyethyl)phosphine and dithiothreitol for use in protein biochemistry. *Analytical Biochemistry*, 273(1):73 – 80, 1999. ISSN 0003-2697. doi: http://dx.doi.org/10.1006/abio.1999.4203. URL http://www.sciencedirect.com/science/article/pii/S0003269799942033.

[15] April K.Y. Wong and Ulrich J. Krull. Surfaces for tuning of oligonucleotide biosensing selectivity based on surface-initiated atom transfer radical polymerization on glass and silicon substrates. *Analytica Chimica Acta*, 639(12):1 – 12, 2009. ISSN 0003-2670. doi: http://dx.doi.org/10.1016/j.aca.2009.03.005. URL http://www.sciencedirect.com/science/article/pii/S0003267009003821.

[16] T. Aqua, R. Naaman, and S. S. Daube. Controlling the adsorption and reactivity of dna on gold. *Langmuir*, 19(25):10573–10580, 2003. doi: 10.1021/la035116y. URL http://pubs.acs.org/doi/abs/10.1021/la035116y.

[17] Rodolphe Marie, Henriette Jensenius, Jacob Thaysen, Claus B Christensen, and Anja Boisen. Adsorption kinetics and mechanical properties of thiol-modified dna-oligos on gold investigated by microcantilever sensors. *Ultramicroscopy*, 91(14):29 – 36, 2002. ISSN 0304-3991. doi: http://dx.doi.org/10.1016/S0304-3991(02)00079-7. URL http://www.sciencedirect.com/science/article/pii/S0304399102000797. Proceedings of the third International Conference on Scaning Prob e Microscopy, Sensors and Nanostructures.

[18] Christoph Vannahme, Cameron L. C. Smith, Mads Brkner Christiansen, and Anders Kristensen. Emission wavelength of multilayer distributed feedback dye lasers. *Applied Physics Letters*, 101 (15):151123, 2012. doi: http://dx.doi.org/10.1063/1.4759131. URL `http://scitation.aip.org/content/aip/journal/apl/101/15/10.1063/1.4759131`.

[19] Harold P. Erickson. Size and shape of protein molecules at the nanometer level determined by sedimentation, gel filtration, and electron microscopy. 11, December 2009. URL `http://www.springerprotocols.com/Abstract/doi/10.1007/s12575-009-9008-x`.

[20] Chun Ge, Meng Lu, Xun Jian, Yafang Tan, and Brian T. Cunningham. Large-area organic distributed feedback laser fabricated by nanoreplica molding and horizontal dipping. *Opt. Express*, 18 (12):12980–12991, Jun 2010. doi: 10.1364/OE.18.012980. URL `http://www.opticsexpress.org/abstract.cfm?URI=oe-18-12-12980`.

[21] M. Lu, S. S. Choi, U. Irfan, and B. T. Cunningham. Plastic distributed feedback laser biosensor. *Applied Physics Letters*, 93(11):111113 –111113–3, sep 2008. ISSN 0003-6951. doi: 10.1063/1.2987484.

[22] Christoph Vannahme, Michael C. Leung, Frank Richter, Cameron L. C. Smith, Ptur G. Hermannsson, and Anders Kristensen. Nanoimprinted distributed feedback lasers comprising tio2 thin films: Design guidelines for high performance sensing. *Laser & Photonics Reviews*, 7(6):1036–1042, 2013. ISSN 1863-8899. doi: 10.1002/lpor.201300083. URL `http://dx.doi.org/10.1002/lpor.201300083`.

[23] Ivo Utke, Patrik Hoffmann, and John Melngailis. Gas-assisted focused electron beam and ion beam processing and fabrication. *Journal of Vacuum Science and Technology B*, 26(4):1197–1276, 2008. doi: http://dx.doi.org/10.1116/1.2955728. URL `http://scitation.aip.org/content/avs/journal/jvstb/26/4/10.1116/1.2955728`.

[24] Esmaeil Heydari, Jens Buller, Erik Wischerhoff, Andr Laschewsky, Sebastian Dring, and Joachim Stumpe. Label-free biosensor based on an all-polymer dfb laser. *Advanced Optical Materials*, 2 (2):137–141, 2014. ISSN 2195-1071. doi: 10.1002/adom.201300454. URL `http://dx.doi.org/10.1002/adom.201300454`.

[25] B. Guilhabert, C. Foucher, A-M. Haughey, E. Mutlugun, Y. Gao, J. Herrnsdorf, H.D. Sun, H.V. Demir, M.D. Dawson, and N. Laurand. Nanosecond colloidal quantum dot lasers for sensing. *Opt. Express*, 22(6):7308–7319, Mar 2014. doi: 10.1364/OE.22.007308. URL `http://www.opticsexpress.org/abstract.cfm?URI=oe-22-6-7308`.

[26] Johannes Herrnsdorf, Yue Wang, Jonathan J. D. McKendry, Zheng Gong, David Massoubre, Benoit Guilhabert, Georgios Tsiminis, Graham A. Turnbull, Ifor D. W. Samuel, Nicolas Laurand, Erdan Gu, and Martin D. Dawson. Micro-led pumped polymer laser: A discussion of future pump sources for organic lasers. *Laser & Photonics Reviews*, 7(6):1065–1078, 2013. ISSN 1863-8899. doi: 10.1002/lpor.201300110. URL `http://dx.doi.org/10.1002/lpor.201300110`.

Part III

Conclusions

Chapter 6

Conclusions

The work presented in this thesis is the first demonstration of a DFB laser biosensor incorporating an organic semiconductor gain layer. The aims for DFB laser development presented at the outset of this document were to optimise the DFB laser structure to maximise the sensitivity of the laser to refractive index changes within the superstrate layer, to demonstrate the sensing potential of the T3 DFB laser, including specific biomolecule detection, and to functionalise the T3 laser with oligonucleotide probes for the specific detection of three biomarkers: ApoB, CRP and BNP.

Although there are examples of DFB lasers used for biosensing in the literature [1, 2], the difference between previous examples and the T3 DFB laser presented in this thesis is the type of material employed as the gain layer. T3 is an organic semiconductor that can be used in the form of a neat, thin film as the gain producing region of the DFB laser. This results in a relatively low lasing threshold (30 μJ.cm^{-2}, 5 ns pulse duration was the typical threshold of lasers presented in this thesis) compared to the threshold of equivalent dye-doped DFB laser thresholds (180 μJ.cm^{-2}, 10 ns pulse duration). The laser threshold is an important parameter in terms of miniaturisation of the sensing system, with a low threshold making pumping with a compact pump source, such as a laser diode, possible. Indeed, laser diode, and LED, pumping of organic semiconductor based DFB lasers has previously been demonstrated [3, 4].

Another benefit of an organic semiconductor gain layer, in comparison to a dye-doped material, is the refractive indices of organic semiconductors are higher. As mentioned previously, a higher gain layer index leads to an increase in the overlap of the laser mode with the biosensing region at the laser surface. The improved sensitivity of a T3 laser relative to a Coumarin based DFB laser was shown by comparing the shift in wavelength due to unit changes in refractive index as a percentage of the laser emission wavelength. For a T3 laser this was 5.1%, with a vlaue of 3.4% for a Coumarin laser. Even when

the addition of a high index cladding layer to the laser surface was considered, for a thin (<20 nm) TiO_2 layer thickness, the T3 DFB laser is expected to show improved surface sensing performance relative to that of the equivalent dye-doped DFB laser. These characteristics, low laser threshold and high sensitivity, and simple fabrication and implementation, make organic semiconductor DFB lasers an attractive option for a biosensing platform.

Optimisation of the thickness of the T3 gain layer was demonstrated through modelling and experiment, with the experimental results closely following the predicted values from the theoretical model. Other parameters of the T3 laser structure that can be optimised include the index of the substrate and the depth of the periodic grating structure. It is likely that optimisation of these parameters may improve the performance (sensitivity and laser threshold) of the T3 laser sensor and may, therefore, be considered as part of the future development of the sensing system.

Following the demonstration of non-specific bulk and surface sensing, specific detection of avidin on a biotin functionalised T3 laser was shown. The importance of the method used to functionalise the laser surface for biomolecule detection was highlighted by the differences in the avidin limit of detection when different polyelectrolyte base layers were deposited on the T3 surface prior to biotin functionalisation. The lowest detectable concentration of avidin (1 μg.mL^{-1}) was achieved for a PPL coated laser and is in stark contrast to the 50 μg.mL^{-1} achieved for a PL coated laser. Bulk and surface sensing results indicate that the T3 DFB laser should, in theory, be able to detect two of the three cardiac biomarkers (CRP and ApoB) identified in Chapter 1, within clinically useful intervals. Detection of the third biomarker identified, BNP, a small protein present in low (>100 pg.mL^{-1}) abundance, is expected to be just out with the current limit of detection of the sensing system but modelling has shown that even detection of BNP is possible. For example, via the addition of a thin TiO_2 cladding layer.

It was shown that the limit of detection of avidin binding to a PPL-biotin functionalised laser was comparable to the biomolecule detection limits for TNFα (0.6 μg.mL^{-1}) and IgG ($\approx$0.5 μg.mL^{-1}) detection with a dye-doped DFB laser sensor [1, 5]. As mentioned previously, it is difficult to make a direct comparison between different sensing technologies where differing binding assays are used. For cardiac biomarker POC detection, the level of sensitivity required depends on the biomarker to be detected and the level at which 'abnormal' biomarker presence is indicative of disease. Optical technologies such as SPR and micro-resonator based technologies can achieve very high resolution, making single molecule detection possible [6, 7]. There may be diagnostic applications where detection of a single biomolecule is useful, however, in cardiac biomarker assessment, generally, the lowest useful biomolecule detection limit will be of the order of pg.mL^{-1}

[8]. It is expected that the DFB laser sensor presented in this thesis could detect CRP and ApoB, as mentioned previously, and potentially BNP with further optimisation of the sensor. Therefore, it is expected that this sensor will be able to at least match the biomarker detection capability of other sensor technologies for detection of these biomarkers. Furthermore, it is expected that the advantages of the DFB laser sensor, such as simple fabrication and implementation, and the potential for excellent sensitivity, specificity and resolution, make organic semiconductor DFB laser technology well suited for POC diagnositics.

The first demonstration of a re-usable DFB laser biosensor was also presented in this thesis. Detection of avidin coupling and subsequent release, was achieved by replacing the biotin functionalisation layer with a biotin analogue, desthiobiotin. Biotin, which has a higher binding affinity for avidin than desthiobiotin, was then used to release desthiobiotin bound avidin. For clinical applications, there are many reasons why single use, disposable tests are widely used, e.g. prevention of cross-contamination and reducing handling of test samples. However, a re-usable biosensing platform may be beneficial in industries such as environmental and food monitoring where large numbers of measurements are required [9, 10].

For any biosensor, serious consideration must be given to the prevention of non-specific biomolecule adsorption which can lead to false positive results and reduced sensitivity. In this thesis, the non-specific adsorption of BSA was shown to be reduced by the functionalisation of the laser surface with biotin. Competition assays with avidin in the presence of BSA also indicated that BSA resulted in no detectable interference for avidin detection. This is a very encouraging result as blood contains significant levels ($\approx$ 50 mg.mL^{-1}) of BSA, amongst other proteins, and preventing interference will be important as the sensing system moves towards biomarker detection in clinical samples. Future development of the sensor will have to widen the investigation into prevention of non-specific adsorption to include other biomolecules that may result in false positive results. And the surface chemistry used for oligonucleotide probe immobilisation will have to be optimised to minimise non-specific adsorption and/or a post functionalisation blocking step may have to be developed.

Finally, potential routes for functionalisation of the T3 laser surface with oligonucleotide probes were identified. Click and sulfhydryl chemistries are both potentially viable options for the attachment of oligonucleotides to the device surface. Both methods do require further investigation as detection of hybridisation events has not yet been observed. Future development will focus on better understanding the click and sulfhydryl functionalisation events and/or other functionalisation techniques may be developed.

Once the optimum technique for probe immobilisation has been identified and the successful detection of complementary oligo hybridisation has been demonstrated, the step to functionalisation of the surface for cardiac biomarker detection should be relatively straightforward.

References

[1] M. Lu, S. S. Choi, U. Irfan, and B. T. Cunningham. Plastic distributed feedback laser biosensor. *Applied Physics Letters*, 93(11):111113 –111113–3, 2008. ISSN 0003-6951. doi: 10.1063/1.2987484.

[2] Chun Ge, Meng Lu, Xun Jian, Yafang Tan, and Brian T. Cunningham. Large-area organic distributed feedback laser fabricated by nanoreplica molding and horizontal dipping. *Optics Express*, 18(12):12980–12991, 2010. doi: 10.1364/OE.18.012980. URL `http://www.opticsexpress.org/abstract.cfm?URI=oe-18-12-12980`.

[3] T. Riedl, T. Rabe, H.-H. Johannes, W. Kowalsky, J. Wang, T. Weimann, P. Hinze, B. Nehls, T. Farrell, and U. Scherf. Tunable organic thin-film laser pumped by an inorganic violet diode laser. *Applied Physics Letters*, 88(24):241116 –241116–3, 2006. ISSN 0003-6951. doi: 10.1063/1.2211947.

[4] Y. Yang, G. A. Turnbull, and I. D. W. Samuel. Hybrid optoelectronics: A polymer laser pumped by a nitride light-emitting diode. *Applied Physics Letters*, 92(16):163306, 2008. doi: 10.1063/1.2912433. URL `http://link.aip.org/link/?APL/92/163306/1`.

[5] Yafang Tan, Chun Ge, A. Chu, Meng Lu, W. Goldshlag, Cheng Sheng Huang, A. Pokhriyal, S. George, and B.T. Cunningham. Plastic-based distributed feedback laser biosensors in microplate format. *Sensors Journal, IEEE*, 12(5):1174 –1180, 2012. ISSN 1530-437X. doi: 10.1109/JSEN.2011.2163933.

[6] Srdjan S. Aimovi, Mark P. Kreuzer, Mara U. Gonzlez, and Romain Quidant. Plasmon near-field coupling in metal dimers as a step toward single-molecule sensing. *ACS Nano*, 3(5):1231–1237, 2009. doi: 10.1021/nn900102j. URL `http://dx.doi.org/10.1021/nn900102j`. PMID: 19385661.

[7] Martin Baaske and Frank Vollmer. Optical resonator biosensors: Molecular diagnostic and nanoparticle detection on an integrated platform. *ChemPhysChem*, 13(2):427–436, 2012. ISSN 1439-7641. doi: 10.1002/cphc.201100757. URL `http://dx.doi.org/10.1002/cphc.201100757`.

[8] Mazher-Iqbal Mohammed and Marc P. Y. Desmulliez. Lab-on-a-chip based immunosensor principles and technologies for the detection of cardiac biomarkers: a review. *Lab Chip*, 11:569–595, 2011. doi: 10.1039/C0LC00204F. URL `http://dx.doi.org/10.1039/C0LC00204F`.

[9] K.R. Rogers and J.N. Lin. Biosensors for environmental monitoring. *Biosensors and Bioelectronics*, 7(5):317 – 321, 1992. ISSN 0956-5663. doi: http://dx.doi.org/10.1016/0956-5663(92)85026-7. URL `http://www.sciencedirect.com/science/article/pii/0956566392850267`.

[10] Evangelyn C. Alocilja and Stephen M. Radke. Market analysis of biosensors for food safety. *Biosensors and Bioelectronics*, 18(56):841 – 846, 2003. ISSN 0956-5663. doi: http://dx.doi.org/10.1016/S0956-5663(03)00009-5. URL `http://www.sciencedirect.com/science/article/pii/`

S0956566303000095. Selected papers from the Seventh World Congress on Biosensors Kyoto, Japan 15-17 May 2002.

Part IV

Appendix

Appendix A

Model details

In Chapter 2, the models used to simulate the response of the DFB laser in various scenarios were described. The models used were originally developed by Dr Nicolas Laurand in Mathcad. The multilayer model used for the calculation of the effective refractive index was translated into Matlab. The Matlab code used for the results presented in this thesis is provided in Sections A.1-A.4. The Mathcad code for the intensity mode profile and overlap with the DFB laser structure and the multilayer model for biomolecule binding is provided in Section A.5.

A.1 Calculation of the transfer matrix

```
1
2  function [Mt] = transfer_M_product(pitch, Layers, beta)
3      % This function calculates the product of the transfer matrix Mt.
4      % Some parameters for the matrix are also defined here.
5      % The output is used by the TE_dispersion function to determine
6      % the dispersion equation to be solved
7
8      % [Mt] = transfer_M_product(pitch, Layers, beta)
9      % This script will take in the user defined values for pitch, beta and
10     % the inputs into the layers matrix - these are entered on the script
11     % "DFB_layers_script".
12
13     % The output is the product of the transfer matrix
14
15
16     %  Wavenumber
17     k0 = 2 .* pi ./ (beta .* pitch);
```

```
18
19      %  Refractive indices for the layers, n is the first column of the
20      %  "Layers" matrix
21      n = Layers(:,1);
22
23      %  Thickness of the layers, thickness is the second column of the
24      %  "Layers" matrix
25      thickness = Layers(:,2);
26
27      %  Directional propagation constant of mode through each layer (X ...
        times 1 matrix)
28      alpha_layers = (n .^2 - beta .^2) .^(1/2);
29
30      %  Phase thickness for the layers (X times 1 matrix)
31      Phi = k0 .* alpha_layers .* thickness;
32
33      %  Parameters for TE polarisation
34      %  A Z0 function has been created to store the value of the ...
        inpedance of free space
35      gamma_layers = alpha_layers ./ Z0();
36
37      %  Field transfer matrix relates the field amplitudes at one ...
        position to
38      %  the corresponding amplitudes at a second position.  i.e. at ...
        each of the
39      %  boundaries.  Mt is determined for each value of Phi
40
41       Mt = [   cos(Phi(1)),                    (-1i ./gamma_layers(1)) ...
        .* sin(Phi(1));
42              -1i .* gamma_layers(1) .* sin(Phi(1)),             ...
        cos(Phi(1))     ];
43
44
45       % The for loop calculates the product of each of the matrices
46       % produced for each value of Phi.  The output is a 2x2 matrix.
47       for ind = 2:length(Phi)
48
49          Mt = Mt * [   cos(Phi(ind)),                    (-1i ...
        ./gamma_layers(ind)) .* sin(Phi(ind));
50                      -1i .* gamma_layers(ind) .* sin(Phi(ind)),          ...
           cos(Phi(ind))     ];
51
52
53       end
54
55  end
```

A.2 Calculation of the dispersion function

```
1
2  function [Dispersion] = TE_dispersion(pitch, n_sup, A, B, C, Layers, beta)
3
4      % This function calculates the dispersion equation using Mt.  The ...
       output is used by the neffcalc
5      % function to determine the effective refractive index
6
7      % [Field] = TE_field(pitch, n_sup, A, B, C, Layers, beta)
8      % This script will take in the user defined values for pitch, ...
       n_sup, A, B, C, beta and the inputs
9      % into the layers matrix - these are entered on the script ...
       "DFB_layers_script".
10
11     % The output is the dispersion function that is to be solved by ...
       the neffcalc function
12
13
14     %  Refractive index of substrate (NOA65)taking into account ...
       dispersion effects
15     n_sub = A + B ./((beta .* pitch) ./1e-9).^2 + C ./((beta .* pitch) ...
       ./1e-9).^4;
16     %  If a different substrate is used, i.e. NOA85, then put number ...
       in as below
17     % n_sub = 1.55;
18
19     % Directional propagation constant of mode through substrate
20     alpha_sub = (n_sub .^2 - beta .^2) .^(1/2);
21
22     % Directional propagation constant of mode through superstrate
23     alpha_sup = (n_sup .^2 - beta .^2) .^(1/2);
24
25     gamma_sub = alpha_sub ./ Z0();
26     gamma_sup = alpha_sup ./ Z0();
27
28     % n_a, this inserts the refractive index for n_a into the layers ...
       matrix
29     Layers (end,1) = 1.7385 + (9.511e8 .*2 .* exp( - ((beta .* pitch) ...
       ./ 1e-9) ./ 18.1467));
30     % when you want to define n_a
31     % Layers (end,1) = 1.52;
32
33     % The transfer_M_product function calculates Mt.  This is inputed here
34     % and used in the Dispersion equation below.
35     [Mt] = transfer_M_product(pitch, Layers, beta);
```

```
36
37      Dispersion = imag( gamma_sup .* Mt(1,1) ...
38                       + gamma_sup .* gamma_sub .* Mt(1,2) ...
39                       + Mt(2,1) ...
40                       + gamma_sub .* Mt(2,2) );
41
42  end
```

A.3 Calculation of β

```
1
2   function [neff, Dispersion] = neffcalc(pitch, n_sup, A, B, C, Layers)
3
4       % This function solves the dispersion equation for the TE wave
5
6       % [neff, field] = neffcalc(pitch, n_sup, A, B, C, Layers)
7       % This script will take in the user defined values for pitch, ...
        n_sup, A, B,
8       % C, and the inputs into the layers matrix - these are entered on ...
        the script "DFB_layers_script".
9
10      % The outputs are values of n_eff and the electric field amplitudes
11
12      % fminopts allows you to control the optimisation parameters.  ...
        "TolX" is the
13      % termination tolerance on x which is beta in this case, "TolFun" ...
        is the
14      % termination tolerance on the function value.  We want to ...
        minimise the
15      % dispersion equation for the E field whilst keeping the value ...
        positive by trying
16      % different values of beta.
17
18      fminopts = optimset( TolX , 1e-6,  TolFun , 1e-8);
19
20      % "fminsearch" is a Matlab function that finds the minimum of a ...
        scalar function of several
21      % variables, starting at an initial estimate (set here to 1.8). ...
        This is generally
22      % referred to as unconstrained nonlinear optimization.
23
24      % Fminsearch expects there to only be one input, as we have 7 ...
        inputs, an anonymous
```

```
25      % function (f_to_minimise) is used to tell it that beta is the ...
        value to be minimised.
26
27      neff = abs( fminsearch(@(beta) f_to_minimise(pitch, n_sup, A, B, ...
        C, Layers, beta), 1.8, fminopts) );
28
29
30      % TE_dispersion is the script containing the dispersion equation ...
        for the E field and Mt
31      % and various other parameters required for the calculation of ...
        each M
32      Dispersion = TE_dispersion(pitch, n_sup, A, B, C, Layers, neff);
33
34  end
35
36      % This is the anonymous function.  As this is placed in this script
37      % below the TE_field function, only the other functions within this
38      % script can see this function. This controls how fminsearch finds a
39      % "good" value of beta.  If beta produces a negative field equation
40      % the score of this number is multiplied by 20, making the score ...
        higher
41      % means that the beta value will be rejected and a new beta will ...
        be tried.
42  function Dispersion = f_to_minimise(pitch, n_sup, A, B, C, Layers, beta)
43
44      Dispersion = TE_dispersion(pitch, n_sup, A, B, C, Layers, abs(beta));
45
46      if Dispersion < 0
47          Dispersion = 20 * Dispersion;
48      end
49
50      Dispersion = abs(Dispersion);
51
52  end
```

A.4 Script used to define DFB laser parameters

```
1
2
3   % DFB_layers_script.m
4   % Matlab version of NL s Mathcad programme to calculate the shift expected
5   % with changing refractive index for the build up of layers on the laser
6   % surface
7
```

```
8
9
10 % [ neff(ind), field(ind)] = neffcalc(pitch, n_sup, A, B, C, Layers)
11 % This script will take in the user defined values for pitch, n_sup, ...
       A, B,
12 % C, and the inputs into the layers matrix.
13
14 % The output is a graph of layer thickness versus shift in wavelength ...
       for TE modes.
15
16 % ******When simulating with Ti02 layer the best guess for neff may ...
       have to be increased in neffcalc******
17
18 % Define the value of n_sup
19 n_sup = 1.35;
20
21
22 % Take into account the wavelength dependent index of the substrate ...
       (Norland 65)using a
23 % Cauchy relation (from Thorlabs website)
24
25 A = 1.50631;
26 B = 5435.62;
27 C = 2.77798e7;
28
29 % Define the value of Bragg wavelength in nm
30 lambda = 430e-9;
31
32 % Define the pitch of the grating in nm
33 pitch = 277e-9;
34
35 % Define the thickness of layers La and Lb in nm
36 Lb = 10 * 1e-9;
37 La = 0 * 1e-9;
38
39 % The parameters of the layers are inserted into the matrix below.  The
40 % loop takes in the laser parameters and calls the "neffcalc" function
41 % which is used to determine the effective refractive index (see notes
42 % within "neffcalc".  An n_eff value is produced for each increment of Lb
43 for ind = 1:numel(Lb)
44
45     Layers = [ 1.45, La; 1.49, Lb(ind); NaN, 75e-9 ];
46
47     [ neff(ind), Dispersion(ind)] = neffcalc(pitch, n_sup, A, B, C, ...
       Layers);
48
49 end
```

A.5 Mathcad models of the intensity mode profile and overlap and the multilayer model for biomolecule binding

Multilayer planar waveguide - Calculations of modal effective refractive index - Extension to DFB structures and use for sensing applications

Ref 'Thin-films field-transfer matrix theory of planar multilayer waveguides and reflection from prism-loaded waveguides', J. Opt. Soc. Am. A, 1, 7, 742 (1984)

1 / Multilayer planar waveguide

Constant

$\Lambda := 276 \cdot nm$

$k(\beta) := \frac{2 \cdot \pi}{\Lambda \cdot \beta}$

$Z0 := \frac{374.73031346\Omega}{\Omega}$

Impedance of free space - use the value unitless here because Mathcad does not handle matrix elements of different units

$na(\beta) := 1.7385 + 9.51110^{8} \cdot 2 \cdot exp\left(\frac{-\beta \cdot \frac{\Lambda}{nm}}{18.1467}\right)$

Equation that fits the index measurement of T3, taken by ellipsometry, from St Andrews

Refractive indices for substrate and superstrate

$A := 1.5063$ $B := 5435.6$ $C := 2.777981 0^{7}$

$nsub(\beta) := A + \frac{B}{\left(\frac{\beta \cdot \Lambda}{nm}\right)^{2}} + \frac{C}{\left(\frac{\beta \cdot \Lambda}{nm}\right)^{4}}$

Cauchy formula for the NOA

$nsup := 1.340$

Structure

$X := 3$ Total number of layers excluding substrate and supersrate

For user to enter layer structure data - each matrix row represent a layer (layer 1, 2, 3 etc...). The first column is the refractive index and the second column is the layer thickness in nm. First row should indicate the layer closest to the superstrate and then follow the order of the structure up to the last layer before the substrate. The number of rows must match X value right above.

$$Layers(\beta) := \begin{pmatrix} 1.46 & 10 \\ 1.49 & 2 \\ na(\beta) & 75 \end{pmatrix}$$

$$n(\beta) := Layers(\beta)^{\langle 0 \rangle}$$

$$L(\beta) := Layers(\beta)^{\langle 1 \rangle} \cdot nm$$

Transfer matrix calculation

Calculation of Mt the transfer matrix of the layers between substrate and superstrate.

$$j := 0..X - 1$$

$$\alpha(j,\beta) := \left| \left(n(\beta)_j \right)^2 - \beta^2 \right|^{\frac{1}{2}} \qquad \alpha sub(\beta) := \left(nsub(\beta)^2 - \beta^2 \right)^{\frac{1}{2}} \qquad \alpha sup(\beta) := \left(nsup^2 - \beta^2 \right)^{\frac{1}{2}}$$

$$\Phi(j,\beta) := k(\beta) \cdot \alpha(j,\beta) \cdot L(\beta)_j$$

TE modes

$$\gamma(j,\beta) := \frac{\alpha(j,\beta)}{Z0} \qquad \gamma sub(\beta) := \frac{\alpha sub(\beta)}{Z0} \qquad \gamma sup(\beta) := \frac{\alpha sup(\beta)}{Z0}$$

TM modes

$$\gamma TM(j,\beta) := \frac{\alpha(j,\beta)}{\left(n(\beta)_j \right)^2} \cdot Z0$$

$$M(j,\beta) := \begin{pmatrix} \cos(\Phi(j,\beta)) & \frac{-i}{\gamma(j,\beta)} \cdot \sin(\Phi(j,\beta)) \\ -i \cdot \gamma(j,\beta) \cdot \sin(\Phi(j,\beta)) & \cos(\Phi(j,\beta)) \end{pmatrix}$$

$$MTM(j,\beta) := \begin{pmatrix} \cos(\Phi(j,\beta)) & \frac{-i}{\gamma TM(j,\beta)} \cdot \sin(\Phi(j,\beta)) \\ -i \cdot \gamma TM(j,\beta) \cdot \sin(\Phi(j,\beta)) & \cos(\Phi(j,\beta)) \end{pmatrix}$$

$$Mt(\beta) := \prod_{j=0}^{X-1} M(j,\beta) \qquad MtTM(\beta) := \prod_{j=0}^{X-1} MTM(j,\beta)$$

$\beta := 1.3, 1.3001 .. 1.849$

$Im\left[\gamma sup(\beta)\cdot Mt(\beta)_{0,0} + \gamma sup(\beta)\cdot\gamma sub(\beta)\cdot Mt(\beta)_{0,1} + (Mt(\beta))_{1,0} + \gamma sub(\beta)\cdot Mt(\beta)_{1,1}\right]$

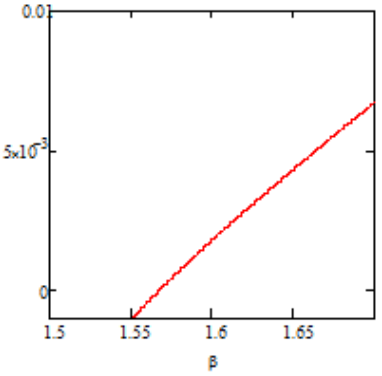

Determination of effective refractive indices for:

TE modes

$i := 0 \qquad \beta := 1.7999$

$neffstemp :=$ while $\beta > nsub(\beta)$
  $neff_i \leftarrow$ while $\left|Im\left(\gamma sup(\beta)\cdot Mt(\beta)_{0,0} + \gamma sup(\beta)\cdot\gamma sub(\beta)\cdot Mt(\beta)_{0,1} + Mt(\beta)_{1,0} + \gamma sub(\beta)\cdot Mt(\beta)_{1,1}\right)\right| > 0.0001$
    $\beta \leftarrow \beta - 0.0001$
  β
  $\beta \leftarrow neff_i - 0.01$
  $i \leftarrow i + 1$
$neff$

$neffstemp = \begin{pmatrix} 1.56949 \\ 1.39029 \end{pmatrix}$

$$neff := \left| \begin{array}{l} \text{for } i \in 0..last(nefftemp) - 1 \text{ if } last(nefftemp) > 0 \\ \quad neff_i \leftarrow nefftemp_i \\ neff \leftarrow nefftemp \text{ otherwise} \\ neff \end{array} \right.$$

$neff = (1.56949)$

Modes profiles - TE

This section plots the mode profile for the TE modes. To choose which modes to plot (if several modes exist) the correct effective refractive index neff as calculated above need to be chosen (for example neff0 for the TE0 mode).

Ref:

The approach taken here consists in initialising the amplitude of the fields U and V (as defined in above ref) at the interface of the multilayer with the substrate. The field in the substrate and therefore at this interface are linked by V=γ U. U is arbitrarily chosen as 1 at the interface. In our notation, the interface between the first layer and the superstrate is the interface 0 and therefore the interface at the substrate where the field is initialised is the interface number X (X being the number of layers between the superstrate and the substrate.

Once Ux and Vx are known it is a simple manner of using the transfer matrix of each layer to deduce the fields at each interface (from X to 0).

Once all the fields at interface are known, the form of the fields in each layer is obtained using eq 34 from the ref. The field in the substrate and superstrate are evanescent.

Initialisation

$j := X$ $\quad neff := neff_0$

$Us := 1$ $\quad Vs := \gamma sub(neff) \cdot Us$

$U_j := Us$ $\quad V_j := Vs$ $\quad \beta := neff$

Determination of the amplitudes at each interface

$$U := \left| \begin{array}{l} \text{while } j \geq 1 \\ \quad \left| \begin{array}{l} U_{j-1} \leftarrow M(j-1,neff)_{0,0} \cdot U_j + M(j-1,neff)_{0,1} \cdot V_j \\ V_{j-1} \leftarrow M(j-1,neff)_{1,0} \cdot U_j + M(j-1,neff)_{1,1} \cdot V_j \\ j \leftarrow j-1 \end{array} \right. \\ U \end{array} \right.$$

$$V := \left| \begin{array}{l} \text{while } j \geq 1 \\ \quad \left| \begin{array}{l} U_{j-1} \leftarrow M(j-1,neff)_{0,0} \cdot U_j + M(j-1,neff)_{0,1} \cdot V_j \\ V_{j-1} \leftarrow M(j-1,neff)_{1,0} \cdot U_j + M(j-1,neff)_{1,1} \cdot V_j \\ j \leftarrow j-1 \end{array} \right. \\ V \end{array} \right.$$

Calculation of the mode profile

Note that for TE mode U=E

$$E(x) := \left| \begin{array}{l} E \leftarrow U_0 e^{-1 \cdot k(\beta) \cdot nsub(neff) \cdot x \cdot ns} \quad \text{if } x < 0 \\ E \leftarrow U_{ns} \quad \text{if } x > \sum_{k=0}^{X-1} \left(Layers(\beta)^{\langle 1 \rangle} \right)_k \\ E \leftarrow \left| \begin{array}{l} j \leftarrow 0 \\ \text{while } j \leq X-1 \\ \quad \left| \begin{array}{l} E \leftarrow U_{j+1} \cdot \cos\left[k(\beta) \cdot \alpha(j,neff) \cdot \left[\left[x - \left[\sum_{k=0}^{j} \left(Layers(\beta)^{\langle 1 \rangle} \right)_k \right] \right] \cdot ns \right] \right] + \frac{i}{\gamma(j,neff)} \cdot V_{j+1} \cdot \sin\left[k(\beta) \cdot \alpha(j,neff) \cdot \left[\left[x - \left[\sum_{k=0}^{j} \left(Layers(\beta)^{\langle 1 \rangle} \right)_k \right] \right] \cdot ns \right] \right] \\ \text{break if } 0 \leq x \leq \sum_{k=0}^{j} \left(Layers(\beta)^{\langle 1 \rangle} \right)_k \\ j \leftarrow j+1 \end{array} \right. \\ E \end{array} \right. \quad \text{if } 0 \leq x \leq \sum_{k=0}^{X-1} \left(Layers(\beta)^{\langle 1 \rangle} \right)_k \\ E \end{array} \right.$$

Index Profile

$$Index(x) := \left| \begin{array}{l} Index \leftarrow nsup \quad \text{if } x < 0 \\ Index \leftarrow nsub(\beta) \quad \text{if } x > \sum_{k=0}^{X-1} \left(Layers(\beta)^{\langle 1 \rangle} \right)_k \\ Index \leftarrow \left| \begin{array}{l} j \leftarrow 0 \\ \text{while } j \leq X-1 \\ \quad \left| \begin{array}{l} Index \leftarrow n(\beta)_j \\ \text{break if } 0 \leq x \leq \sum_{k=0}^{j} \left(Layers(\beta)^{\langle 1 \rangle} \right)_k \\ j \leftarrow j+1 \end{array} \right. \\ Index \end{array} \right. \quad \text{if } 0 \leq x \leq \sum_{k=0}^{X-1} \left(Layers(\beta)^{\langle 1 \rangle} \right)_k \\ Index \end{array} \right.$$

Plot intensity mode profiles and the refractive index structure

$x := -100, -99.9 .. 60$

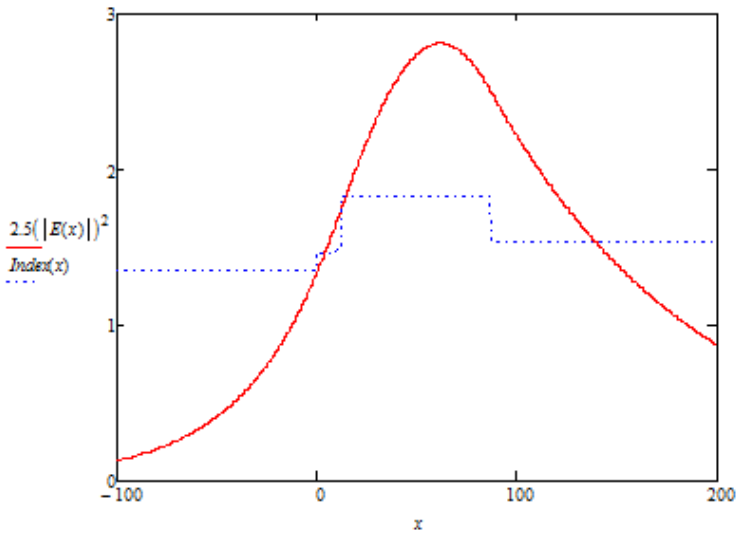

Calculation of the overlap factor

This section calculates the overlaps of the mode with the last layer of the multilayer section (i.e. the last layer before the substrate or for our typical DFB laser the active region)

$$A := \begin{vmatrix} A \leftarrow 0 \\ \text{for } N \in \sum_{i=0}^{X-2} \frac{L(\beta)_i}{nm} .. \sum_{i=0}^{X-1} \frac{L(\beta)_i}{nm} \\ \quad A \leftarrow A + (|E(N)|)^2 \\ A \end{vmatrix}$$

$$Agrating := \begin{vmatrix} A \leftarrow 0 \\ \text{for } N \in \sum_{i=0}^{X-1} \frac{L(\beta)_i}{nm} .. \left(\sum_{i=0}^{X-1} \frac{L(\beta)_i}{nm}\right) - 50 \\ \quad A \leftarrow A + (|E(N)|)^2 \\ A \end{vmatrix}$$

$$\Gamma := \frac{A}{\sum_{x=-10000}^{10000} (|E(x)|)^2}$$

$$\Gamma grating := \frac{Agrating}{\sum_{x=-10000}^{10000} (|E(x)|)^2}$$

$$Abio := \begin{vmatrix} A \leftarrow 0 \\ \text{for } N \in 0.. \frac{L(\beta)_0}{nm} \\ \quad A \leftarrow A + (|E(N)|)^2 \\ A \end{vmatrix}$$

$$Asup := \begin{vmatrix} A \leftarrow 0 \\ \text{for } N \in 0..-10000 \\ \quad A \leftarrow A + (|E(N)|)^2 \\ A \end{vmatrix}$$

$$\Gamma bio := \frac{Abio}{\sum_{x=-10000}^{10000} (|E(x)|)^2}$$

$$\Gamma sup := \frac{Asup}{\sum_{x=-10000}^{10000} (|E(x)|)^2}$$

$\Gamma = 0.35954531316$

$\Gamma bio = 0.03094933568$

$\Gamma grating = 0.25918429137$

$\Gamma TiO2 = 0.00958377661$

$\Gamma sup = 0.10754503015$

Multilayer planar waveguide - Calculations of modal effective refractive index - Extension to DFB structures and use for sensing applications

Ref 'Thin-films field-transfer matrix theory of planar multilayer waveguides and reflection from prism-loaded waveguides', J. Opt. Soc. Am. A, 1, 7, 742 (1984)

1 / Multilayer planar waveguide

Constant

$\Lambda := 277 \cdot nm$

$k(\beta) := \frac{2 \cdot \pi}{\Lambda \cdot \beta}$

$Z0 := \frac{374.73031346\,\Omega}{\Omega}$

Impedance of free space - use the value unitless here because Mathcad does not handle matrix elements of different units

$na(\beta) := 1.7385 + 9.51110^{8} \cdot 2 \cdot exp\left(\frac{-\beta \cdot \frac{\Lambda}{nm}}{18.1467}\right)$

Equation that fits the index measurement of T3, taken by ellipsometry, from St Andrews

Refractive indices for substrate and superstrate

$A := 1.5063$ $B := 5435.6$ $C := 2.7779810^{7}$

$nsub(\beta) := A + \frac{B}{\left(\frac{\beta \cdot \Lambda}{nm}\right)^{2}} + \frac{C}{\left(\frac{\beta \cdot \Lambda}{nm}\right)^{4}}$

Cauchy formula for the NOA

$nsup := 1.3$

Refractive index for thin-layer of immobilised analytes (based on effective medium approximation, Bruggeman)

$s2 := 1.46^{2}$

$s1 := 1.35^{2}$

$sav := 1$

Given

$(1 - p) \cdot \frac{s1 - sav}{s1 + 2 \cdot sav} + p \cdot \frac{s2 - sav}{s2 + 2 \cdot sav} = 0$

$s(p) := Minerr(sav)$

$nb(p) := \sqrt{s(p)}$

$nb(0.5) = 1.4046413614$

Structure

$X := 4$ Total number of layers excluding substrate and superstrate

For user to enter layer structure data - each matrix row represent a layer (layer 1, 2, 3 etc...). The first column is the refractive index and the second column is the layer thickness in nm. First row should indicate the layer closest to the superstrate and then follow the order of the structure up to the last layer before the substrate. The number of rows must match X value right above.

$$Layers(\beta, p) := \begin{pmatrix} nb(p) & 4 \\ 1.5 & 1.5 \\ 2.45 & 20 \\ na(\beta) & 75 \end{pmatrix}$$

$n(\beta, p) := Layers(\beta, p)^{\langle 0 \rangle}$

$L(\beta, p) := Layers(\beta, p)^{\langle 1 \rangle} \cdot nm$

Transfer matrix calculation

Calculation of Mt the transfer matrix of the layers between substrate and superstrate.

$j := 0..X - 1$

$$\alpha(j, \beta, p) := \left[\left(n(\beta, p)_j\right)^2 - \beta^2\right]^{\frac{1}{2}} \quad \alpha sub(\beta) := \left(nsub(\beta)^2 - \beta^2\right)^{\frac{1}{2}} \quad \alpha sup(\beta) := \left(nsup^2 - \beta^2\right)^{\frac{1}{2}}$$

$\Phi(j, \beta, p) := k(\beta) \cdot \alpha(j, \beta, p) \cdot L(\beta, p)_j$

TE modes

$$\gamma(j, \beta, p) := \frac{\alpha(j, \beta, p)}{Z0} \quad \gamma sub(\beta) := \frac{\alpha sub(\beta)}{Z0} \quad \gamma sup(\beta) := \frac{\alpha sup(\beta)}{Z0}$$

TM modes

$$\gamma TM(j, \beta, p) := \frac{\alpha(j, \beta, p)}{\left(n(\beta, p)_j\right)^2} \cdot Z0$$

$$M(j,\beta,p) := \begin{pmatrix} \cos(\Phi(j,\beta,p)) & \frac{-i}{\gamma(j,\beta,p)}\cdot\sin(\Phi(j,\beta,p)) \\ -i\cdot\gamma(j,\beta,p)\cdot\sin(\Phi(j,\beta,p)) & \cos(\Phi(j,\beta,p)) \end{pmatrix}$$

$$MTM(j,\beta,p) := \begin{pmatrix} \cos(\Phi(j,\beta,p)) & \frac{-i}{\gamma TM(j,\beta,p)}\cdot\sin(\Phi(j,\beta,p)) \\ -i\cdot\gamma TM(j,\beta,p)\cdot\sin(\Phi(j,\beta,p)) & \cos(\Phi(j,\beta,p)) \end{pmatrix}$$

$$Mt(\beta,p) := \prod_{j=0}^{X-1} M(j,\beta,p) \qquad MtTM(\beta,p) := \prod_{j=0}^{X-1} MTM(j,\beta,p)$$

$\beta := 1.5, 1.501 .. 1.84$

$Im(\gamma sup(\beta)\cdot Mt(\beta,0.5)_{0,0}+\gamma sup(\beta)\cdot\gamma sub(\beta)\cdot Mt(\beta,0.5)_{0,1}+Mt(\beta,0.5)_{1,0}+\gamma sub(\beta)\cdot Mt(\beta,0.5)_{1,1})$

$Im(\gamma sup(\beta)\cdot Mt(\beta,1)_{0,0}+\gamma sup(\beta)\cdot\gamma sub(\beta)\cdot Mt(\beta,1)_{0,1}+Mt(\beta,1)_{1,0}+\gamma sub(\beta)\cdot Mt(\beta,1)_{1,1})$

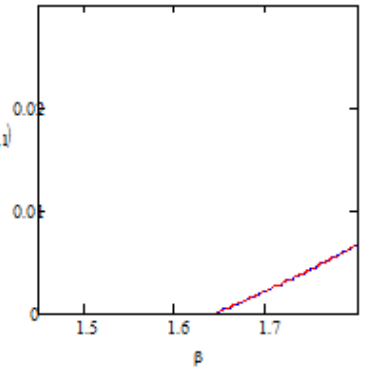

Determination of effective refractive indices for:

TE modes

$i := 0$ $\beta := 1.7$

$neffitem(p) :=$ while $\beta > nsub(\beta)$
- $neff_i \leftarrow$ while $Im(\gamma sup(\beta)\cdot Mt(\beta,p)_{0,0}+\gamma sup(\beta)\cdot\gamma sub(\beta)\cdot Mt(\beta,p)_{0,1}+Mt(\beta,p)_{1,0}+\gamma sub(\beta)\cdot Mt(\beta,p)_{1,1}) > 0.0004$
  - $\beta \leftarrow \beta - 0.0001$
  - β
- $\beta \leftarrow neff_i - 0.04$
- $i \leftarrow i+1$

$neff$

$$nefftemp(0.7) = \begin{pmatrix} 1.6547 \\ 1.4087 \end{pmatrix}$$

$$neff(p) := \left| \begin{array}{l} \text{for } i \in 0..last(nefftemp(p)) - 1 \quad \text{if } last(nefftemp(p)) > 0 \\ \quad neff(p) \leftarrow nefftemp(p)_i \\ neff(p) \leftarrow nefftemp(p) \quad otherwise \\ neff(p) \end{array} \right.$$

$$nefftemp(1)_0 = 1.6551$$

$$i := -1 \qquad K := 2515 \qquad B := 1$$

$$p(x) := B \cdot \frac{x}{K + x} \qquad p(1000) = 0.28449502134$$

$$Neff := \left| \begin{array}{l} \text{for } x \in 0, 1, 5, 10, 50, 100, 200, 300, 400, 500, 1000, 5000, 10000, 50000, 100000, 500000 \\ \quad i \leftarrow i + 1 \\ \quad Neff_i \leftarrow nefftemp(p(x))_0 \\ Neff \end{array} \right.$$

$\Delta neff$

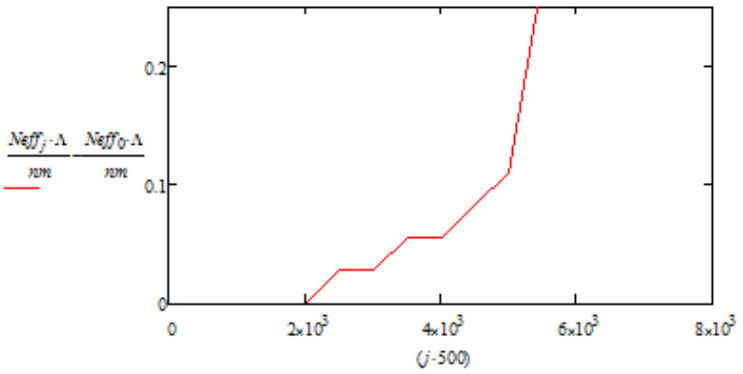

Publications

Journals

[1] Anne-Marie Haughey, Caroline Foucher, Benoit Guilhabert, Alexander Kanibolotsky, Peter Skabara, Glenn A Burley, Martin D Dawson and Nicolas Laurand, *FD 174: Hybrid organic semiconductor lasers for bio-molecular sensing*, Faraday Discussions, Available online ahead of print (2014)

[2] Benoit Guilhabert, C. Foucher, Anne-Marie Haughey, Evren Mutlugun, Yuan Gao, Johannes Herrnsdorf, Handong Sun, Hilmi V Demir, Martin D Dawson and Nicolas Laurand, *Nanosecond colloidal quantum dots lasers for sensing*, Optics Express **22** (6), 7308-7319 (2014)

[3] Anne-Marie Haughey, Benoit Guilhabert, Alexander Kanibolotsky, Peter Skabara, Martin D Dawson, Glenn A Burley and Nicolas Laurand, *An oligofluorene truxene based distributed feedback laser for biosensing applications*, Biosensors and Bioelectronics **54**, 679-686 (2014)

[4] Anne-Marie Haughey, Benoit Guilhabert, Alexander Kanibolotsky, Peter Skabara, Martin D Dawson, Glenn A Burley and Nicolas Laurand, *An organic semiconductor laser based on star-shaped truxene-core oligomers for refractive index sensing*s, Sensors and Actuators B Chemical **185**, 132-139 (2013)

Conferences

(Presenter highlighted by bold letters)

[5] **Anne-Marie Haughey**, Benoit Guilhabert, Martin D Dawson, Glenn A Burley, Nicolas Laurand, *Distributed feedback laser for biosensing applications* (poster), IEEE Engineering in Medicine and Biology Society 2014

[6] **Anne-Marie Haughey**, Benoit Guilhabert, Martin D Dawson, Glenn A Burley, Nicolas Laurand, *Specific biosensing with an oligofluorene truxene distributed feedback laser* (oral), SPIE Europe Conference 2014

[7] **Anne-Marie Haughey**, Sare De Ornellas, Benoit Guilhabert, Martin D Dawson, Glenn A Burley, Nicolas Laurand, *Distributed feedback laser for biosensing applications* (oral), NANOMED 2014

[8] **Benoit Guilhabert**, C. Foucher, Anne-Marie Haughey, Evren Mutlugun, Yuan Gao, Johannes Herrnsdorf, Handong Sun, Hilmi V Demir, Martin D Dawson and Nicolas Laurand, *CdSe/Zns colloidal quantum dots for solution-processed DFB laser sensors and hybrids with inorganic membranes* (poster), Quantum Dot Day, 2014

[9] **Anne-Marie Haughey**, Glenn A Burley, Alexander Kanibolotsky, Peter Skabara, Martin D Dawson and Nicolas Laurand, *Organic distributed feedback laser biosensor* (oral), IEEE Photonics 2013

[10] **Anne-Marie Haughey**, Benoit Guilhabert, Alexander Kanibolotsky, Peter Skabara, Martin D Dawson, Glenn A Burley and Nicolas Laurand, *Organic distributed feedback biosensor* (oral), Photon 12 2012

Sensors and Actuators B 185 (2013) 132–139

Contents lists available at SciVerse ScienceDirect

Sensors and Actuators B: Chemical

journal homepage: www.elsevier.com/locate/snb

An organic semiconductor laser based on star-shaped truxene-core oligomers for refractive index sensing

A.-M. Haughey[a,*], B. Guilhabert[a], A.L. Kanibolotsky[b], P.J. Skabara[b], G.A. Burley[b], M.D. Dawson[a], N. Laurand[a]

[a] Institute of Photonics, SUPA, University of Strathclyde, Glasgow G4 0NW, UK
[b] WestCHEM, Department of Pure and Applied Chemistry, University of Strathclyde, Glasgow G1 1XL, UK

ARTICLE INFO

Article history:
Received 8 January 2013
Received in revised form 28 March 2013
Accepted 1 April 2013
Available online 17 April 2013

Keywords:
Organic
Semiconductor
Laser
Sensor
Plastic
Truxene

ABSTRACT

The sensing capabilities of an all-organic semiconductor distributed feedback laser based on star-shaped truxene-core molecules are described. Two assays are presented as a proof-of-principle demonstration. In the first, concentration changes in the range of 5–60% (v/v) glycerol solution in water were measured with a bulk detection sensitivity of 21 nm per refractive index unit. Secondly, layer-by-layer adsorption of polyelectrolytes to the laser surface, up to a thickness of ≈45 nm, was measured. The experimental results from both assays are compared to, and shown to agree with, a theoretical model. Organic semiconductor lasers of this type have a number of attractions including ease of large-scale fabrication, incorporation into existing assay equipment and no rigid optical alignment constraints for excitation and collection of emission, which makes them well-suited to sensing applications. Therefore, it is expected that this technology will be useful in biosensing applications where label-free samples are investigated.

1. Introduction

Optical sensor technologies are used widely throughout a diverse range of industries and are ideal platforms for highly sensitive and possibly specific, non-intrusive sensing. In particular, their capacity for label-free detection and flexibility for multiplexing and incorporation into lab-on-a-chip systems as well as standard assay formats make them well suited to the detection of biologically relevant analytes within the life sciences. Consequently, a number of optical biosensors including photonic crystal [1,2], surface plasmon-polariton [3] and micro-resonator [4] devices are the focus of intensive investigation, while early versions of some of these technologies can be found in commercially deployed systems [5,6]. Each of these technologies has inherent advantages and disadvantages. For example, micro-resonator based sensors possess very high resolution, making single molecule detection possible, but can be difficult to implement as stringent optical alignment is often required [7,8]. Also, microresonators with a high *Q*-factor generally achieve their higher resolution at the expense of sensitivity, i.e. a reduction in the magnitude of the shift in wavelength per refractive index unit (RIU).

A recent addition to this family of biosensors is the organic distributed feedback (DFB) laser platform [9,10], an active cavity sensor that enables both sensitivity and high resolution. The surface of a DFB laser can be functionalised for the detection of specific analytes; upon binding target analytes, there will be a small change in the refractive index at the laser surface which translates to a corresponding change in the emission wavelength that is detected. Although the *Q*-factor for such laser cavities is typically lower than that of a micro-resonator, this is compensated by the fact that these sensors are active cavities and stimulated emission results in narrow resonances for single mode emission [10]. Hence the resolution of the overall system is high, despite the *Q*-factor of the cavity being moderate. In addition, DFB laser sensors have a number of attractive attributes which are particularly well suited to label-free biosensing applications, including (i) simple implementation; the laser generates and outputs its own coherent (spectrally narrow) light for sensing, therefore relaxing optical alignment tolerances compared to other solutions [10,11], (ii) the platform can be fabricated through solution-processing and soft-material patterning, to enable large scale production [12,13] and (iii) an all-organic laser structure can be made to be mechanically flexible or conformable, thereby providing a platform where the sensing surface need not

* Corresponding author. Tel.: +44 141 548 4666.
E-mail addresses: annemarie.haughey@strath.ac.uk (A.-M. Haughey), benoit.guilhabert@strath.ac.uk (B. Guilhabert), alexander.kanibolotsky@strath.ac.uk (A.L. Kanibolotsky), peter.skabara@strath.ac.uk (P.J. Skabara), glenn.burley@strath.ac.uk (G.A. Burley), m.dawson@strath.ac.uk (M.D. Dawson), nicolas.laurand@strath.ac.uk (N. Laurand).

0925-4005/$ – see front matter © 2013 Elsevier B.V. All rights reserved.
http://dx.doi.org/10.1016/j.snb.2013.04.026

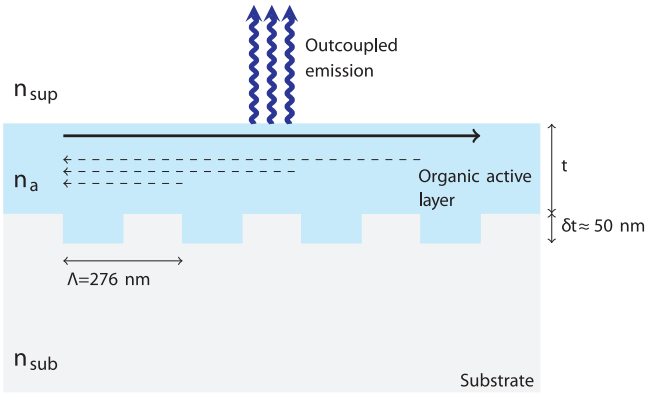

Fig. 1. Schematic representation of the DFB laser structure. The substrate is imprinted with a grating structure with a 276 nm period and a grating depth of 50 nm. The organic active layer is spin-coated directly on top and has a thickness of ≈70 nm. Solid and dashed arrows represent incident and Bragg reflected waves respectively.

be planar and facilitates integration into existing assay equipment [10,14]. Currently their wider utility as a sensing platform has not been extensively explored.

The only DFB laser biosensor reported to date uses a dye-doped polymer (active laser material incorporated in a transparent plastic matrix) as the gain material [9,15]. This biosensor can detect different biomolecules with a sensitivity of 17–100 nm per RIU with resolution of 0.15–0.09 nm, respectively [9,15]. By utilising an organic semiconductor rather than a dye-doped polymer as gain material, there is potential both to match these sensitivity and resolution values and to enhance the overall sensor characteristics. Organic semiconductors are much less prone to quenching than dyes, which makes the use of a dense solid-state film of 'neat' active material for the fabrication of lasers possible [16]. The refractive index of such a neat thin film is greater than that of a dye-doped polymer, leading to higher light-matter interactions and the expectation of higher efficiencies. The lowest reported oscillation thresholds for organic lasers were obtained with neat organic semiconductors [17] and the recently demonstrated LED-pumped plastic lasers were also based on this type of gain material [18]. Finally, organic semiconductors are capable of charge transport [19,20]. Therefore, should the challenges of electrically pumping organic semiconductor lasers be overcome, an organic semiconductor laser sensor would be well positioned to exploit such advances and remove the need for optical excitation of the gain material.

In this paper, we present a DFB laser sensor that consists of a nanostructured plastic substrate over-coated with a thin film of star-shaped, truxene-based light-emitting material acting as the gain region. We demonstrate that the laser sensor can detect changes in bulk glycerol solution concentrations and the thin (<5 nm) layer-by-layer adsorption of polyelectrolytes to the laser surface. The sensing concept, including a simple analytical model used to validate experimental results and inform the fine tuning of the device structure, and the principal characteristics of our lasers are outlined.

2. Materials and methods

2.1. Device concept and design

The laser sensor is based on a second-order vertically emitting DFB laser. The structure consists of a three-layer planar waveguide with a thin gain layer of thickness t and refractive index n_a; and substrate and superstrate layers with refractive indices of n_{sub} and n_{sup} respectively, as shown in Fig. 1. The substrate is patterned with a periodic nanostructure (period, Λ, 276 nm; grating depth, δt, 50 nm) which provides both the out-coupling and feedback mechanism for the laser. The gain layer is an organic semiconductor composed of fluorescent tris(terfluorenyl)truxene (T3): monodisperse star-shaped oligomers which have high photoluminescence quantum yields in both solution and the solid-state and form low-loss waveguiding films onto a substrate when deposited from solution [12,14,21,22]. Low threshold laser oscillation utilising this gain material has recently been demonstrated [22]. T3 has peak absorbance at 370 nm and emission peaks at 425 and 442 nm, with a refractive index of 1.81 at 430 nm in a thin film [22] which is higher than the refractive indices of the substrate and superstrate, i.e. forming a planar waveguide.

Emission from the DFB laser is governed by the Bragg equation, Eq. (1), where λ is the Bragg wavelength (the mode emitted from the laser surface oscillates at or close to this wavelength), n_{eff} is the effective refractive index of the mode (which is a function of the refractive indices of the three layers of the DFB structure and the gain layer thickness), and Λ is the grating period as defined previously.

$$\lambda = n_{eff}\Lambda \quad (1)$$

For a second-order grating, counter-propagating modes couple through the second order of diffraction while the first order couples waves vertically out of the laser structure as shown in Fig. 1. It is this out-coupled laser emission that is detected for wavelength monitoring and hence sensing.

Eq. (1) demonstrates that changes in the effective refractive index result in a change in the wavelength of the emission from the DFB laser. All values used to determine n_{eff}, excluding n_{sup}, are fixed, therefore changes in the optical properties at the DFB laser surface can be detected by monitoring the shift in the emission wavelength of the laser.

2.2. Fabrication of DFB structure

The diffraction grating within the substrate layer was obtained by replicating a silica master grating into Norland 65 optical epoxy (Norland Products Inc., Cranbury, NJ). For this, the epoxy was drop-coated onto the master grating surface and a 15 mm × 15 mm commercially available acetate sheet of 0.1 mm thickness was placed on top of the epoxy which was subsequently photocured with a UV lamp (exposure dose ≈30 J cm^{-2}, spectrum centred at 370 nm). After curing, the grating-imprinted epoxy was peeled from the master grating and cured under the UV lamp for a further 60 min.

The T3 oligomer solution was prepared by adding T3 to toluene (Fisher Scientific, Leicestershire UK) at a concentration of 20 mg mL^{-1}. The solution was vortexed briefly to ensure the T3 was completely dissolved. 20 μL of solution was subsequently spin-coated on the surface of the grating imprinted epoxy at 3.2 krpm for 90 s (toluene is expected to have no effect on the cured epoxy structure as suggested by the supplier [23]). The thickness of the oligomer layer for a range of spinning speed was investigated in order to obtain single transverse mode operation and the maximum shift in Bragg wavelength for each unit change in n_{sup}. It was found that a speed of 3.2 krpm resulted in an oligomer layer of thickness within the region of 70 ± 10.0 nm as measured using atomic force microscopy and in the maximum shift in wavelength as demonstrated for the current structure by experimental and modelled data. This standardised fabrication process results in single mode DFB laser structures for >95% of devices. Spin coating of the oligomer layer is not feasible for large scale production of laser devices. 'Horizontal dipping' is a process that has been used to fabricate similar laser structures over a relatively large surface area [13] and could replace the spin-coating step described here. In

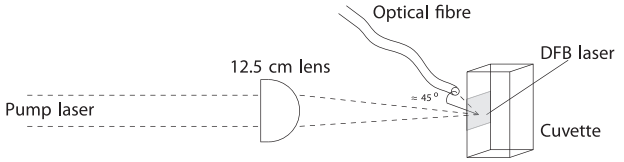

Fig. 2. The optical set-up for pumping the DFB lasers and collecting the outcoupled emission. Light from a frequency-tripled, Q switched Nd:YAG laser was extended and attenuated before being focused by a 12.5 cm lens at an angle of ≈45° on to the DFB laser held within a cuvette. Emission from the DFB laser is collected normal to the laser surface by a 50-μm core optical fibre and transferred to a grating-coupled CCD spectrometer.

addition, room-temperature nanoimprint lithography could provide a method of patterning the oligomer layer directly with a grating structure and simplifying the fabrication further [24,25].

2.3. Model for the determination of the laser wavelength shifts upon sensing

The effective refractive indices of DFB laser modes can be determined by solving Maxwell's equations as described by a number of different numerical models [26–29]. In this paper, a modified one-layer slab model of the DFB laser was used for numerical evaluation of the effective refractive indices of the laser modes, as well as the expected laser wavelength shifts in the case of bulk refractive index sensing. The effect of the periodic modulation induced by the grating was taken into account. The approach involved approximating the DFB laser structure as a periodic juxtaposition of two slab waveguides with the periodicity given by the grating. These two waveguides comprise of a semi-infinite substrate of refractive index n_{sub}, a core region made of the organic T3 oligomer with an index n_a and a thickness t and $t + \delta t$ respectively (δt being the modulation depth of the grating as indicated in Fig. 1) and a semi-infinite superstrate region of index n_{sup}. The value of δt was set at 50 nm, which corresponds to the experimental structures. Intermediate effective refractive indices of these two guides, n_{eff1} and n_{eff2}, were then calculated by considering them independent from each other and solving the corresponding slab waveguide dispersion relation for a given transverse mode [28,29]. The approximation made was that the grating modulation does not affect the laser mode (the difference between n_{eff1} and n_{eff2} at an oligomer layer thickness of 70 nm was calculated as 0.0415), which is considered to be equivalent to an overall guided mode having a refractive index $n_{eff} = (n_{eff1} + n_{eff2})/2$. All transverse modes could be obtained in this way; experimentally, all our lasers were found to oscillate on the fundamental TE_0 mode only and therefore only this mode was analysed. The refractive index dispersions of both the substrate material, Norland 65 optical epoxy, and of the organic semiconductor were also taken into account in the model. The dispersion of the substrate was obtained using Cauchy's equation, Eq. (2), with $A = 1.50631$, $B = 5435.62$ and $C = 2.77798 \times 10^7$ as given by the supplier [30]. The refractive index dispersion for T3 was taken from our published results [22].

$$n_{sub}(\lambda) = A + \frac{B}{\lambda^2} + \frac{C}{\lambda^4} \quad (2)$$

Once the effective refractive index of the mode was determined, the oscillating wavelength of the laser was calculated using Eq. (1). This wavelength was calculated for varying thickness t and for different values of n_{sup} in order to predict the wavelength shift of different solutions. This intuitive model can also be used to investigate optimisation of the DFB sensor structure, for example to improve sensitivity.

For surface sensing (e.g. nano-layer adsorption detection), the model was extended to a multilayer structure, still enclosed between semi-infinite substrate and superstrate [31]. An arbitrary number of layers of thickness t_i and refractive index n_i can be added above the T3 layer, i being the number index of the layer. In this instance, the dispersion relation to be solved depends on the elements of the multilayer transmission matrix [31]. The expected shift for the build-up of polyelectrolytes on top of the laser was calculated for the TE_0 mode. All other parameters were as described above. In the same way, the model could be used to predict the wavelength shift for biomolecule adsorption to the laser surface.

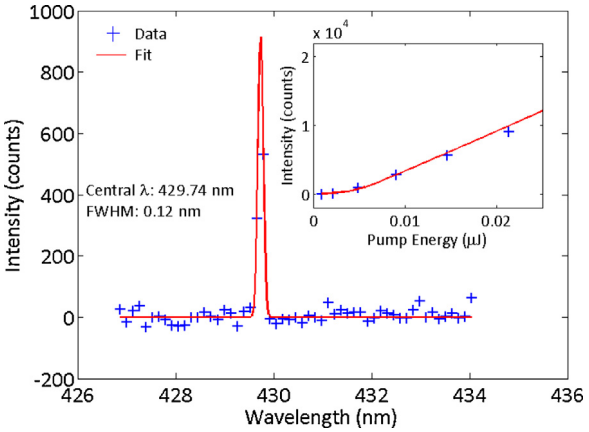

Fig. 3. A representative laser emission spectrum using our DFB laser. Data are fitted to a Gaussian curve in order to determine the peak wavelength. Laser emission is typically observed to be around 430 nm and the linewidth, $\Delta\lambda$, of the spectral peak is at the limit of our spectrometer. The insert shows the emission intensity with increasing pump power, demonstrating a threshold energy of approximately 2.5 nJ.

3. Results

3.1. Optical characterisation

The beam from a frequency-tripled, Q switched Nd:YAG laser (355 nm, 10 Hz repetition rate) was extended and attenuated before being focused by a 12.5 cm lens on the DFB laser held within a quartz cuvette. The DFB laser was attached to one inner face of the cuvette so that the T3 surface was exposed to the solvent within the cuvette. Measurements of the emission from the DFB laser were performed by photopumping the DFB laser through the cuvette wall, at an angle of approximately 45° to the surface normal. Outcoupled emission was collected via a 50-μm core optical fibre, positioned normal to the cuvette surface as shown in Fig. 2. The other end of the fibre was directly plugged into a grating-coupled CCD spectrometer channel with resolution of 0.13 nm.

Fig. 3 shows the laser spectrum observed when the sensor surface is exposed to air. Reducing the pump spot area from 60×10^{-3} mm^2 to 4×10^{-3} mm^2 resulted in a decrease in linewidth, $\Delta\lambda$, from 0.2 nm to the resolution limit of the spectrometer (0.13 nm). The central wavelength and linewidth was determined from a Gaussian fit to the data. As the linewidth of laser emission is at the limit of the spectrometer resolution, spectra are often fitted using only two data points, as shown in Fig. 3, this may lead to a fitting error but it is considered to provide the best estimate of the central wavelength and linewidth [13]. By analogy with passive resonators, a Q-factor ($\lambda/\Delta\lambda$) for a laser oscillator can be defined. Although this factor then refers to different physical processes for different types of devices, it can be universally used to characterise the spectral purity of sensor systems based on spectral measurements. The Q-factor for the overall DFB laser system, as calculated from the fitted data in Fig. 3, is 3580 and is limited here by the resolution of the spectrometer. The inset in Fig. 3 shows the relationship between the laser emission intensity and the pump beam energy,

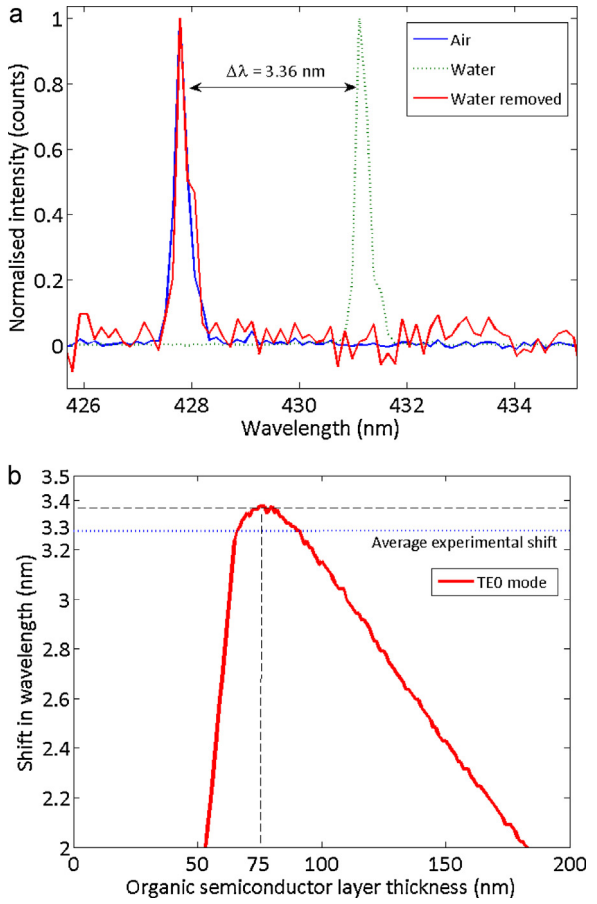

Fig. 4. (a) Typical emission spectra observed in air and water. (b) Modelled shift in wavelength versus thickness of the organic semiconductor layer for DFB laser. At a 75 nm thickness the expected shift in wavelength due to water is 3.38 nm, comparable to the average experimental result of 3.33 ± 0.07 nm.

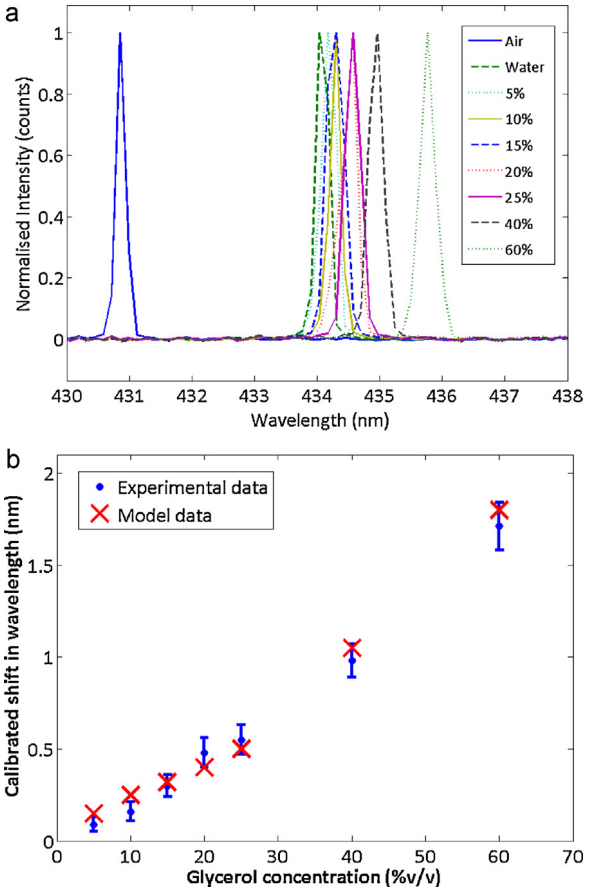

Fig. 5. (a) Redshift in lasing wavelength with increasing glycerol concentration. (b) Comparison of experimental and theoretical shift for increasing glycerol concentration. Error bars indicate the standard deviation between the shift in wavelength observed for each glycerol concentration for different positions within a single laser sensor and between different laser sensors.

demonstrating a threshold energy of 2.5 nJ which corresponds to a fluence of approximately 60 μJ cm^{-2}. In solution, the threshold fluence tends to decrease and is around two times lower than the air measurement.

3.2. Comparison of theoretical and experimental wavelength values

A T3 laser was fabricated as described above and taped to an inner face of a large quartz cuvette (Starna Scientific Ltd, Essex, UK). The T3 laser was optically pumped with a Nd:YAG laser and the optical fibre adjusted for maximum light coupling. The emission spectra were recorded in air; the cuvette was then filled with de-ionised (DI) water (Millipore, Watford UK), refractive index 1.34 at 430 nm, and the spectral data recorded again. The DI water was then pipetted from the cuvette and the emission spectra recorded. A typical set of air–water–air spectra are shown in Fig. 4a. The shift in wavelength observed for the change in refractive index due to the water was on average 3.33 ± 0.07 nm. The theoretical shift in wavelength for the difference in refractive index between air and water was calculated using the model described previously. The output from the model is the expected shift for a range of organic semiconductor layer thicknesses, as shown in Fig. 4b. At a thickness of 75 nm, which is within the thickness range measured for the laser, the expected shift is 3.38 nm, which is very close to the experimental shift.

3.3. Bulk refractive index sensing

Glycerol solutions of varying concentrations, and therefore varying refractive indices, were created by serially diluting 60% (v/v) glycerol in DI water down to a 5% solution. A T3 laser was taped into the cuvette as per previous set-up (Fig. 2). A set of air–water–air emission spectra were recorded before adding the 5% glycerol solution to the cuvette and recording the spectra. The 5% glycerol solution was removed and the emission wavelength returned to the 'air' wavelength before the next glycerol solution was added to the cuvette. This process was repeated for all glycerol concentrations with the emission wavelength returning to the air wavelength upon solution removal each time. The measurements were also repeated for excitation at different positions within the DFB laser sensor. The emission spectra for each of the glycerol measurements are shown in Fig. 5a. Due to small differences in the thickness of the gain layer over the surface area of the DFB laser, and between laser structures, there can be a slight difference between the shifts in emission wavelength per refractive index unit. However, these differences were accounted for by calibrating the glycerol spectra to the shift attributed to water for each set of measurements. The calibrated average shifts in wavelength for each of the glycerol concentrations are shown in Fig. 5b. In addition, there can be small differences between the linewidth for spectra recorded in air and in solution. For example, the linewidth for the initial air spectra, shown in Fig. 5a, and upon removal of the 60% glycerol solution were 0.18 nm and 0.17 nm respectively, and the linewidths for the 5% and 60% glycerol solution spectra

were 0.27 nm and 0.29 nm respectively. It is expected that the small increase in linewidth between air and solution measurements may be due to a slight swelling of the oligomer layer when in solution.

Our theoretical model was also used to generate the expected shift in wavelength for each of the different glycerol concentrations. The refractive indices for each of the glycerol solutions at 450 nm [32] were inserted into the model for n_{sup} and the shift in wavelength for an organic semiconductor layer thickness of 75 nm was recorded. The modelled data are plotted alongside the experimental data in Fig. 5b, showing good agreement.

3.4. Detection of adsorbed nano-layers

In order to demonstrate detection of layer-by-layer adsorption of thin films at the DFB laser sensor surface, a stack of alternately charged polyelectrolyte nano-layers were adsorbed on top of the organic semiconductor. The polyelectrolytes used, poly(ethyleneimine) (PEI), poly(allylamine hydrochloride) (PAH) and poly(sodium 4-styrenesulfonate) (PSS), have been well characterised and are known to form a self-limiting monolayer, the thickness of which can be controlled by varying the salt concentration of the solution. The initial layers closest to the sensor surface are expected to be thinner than subsequent layers, with the thickness increasing until a plateau is reached around the sixth anionic–cationic layer [33,34], at which point alternating layers are expected to have a constant thickness of ≈4–5 nm and a refractive index of 1.49 when deposited from a solution containing 0.9 M NaCl [35]. Polyelectrolyte solutions of anionic PSS (M_W = 70,000) and cationic PAH (M_W = 58,000) and branched-PEI (M_W = 60,000) were prepared without further purification in 0.9 M pH 7 NaCl (all Sigma Aldrich, UK) to a concentration of 5 mg mL^{-1}. The laser fabrication was altered slightly to incorporate mounting of the DFB laser within a small, custom-made demountable cuvette (Comar Instruments, Cambridge, UK) – the substrate was fixed to the inner surface of the cuvette using Norland 65 optical epoxy, photocured under the UV lamp for 3 min before spin-coating 20 μL of 20 mg mL^{-1} T3 solution onto the substrate. Emission spectra in air, water and NaCl were recorded before adding the PEI solution to the cuvette. The solution was left in the cuvette for 10 min and spectra were recorded every 30 s. The PEI solution was removed and the cuvette and laser sensor were washed twice with NaCl. Five sets of PSS–PAH layers were then formed on the laser surface following the same protocol as for the PEI adsorption with two NaCl washes between each new layer. Fig. 6a shows the wavelength shift relative to the shift due to NaCl solution for each of the polyelectrolyte layers with time. The insert in Fig. 6a shows a schematic of the laser sensor with adsorbed polyelectrolyte layers and the refractive index associated with each layer.

The output from the multilayer model with the refractive index of each layer and the superstrate (i.e. NaCl solution) set to 1.49 and 1.36, respectively, is shown in Fig. 6b. The average shift in wavelength for each adsorbed polyelectrolyte layer (refractive index 1.49) obtained from Fig. 6a is also plotted in Fig. 6b considering two scenarios: (i) each layer is considered to be 5 nm thick (blue ×) and (ii) the thicknesses of the first six layers are matched to overlap the modelled data while the subsequent layers are considered to be 5 nm thick (red +). Case (ii) is justified because it takes approximately six deposited layers before uniform adsorption is achieved and subsequent deposited layers have a constant thickness.

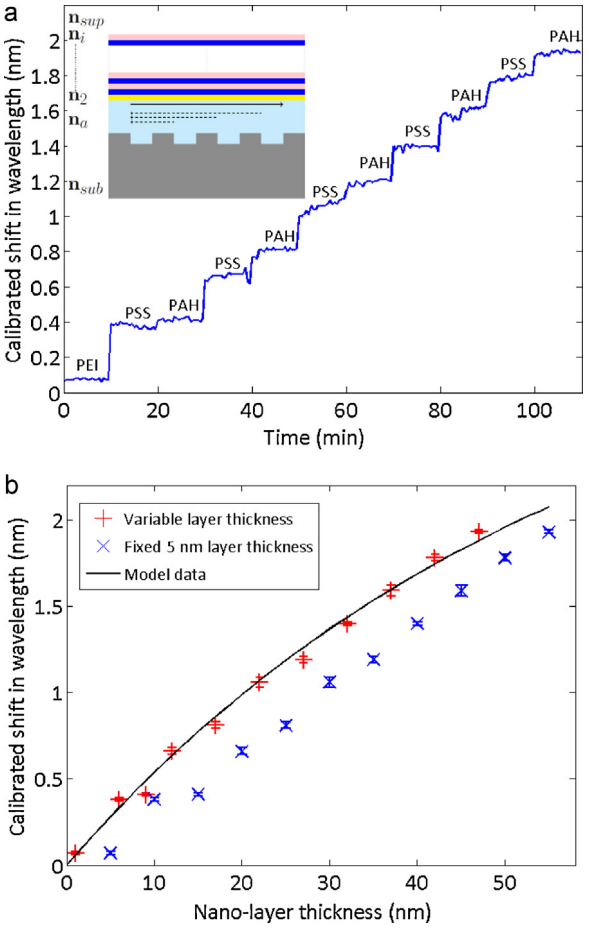

Fig. 6. (a) The increase in wavelength shift with the addition of each polyelectrolyte layer, adsorbed over a 10-min period. Insert schematic shows the laser structure and associated refractive indices for the substrate (n_{sub}), organic oligomer layer (n_a) and superstrate (n_{sup}) with i adsorbed polyelectrolyte layers (n_2 to n_i). (b) The mean shift in wavelength for each adsorbed polyelectrolyte layer is plotted alongside the output from the multilayer model. Error bars indicate the standard deviation of the shift in wavelength over the spectra recorded every 30 s for 10 min.

4. Discussion

Sensitivity and specificity are important factors for any sensor and as the laser sensor signal in this case is a shift in laser emission wavelength, spectral purity is critical. In order to maximise the sensitivity of the DFB laser, the linewidth was minimised by decreasing the size of the focused pump spot. Doing so minimised the number of lateral modes which can oscillate and are known to affect the linewidth [36]. The resulting *Q*-factor of the laser sensor system was found to be 3580 limited here (as mentioned above) by the spectrometer resolution and not the laser itself. Further narrowing of the emission linewidth, via further reduction in the pump spot size and further tuning of the laser structure, and the use of a spectrometer with improved resolution, should lead to an increase in the *Q*-factor for the system. The current laser structures typically have a threshold fluence of approximately 60 μJ cm^{-2} in air and 30 μJ cm^{-2} in DI water. The decrease in threshold when the laser is immersed in a liquid, relative to that in air, is caused by the increase in the superstrate refractive index. This increase pulls the laser mode away from the substrate, which results in a better overlap with the organic semiconductor gain region. The threshold fluence in water corresponds to a power density of the order of 6 kW cm^{-2} and therefore it is expected that optical pumping will eventually be possible with a 'Blu-ray' gallium nitride (GaN) laser diode, as has already been demonstrated for other organic lasers [37]. There is also scope for LED pumping if the threshold is reduced further [18]. Diode-laser and/or LED pumping will be important for the miniaturisation of the sensor system. Reaching these targets will necessitate tuning of the organic semiconductor absorption to the optimum spectral window for GaN technology

(405–450 nm). Large numbers of emission spectra (>360) have been captured for a single position within a DFB laser. Although there is a slight decrease in emission intensity with longer pumping time, the linewidth remains narrow (for example, a linewidth of 0.27 nm and 0.30 nm were recorded for the initial measurement in air and the final measurement after adsorption of 9 PAH–PSS layers respectively, data not shown) and the emission wavelength does not change (for example, the wavelength for the air spectra shown in Fig. 5a is 430.87 nm and upon removal of the 60% glycerol solution the wavelength was 430.86 nm, as determined from a Gaussian fit), demonstrating that the photostability of the gain material is sufficient for such measurements. Nonetheless, work is on-going to improve photostability and reduce the lasing threshold.

The average experimental shift with water (3.33 ± 0.07 nm) agreed well with the modelled value of 3.38 nm. Similarly, data and model match closely in Fig. 5b indicating that the model can be used to predict the shift in wavelength induced by changes in bulk refractive index. Therefore, the theoretical model can be used with confidence to inform design changes to the DFB laser structures that may improve the performance of the sensor.

Fig. 5a shows the shift in wavelength observed across the range of glycerol solutions tested. 5% and 60% glycerol solutions have refractive indices of 1.35 and 1.43 respectively at 450 nm [32] and these values are not expected to be too dissimilar at 430 nm. The experimental and theoretical shift for the 60% glycerol solution was approximately 1.7 nm relative to the shift with DI water. This corresponds to a bulk detection sensitivity ($\lambda_{shift}/\Delta n$), where λ_{shift} is the shift in wavelength and Δn is the change in refractive index, of approximately 21 nm per RIU. This is currently lower than the sensitivity reported for an optimised dye-doped DFB laser sensor ($\approx$100 nm per RIU) [10]. An improvement in the bulk detection sensitivity by optimising the waveguide structure and/or by simply operating at a longer wavelength will be a focus for subsequent sensor designs. For example, reducing the refractive index of the substrate to $\approx$1.35, i.e. making a more symmetric structure and pushing the laser mode towards the sensing region, results in the expected shift for the 60% glycerol solution increasing to 3.7 nm which corresponds to a doubling of the shift observed per RIU. Furthermore, utilising a different organic semiconductor as the gain layer that operates at a laser wavelength of 530 nm, such as [38], and changing the grating period to 340 nm to maintain second-order diffraction, will permit a greater shift in laser wavelength per bulk refractive index change of the superstrate than would be achieved with a laser operating at $\approx$430 nm. Such changes could result in a four times increase in the bulk sensitivity ($\approx$80 nm per RIU). Although bulk detection sensitivity is a value often used to assess optical sensors, the response of the sensor to detection of interactions at the surface provides a more appropriate measure of the sensor performance in biosensing applications.

The adsorption of nano-layers on the laser was performed in order to investigate the capability of detecting adsorption of molecules at the laser surface. The results shown in Fig. 6a demonstrate that our sensor is indeed sensitive enough to detect the addition of each adsorbed nano-layer. Furthermore, Fig. 6 shows that the laser is sensitive to adsorption of nano-layers relatively far from the sensor surface, the effective sensing area extends to >40 nm and preliminary data, not presented here, demonstrates that detection of adsorbed layers >70 nm from the laser surface is possible. Retained sensitivity at some distance from the immediate vicinity of the laser surface will be useful when functionalised layers are constructed on the laser surface in order to facilitate specific adsorption/binding events, which we intend to investigate.

Fig. 6b shows the mean shift in wavelength versus adsorbed layer thickness for the experimental data (i) with layer thickness assumed to be constant (5 nm), (ii) with layer thickness assumed to vary for the initial six layers before an equilibrium thickness of 5 nm is reached and the output from the multilayer model. The mean shift in wavelength due to adsorption of each polyelectrolyte layer correlates well with the output from the multilayer model for surface sensing only when the variation in the thickness of the first polyelectrolytes layers is taken into account. The thickness of adsorbed layers is expected to vary with the layers closest to the surface being thinner than the outermost layers which are expected to have a constant thickness of approximately 4–5 nm for the solution conditions (0.9 M NaCl) [35]. Therefore, scenario (ii) is expected to be a better representation of the actual thickness of the initial polyelectrolyte layers. We intend to test this model further with specific adsorption and binding of biomolecules to the laser surface.

5. Conclusion

An all-organic plastic DFB laser based on custom-synthesised semiconductor molecules that is simple to fabricate, does not require complex optical alignment and can be directly incorporated into existing assay equipment, and has an emission wavelength sensitive to changes in conditions at its surface is demonstrated. Changes in refractive index of bulk solutions and the layer-by-layer adsorption of polyelectrolytes to the laser surface were measured and those experimental results were shown to correlate well with theoretical results from a simple numerical model. Further improvement in the sensitivity of the laser sensor can be achieved by fine tuning the laser structure, e.g. decreasing the refractive index of the substrate and the emission wavelength of the organic semiconductor, and can be informed by the model. Furthermore, the use of a truxene-based organic oligomer with specific functional groups as the gain medium means that incorporation of specific biomolecular probes into the organic oligomer backbone itself should be feasible which in turn would simplify the biosensor fabrication and could improve the sensitivity in certain cases; for example by enabling volume sensing on top of surface sensing if the active layer was made permeable to analytes. Future work will focus on detecting specific binding events at the laser surface. In particular, functionalisation of adsorbed nano-layers with biomolecules will be investigated in parallel with direct functionalisation of the organic oligomer. It is anticipated that the DFB laser sensor will be suitable for clinical and life-science sensing applications.

Acknowledgement

This work was supported by EPSRC grants EP/J021962/1 and EP/I029141/1 and is hereby gratefully acknowledged.

References

[1] M. Kristensen, A. Krüger, N. Groothoff, J. García-Rupérez, V. Toccafondo, J. García-Castelló, M.J.B. nuls, S. Peransi-Llopis, A. Maquieira, Photonic crystal biosensor chip for label-free detection of bacteria, Optical Sensors, Optical Society of America (2011) SWB1 http://www.opticsinfobase.org/abstract.cfm?URI=Sensors-2011-SWB1

[2] S.M. Shamah, B.T. Cunningham, Label-free cell-based assays using photonic crystal optical biosensors, Analyst 136 (2011) 1090–1102, http://dx.doi.org/10.1039/C0AN00899K.

[3] V. Koubová, E. Brynda, L. Karasová, J. Škvor, J. Homola, J. Dostálek, P. Tobiška, J. Rošický, Detection of foodborne pathogens using surface plasmon resonance biosensors, Sensors and Actuators B: Chemical 74 (1–3) (2001) 100–105, http://dx.doi.org/10.1016/S0925-4005(00)00717-6, http://www.sciencedirect.com/science/article/pii/S0925400500007176

[4] M. Baaske, F. Vollmer, Optical resonator biosensors: Molecular diagnostic and nanoparticle detection on an integrated platform, ChemPhysChem 13 (2) (2012) 427–436, http://dx.doi.org/10.1002/cphc.201100757 http://dx.doi.org/10.1002/cphc.201100757

[5] J. Homola, S.S. Yee, G. Gauglitz, Surface plasmon resonance sensors: review, Sensors and Actuators B: Chemical 54 (1-2) (1999) 3–15, http://dx.doi.org/10.1016/S0925-4005(98)00321-9 http://www.sciencedirect.com/science/article/pii/S0925400598003219

[6] B. Cunningham, J. Qiu, P. Li, B. Lin, Enhancing the surface sensitivity of colorimetric resonant optical biosensors, Sensors and Actuators B: Chemical 87 (2) (2002) 365–370, http://dx.doi.org/10.1016/S0925-4005(02)00273-3 http://www.sciencedirect.com/science/article/pii/S0925400502002733
[7] F. Volmer, S. Arnold, Whispering-gallery-mode biosensing: label-free detection down to single molecules, Nature Methods 5 (7) (2008) 591–596, http://dx.doi.org/10.1038/nmeth.1221 http://www.nature.com/nmeth/journal/v5/n7/full/nmeth.1221.html
[8] A.M. Armani, R.P. Kulkarni, S.E. Fraser, R.C. Flagan, K.J. Vahala, Label-free, single-molecule detection with optical microcavities, Science 317 (5839) (2007) 783–787, http://dx.doi.org/10.1126/science.1145002, http://www.sciencemag.org/content/317/5839/783.full.pdf, http://www.sciencemag.org/content/317/5839/783.abstract
[9] M. Lu, S.S. Choi, C.J. Wagner, J.G. Eden, B.T. Cunningham, Label free biosensor incorporating a replica-molded, vertically emitting distributed feedback laser, Applied Physics Letters 92 (26) (2008) 261502, http://dx.doi.org/10.1063/1.2913007 http://dx.doi.org/doi/10.1063/1.2913007
[10] Y. Tan, C. Ge, A. Chu, M. Lu, W. Goldshlag, C.S. Huang, A. Pokhriyal, S. George, B. Cunningham, Plastic-based distributed feedback laser biosensors in microplate format, Sensors Journal, IEEE 12 (5) (2012) 1174–1180, http://dx.doi.org/10.1109/JSEN.2011.2163933.
[11] F. Vollmer, D. Braun, A. Libchaber, M. Khoshsima, I. Teraoka, S. Arnold, Protein detection by optical shift of a resonant microcavity, Applied Physics Letters 80 (21) (2002) 4057–4059, http://dx.doi.org/10.1063/1.1482797.
[12] B. Guilhabert, N. Laurand, J. Herrnsdorf, Y. Chen, A.R. Mackintosh, A.L. Kanibolotsky, E. Gu, P.J. Skabara, R.A. Pethrick, M.D. Dawson, Amplified spontaneous emission in free-standing membranes incorporating star-shaped monodisperse p-conjugated truxene oligomers, Journal of Optics 12 (3) (2010) 035503 http://stacks.iop.org/2040-8986/12/i=3/a=035503
[13] C. Ge, M. Lu, X. Jian, Y. Tan, B.T. Cunningham, Large-area organic distributed feedback laser fabricated by nanoreplica moulding and horizontal dipping, Optics Express 18 (12) (2010) 12980–12991, http://dx.doi.org/10.1364/OE.18.012980 http://www.opticsexpress.org/abstract.cfm?URI=oe-18-12-12980
[14] J. Herrnsdorf, B. Guilhabert, Y. Chen, A. Kanibolotsky, A. Mackintosh, R. Pethrick, P. Skabara, E. Gu, N. Laurand, M. Dawson, Flexible blue-emitting encapsulated organic semiconductor dfb laser, Optics Express 18 (25) (2010) 25535–25545, http://dx.doi.org/10.1364/OE.18.025535 http://www.opticsexpress.org/abstract.cfm?URI=oe-18-25-25535
[15] M. Lu, S.S. Choi, U. Irfan, B.T. Cunningham, Plastic distributed feedback laser biosensor, Applied Physics Letters 93 (11) (2008), http://dx.doi.org/10.1063/1.2987484, 111113-111113-3.
[16] M.A. Díaz-García, F. Hide, B.J. Schwartz, M.R. Andersson, Q. Pei, A.J. Heeger, Plastic lasers: Semiconducting polymers as a new class of solid-state laser materials, Synthetic Metals 84 (1–3) (1997) 455–462, http://dx.doi.org/10.1016/S0379-6779(97)80829-6, International Conference on Science and Technology of Synthetic Metals. http://www.sciencedirect.com/science/article/pii/S0379677997808296
[17] C. Karnutsch, C. Pflumm, G. Heliotis, J.C. deMello, D.D.C. Bradley, J. Wang, T. Weimann, V. Haug, C. Gartner, U. Lemmer, Improved organic semiconductor lasers based on a mixed-order distributed feedback resonator design, Applied Physics Letters 90 (13) (2007) 131104, http://dx.doi.org/10.1063/1.2717518 http://link.aip.org/link/?APL/90/131104/1
[18] Y. Yang, G.A. Turnbull, I.D.W. Samuel, Hybrid optoelectronics: a polymer laser pumped by a nitride light-emitting diode, Applied Physics Letters 92 (16) (2008) 163306, http://dx.doi.org/10.1063/1.2912433 http://link.aip.org/link/?APL/92/163306/1
[19] J. Roncali, P. Leriche, A. Cravino, From one- to three-dimensional organic semiconductors: In search of the organic silicon? Advanced Materials 19 (16) (2007) 2045–2060, http://dx.doi.org/10.1002/adma.200700135 http://dx.doi.org/10.1002/adma.200700135
[20] I.D.W. Samuel, G.A. Turnbull, Organic semiconductor lasers, Chemical Reviews 107 (4) (2007) 1272–1295, http://dx.doi.org/10.1021/cr050152i, http://pubs.acs.org/doi/pdf/10.1021/cr050152i, http://pubs.acs.org/doi/abs/10.1021/cr050152i
[21] A.L. Kanibolotsky, R. Berridge, P.J. Skabara, I.F. Perepichka, D.D.C. Bradley, M. Koeberg, Synthesis and properties of monodisperse oligofluorene-functionalized truxenes: highly fluorescent star-shaped architectures, Journal of the American Chemical Society 126 (42) (2004) 13695–13702, http://dx.doi.org/10.1021/ja039228n, pMID: 15493927, http://pubs.acs.org/doi/pdf/10.1021/ja039228n, http://pubs.acs.org/doi/abs/10.1021/ja039228n
[22] G. Tsiminis, Y. Wang, P.E. Shaw, A.L. Kanibolotsky, I.F. Perepichka, M.D. Dawson, P.J. Skabara, G.A. Turnbull, I.D.W. Samuel, Low-threshold organic laser based on an oligofluorene truxene with low optical losses, Applied Physics Letters 94 (24) (2009), http://dx.doi.org/10.1063/1.3152782, 243304-243304-3.
[23] (March 2013). https://www.norlandprod.com/techrpts/chemresit.html
[24] D. Pisignano, L. Persano, P. Visconti, R. Cingolani, G. Gigli, G. Barbarella, L. Favaretto, Oligomer-based organic distributed feedback lasers by room-temperature nanoimprint lithography, Applied Physics Letters 83 (13) (2003) 2545–2547, http://dx.doi.org/10.1063/1.1613362 http://link.aip.org/link/?APL/83/2545/1
[25] E. Mele, A. Camposeo, R. Stabile, P.D. Carro, F.D. Benedetto, L. Persano, R. Cingolani, D. Pisignano, Polymeric distributed feedback lasers by room-temperature nanoimprint lithography, Applied Physics Letters 89 (13) (2006) 131109, http://dx.doi.org/10.1063/1.2357116 http://link.aip.org/link/?APL/89/131109/1
[26] C.L.C. Smith, J.U. Lind, C.H. Nielsen, M.B. Christiansen, T. Buss, N.B. Larsen, A. Kristensen, Enhanced transduction of photonic crystal dye lasers for gas sensing via swelling polymer film, Optics. Letters 36 (8) (2011) 1392–1394, http://dx.doi.org/10.1364/OL.36.001392 http://ol.osa.org/abstract.cfm?URI=ol-36-8-1392
[27] C. Vannahme, C.L.C. Smith, M.B. Christiansen, A. Kristensen, Emission wavelength of multilayer distributed feedback dye lasers, Applied Physics Letters 101 (15) (2012) 151123, http://dx.doi.org/10.1063/1.4759131 http://link.aip.org/link/?APL/101/151123/1
[28] P.K. Tien, Light waves in thin films and integrated optics, Applied Optics 10 (11) (1971) 2395–2413, http://dx.doi.org/10.1364/AO.10.002395 http://ao.osa.org/abstract.cfm?URI=ao-10-11-2395
[29] H. Kogelnik, An introduction to integrated optics, IEEE Transactions on Microwave Theory and Techniques 23 (1) (1975) 2–16, http://dx.doi.org/10.1109/TMTT.1975.1128500.
[30] (September 2012). http://www.thorlabs.com/newgrouppage9.cfm?objectgroup_id=196
[31] J. Chilwell, I. Hodgkinson, Thin-films field-transfer matrix theory of planar multilayer waveguides and reflection from prism-loaded waveguides, Journal of the Optical Society of America A 1 (7) (1984) 742–753, http://dx.doi.org/10.1364/JOSAA.1.000742 http://josaa.osa.org/abstract.cfm?URI=josaa-1-7-742
[32] J. Krivacic, D. Urry, Ultraviolet and visible refractive indices of spectroquality solvents: II. aqueous solutions of polyhydroxy solutes, Analytical Biochemistry 43 (1) (1971) 240–246, http://dx.doi.org/10.1016/0003-2697(71)90129-1 http://www.sciencedirect.com/science/article/pii/0003269771901291
[33] J. Schmitt, T. Gruenewald, G. Decher, P.S. Pershan, K. Kjaer, M. Loesche, Internal structure of layer-by-layer adsorbed polyelectrolyte films: a neutron and x-ray reflectivity study, Macromolecules 26 (25) (1993) 7058–7063, http://dx.doi.org/10.1021/ma00077a052, http://pubs.acs.org/doi/pdf/10.1021/ma00077a052, http://pubs.acs.org/doi/abs/10.1021/ma00077a052
[34] M. Lösche, J. Schmitt, G. Decher, W.G. Bouwman, K. Kjaer, Detailed structure of molecularly thin polyelectrolyte multilayer films on solid substrates as revealed by neutron reflectometry, Macromolecules 31 (25) (1998) 8893–8906, http://dx.doi.org/10.1021/ma980910p, http://pubs.acs.org/doi/pdf/10.1021/ma980910p, http://pubs.acs.org/doi/abs/10.1021/ma980910p
[35] G. Ladam, P. Schaad, J.C. Voegel, P. Schaaf, G. Decher, F. Cuisinier, In situ determination of the structural properties of initially deposited polyelectrolyte multilayers, Langmuir 16 (3) (2000) 1249–1255, http://dx.doi.org/10.1021/la990650k, http://pubs.acs.org/doi/pdf/10.1021/la990650k, http://pubs.acs.org/doi/abs/10.1021/la990650k
[36] S. Riechel, U. Lemmer, J. Feldmann, T. Benstem, W. Kowalsky, U. Scherf, A. Gombert, V. Wittwer, Laser modes in organic solid-state distributed feedback lasers, Applied Physics B: Lasers and Optics 71 (2000) 897–900, http://dx.doi.org/10.1007/s003400000467.
[37] T. Riedl, T. Rabe, H.-H. Johannes, W. Kowalsky, J. Wang, T. Weimann, P. Hinze, B. Nehls, T. Farrell, U. Scherf, Tunable organic thin-film laser pumped by an inorganic violet diode laser, Applied Physics Letters 88 (24) (2006), http://dx.doi.org/10.1063/1.2211947.
[38] A. Rose, Z. Zhu, C. Madigan, T. Swager, V. Bulovic, Sensitivity gains in chemosensing by lasing action in organic polymers, Nature 434 (7035) (2005) 876–879, http://dx.doi.org/10.1038/nature03438.

Biographies

Anne-Marie Haughey received the M.Phys. degree in physics from University of Edinburgh, U.K., in 2007. She was a Knowledge Transfer Associate with University of Dundee and LUX Innovate from 2007 until 2010. She is currently working towards an Eng.D. in medical devices with the Institute of Photonics, Glasgow.

Benoit Guilhabert received the Engineering degree from the École Nationale Supérieure d'Ingénieurs du Mans, Le Mans, France, in 2003, the D.E.A. degree in optical sensors and instrumentation from the Université du Maine, Le Mans, in 2004, and the Ph.D. degree from the University of Strathclyde, Glasgow, U.K., in 2008. He is currently a Researcher with the Institute of Photonics, Glasgow.

Alexander L. Kanibolotsky being on leave from the Institute of Physical Organic and Coal Chemistry of the National Academy of Sciences of Ukraine (IPOCC NASU), where he holds the position of Senior Research Scientist, is currently Research Fellow in the group of Professor Peter J. Skabara at the University of Strathclyde. His current research activities are in the synthesis and characterisation of molecular and macromolecular systems for electronic and optoelectronic applications.

Peter J. Skabara holds the Young Chair of Chemistry and is currently Head of Pure and Applied Chemistry at the University of Strathclyde. The main research theme in the Skabara group is the synthesis and application of conjugated materials as organic semiconductors. The activities involve the preparation and characterisation of heteroatomic molecular, oligomeric and polymeric materials (electron donors), as well as fluorene derivatives (electron acceptors or monodisperse oligomers).

Glenn A. Burley received his Bachelor in Medicinal Chemistry in 1996 and his Ph.D. in synthetic organic chemistry in 2000. After a postdoctoral position with the late Professor Roger Taylor and Professor Sir Harry Kroto (2001–2003), Glenn was awarded an Alexander von Humboldt research fellowship in 2006 and conducted research in the area of nucleic acid chemistry within the group of Professor Thomas Carell (University of Munich, Germany). Glenn is currently a Senior Lecturer in the Department of Pure & Applied Chemistry at the University of Strathclyde.

Martin D. Dawson received the Ph.D. degree in laser physics from Imperial College, London, U.K., in 1985. Since then, he was a Post-Doctoral Researcher with North Texas State University, Denton, and the University of Iowa, Iowa City. In 1991, he joined SLE Oxford, U.K., as a Senior Researcher. Since 1996, he has been with the Institute of Photonics, University of Strathclyde, Glasgow, U.K., where he was promoted to Professor in 2001.

Nicolas Laurand received the Engineering degree in optics and optoelectronics from the École Nationale Supérieure des Sciences Appliquées et de Technologie, Lannion, France, in 2000, and the Ph.D. degree from the University of Strathclyde, Glasgow, U.K., in 2006. He was an Optical Engineer with DiCon Fiberoptics, Richmond, CA, from 2000 until 2003. He is currently an Associate Team Leader with the Institute of Photonics, Glasgow.

Biosensors and Bioelectronics 54 (2014) 679–686

Contents lists available at ScienceDirect

Biosensors and Bioelectronics

journal homepage: www.elsevier.com/locate/bios

An oligofluorene truxene based distributed feedback laser for biosensing applications ☆

Anne-Marie Haughey [a,*], Benoit Guilhabert [a], Alexander L Kanibolotsky [b], Peter J Skabara [b], Martin D Dawson [a], Glenn A Burley [b,*], Nicolas Laurand [a,*]

[a] Institute of Photonics, SUPA, University of Strathclyde, Glasgow G4 0NW, UK
[b] WestCHEM, Department of Pure and Applied Chemistry, University of Strathclyde, Glasgow G1 1XL, UK

ARTICLE INFO

Article history:
Received 4 October 2013
Received in revised form
14 November 2013
Accepted 18 November 2013
Available online 25 November 2013

Keywords:
Organic
Laser
Biosensor
Oligofluorene truxene

ABSTRACT

The first example of an all-organic oligofluorene truxene based distributed feedback laser for the detection of a specific protein–small molecule interaction is reported. The protein avidin was detected down to 1 μg mL^{-1} using our biotin-labelled biosensor platform. This interaction was both selective and reversible when biotin was replaced with desthiobiotin. Avidin detection was not perturbed by Bovine Serum Albumin up to 50,000 μg mL^{-1}. Our biosensor offers a new detection platform that is both highly sensitive, modular and potentially re-usable.

1. Introduction

Evanescent optical sensors are analytical devices that measure changes in refractive index at the device surface. These sensors are highly attractive medical diagnostic platforms for the following reasons: (i) they provide a sensitive platform for the label-free detection of a range of analytes, possibly in real-time, (ii) they offer the potential for the detection of multiple analytes (multiplexing), (iii) they can be integrated into lab-on-chip devices and (iv) their photon-based detection method is non-contact and non-destructive. The latter characteristic gives optical biosensors a number of distinct advantages over sensors based on other transducer technologies, such as electrochemical or acoustic sensors, including unrivaled sensitivity and imperviousness to extraneous effects such as disturbance from ionizing radiation and stray impedances (Ramsden, 1997). Optically pumped distributed feedback (DFB) laser sensors represent an important category of evanescent optical biosensor and have significant potential as a versatile platform technology for the detection of biomolecules. Like other surface sensors, DFB laser sensors can be primed to detect specific analytes by functionalizing the device surface with probe molecules that selectively bind to the analyte of interest (Lu et al., 2008b; Tan et al., 2012). A change in the laser emission wavelength, as a function of analyte binding to the probe, is then used as the signal transduction event. As these sensors are based on an active cavity, where light generated close to resonance with the DFB cavity is amplified by stimulated emission, the resulting laser emission is spectrally narrow. Therefore, high spectral resolution can be achieved in parallel with excellent sensitivity (Tan et al., 2012). Furthermore, because the sensor generates and outputs its own coherent light for sensing, precise and cumbersome optical alignment (required for many optical sensors, microresonator-based evanescent sensors and plasmonic sensors for example Armani et al., 2007; Vollmer et al., 2002) is not necessary, potentially reducing the footprint and cost of the device (Tan et al., 2012; Yang et al., 2008).

We present in this work, for the first time to our knowledge, an all-organic DFB laser biosensing platform using an *organic semiconductor gain medium*. This provides highly sensitive analyte detection which, importantly, is shown to be *reversible*. The specific organic semiconductor used is composed of neat fluorescent tris(terfluorenyl)truxene (T3) which is a monodisperse star-shaped oligomer (Kanibolotsky et al., 2004). In comparison to conjugated polymers, monodisperse oligomers are characterized by well-defined and uniform molecular structure as well as superior chemical purity, characteristics that are critical to the

* Corresponding authors. Tel.: +44 141 548 4120.
E-mail addresses: annemarie.haughey@strath.ac.uk (A.-M. Haughey), benoit.guilhabert@strath.ac.uk (B. Guilhabert), alexander.kanibolotsky@strath.ac.uk (A. L Kanibolotsky), peter.skabara@strath.ac.uk (P. J Skabara), m.dawson@strath.ac.uk (M. D Dawson), glenn.burley@strath.ac.uk (G. A Burley), nicolas.laurand@strath.ac.uk (N. Laurand).

0956-5663/$ - see front matter © 2013 The Authors. Published by Elsevier B.V. All rights reserved.
http://dx.doi.org/10.1016/j.bios.2013.11.054

performance and reproducibility of our DFB laser sensors. Furthermore, the advantages of using an organic semiconductor as the gain material, rather than the dye-doped polymers of current DFB laser sensors (Lu et al., 2008a, 2008b), include high resistance to photo-emission quenching, excellent thin film processability and a higher refractive index (Díaz-García et al., 1997). The latter results in a higher confinement of the laser mode and to an enhancement of the evanescent field interaction with the laser surface and hence sensitivity. Recently we reported that bulk solution refractive index changes can be detected with a T3 DFB laser sensor and that the sensor surface is amenable to adsorption of polyelectrolytes (Haughey et al., 2013). We have also demonstrated that the layer-by-layer adsorption of polyelectrolytes continued to be resolved beyond a stack thickness of 40 nm. The 'plastic' nature of our DFB laser devices means that large scale production is straight-forward, as they can be fabricated using well established solution-processing and soft material patterning processes (Guilhabert et al., 2010; Ge et al., 2010). In addition, plastic DFB laser sensors can also be integrated into existing assay equipment, such as microtiter plates, which are routinely used for high-throughput biosensing measurements (Tan et al., 2012).

Herein we demonstrate that the addition of a polyphenylalanine lysine (PPL) polymer monolayer, onto the T3 gain layer, provides solvent-accessible functional groups for functionalization with a biotin probe that can detect avidin down to 1 μg mL^{-1}. The avidin/biotin system was used to demonstrate biomolecular analyte/receptor interaction at the sensor surface as it has a low dissociation constant (K_d) of $\approx 10^{-15}$ M and therefore produces a very stable biotin–avidin complex (Green, 1975). Furthermore, we show that detection of avidin is both specific and reversible by functionalizing the surface with desthiobiotin, which has a lower affinity for avidin, and observe avidin release from the desthiobiotin surface by the addition of biotin, demonstrating the potential to 're-use' this sensor.

2. Methods

2.1. Materials

PPL (MW 20,000–50,000), poly-L-lysine (PL) (MW 30,000–70,000), polyethyleneimine (PEI) (MW 750,000), phosphate buffered saline (PBS) tablets, sodium chloride (NaCl) tablets, bovine serum albumin (BSA) and Dimethyl Sulfoxide (DMSO) were purchased from Sigma Aldrich. Toluene, avidin and sulfo-N-hydroxysuccinimide biotin (NHS-biotin) were purchased from Fisher Scientific UK. N-hydroxysuccinimide desthiobiotin (NHS-desthiobiotin) was purchased from Berry&Associates Inc. T3 is synthesized in-house. The structures of the T3, polyelectrolytes, NHS-biotin and NHS-desthiobiotin used in this study are shown in Fig. 1. Norland 65 (optical epoxy used for laser substrate) was acquired from Norland Products. Water for experiments was purified by a Milli-Q system (Millipore). All chemicals were used as received. Silica master gratings were fabricated to our design at MC2, Chalmers University, Sweden. A custom-made demountable cuvette used throughout the study, was purchased from Comar Instruments.

2.2. Fabrication of DFB laser device

The diffraction grating imprinted substrate was obtained by replicating a silica master grating into a photo-curable optical epoxy. For this, the Norland 65 was drop-coated onto a silica master grating surface and a 15 mm x 15 mm commercially available acetate sheet of 0.1 mm thickness was placed on top of the epoxy. The epoxy was photo-cured with a UV lamp for 50 s, (exposure dose ≈ 300 J cm^{-2}, spectrum centred at 370 nm) and the grating-imprinted epoxy was peeled from the master grating. The epoxy/acetate sheet was trimmed to ≈ 7 mm $\times$ 12 mm and further curing of the substrate was performed under the UV lamp for an additional 60 min. Just prior to use, the grating-imprinted epoxy was fixed to the flat surface of a demountable cuvette using a drop of Norland 65 and cured for 4 minutes with the UV lamp.

A toluene solution of T3 (20 mg mL^{-1}) was spin-coated on the surface of the grating imprinted epoxy at 3.2 krpm for 90 s. Toluene is reported to have no effect on the cured epoxy, therefore, we do not expect any deformation of the grating structure (Norland, 2013). The thickness of the T3 layer for a range of spinning speeds has been investigated to optimize laser operation for single transverse mode emission and the maximum shift in Bragg wavelength for each unit change in superstrate refractive index. A speed of 3.2 krpm resulted in a T3 layer thickness of $\approx 70 \pm 10.0$ nm and $> 95\%$ of devices fabricated demonstrate single transverse mode (TE_0) emission.

2.3. Fabrication of the T3 biosensing platform

In order to exploit the DFB laser for sensing specific analytes, the T3 surface was coated with a polyelectrolyte monolayer (e.g. PPL) to assimilate amine functionality to the sensor surface; biotin groups were then incorporated on the sensor by coupling with NHS-biotin. This method has been used to facilitate detection of a range of analytes (Ruiz-Taylor et al., 2001; Jenison et al., 2001).

2.4. Characterisation of the optical properties of the DFB lasers

The beam of a frequency-tripled, Q-switched Nd:YAG laser (355 nm, 10 Hz repetition rate, 5 ns pulses) was used to excite the laser sensor, fixed within the demountable cuvette, with a spot of ≈ 24 μm by ≈ 50 μm. Measurements of emission from the laser sensor were performed by photopumping the sensor structure through the glass cuvette and epoxy substrate, at an angle of $\approx 45^\circ$ to the surface normal. Pumping at an angle of $\approx 45^\circ$ to the surface normal is done to make collection of laser emission (which is normal to the sensor surface) as simple as possible. The lasers could be pumped transversally, i.e. in the direction perpendicular to the organic thin-film. In other words, 'coupling' *per se* of the pump into the film plane is not necessary. The only requirement is that the pump hits an area of the laser (within the 5 $\times$ 5 mm active surface). Vertical outcoupled emission through the substrate was collected via a 50−μm core optical fiber, positioned normal to the cuvette surface. The fiber was connected to a grating-coupled CCD spectrometer channel that had a resolution of 0.13 nm.

2.5. Specific avidin detection

Polyelectrolyte functionalized surfaces were achieved using similar protocols reported previously (Al-Hakim and Hull, 1986; Kim et al., 2005). PEI was prepared in 0.9 M NaCl to a concentration of 5 mg mL^{-1}. The laser sensor was washed with 0.9 M NaCl before immersing the laser in PEI solution for 10 min. After removal of the PEI solution, the sensor was washed with NaCl and then 10 mM pH 7.4 PBS. The emission wavelength from the sensor, whilst immersed in PBS, was recorded. NHS-biotin, dissolved in 10 mM PBS to a concentration of 0.2 mg mL^{-1}, was added to the cuvette for 20 min. The emission wavelength was recorded upon adding and prior to removal of the biotin solution. The NHS-biotin solution was removed and the cuvette was washed with PBS before recording the emission wavelength in PBS. A dilution series of Avidin (1–500,000 ng mL^{-1}) in 10 mM PBS was used to determine the limit of detection of the sensing platform. The emission wavelength was recorded upon immersion

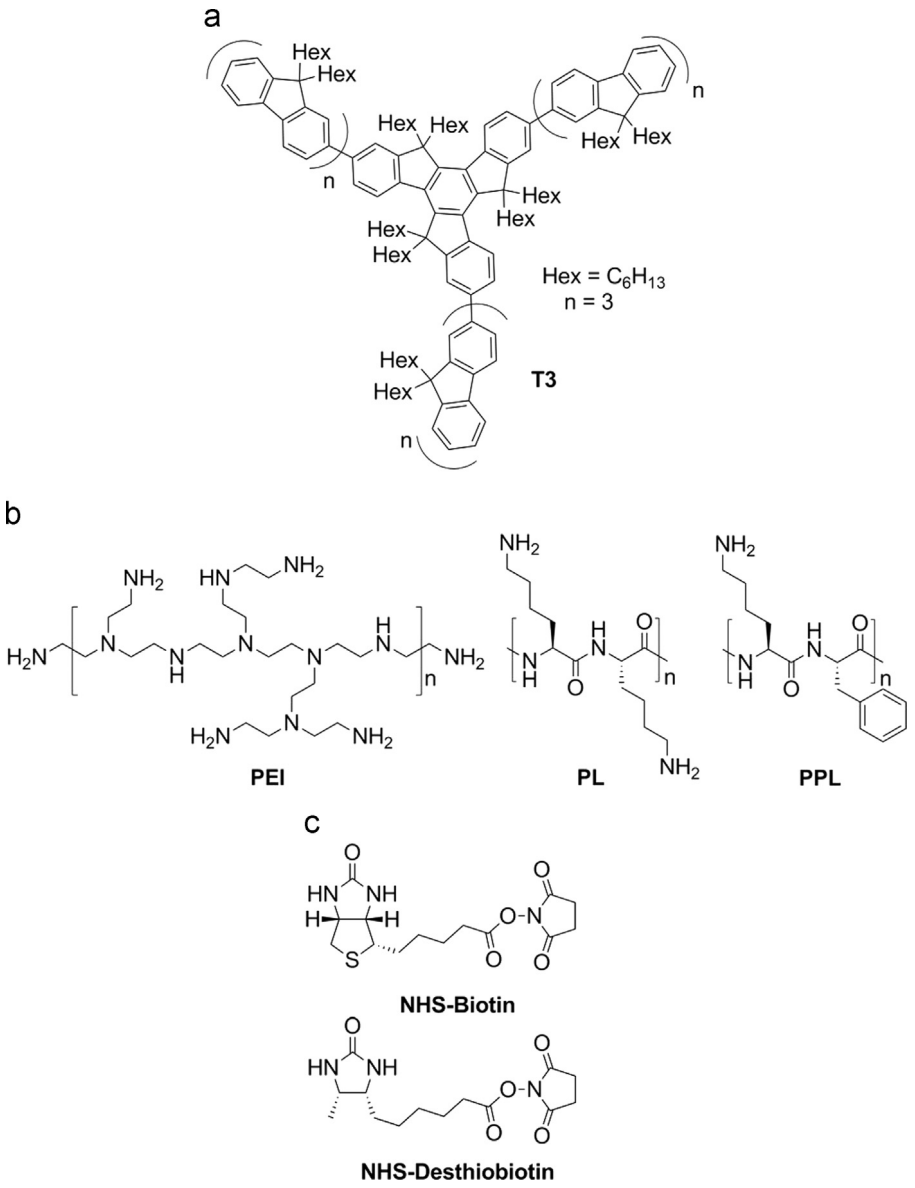

Fig. 1. Chemical structures of the compounds used in this study: oligofluorene truxene (a), polyelectrolytes (b) and biotins (c).

of the sensor in avidin solution and after 20 min, just prior to removal of the solution. The sensor was washed with PBS and the final emission wavelength recorded in PBS. This process was repeated, with a different laser sensor, for each of the avidin concentrations.

This general protocol was used for the fabrication of the T3 layer with PPL and PL in place of PEI. PPL and PL solutions were at a concentration of 1 mg mL^{-1} in 10 mM PBS therefore, PBS was used in place of NaCl. The shift in wavelength produced by each avidin concentration was determined by subtracting the emission wavelength recorded in PBS, prior to the addition of avidin solution, from the final emission wavelength recorded in PBS. The relative shift in wavelength demonstrates the shift due to the presence of avidin remaining bound to the biotin functionalized laser surface after washing.

In order to determine the avidin limit of detection for each of the polyelectrolyte-biotin functionalized sensors, repeated measurements ($4\times$) of avidin binding (10 μg mL^{-1}) were performed on different lasers. The standard deviation of the shift in wavelength attributed to avidin binding of these independent measurements was 0.02 nm. A shift in wavelength is deemed to be 'detectable' if it has a magnitude of three times the standard deviation (Cunningham, 2008). Therefore, the minimum level of avidin detection is defined as the avidin concentration resulting in a shift in wavelength ≥ 0.06 nm.

2.6. Reversible specific avidin detection

Sensors were functionalized with PPL and desthiobiotin as described in Section 2.4 for a PPL functionalized sensor. A solution of NHS-desthiobiotin in DMSO was added to 10 mM PBS to a concentration of 0.2 mg mL^{-1}, with a final DMSO concentration of 2% v/v.

10 mM PBS solution was used for all wash steps prior to and following immersion of the sensor in avidin/biotin. The relative shift in emission wavelength for the demonstration of reversible avidin sensing and for determining the avidin limit of detection was obtained as described in Section 2.4.

2.7. Investigation of non-specific protein adsorption using BSA

The non-specific adsorption of BSA to our PPL, PPL-biotin and PPL-desthiobiotin functionalized sensor was investigated for four BSA concentrations (1, 10, 500 and 50,000 μg mL^{-1}). BSA solutions were prepared in 10 mM PBS. Sensors were coated with PPL as previously described in Section 2.4. The emission wavelength, with the sensor immersed in PBS, was recorded. A BSA solution was then added to the cuvette and the emission wavelength recorded. After 20 min, the emission wavelength was recorded again before removing the BSA solution from the cuvette. The sensor was washed with PBS before a final emission wavelength was recorded with the sensor immersed in PBS. This was repeated for each BSA concentration, with a new sensor for each measurement, and was performed three times for each BSA concentration. The procedure was also repeated for a PPL-biotin and PPL-desthiobiotin functionalized sensor.

Competition assays using BSA and avidin were performed with a PPL-biotin and a PPL-desthiobiotin functionalized laser sensor. A range of BSA concentrations (1–50,000 μg mL^{-1}), with 2.5 μg mL^{-1} avidin, were prepared in 10 mM PBS. The relative shift in wavelength due to BSA and/or avidin was determined in the same way as described for BSA.

3. Results and discussion

3.1. Principles of DFB laser structure and operation

The structure of our DFB laser is shown in Fig. 2a. This sensing platform has a three-layer planar waveguide structure with a thin gain layer sandwiched between substrate (optical epoxy, see Methods) and superstrate (e.g. surface adsorbed molecules and buffer solution) regions. The surface of the substrate is nanopatterned with a grating structure of 276 nm period (Λ) and ≈50 nm modulation depth. The organic semiconductor gain layer is composed of T3 (Fig. 1a). The structure of T3 is a monodisperse star-shaped oligomer which has high photoluminescence quantum yields in both solution and the solid-state, and forms low-loss waveguiding films onto a substrate when deposited from solution (Guilhabert et al., 2010; Kanibolotsky et al., 2004; Herrnsdorf et al., 2010; Tsiminis et al., 2009). T3 has peak absorbance at 370 nm with photoluminescence emission peaks at 425 and 442 nm. For sensor operation, the T3 molecules are optically excited by a pulsed UV (355 nm) pump laser. The refractive index of T3 is 1.81 at 430 nm in a thin film, which is higher than the refractive indices of the substrate and superstrate (Tsiminis et al., 2009). This change in refractive index results in the confinement of light within the gain layer by total internal reflection, i.e. forming a planar waveguide, which is 'perturbed' by the nanostructure. The periodicity of the nanostructure provides both the out-coupling and feedback mechanism for the laser modes through first and second diffraction orders, respectively.

Laser emission from the DFB laser sensor is described by the Bragg equation, Eq. (1), where λ is the Bragg wavelength (emission from the laser is at, or close to, this wavelength), n_{eff} is the effective refractive index of the laser mode and is dependent on the refractive indices for each of the three layers of the DFB laser structure and the gain layer thickness, and Λ is the grating period as defined previously:

$$\lambda = n_{eff}\Lambda \tag{1}$$

The periodic nanostructure imprinted in our sensor substrate is a second-order grating, which causes counter-propagating modes to couple through the second order of diffraction while first order modes are coupled vertically out of the laser structure, as shown in Fig. 2a. It is this out-coupled laser emission that can be detected for wavelength monitoring and hence sensing.

Eq. (1) demonstrates that changes in the effective refractive index result in a change in the wavelength of emission from the DFB laser. n_{eff} depends on parameters, which are all fixed except for the refractive index of the superstrate. Therefore, changes in the optical properties at the laser surface correlate with shifts in the emission wavelength of the laser.

3.2. Optical characterization

The laser emission spectrum observed for a sensor immersed in PBS solution, functionalized with PPL and biotin, and after exposure to 2.5 μg mL^{-1} avidin solution, is shown in Fig. 3. Emission from all laser sensors was at the resolution limit of the spectrometer used (0.13 nm). The central wavelength and linewidth were determined from a Gaussian fit to the data. As the linewidth of laser emission was at, or below, the limit of the spectrometer resolution, spectra were fitted using either two or three data points above the noise (Fig. 3). Data fitting provided the best estimate of the central wavelength and linewidth within the current spectrometer limitations (Ge et al., 2010). The spectral linewidth of laser emission remaining narrow after functionalization with PPL and biotin, and exposure to avidin, demonstrated that the further addition of monolayers on the sensor surface did not compromise the characteristics of the laser emission. The inset

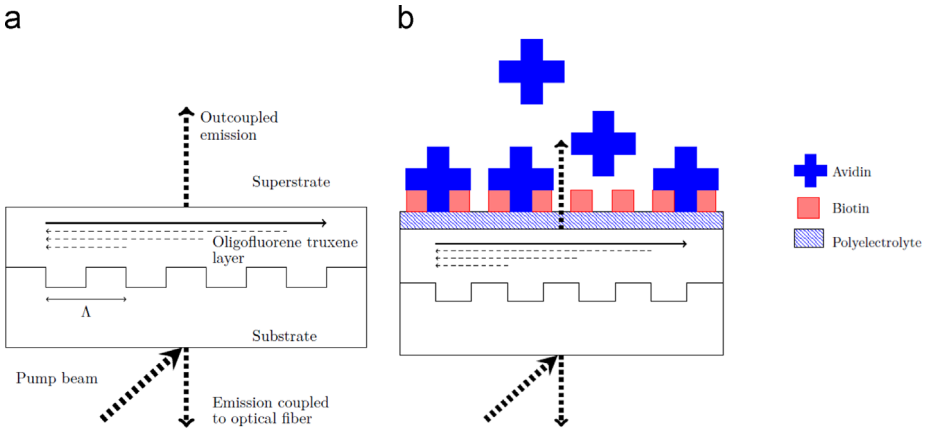

Fig. 2. Schematic illustration of our DFB laser biosensor (a) and functionalization of the sensor surface with polyelectrolyte and biotin for avidin sensing (b). The dashed and arrowed lines within the structure represent feedback from successive periods of the grating.

in Fig. 3 shows the relationship between the laser emission intensity and the pump beam energy, with the sensor exposed to air, demonstrating a threshold energy of 2.5 nJ, corresponding to a fluence of 60 μ J cm^{-2} with 5 ns pulse duration. Our group has previously reported on the lifetime of T3 DFB lasers identical to those described in this paper (Foucher et al., 2013). Lifetime measurements indicated that when submerged in water, the laser remained operational beyond exposure to 10,000 pulses, with a pulse fluence approximately 250 times that of the threshold fluence. 10,000 pulses correspond to a period of time >15 min. As each measurement with our laser sensor corresponds to pumping the sensor for a maximum of 5 s, the laser should allow for >200 measurements at one particular location on the laser. It should be noted that sensing measurements are performed at a fluence closer to that of the laser threshold, therefore, the estimate of 200 measurements is greatly underestimated. It has also been reported that the emission wavelength of the laser remains constant over time (Haughey et al., 2013), even as the intensity of the laser emission diminishes (Foucher et al., 2013).

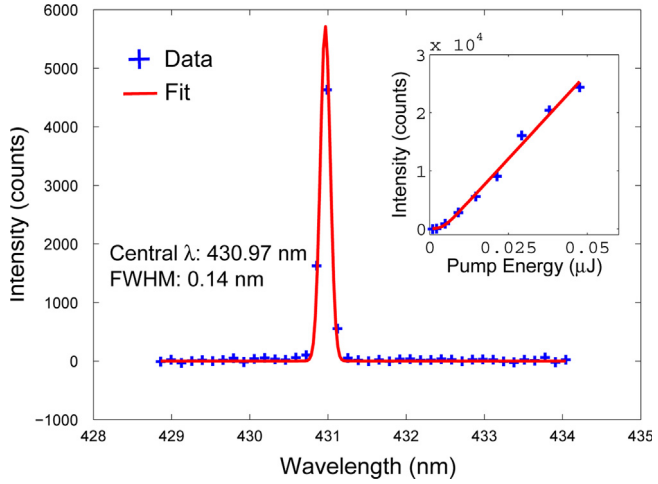

Fig. 3. Spectral emission from a laser functionalized with PPL and biotin, and after exposure to 2.5 μg mL^{-1} avidin. Inset shows the oscillation threshold (2.5 nJ) for a DFB laser in air.

3.3. Specific detection of avidin

Our approach to functionalization of the sensor surface and subsequent specific detection of avidin is the focus of the remainder of Section 3. Functionalization of the sensor surface for avidin detection is illustrated schematically in Fig. 2b. We present results demonstrating the effect the chosen polyelectrolyte layer, used for functionalization of the sensor, has on avidin detection in Section 3.4. Our demonstration of reversible avidin detection is detailed in Sections 3.5 and 3.6 presents our investigation into the non-specific adsorption of proteins to the sensor surface.

Functionalization of our DFB laser sensor with biotin was achieved by adsorption of a polyelectrolyte containing amine groups and subsequent functionalization with NHS-biotin (Erol et al., 2006). Three polyelectrolytes (PEI, PL and PPL), with chemical structures shown in Fig. 1b, were explored in order to survey which polymer would provide the greatest level of biotin functionalization and thus the lowest limit of detection for avidin sensing. The chemical structures for NHS-biotin and the three polyelectrolytes used in this study are shown in Fig. 1c.

Branched PEI was previously used as the base monolayer for stacking of alternately charged polyelectrolytes and was therefore the initial polyelectrolyte chosen to investigate biotin functionalization (Haughey et al., 2013). The primary amine groups of PEI enabled facile functionalization with the activated ester of NHS-biotin. A number of DFB laser sensors were functionalized with PEI and biotin and the average relative shift in emission wavelength (with the non-functionalized laser as reference), attributed to biotin covalently linked to the sensor surface, was 0.17 ± 0.07 nm. Each of these sensors were subsequently exposed to an

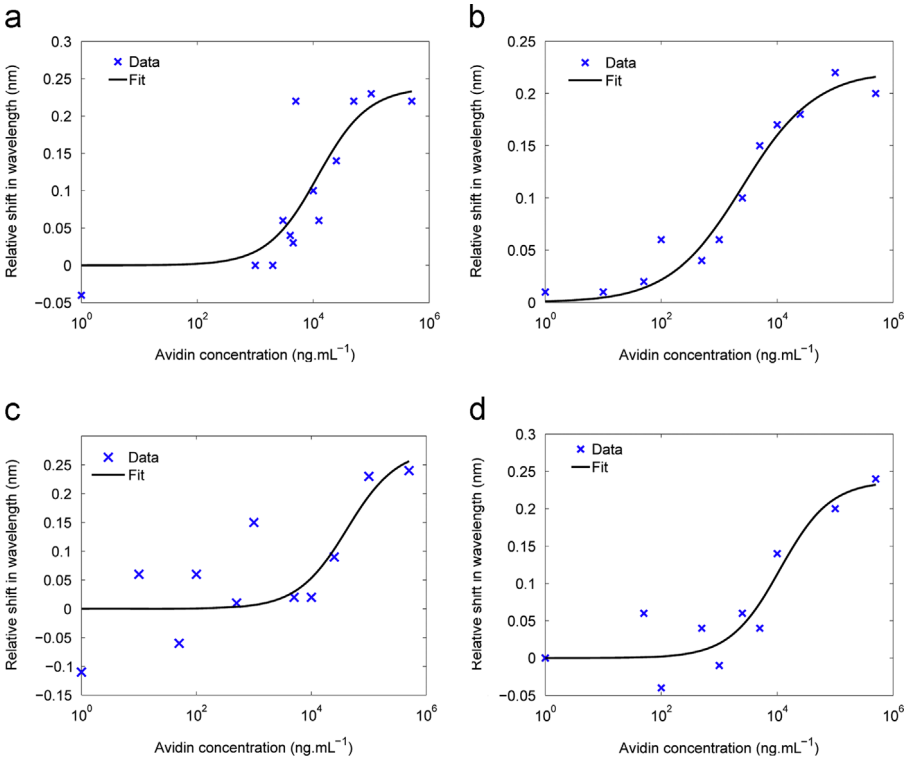

Fig. 4. Specific avidin sensing study for sensors functionalized with biotin and PEI (a), PPL (b), PL (c) and desthiobiotin and PPL (d). The data was fitted using Eq. (2).

avidin solution over a range of concentrations. The relative shifts in emission wavelength after exposure to each avidin concentration are shown in Fig. 4a. The data in Fig. 4a was fitted using the Michaelis–Menten equation (Attie and Raines, 1995):

$$y = \frac{B_{max} \cdot x}{K_d + x} \quad (2)$$

Eq. (2) can be used to describe protein binding reactions, where y is the relative shift in wavelength corresponding to avidin binding to sensor surface, B_{max} represents the maximum relative shift in wavelength, which is directly proportional to the maximum binding capacity of the biotin functionalized sensor, x is the avidin concentration and K_d is the dissociation constant that represents the avidin concentration for which the number of avidin molecules bound to the sensor surface results in a shift of $B_{max}/2$. The avidin limit of detection for a PEI-biotin functionalised DFB laser sensor was $\approx 5\ \mu g\ mL^{-1}$ and a dissociation constant of 2.0^{-7} M, the R-squared value for the fit to the data was 0.83.

In order to test the specificity of avidin detection, an avidin binding assay was performed on a DFB laser sensor functionalized with PEI alone. A 100 $\mu g\ mL^{-1}$ avidin solution, chosen as it results in a maximum shift in wavelength for a biotin coated sensor, produced a negative shift in wavelength (-0.12 nm). This relatively large negative shift is presumably due to the extra immersion of the laser sensor in various solutions which may remove more unbound PEI than the standard single wash. We conclude that avidin does not bind to the surface of a PEI coated laser in the absence of subsequent biotin functionalization, indicating that avidin binding for a PEI-biotin functionalized sensor is specific.

Replacing the initial PEI base layer with PPL resulted in an average relative shift in emission wavelength, due to biotin binding to the PPL coated surface, of 0.28 ± 0.09 nm. Fig. 4b shows the relative shift in wavelength for each avidin concentration for PPL-biotin functionalized sensors. There was an improvement in the fit to the data, relative to the fit of data for a PEI-biotin coated sensor, with an R-squared value of 0.98. The avidin limit of detection for a PPL-biotin functionalized laser sensor was $\approx 1\ \mu g\ mL^{-1}$, which is five times lower than the avidin limit of detection for a laser sensor with PEI as the initial monolayer and the corresponding dissociation constant was 3.6^{-8} M.

The specificity of avidin binding was investigated by immersing a PPL functionalized laser in a 25 $\mu g\ mL^{-1}$ avidin solution. This concentration was at the saturation point of avidin detection for a PPL-biotin functionalized sensor. As for the PEI control, there was a negative (-0.17 nm) shift in emission wavelength upon removal of avidin solution indicative of specific binding to the biotin-functionalized monolayer. We hypothesize that the improvement in the limit of detection of avidin when PPL was used in place of PEI was due to the pi-stacking of the phenyl substituents of the phenylalanine groups on the T3 surface. In order to test this hypothesis, the PPL base layer was replaced with PL. The relative shift in emission wavelength for biotin binding at the surface of a PL functionalized sensor was significantly lower than that for a PEI and PPL functionalized sensor, at 0.07 ± 0.07 nm. In addition, there was a significant increase in the variability of the shift in wavelength produced by biotin binding. We infer that the initial PL layer may not be a confluent, uniform monolayer for each sensor, therefore, reducing the density of available amine binding sites which in turn results in a marked increase in variability from sensor to sensor. The avidin detection data for a PL-biotin functionalized sensor is shown in Fig. 4c where the avidin limit of detection was $\approx 50\ \mu g\ mL^{-1}$, an order of magnitude higher than the avidin limit of detection when the sensor was functionalized with PEI. The associated dissociation constant was 6.9^{-7} M. The data also produced a poor fit to the Michaelis–Menten equation, with an R-squared value of 0.80, and a decrease in the dynamic range for avidin detection.

Table 1
Relative shift in wavelength due to biotin coupling to sensors functionalized with PEI, PPL or PL and desthiobiotin coupling to a PPL functionalized sensor, the corresponding avidin limit of detection for each of those sensors and the dissociation constants extracted from the Michaelis–Menten fit to the data.

Polyelectrolyte	Relative shift in wavelength		Avidin limit of detection ($\mu g\ mL^{-1}$)	Dissociation const. (M)
	Biotin coupling (nm)	Desthiobiotin coupling (nm)		
PEI	0.17 ± 0.07		5	2.0^{-7}
PPL	0.28 ± 0.09		1	3.6^{-8}
PL	0.07 ± 0.07		50	6.9^{-7}
PPL		0.14 ± 0.08	2.5	1.8^{-7}

We therefore conclude that functionalization of the sensor with PPL resulted in the lowest avidin limit of detection; the results are summarized in Table 1. A base layer of PEI resulted in a significant increase in avidin limit of detection, relative to that of PPL, at 1 $\mu g\ mL^{-1}$ and a limit of detection of 50 $\mu g\ mL^{-1}$ when PL was used. The differences in the limit of detection values correlate with the relative shift in emission wavelength attributed to biotin coupling. A redshift in emission wavelength is a result of an increase in the effective refractive index of the sensor, as described in Eq. (1). Therefore, the area density of biotin molecules bound to the sensor surface correlates to the magnitude of the relative shift in wavelength detected, i.e. higher levels of biotin coupling result in a greater redshift in emission wavelength. The greatest relative shift in emission wavelength for biotin coupling, 0.28 ± 0.09 nm, was observed when PPL was used for the base layer and the smallest shift, 0.07 ± 0.07 nm, was observed when PL was used for the initial layer. We therefore infer that the sensor surface is functionalized with the greatest number of biotin molecules when PPL is used as the polyelectrolyte base layer.

There is no direct comparison available in the literature for specific avidin detection achieved with a DFB laser sensor. TNF-α and Human IgG antibody detection has been reported for a dye-doped DFB laser sensor, with detection limits of 0.6 $\mu g\ mL^{-1}$ and $\approx 0.5\ \mu g\ mL^{-1}$, respectively (Tan et al., 2012; Lu et al., 2008a). Avidin detection with a biotin functionalized sensor has previously been reported for a number of photonic biosensors, e.g. microring and slotted photonic crystal based sensors (Scullion et al., 2011; DeVos et al., 2007), where the avidin limit of detection is in the range of 0.01–1 $\mu g\ mL^{-1}$, demonstrating that the detection limit for avidin of our laser is comparable to waveguide based devices. We note that the sensitivity of our laser sensor could be markedly improved by optimizing the spectral measurement in order to increase the detection resolution. Further improvements in sensitivity may also be achieved by optimizing the sensor structure, for example reducing the refractive index of the substrate to match that of the superstrate layer would result in a more symmetric structure and would cause a greater overlap between the laser mode and the sensing region (Haughey et al., 2013).

3.4. Reversible specific avidin detection

Due to the strong binding affinity of biotin–avidin ($K_d \approx 10^{-15}$ M), a combination of extreme conditions, such as high temperature and low pH, are required to release avidin from the surface. For many applications, irreversible binding will be a distinct advantage as the risk of disruption to binding events is minimized. However, reversing binding events is desirable if the assay is to be repeated thus rendering the sensor platform

're-usable'. Desthiobiotin (structure shown in Fig. 1c) is a biotin analogue with a lower binding affinity ($K_d \approx 10^{-11}$ M) for avidin and has been used in reversible avidin binding assays (Hirsch et al., 2002; Wong et al., 2013).

As the lowest avidin limit of detection was achieved for a laser functionalized with an initial layer of PPL, PPL was the polyelectrolyte used to investigate the capacity of reversible binding of a desthiobiotin–avidin binding using our detection platform. Desthiobiotin functionalization of the sensor surface was achieved using NHS-desthiobiotin (Wong et al., 2013). Fig. 5a shows the reversibility of avidin coupling to desthiobiotin. Relative shifts in wavelengths of 0.08, 0.09 and 0.09 nm were observed after each exposure to avidin solution (10 μg mL^{-1}). Upon removal of avidin solution and a PBS wash, the sensor was immersed in a biotin solution (0.2 mg mL^{-1}) where the associated relative shifts in wavelength after exposure to the biotin solutions were −0.05, −0.06 and −0.13 nm. Fig. 5a clearly shows that most of the avidin bound to the desthiobiotin functionalized sensor was removed after immersion in the biotin solution and that avidin binding to the desthiobiotin layer was reproducible. When biotin was used in place of desthiobiotin, the addition of biotin after avidin binding resulted in no change in the emission wavelength from the sensor, indicating that there was no removal of avidin from the sensor and no detectable biotin binding. We surmise that the reversibility of the assay when desthiobiotin was used is due to the lower binding affinity of desthiobiotin (10^{-11} M) to avidin relative to that of biotin (10^{-15} M). Therefore, the immersion of the sensor in a biotin solution leads to the release of avidin upon washing with PBS. This results in a negative shift in the emission wavelength that corresponds to the magnitude of the shift in wavelength attributed to avidin coupling.

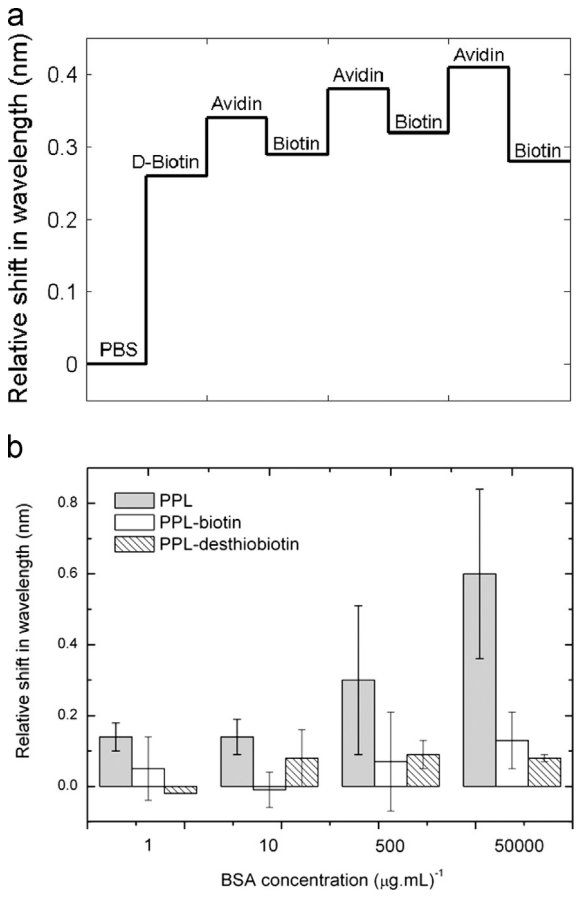

Fig. 5. The shifts in wavelength relative to a baseline PBS wavelength are shown for a sensor functionalized with PPL. The shifts in wavelength attributed to desthiobiotin (D-Biotin) and avidin are shown as well as the relative wavelength upon avidin removal by immersion of the sensor in biotin solution (a). And average relative shift in wavelength attributed to non-specific adsorption of BSA to a sensor functionalized with PPL or PPL and biotin. Error bars represent the standard deviation of the mean (b).

The avidin detection assay was then performed using a PPL-desthiobiotin functionalized sensor. Fig. 4d shows the relative shift in wavelength for each avidin concentration for PPL-desthiobiotin functionalized sensors and the results are included in Table 1. The average relative shift in wavelength due to desthiobiotin binding to the PPL surface was 0.14 ± 0.08 nm. The data in Fig. 4d was fitted to the Michaelis–Menten equation and an *R*-squared value of 0.94. The limit of detection for a PPL-desthiobiotin functionalized sensor was 2.5 μg mL^{-1}, between that of a PEI-biotin and PPL-biotin functionalized sensor and the dissociation constant was 1.8^{-7} M. We therefore conclude that specific, and reversible, avidin detection can be achieved through the replacement of biotin with desthiobiotin for the functionalization of the laser sensor.

3.5. Non-specific BSA adsorption

Non-specific adsorption to our detection platform was then determined using BSA. Albumin is present in abundance in blood samples and could potentially interfere with the detection of specific analytes. Fig. 5b shows the mean response of our sensor, functionalized with either PPL, PPL-biotin or PPL-desthiobiotin, after exposure to BSA solutions of varying concentrations (measured in triplicate). BSA has a pI of 4.7 and is thus negatively charged at pH 7.4. As a result, a significant redshift in emission wavelength was attributed to non-specific adsorption of BSA to the positively charged surface of a PPL coated sensor. There was a reduction in the shift in wavelength across all BSA concentrations for PPL-biotin and PPL-desthiobiotin functionalized laser sensors, presumably as consequence of the biotin layer masking the positive charge of the underlying PPL layer. We assume that this suppresses the electrostatic attraction between the positively charged PPL and negative BSA, which in turn suppresses the non-specific adsorption of BSA to the sensor surface (Williams et al., 2013).

The effect of non-specific adsorption of BSA on specific avidin sensing, with PPL-biotin and PPL-desthiobiotin functionalized sensors, was investigated by performing a competition assay with BSA solutions at a range of concentrations (1–50,000 μg mL^{-1}) containing 2.5 μg mL^{-1} of avidin. No increase in emission wavelength as a function of increasing BSA concentration was observed. The average shift in emission wavelength was 0.09 ± 0.04 nm (biotin) and 0.03 ± 0.05 nm (desthiobiotin). These values correspond to the relative shifts in emission wavelengths observed for detection of 2.5 μg mL^{-1} avidin when no BSA is present (Fig. 4b and d). We therefore conclude that the presence of BSA does not affect the specific detection of avidin even at concentrations comparable to those found in serological samples, and that there was no detectable non-specific adsorption of BSA in the presence of avidin at a concentration of 2.5 μg mL^{-1}. This is an important observation in downstream optimization of the specificity of the DFB laser sensor for specific biosensing applications.

4. Conclusions

We report what is to our knowledge the first application of an oligofluorene truxene based DFB laser sensor for the sensitive detection of biomolecules. Our laser design can be fabricated using well established and scalable processes and does not require precise optical alignment. Furthermore our design can be readily

incorporated into existing assay equipment. The design is highly compatible for biomolecule sensing, with the sensing of avidin used as proof of concept in this study. This detection limit was comparable to existing DFB laser sensors, however further optimization of the sensor, and improvement to the spectrometer resolution, could improve the sensitivity of our sensor even further. The potential for a re-usable sensing system was demonstrated and our chosen system for functionalization of the sensor surface was shown to prevent the non-specific adsorption of BSA up to $50,000\ \mu g\ mL^{-1}$. Future work will focus on optimizing the functionalization of the sensor for the specific detection of nucleic acids, peptides and proteins and miniaturization of the sensing platform to achieve a compact system.

Acknowledgments

The authors gratefully acknowledge financial support by the EPSRC (EP/J021962/1 and EP/I029141/1).

References

Al-Hakim, A.H., Hull, R., 1986. Nucl. Acids Res. 14 (24), 9965–9976.
Armani, A.M., Kulkarni, R.P., Fraser, S.E., Flagan, R.C., Vahala, K.J., 2007. Science 317 (5839), 783–787.
Attie, A.D., Raines, R.T., 1995. J. Chem. Educ. 72 (2), 119.
Cunningham, B., 2008. Label Free Biosensors - Techniques and Applications. Cambridge University Press. pp. 1–28.
Dííaz-García, M.A., Hide, F., Schwartz, B.J., Andersson, M.R., Pei, Q., Heeger, A.J., 1997. Synth. Met. 84 (1–3), 455–462.
DeVos, K., Bartolozzi, I., Schacht, E., Bienstman, P., Baets, R., 2007. Opt. Express 15 (12), 7610–7615.
Erol, M., Du, H., Sukhishvili, S., 2006. Langmuir 22 (26), 11329–11336.
Foucher, C., Guilhabert, B., Kanibolotsky, A., Skabara, P., Laurand, N., Dawson, M., 2013. Optical Mater. Express 3 (5), 584–597.
Ge, C., Lu, M., Jian, X., Tan, Y., Cunningham, B.T., 2010. Opt. Express 18 (12), 12980–12991.
Green, N.M., 1975. Advances in Protein Chemistry, vol. 29. Academic Press, pp. 85–133.
Guilhabert, B., Laurand, N., Herrnsdorf, J., Chen, Y., Mackintosh, A.R., Kanibolotsky, A.L., Gu, E., Skabara, P.J., Pethrick, R.A., Dawson, M.D., 2010. J. Opt. 12 (3), 035503.
Haughey, A.-M., Guilhabert, B., Kanibolotsky, A., Skabara, P., Burley, G., Dawson, M., Laurand, N., 2013. Sens. Actuators B 185 (0), 132–139.
Herrnsdorf, J., Guilhabert, B., Chen, Y., Kanibolotsky, A., Mackintosh, A., Pethrick, R., Skabara, P., Gu, E., Laurand, N., Dawson, M., 2010. Opt. Express 18 (25), 25535–25545.
Hirsch, J.D., Eslamizar, L., Filanoski, B.J., Malekzadeh, N., Haugland, R.P., Beechem, J.M., Haugland, R.P., 2002. Anal. Biochem. 308 (2), 343–357.
Jenison, R., La, H., Haeberli, A., Ostroff, R., Polisky, B., 2001. Clin. Chem. 47 (10), 1894–1900.
Kanibolotsky, A.L., Berridge, R., Skabara, P.J., Perepichka, I.F., Bradley, D.D.C., Koeberg, M., 2004. J. Am. Chem. Soc. 126 (42), 13695–13702, PMID: 15493927.
Kim, M.S., Seo, K.S., Khang, G., Lee, H.B., 2005. Langmuir 21 (9), 4066–4070.
Lu, M., Choi, S.S., Irfan, U., Cunningham, B.T., 2008a. Appl. Phys. Lett. 93 (11), 111113–111113-3.
Lu, M., Choi, S.S., Wagner, C.J., Eden, J.G., Cunningham, B.T., 2008b. Appl. Phys. Lett. 92 (26), 261502.
Norland, 2013. ⟨https://www.norlandprod.com/techrpts/chemresit.html⟩.
Ramsden, J.J., 1997. J. Mol. Recognit. 10 (3), 109–120.
Ruiz-Taylor, L.A., Martin, T.L., Zaugg, F.G., Witte, K., Indermuhle, P., Nock, S., Wagner, P., 2001. Proc. Natl. Acad. Sci. 98 (3), 852–857.
Scullion, M., Falco, A.D., Krauss, T., 2011. Biosens. Bioelectr. 27 (1), 101–105.
Tan, Y., Ge, C., Chu, A., Lu, M., Goldshlag, W., Huang, C.S., Pokhriyal, A., George, S., Cunningham, B., 2012. IEEE Sens. J. 12 (5), 1174–1180.
Tsiminis, G., Wang, Y., Shaw, P.E., Kanibolotsky, A.L., Perepichka, I.F., Dawson, M.D., Skabara, P.J., Turnbull, G.A., Samuel, I.D.W., 2009. Appl. Phys. Lett. 94 (24), 243304–243304-3.
Vollmer, F., Braun, D., Libchaber, A., Khoshsima, M., Teraoka, I., Arnold, S., 2002. Appl. Phys. Lett. 80 (21), 4057–4059.
Williams, E.H., Schreifels, J.A., Rao, M.V., Davydov, A.V., Oleshko, V.P., Lin, N.J., Steffens, K.L., Krylyuk, S., Bertness, K.A., Manocchi, A.K., Koshka, Y., 2013. J. Mater. Res. 28, 68–77.
Wong, N.Y., Xing, H., Tan, L.H., Lu, Y., 2013. J. Am. Chem. Soc. 135 (8), 2931–2934.
Yang, Y., Turnbull, G.A., Samuel, I.D.W., 2008. Appl. Phys. Lett. 92 (16), 163306.

Faraday Discussions

Accepted Manuscript

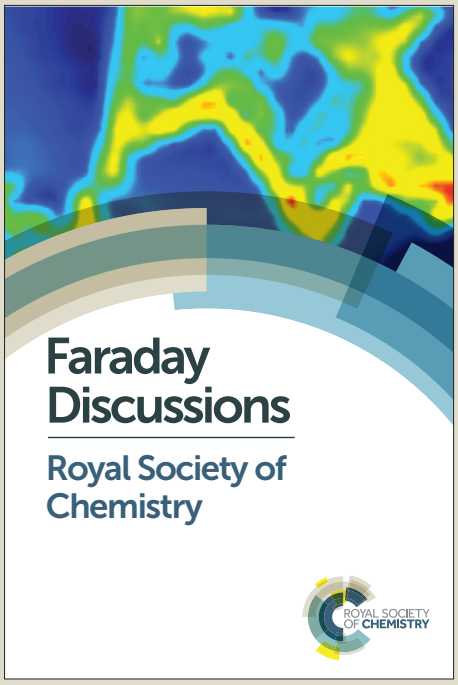

This article can be cited before page numbers have been issued, to do this please use: A. Haughey, C. Foucher, B. Guilhabert, A. Kanibolotsky, P. Skabara, G. A. Burley, M. D. Dawson and N. Laurand, *Faraday Discuss.*, 2014, DOI: 10.1039/C4FD00091A.

Faraday Discussions

RSCPublishing

ARTICLE

View Article Online
DOI: 10.1039/C4FD00091A

Hybrid organic semiconductor lasers for bio-molecular sensing

Cite this: DOI: 10.1039/xoxxoooooox

A.-M. Haughey,[a] C. Foucher,[a] B. Guilhabert,[a] A. L. Kanibolotsky,[b] P. J. Skabara,[b] G. Burley,[b] M. D. Dawson[a] and N. Laurand[a]

Received ooth January 2012,
Accepted ooth January 2012

DOI: 10.1039/xoxxooooox

www.rsc.org/

Bio-functionalised luminescent organic semiconductors are attractive for biophotonics because they can act as efficient laser materials while simultaneously interacting with molecules. In this paper, we present and discuss a laser biosensor platform that utilises a gain layer made of such an organic semiconductor material. The simple structure of the sensor and its operation principle are described. Nanolayer detection is shown experimentally and analysed theoretically in order to assess the potential and the limits of the biosensor. The advantage conferred by the organic semiconductor is explained and comparisons to laser sensors using alternative dye-doped materials are made. Specific biomolecular sensing is demonstrated and routes to functionalisation with nucleic acid probes, and future developments opened up by this achievement, are highlighted. Finally, attractive formats for sensing applications are mentioned, as well as colloidal quantum dots, which could in the future be used in conjunction with organic semiconductors.

A Introduction

The development of personalised medicine requires that specific diagnostic tools be made available for use at the point-of-care. In particular, sensitive and compact platforms that can flexibly and accurately identify disease biomarkers, e.g. from a patient's blood sample, and do so in the shortest time are critically needed.[1,2] These diagnostic platforms should be simple to implement and operate in order to maximise practicality and minimise overall cost. Label-free optical biosensors enabled by advanced functional materials, including bio-functionalised organics, have the potential to address the challenge. Here, we describe an organic semiconductor (OS) laser as a technology platform for such label-free biosensing.

Label-free biosensors in general use evanescent optical waves in order to measure minute changes in the dielectric permittivity caused by the presence of analytes at an interface between the device and the biological environment.[3-11] Such sensors are attractive because of their non-electrical detection, sensitivity and specificity. Several label-free optical sensor technologies currently exist.[3] Each has its advantages and downsides but not all of them are easily scalable to the level of miniaturisation required for future point-of-care use. It is often necessary to sacrifice detection resolution and/or sensitivity for ease of implementation and vice-versa. This is because the transduction mechanisms for reading the dielectric permittivity changes, i.e. for sensing, are based on resonating structures.[3-11] The sensing function is realised by monitoring the change of an optical resonance, for example by direct reading of the optical spectrum. The overall sensitivity of such sensor systems is then a combination of the magnitude of a resonance shift (caused by the presence of analytes) and of the intrinsic resonance bandwidth, which determines the minimum detectable shift. Optimising the sensitivity of an evanescent wave biosensor therefore means maximising the resonance shift (which can be done by maximising the optical wave intensity in the region where the analytes are present) while minimising the resonance bandwidth. Doing both simultaneously is not straightforward, as there exists a trade-off between resonance bandwidth and the strength of the wave/analyte interaction.

A plastic laser sensor platform, that can take the form of a distributed feedback[12,13] or a photonic-crystal active resonator,[14-15] can mitigate this trade-off while maintaining a simple architecture for ease of application. In such a device the narrow resonance bandwidth is obtained through the coherence of laser action without sacrifying the strength of the field (in this case the laser mode) interaction with the sensing region. The great potential of this solution for the detection of bio-molecules has been shown. However, the first generation of plastic laser sensors utilised a dye-doped composite, i.e. dyes

diluted in a polymeric matrix, as the optical gain region. The relatively low dielectric permittivity contrast between such a diluted medium (n ≈ 1.5) and a biological environment (n ≈ 1.4) limits the strength of the laser mode intensity at the sensing interface. Therefore, the approach necessitates the addition of a thin inorganic layer (TiO_2 n ≈ 1.8 to 2.4) on top of the surface of the laser to boost the field at the interface and hence the sensitivity. This additional step adds complexity to the fabrication and means that it is not entirely done by solution processing thereby cancelling some of the advantages of the technology.

We propose a novel embodiment of the plastic laser sensor where the laser material is made of a neat OS medium. This approach leads to a simple device architecture where no additional inorganic layer is necessary to obtain high sensing performance[16-17] thanks to the relatively high dielectric permittivity of the dense OS medium. In turn, the fabrication of sensors can be entirely based on solution-processing techniques. Importantly for point-of-care, an OS laser configuration can be made suitable for compact optical-pumping arrangements using either InGaN laser diodes or LEDs[18-20] – thereby paving the way for miniaturisation of the biosensor system. Other key attributes of the OS laser biosensor include (i) wavelength flexibility across the visible by molecular engineering of the OS material – an attractive feature for multiplexing; (ii) compatibility with a variety of material platforms, thereby facilitating integration in legacy sensing equipment as well as the development of new sensor formats; and (iii) the possibility to envision direct hybridisation of the OS material at the molecular level to combine the functionalities of light amplification with those of bio-molecular interactions.

In this paper, we start in part B by presenting the design, concept and characteristics of the OS laser biosensor. In part C, we show that this laser platform can detect a nanolayer that is adsorbed onto the surface of the OS and explain the sensitivity advantage of using a dense OS as the gain medium. In part D, we demonstrate specific bio-molecular sensing, show DNA functionalisation of the OS laser and discuss opportunities opened up by these demonstrations. We briefly discuss possible OS lasers in array-format that are attractive for implementing particular sensing concepts. We end by mentioning another promising solution-processed material for hybrid laser biosensors, colloidal quantum dots, which could in the future be used in conjunction with OS.

B Organic laser sensor: design, materials and concept

The OS laser sensor considered here is based on a planar distributed-feedback structure as shown in Fig. 1(a). It consists of a transparent, nanopatterned substrate overcoated with a thin-film of OS that acts as the laser material and provides the interface with the sensing region. For sensing, the OS layer is put into contact with the biological environment (e.g. a drop of fluid to be tested can simply be deposited or flowed over the laser surface). The laser mode oscillates in the plane of the OS

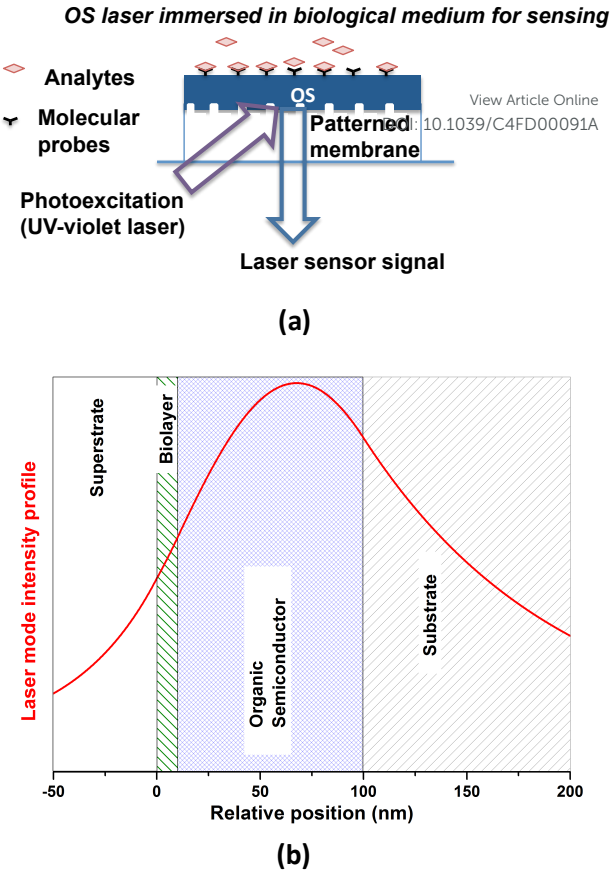

Fig. 1 (a) Schematic representing the implementation of the organic laser sensor; **(b)** laser mode intensity cross-section showing the overlap with the different regions of the laser structure.

layer and, as can be seen in Fig. 1(b), interacts with the biological environment ('superstrate' and 'biolayer') through its evanescent tails. The red curve in Fig 1(b) represents the laser mode intensity profile overlapped with the different regions of the planar laser. For ease-of-implementation, the nanopattern period is chosen to equal one wavelength of the desired laser emission. This laser emission has a vertically outcoupled component that can be collected for detection through the substrate of the device, i.e. on the same side as the pump excitation (Fig 1a). For biosensing, the sensor needs to be able to detect analytes specifically. Therefore, the surface of the laser is functionalised with molecular probes whose role is to capture and immobilise the molecules to be detected that might be present in the biological medium. Once captured, these immobilised analytes form a (possibly non-homogeneous) layer on the laser surface. The dielectric permittivity of this 'biolayer' is slightly higher than the more diluted biological medium, referred to as the superstrate in Fig. 1(b). This in turn affects the laser wavelength, which can be monitored for biosensing.

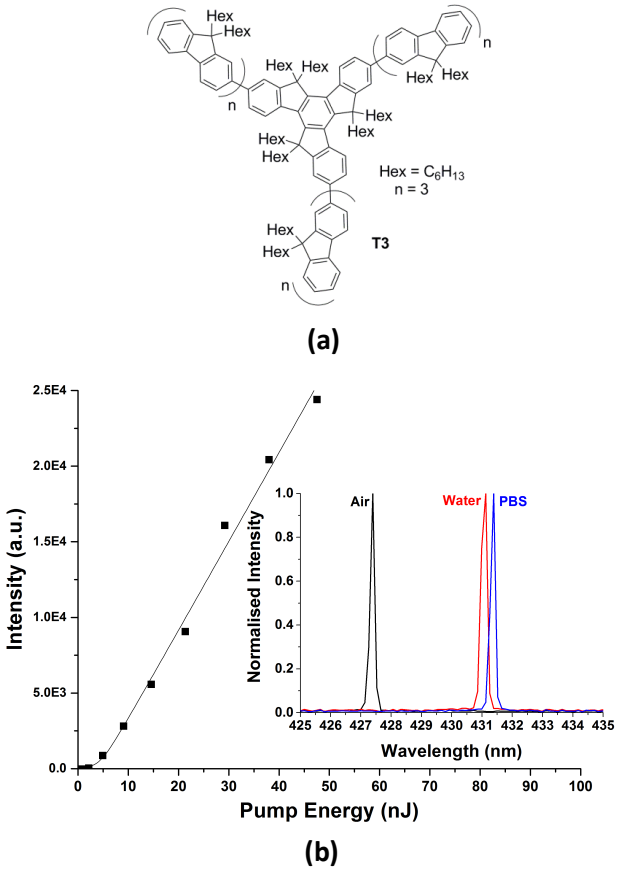

Fig. 2 (a) Representation of the T3 molecule; **(b)** Laser transfer function (in air); Inset: Laser spectrum with the superstrate being, respectively, air, water and PBS.

The laser wavelength is basically given by the product of the pattern periodicity, Λ, with the value of the mode effective index, n_{eff}. The latter is obtained by averaging the refractive indices of the substrate, OS, biolayer and superstrate weighted by the respective overlap values of these regions with the laser mode. The formation of a biolayer on the surface of the laser modifies the effective index and hence changes the laser wavelength. The magnitude of this change is dependent on the mode overlap with the biolayer and the refractive index of the latter. Hence, it depends on the amount of analyte and monitoring the wavelength enables the sensing function (although other parameters could be monitored as well). The mode overlap with the biolayer can be optimised for sensitivity by maximising the refractive index of the laser gain material and minimising its thickness. An OS laser material is therefore advantageous because it forms a 'dense' laser medium that has a high refractive index and can accommodate a low thickness without compromising the laser performance.

We use star-shape oligofluorene truxene molecules to form the OS layer of our laser sensors (see Fig. 2a). Each of the three arms of the molecule, attached to a truxene core, consists of a repeat of fluorene units.[21] In our case the number of units per arm is three and we therefore refer to this truxene-core material as T3. T3 macromolecules are efficiently excited with light in the 350-390nm range and emit in the blue part of the spectrum. They can also form high-quality solid-state thin-films with high T3 density ideal for planar lasers.[22,23] The thickness of the T3 layer is set to be 70 nm +/- 10 nm, thin enough to maximise sensitivity and thick enough to sustain a TE-polarised optical mode. This layer of T3 is deposited onto a nanopatterned imprinted epoxy substrate. The periodicity of the pattern is Λ=277 nm. Such all-organic lasers can be easily incorporated into cuvettes or integrated into microtiter plates.

View Article Online
DOI: 10.1039/C4FD00091A

The laser sensors are excited with 5ns long pulses of 355nm pump light. A typical laser transfer function of such a laser (operated in air) is plotted in Fig. 2b. Despite the low T3 thickness, the oscillation threshold is 5 nJ and this value is even lower (a couple of nJ) when the laser is operated in a liquid superstrate such as water or buffer. The top inset of Fig. 2 displays the laser spectra when the superstate is, respectively, air, water and phosphate buffered saline (PBS). The laser linewidth is limited by the spectrometer resolution in the three cases. The laser wavelength is seen to redshift for increasing refractive index of the superstrate: Δλ (air-to-water) = 3.73+/-0.06 nm and Δλ (air-to-PBS) = 4.00+/-0.06 nm. The respective refractive index of air, water and PBS solution is approximately 1, 1.34 and 1.35. Measurements of refractive index changes of the superstrate in such a way are repeatable and have been used to measure the concentration of glycerol/water solutions and have served to validate the sensing approach.[16]

To operate as a biosensor the photostability of the OS laser over the duration of an experiment is critical. T3 lasers operated in air have a 1/e degradation dosage of 10 J/cm^2, while it is close to 20 J/cm^2 when operated in a water environment (see Fig. 3). In the experimental conditions of our sensor, this corresponds to more than 10 to 20x10^5 pulses. Over such a number of pulses the oscillation wavelength does not vary. Because a single sensing measurement requires less than 10 to 20 pulses there

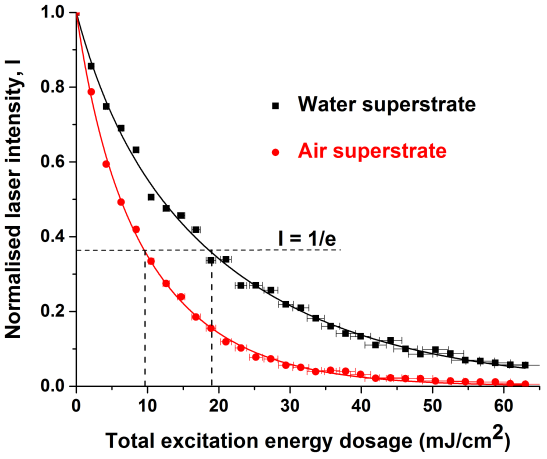

Fig. 3 Laser output intensity versus the total pump energy dosage when the device is operated in air and in water.

are no parasitic errors due to photodegradation effects. In fact, the T3 laser photostability is high enough that it should enable dynamic/continuous sensing over tens of minutes if exciting the laser sensor at a pulse repetition rate of 10 Hz.

C Nanolayer detection and comparison with dye-doped lasers

The biosensing principle of the laser platform is to detect molecules immobilised onto the surface of the OS material. This is different than sensing a change in the bulk refractive index of the superstrate as was shown in Fig. 2, inset. To observe the physical effect that a biolayer will have on the laser biosensor response, as well as to assess the capability and get a first idea of the sensing limit of the technology platform independently of biochemical surface functionalisation, nm-thick layers of polyelectrolytes can be built up onto the OS surface. For this, we use poly(ethyleneimine) (PEI), poly(allylamine hydrochloride) (PAH) and poly(sodium 4-styrenesulfonate) (PSS). These are well studied and form monolayers of known thickness (5 nm) and refractive index (1.49, close to that of most proteins) after a few initial layers of varying thicknesses.[24,25] To adsorb each polyelectrolyte layer, the laser biosensor is immersed in solutions of the corresponding polyelectrolytes (all at 5 mg/mL in NaCl) for 10 minutes with intermediate washing steps. The first deposited layer is PEI and the successive layers forms a stack of PSS and PAH. After each layer deposition and surface washing, the laser wavelength is measured when immersed in a reference NaCl solution. The wavelength shift of the laser induced by this growth of nanolayers on top of the OS laser is shown in Fig. 4(a). After the first 3 layers, the wavelength redshifts linearly up to the 11th layer. The slope of the wavelength shift per nm of adsorbed material is 3.7% as indicated in Fig. 4(b). This means that the laser sensor can detect thicknesses of adsorbed material from the nanometre scale up to several tens of nanometres. In principle, the smallest thickness that could be detected is limited by the resolution of the current system (+/- 0.06 nm), corresponding to <2 nm. This equates to proteins in the range of 5 kDa,[26] i.e. the OS laser sensor has the potential to detect most of the relevant biomarkers. This assumes that proteins cover the whole of the laser surface, which might be the case only in the limit of high concentration. Nevertheless it demonstrates the intrinsic capability of the sensor while ignoring any amplification stage (that could be used to further boost the sensitivity).

Adsorption of a nanolayer is also a useful tool to compare

View Article Online
DOI: 10.1039/C4FD00091A

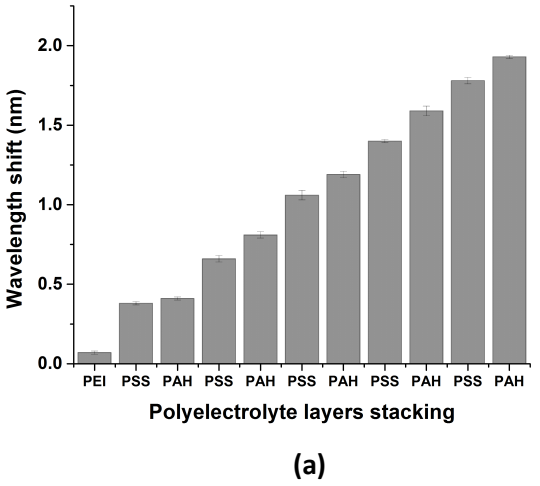

Fig. 4 (a) Laser wavelength shift upon polyelectrolyte layers stacking. The first layer is made of PEI while each successively adsorbed polyelectrolytes are respectively PSS and PAH. **(b)** Laser wavelength shift versus adsorbed nanolayer thickness.

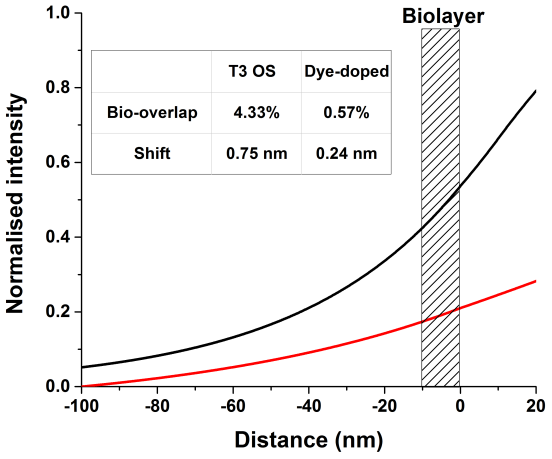

Fig. 5 Mode intensity profile in the vicinity of the laser/biolayer interface (position at 0 nm on graph). Red curve: case of the dye-doped laser; Black curve: case of the T3 OS laser. A 10nm thick biolayer is considered (patterned area between -10 nm and 0 nm). The mode overlap, and hence the wavelength shift, is higher for the T3 OS laser.

different surface sensing platforms independent of considerations for the chemistry of surface molecular probes. Here, we model our OS laser sensor and a similar laser structure that instead uses a dye-doped polymer for the gain region. Our model is based on a modified planar waveguide approach where we considered the dispersion of the different layers of the structure. This model has been shown to accurately predict and replicates experimental results for our OS laser.[16,17] We have verified that it replicates published results of dye-doped laser sensors as well. We consider our T3 OS laser (details given previously) and a dye-doped laser emitting at 590 nm with a refractive index for the gain region of 1.51 and a pattern periodicity Λ=400 nm. The model determines in both cases the effective refractive index for the TE_0 mode, the mode profile, the overlap with the biolayer and the expected wavelength shift. The mode intensity profiles are represented in Fig. 5 along with the overlap values and the wavelength shifts for a 10nm biolayer with refractive index of 1.45. Both overlap and wavelength shifts are higher (4.37% vs 0.57% and 0.75 nm vs 0.24 nm) for the OS laser. The higher sensitivity of the OS laser is due to the higher index contrast between the laser and the biolayer. The dye-doped laser cannot match this sensitivity without an additional TiO_2 layer. Overall this section demonstrates that our T3 laser (and by extension other lasers made from neat OS) represents a simple yet potentially sensitive biosensing platform.

D Specific bio-molecular detection and DNA functionalisation

Specific detection of molecules requires surface functionalisation of the laser with molecular probes (Fig. 1a). We show, as proof-of-principle, specific detection of avidin by functionalising the T3 laser surface with biotin as the molecular probe. The approach for functionalisation utilises adsorption of a monolayer of a polyelectrolyte, polyphenylalanine lysine, or PPL (see inset of Fig. 6 for schematic representation of PPL). For this, a similar approach to layer adsorption described in section C was taken. Specifically, a solution of PPL in PBS (10 mM PBS, pH of 7.4) was prepared at a concentration of 1 mg/mL. The laser was immersed in this solution for 10 minutes and then washed and rinsed with PBS. The nanolayer of PPL provides accessible primary amine functional groups that can be used to anchor molecular probes on the laser surface. Here, the coated laser was immersed in a N-hydroxysuccinimide(NHS)-biotin/PBS solution for 20 minutes in order to attach biotin molecules onto the laser. The laser surface was then washed again in PBS. For sensing experiments, the biotin-functionalised laser was immersed in solutions of avidin/PBS of different concentrations for 20 minutes before a washing step to remove unbound avidin molecules.

Results of wavelength shift due to avidin attachment to the biotin laser as a function of avidin concentration are plotted in the main part of Fig. 6. Between 100 ng/mL and 1000 ng/mL the wavelength is seen to redshift with increasing avidin concentration. The behaviour saturates at a concentration

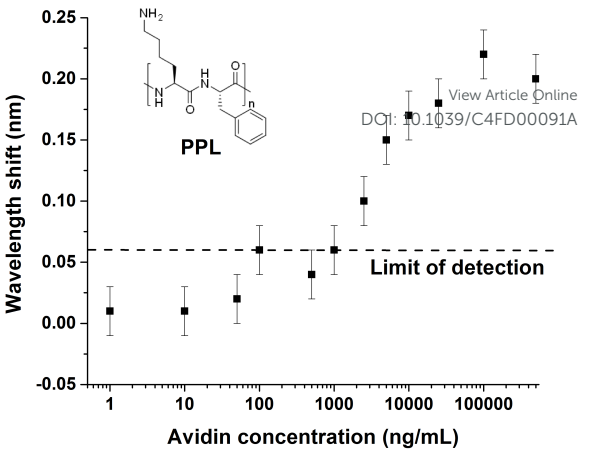

Fig. 6 Laser wavelength shift caused by avidin-biotin binding onto the laser surface as a function of avidin concentration. Inset: schematic of PPL monomer. PPL is used as an intermediate functionalisation layer on the T3 laser surface. It presents amine groups that are then reacted with NHS functionalised molecules (biotin here).

above 25 mg/mL. This saturating behaviour follows a Langmuir equation that relates to the coverage of molecules on a surface and is caused in this case by avidin molecules occupying all available biotin sites on the laser. The limit of detection corresponds to a concentration of 1000 ng/mL (shift of 0.06 nm). Currently, the limiting factor is the resolution of the system (convolution of the laser linewidth and of the spectrometer intrinsic resolution). Further refinement of the laser structure and the use of a spectrometer with a higher resolution will improve this limit of detection. We have also verified that this sensing capability is unaffected by the presence of albumin at a concentration equivalent to that found in blood.[17] This is significant as albumin molecules tend to non-specifically stick to surfaces and this is known to cause problems in some biosensors.

This biomolecular sensing demonstration proves the potential of OS lasers for such applications. The next step is to devise functionalisation pathways for specific sensing of relevant biomarkers and to assess the limit of the technology in this case. The most common of commercial biosensors (e.g. ELISA assays) use antibodies but we think nucleic acid (NA) probes are well suited for functionalising OS lasers. NA probes have the advantage to be more environmentally stable than antigens/antibodies and they can also be synthetically programmed. With this approach the NA probes could immobilise on the laser surface the mRNA of protein biomarkers. Alternatively, aptamers could be used to directly immobilised proteins. As a first step on this route, we demonstrate NA attachment onto our T3 OS laser. We react an amide-to-maleimide crosslinker (Sulfosuccinimidyl-4-[N-maleimidomethyl]cyclohexane-1-carboxylate or SMCC) with

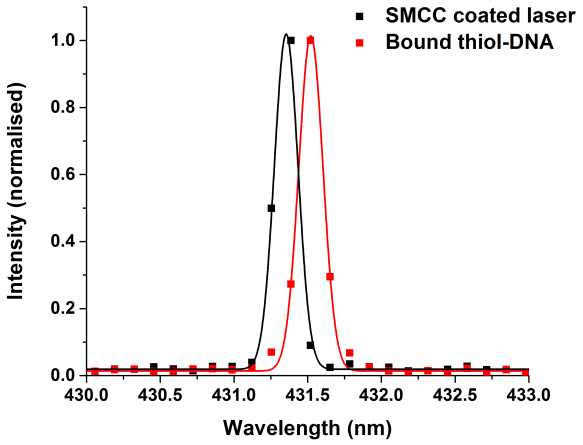

Fig. 7 Laser wavelength shift caused by binding of thiol-DNA onto the surface of an SMCC-coated laser.

the amine functional groups available onto the PPL-coated OS laser. This makes maleimide moieties available on the laser surface for further functionalisation. Fig. 7 represents the wavelength of such an SMCC functionalised laser before and after treatment with a solution of thiol-DNA. The shift (0.17 +/ 0.06 nm) is attributed to attachment of DNA onto the laser through the thiol-maleimide reaction. This represents a possible route to sensing with NA-probes.

An alternative and exciting avenue, albeit possibly synthetically challenging, will be to directly hybridise the NA probes with the OS molecules. Such a step, if viable, would enable an OS laser intrinsically bio-functionalised and 'sensing ready' after fabrication. This will create interesting opportunities for photonics and biochemistry and could lead to improved sensitivities.

Increasing the throughput of a biosensor can be obtained by (i) spatial multiplexing and by (ii) spectral multiplexing thereby enabling the parallel detection of different biomarkers. Both approaches could be combined. A possible way to realise spatial multiplexing is to have an array of OS lasers with each laser element being functionalised with a different type of molecular probes. The simplicity of the all-solution processing fabrication of the OS lasers lends itself to the assembly of such array of lasers. OS lasers in such a geometry compatible for integration with arrays of InGaN light-emitting diode excitation sources have been demonstrated.[27] Another way for spatial multiplexing is to functionalise a single OS laser, having a wide sensing area, with different molecular probes at different positions. Again, OS lasers are well suited for this as their active sensing area can be scaled from below 1 mm^2 up to several cm^2.[13] Spectral multiplexing would enable simultaneous reading of closely assembled lasers, each emitting at a different wavelength. This will necessitate the use of lasers with different nanopatern periodicity as well as the use of different OS materials for further wavelength coverage.

We will end this paper by mentioning an alternative solution-processing material that could also be utilised for such laser sensing in the future: colloidal quantum dots (CQDs). CQDs are inorganic semiconductor nanocrystals with surfaces that are coated with organic ligands. CQDs can cover a wide wavelength range (and are therefore attractive for spectral multiplexing) by tuning both the size of the CQDs and their alloy composition. The performance of optically-pumped CQD lasers is improving and their potential in format for sensing is real.[28,29] Furthermore, CQD laser sensing will benefit from the advancing functionalities that are being developed for their use as bio-imaging labels. However, the threshold performance of CQD lasers is still two orders of magnitude higher than OS lasers and further improvement is needed. Nevertheless, it is a technology worth watching as in the future it could complement OS in such laser sensing applications.

View Article Online
DOI: 10.1039/C4FD00091A

Conclusions

Light-emitting organic semiconductors are already being investigated for gas sensing using their photoluminescent and/or optical gain properties.[30-31] Here, we see that they also have great potential for biosensing in a laser format. OS can act as the laser material as well as make the interface with the biological environment. The resulting OS lasers could lead to simple and compact label-free biosensing platforms. The DNA functionalization of an OS laser that is shown here opens up opportunities using the power of NA technology, both for device research and bio-applications. The challenge is now to assess the capability and limits of this approach in true applications. The all-solution-processing fabrication capability of OS lasers is one of their advantages. Other solution-based laser materials (e.g. CQDs) might have a role to play as well.

Acknowledgements

The authors would acknowledge the support of EPSRC for this work through the grant 'Hybrid Colloidal Quantum Dot Lasers for Conformable Photonics' (EP/J021962/1) and the platform grant 'Gallium nitride enabled hybrid and flexible photonics' (EP/I029141/1).

Notes and references

[a] University of Strathclyde, Institute of Photonics, Glasgow, UK.
[b] University of Strathclyde, WestCHEM, Department of Pure and Applied Chemistry, Glasgow, UK.

1 C. A. Holland and F. L. Kiechle, Current Opinion in Microbiology, 2005, **8**, 504-509.
2 A. J. Tudos, G. A. J. Besselink and R. B. M. Schasfoort, Lab on a Chip, 2001, **1**, 83-95.
3 X. Fan, I. M. White, S. I. Shopova, H. Zhu, J. D. Suter and Y. Sun, Analytica Chimica Acta, 2008, **620**, 8-26.
4 M. Kristensen, A. Krüger, N. Groothoff, J. García-Rupérez, V. Toccafondo, J. García-Castelló, M.J. Banuls, S. Peransi-Llopis, A.

Maquieira, Optical Sensors, Optical Society of America, 2011, **SWB1** http://www.opticsinfobase.org/abstract.cfm?URI=Sensors-2011-SWB1.
5 S.M. Shamah and B.T. Cunningham, Analyst, 2011, **136**, 1090–1102.
6 V. Koubová, E. Brynda, L. Karasová, J. ˇSkvor, J. Homola, J. Dostálek, P. Tobisˇka, J. Rosˇicky´, Sensors and Actuators B: Chemical, 2001, **74**, 100–105.
7 M. Baaske and F. Vollmer, ChemPhysChem, 2012, **13**, 2, 427–436.
8 J. Homola, S.S. Yee and G. Gauglitz, Sensors and Actuators B: Chemical, 1999, **54**, 3–15.
9 B. Cunningham, J. Qiu, P. Li and B. Lin, Sensors and Actuators B: Chemical, 2002, **87**, 2, 365–370.
10 F. Volmer and S. Arnold, Nature Methods, 2008, **5**, 7, 591–596.
11 A.M. Armani, R.P. Kulkarni, S.E. Fraser, R.C. Flagan and K.J. Vahala, Science, 2007, **317**, 5839, (2007) 783–787.
12 M. Lu, S. S. Choi, C. J. Wagner, J. G. Eden and B. T. Cunningham, Applied Physics Letters, 2008, **92**, 26, 261502.
13 Y. Tan, C. Ge, A. Chu, M. Lu, W. Goldshlag, C. S. Huang, A. Pokhriyal, S. George, B. Cunningham, IEEE Sensors Journal, 2012, **12**, 5, 1174-1180.
14 C. L. C. Smith, J. U. Lind, C. H. Nielsen, M. B. Christiansen, T. Buss, N. B. Larsen, A. Kristensen, Optics Letters, 2011, **36**, 8, 1392-1394.
15 C. Vannahme, C. L. C. Smith, M. B. Christiansen and A. Kristensen, Appl. Phys. Let, 2012, **101**, 151123.
16 A.-M. Haughey, B. Guilhabert, A. L. Kanibolotsky, P. J. Skabara, G. A. Burley, M. D. Dawson and N. Laurand, Sensors and Actuators B: Chemical, 2013, **185**, 132-139.
17 A.-M. Haughey, B. Guilhabert, A. L. Kanibolotsky, P. J. Skabara, G. A. Burley, M. D. Dawson and N. Laurand, Biosensors and Bioelectronics, 2014, 54, 679-686.
18 T. Riedl, T. Rabe, H.-H. Johannes, W. Kowalsky, J. Wang, T. Weimann, P. Hinze, B. Nehls, T. Farrell and U. Scherf, Appl. Phys. Lett., 2006, **88**, 241116.
19 A. E. Vasdekis, G. Tsiminis, J.-C. Ribierre, L. O'Faolain, T. F. Krauss, G. A. Turnbull and I. D. W. Samuel, Optics Express, 2006, **14**, 20, 9211-9216.
20 Y. Yang, G. A. Turnbull, I. D. W. Samuel, Applied Physics Letters, 2008, **92**, 16, 163306.
21 A.L. Kanibolotsky, R. Berridge, P.J. Skabara, I.F. Perepichka, D.D.C. Bradley and M. Koeberg, Journal of the American Chemical Society, 2004, **126**, 42 13695–13702.
22 G. Tsiminis, Y. Wang, P.E. Shaw, A.L. Kanibolotsky, I.F. Perepichka, M.D. Dawson, P.J. Skabara, G.A. Turnbull and I.D.W. Samuel, Applied Physics Letters, 2009, **94**, 24, 243304-243304-3.
23 J. Herrnsdorf, B. Guilhabert, Y. Chen, A. Kanibolotsky, A. Mackintosh, R. Pethrick, P. Skabara, E. Gu, N. Laurand, M. D. Dawson, Optics Express, 2010, **18**, 25, 25535–25545.
24 J. Schmitt, T. Gruenewald, G. Decher, P.S. Pershan, K. Kjaer, M. Loesche, Macromolecules, 1993, **26**, 25, 7058–7063.
25 M. Lösche, J. Schmitt, G. Decher, W.G. Bouwman, K. Kjaer, Macromolecules, 1998, **31**, 25 8893–8906.
26 H.P. Erickson, Biological Procedures Online, 2009, **11**, 1, 32-51.
27 B. Guilhabert, N. Laurand, J. Herrnsdorf, Y. Chen, A. L. Kanibolotsky, C. Orofino, P. J. Skabara and M. D. Dawson, IEEE Photonics Journal, 2012, **4**, 3, 684-690.
28 B. Guilhabert, C. Foucher, A-M. Haughey, E. Mutlugun, Y. Gao, J. Herrnsdorf, H. D. Sun, H. V. Demir, M. D. Dawson and N. Laurand, Opt. Express, 2014, **22**, 7308-7319.
29 C. Foucher, B. Guilhabert, N. Laurand and M.D. Dawson, Appl. Phys. Lett., 2014, **104**, 14, 141108.
30 A. Rose, Z. Zhu, C. Madigan, T. Sager and V. Bulovic, Nature, 2005, **434**, 7035, 876-879.
31 Y. Yang, G. A. Turnbull and I. D. W. Samuel, Advanced Materials, 2010, **20**, 13, 2093-2097.